KU LEUVEN

ARENBERG DOCTORAL SCHOOL
Faculty of Science

Probing positive-parity states in $^{67}_{28}Ni_{39}$ through one-neutron transfer reactions

Jan Diriken

Supervisory Committee:
Prof. dr. M. Huyse, chair
Prof. dr. P. Van Duppen, supervisor
Prof. dr. R. Raabe, co-supervisor
Prof. dr. G. Neyens
Prof. dr. K. Temst
Prof. dr. H. Van Winckel
Prof. dr. S. Freeman
(University of Machester)

Dissertation presented in partial fulfillment of the requirements for the degree of Doctor in Science

July 2013

المنارة للاستشارات

المنارة للاستشارات

Probing positive-parity states in $^{67}_{28}Ni_{39}$ through one-neutron transfer reactions

Jan DIRIKEN

Supervisory Committee:
Prof. dr. M. Huyse, chair
Prof. dr. P. Van Duppen, supervisor
Prof. dr. R. Raabe, co-supervisor
Prof. dr. G. Neyens
Prof. dr. K. Temst
Prof. dr. H. Van Winckel
Prof. dr. S. Freeman
(University of Machester)

Dissertation presented in partial fulfillment of the requirements for the degree of Doctor in Science

July 2013

المنارة للاستشارات

© KU Leuven – Faculty of Science
Celestijnenlaan 200D box 2718, B-3001 Heverlee (Belgium)

Alle rechten voorbehouden. Niets uit deze uitgave mag worden vermenigvuldigd en/of openbaar gemaakt worden door middel van druk, fotocopie, microfilm, elektronisch of op welke andere wijze ook zonder voorafgaande schriftelijke toestemming van de uitgever.

All rights reserved. No part of the publication may be reproduced in any form by print, photoprint, microfilm or any other means without written permission from the publisher.

D/2013/10.705/47
ISBN 978-90-8649-632-7

المنارة للاستشارات

Dit werk kwam tot stand met steun van het

Fonds voor Wetenschappelijk Onderzoek (FWO) Vlaanderen

&

Studie Centrum voor Kernenergie (CSK·CEN, Mol)

المنارة للاستشارات

المنارة للاستشارات

"Science... never solves a problem without creating ten more"
-George Bernard Shaw

المنارة للاستشارات

المنارة للاستشارات

Dankwoord

Een thesis schrijf je zeker en vast niet alleen. Daarom wil ik graag hier even de tijd nemen om iedereen die mij de voorbije jaren heeft bijgestaan even te bedanken.

In de eerste plaats wil ik mijn promotoren Piet, Riccardo en Mark bedanken om mij de kans aan te reiken dit onderzoek te voeren. De vele discussies, al dan niet werk gerelateerd, en het delen van jullie ervaring met mij waren een enorm verrijkende en gedenkenswaardige ervaring.

Many thanks to the members of the examination committee, prof.dr. Gerda Neyens, prof.dr. Hans Van Winckel, prof.dr. Kristiaan Temst and prof.dr. Sean Freeman, for the careful revision and evaluation of my manuscript; and the insightful discussions during the preliminary defense.

Also the people that contributed during the IS469 experiment at CERN-ISOLDE are not to be forgotten, especially Kathrin, Vinzenz, Dennis and Thorsten. Without you performing the experiment would have been virtually impossible. Also many thanks to Freddy, Riccardo and Giacomo who contributed to the analysis and interpretation of the results.

The two post-docs who were responsible for proposing and helping setting up the experiment with me, dr. Nikolaos Patronis and dr. Iain Darby are also warmly acknowledged for the support and enlightening discussions before, during and after the experiment.

Zij die de voorbije jaren al mijn grillen, flauwe moppen, opmerkingen en andere fratsen in bureau 03.81, "*café Coulex*", moesten doorstaan verdienen hier ook een plaats. In het bijzonder Nick, Nele en Kasia: bedankt voor de steun en onvergetelijke momenten.

De overige leden van de kernspectroscopie groep wil ik ook zeker niet vergeten. Een extra bedankje gaat naar Céline, Jytte en Lars voor de talrijke ontspannende momenten.

المنارة للاستشارات

Het ondersteunend administratief IKS personeel: Isabelle, Sally, Martine, Josée, Fabienne en Katia die de voorbije jaren al mijn (last minute) paperassen in orde brachten en mij door de administratieve eindfase van mijn doctoraat loodsten. Ook Luc en Bert voor de IT-ondersteuning; en Willy voor de logistieke bijdragen wil ik hier ook graag even vermelden.

Ook de vrienden die voor de nodige afleiding hebben gezorgd gedurende de voorbije jaren wil ik ook even bedanken. In het bijzonder Joeri en Robbe die van mijn verblijf in Leuven een onvergetelijke, *life-changing* en (ont)spannende periode maakten. Bart en Wim, die voor ontelbare memorabele momenten op het thuisfront in Kortessem en ver daarbuiten zorgden, wil ik hier ook zeker hartelijk bedanken.

En tot slot de mensen die dit traject voor mij mogelijk gemaakt hebben: mijn familie en in het bijzonder mijn ouders. Bedankt voor de onvoorwaardelijke steun!

Jan,

المنارة للاستشارات

Preface

In this thesis the analysis and results of the ^{66}Ni(d,p)^{67}Ni one-neutron transfer reaction experiment are presented, with the aim to gain new insights in the distribution of neutron single-particle strength near ^{68}Ni ($Z = 28, N = 40$). The experimental data were obtained at the REX-ISOLDE radioactive beam facility (CERN, Geneva, Switzerland) using the T-REX particle detection array and Miniball γ-ray detectors. A delayed coincidence technique was developed, allowing to study μs isomers. The main results of this work have been submitted for publication in *Physical Review Letters* (Chapter 4), while a follow-up paper, containing details about the analysis has been submitted for publication in *Physical Review C* (Chapter 5).

These two articles describing the data and result from the ^{66}Ni(d,p)^{67}Ni experiment are

1. J. Diriken, N. Patronis, A.N. Andreyev, S. Antalic, V. Bildstein, A. Blazhev, I.G. Darby, H. De Witte, J. Eberth, J. Elseviers, V.N. Fedosseev, F. Flavigny, Ch. Fransen, G. Georgiev, R. Gernhauser, H. Hess, M. Huyse, J. Jolie, Th. Kröll, R. Krücken, R. Lutter, T. Mertzimekis, B.A. March, D. Muecher, R. Orlandi, A. Pakou, R. Raabe, G. Randisi, P. Reiter, T. Roger, M. Seidlitz, M. Seliverstov, C. Sotty, H. Tornqvist, J. Van De Walle, P. Van Duppen, D. Voulot, N. Warr, F. Wenander, and K. Wimmer (2013).
   "Study of the deformation-driving $\nu d5/2$ orbital in $^{67}_{28}$Ni$_{39}$ using one-neutron transfer reactions"
   Submitted for publication in *Physical Review Letters*

2. J. Diriken, N. Patronis, A.N. Andreyev, S. Antalic, V. Bildstein, A. Blazhev, I.G. Darby, H. De Witte, J. Eberth, J. Elseviers, V.N. Fedosseev, F. Flavigny, Ch. Fransen, G. Georgiev, R. Gernhauser, H. Hess, M. Huyse, J. Jolie, Th. Kröll, R. Krücken, R. Lutter, T. Mertzimekis, B.A. March, D. Muecher, R. Orlandi, A. Pakou, R. Raabe, G. Randisi, P. Reiter, T.

المنارة للاستشارات

Roger, M. Seidlitz, M. Seliverstov, C. Sotty, H. Tornqvist, J. Van De Walle, P. Van Duppen, D. Voulot, N. Warr, F. Wenander, and K. Wimmer (2013).
"Study of the ^{66}Ni(d,p)^{67}Ni one-neutron transfer reaction"
Submitted for publication in *Physical Review C*

In Chapter 1 an introduction is given to the nuclear shell model as well as an overview of the current experimental knowledge of the neutron-rich nickel region. The theoretical framework of transfer reactions is discussed in Chapter 2, while the experimental setup and analysis software are covered in Chapter 3. The main results and global overview of the analysis are given in Chapter 4, which is the letter submitted for publication in Physical Review Letters. A shortened version of the Physical Review C article can be found in Chapter 5, up to and including the analysis strategy. Chapter 6 deals with additional analysis details which are not covered in the Physical Review C article. The results of the analysis are summarized in Chapter 7 and discussed in Chapter 8. Finally, the conclusions of this work and outlook are given in Chapter 9. A collection of relevant spectra is bundled in Appendix A.

In conclusion, the pure measuring conditions and intense ^{66}Ni beam allowed to identify both positive and negative parity states in ^{67}Ni, fix spins and determine relative single-particle strengths. The extracted relative spectroscopic factors hint towards a nearly pure $\nu p_{1/2}$ ground-state configuration and two $5/2^+$ states have been identified at relatively low excitation energy, carrying a considerable amount of $\nu d_{5/2}$ single-particle strength. This observation indicates the importance of the $\nu d_{5/2}$ orbital on the structure in the region around ^{68}Ni and is believed to be essential for the rapid development of quadrupole collectivity in the neutron rich Fe and Cr isotopes below ^{68}Ni. The obtained results are also extensively compared with systematics in the lighter nickel isotopes and proton single-particle trends in the $N = 50$ isotones near ^{90}Zr. The size of the $N = 50$ gap near ^{68}Ni is estimated to be ≈ 2.6 MeV. This value is similar to the $N = 50$ gap size in $^{59-65}$Ni hinting towards limited occupation of the $\nu g_{9/2}$-orbital.

المنارة للاستشارات

Nederlandstalige samenvatting

Het atoommodel van Bohr geeft sinds 1913 een inzicht in de samenstelling van de dagdagelijkse materie en beschrijft de structuur van een atoom waarbij een massieve, positief geladen kern (straal $\sim 10^{-15}$ m) die bijna de volledige massa van het atoom bevat, omgeven wordt door een uitgestrekte wolk van negatief geladen elektronen (straal $\sim 10^{-10}$ m). De individuele bouwstenen van deze atomen, de positief geladen protonen en neutrale neutronen, ook nucleonen genoemd, worden samengehouden door de sterke kernkracht die samen met de afstotende elektromagnetische interactie tussen de protonen onderling de interne structuur van de atoomkern bepaalt. De exacte eigenschappen van de sterke kernkracht buiten de korte reikwijdte (enkele fm) en haar relatieve sterkte (ongeveer 100 maal sterker dan de elektromagnetische kracht) zijn onvoldoende gekend. Voor de meeste atoomkernen, behalve de aller lichtsten, heeft dit in combinatie met het aantal onderlinge interacties tussen de nucleonen in de kern tot gevolg dat de structuur van een atoomkern niet vanuit deze basisprincipes (zogenaamde *ab initio* berekeningen) bepaald kan worden. Door het beperkt aantal deeltjes kunnen ook geen statistische methoden aangewend worden.

Het schillenmodel benadert dit probleem vanuit de vaststelling dat voor bepaalde proton- en neutronaantallen stabielere configuraties gevormd worden, naar analogie met de edelgasconfiguraties bij atomen. De schillenstructuur van de atoomkern is het gevolg van het feit dat de energieniveaus waarin nucleonen geplaatst worden, gegroepeerd zijn in schillen. Wanneer een dergelijke schil gevuld is, stabiliseert dit de structuur van de kern. Vervolgens kan de kernstructuur in de nabijheid van dergelijke *magische kernen* beschreven worden vertrekkende van deze stabiele, gesloten schillenconfiguratie. De interacties tussen het beperkte aantal *valentienucleonen* buiten deze gesloten kern wordt beschreven door effectieve interacties. Hierdoor kunnen eigenschappen van kernen voorspeld worden en door middel van experimentele testen geverifieerd

المنارة للاستشارات

worden. Omgekeerd kunnen experimentele resultaten ook belangrijke informatie verschaffen voor deze theoretische modellen welke gebruikt kunnen worden om bv. de effectieve interacties in de modelruimte op punt te stellen.

De voorbije decennia heeft het kernfysisch onderzoek zich meer gericht op onderzoek naar kernen met extreme proton-neutronverhoudingen, de zogenaamde exotische kernen. Onder deze extreme proton-neutronverhoudingen kunnen verborgen eigenschappen van de sterke interactie aan het licht brengen. Een voorbeeld hiervan zijn de halo-kernen zoals ^{6,8}He en ^{11}Li. Verder blijkt uit zulk onderzoek ook dat de waargenomen magische getallen bij stabiele kernen niet noodzakelijk behouden blijven in exotische kernen en dat onder extreme proton-neutron-verhoudingen nieuwe magische getallen kunnen ontstaan. Dergelijke fenomenen leveren belangrijke inzichten in de details van de wisselwerkingen tussen de nucleonen in een atoomkern en laat een optimalisatie van de bestaande theoretische modellen toe. In sommige gevallen leiden dergelijke waarnemingen er ook toe dat basisveronderstellingen aangepast moeten worden.

In dit werk wordt een specifiek experiment besproken naar de kernstructuur in de omgeving van ^{68}Ni ($Z = 28, N = 40$). Hier vormen de protonen een gesloten $Z = 28$ schil, terwijl de neutronen aanleiding geven tot een gesloten $N = 40$ harmonische oscillator subschil. Deze subschilsluiting wordt gevormd tussen de pf-*orbitalen* met een *negatieve pariteit* en het $g_{9/2}$-orbitaal met positieve pariteit (zie Figuur 1.7 op p. 16). Het begrip pariteit heeft betrekking tot de spiegelsymmetrie van deze orbitalen. De magiciteit van ^{68}Ni werd in het verleden geopperd aangezien de energie van de eerste geëxciteerde toestand erg hoog is in vergelijking met naburige even nikkelisotopen. Verder werd ook een lokaal minimum gemeten in de gereduceerde overgangswaarschijnlijkheid ($B(E2; 2^+ \rightarrow 0^+)$) tussen deze toestand en de grondtoestand, wat wijst op een verminderde collectiviteit en dus sferisch karakter van ^{68}Ni (zie Figuur 1.8 op p. 17). De sterkte van de $N = 40$ schilsluiting werd echter in vraag gesteld daar massametingen geen aanwijzing naar een (sub)schil-sluiting opleverden. Dit wordt verder ondersteund in de neutronrijke ijzer- en chroomkernen rond $N = 40$ waar een sterk collectief gedrag wordt waargenomen en zijn er geen aanwijzingen zijn voor een $N = 40$ subschilsluiting. Recente schillenmodel-berekeningen suggereren dat de sterke ontwikkeling van collectief gedrag en kernvervorming in het gebied rond ^{68}Ni te wijten is aan de aanwezigheid van de $\nu g_{9/2}$-, $\nu d_{5/2}$- en $\nu s_{1/2}$-orbitalen welke een *quasi-SU(3)* orbitaalopvolging vormen en een sterke quadrupool-coherentie induceren. Het feit dat het expliciet incorporeren van het $\nu d_{5/2}$-orbitaal in deze schillenmodel-berekeningen essentieel is om de experimentele trends te reproduceren, onderstreept reeds het belang van dit orbitaal op de kernstructuur in dit massagebied. Dit heeft ook gevolgen voor de structuur van de zeer neutronrijke kern ^{78}Ni ($Z = 28, N = 50$) waarvoor

المنارة للاستشارات

een dubbel-magisch karakter verwacht wordt, aangezien zowel 28 als 50 magische getallen vormen bij stabiele kernen. Echter, het behoud van deze magische getallen in ^{78}Ni is niet gegarandeerd. Recente berekeningen, gebruik makend van *drie-deeltjes-interacties*, tonen aan dat de sterkte van de $N = 50$ schilsluiting bepaald wordt door de bezetting van het $\nu g_{9/2}$ orbitaal (gelegen tussen de $N = 40$ en 50 schilsluitingen). Het bepalen van de grootte van deze $N = 50$ schilsluiting in de buurt van ^{68}Ni kan dus gebruikt worden om een schatting te maken van de grootte in ^{78}Ni.

Met behulp van één-neutron transferreacties op ^{66}Ni werd de structuur van ^{67}Ni bestudeerd, een kern die gezien kan worden als ^{68}Ni gekoppeld met een neutron-gat. Bij dergelijke experimenten worden twee kernen, een ^{66}Ni kern en een deuteriumdeeltje (gebonden proton en neutron), met elkaar in botsing gebracht. Naast het typisch elastisch verstrooiingsproces kan er occasioneel ook een neutron worden overgedragen van het deuteriumdeeltje naar ^{66}Ni. Aangezien de onderliggende ^{66}Ni kern onaangeroerd blijft in deze transferreactie is dit type experiment gevoelig voor het *ééndeeltjeskarakter* van de toestanden in ^{67}Ni. De *angulaire distributie* (waarschijnlijkheid waarmee een deeltje in een bepaalde richting wordt uitgezonden) van het resterende proton is nauw verbonden met spin van de toestand waarnaar het neutron werd overgedragen. De reden hiervoor ligt in het *behoud van angulair moment* waardoor het relatief angulair moment tussen het resterend proton en ^{67}Ni even groot moet zijn als de hoeveelheid angulair moment van het overgedragen neutron ten opzichte van de onderliggende ^{66}Ni-kern. Indien een grote spintoestand gevoed wordt in de reactie (en er dus veel angulair moment wordt overgedragen in de reactie), zal het resterend proton onder een grote hoek ten opzichte van ^{67}Ni worden uitgezonden. Het meten van deze hoekafhankelijkheid kan dus gebruikt worden om de hoeveelheid overgedragen angulair moment te bepalen (zie Figuur 2.7 op p. 67 voor enkele voorbeelden van de gevoeligheid van deze methode). De sterkte waarmee een bepaalde toestand gevoed wordt, hangt af van de bijdrage van de ééndeeltjesconfiguratie tot de *golffunctie* van de toestand. De verhouding van de gemeten werkzame doorsnede tot de verwachte werkzame doorsnede voor een zuivere configuratie wordt ook de *spectroscopische factor* genoemd en duidt de zuiverheid van het ééndeeltjeskarakter van een welbepaalde toestand aan. Het *excitatiespectrum* van deze kern wordt beheerst door een combinatie van één-deeltjesexcitaties en collectieve toestanden. Hier werd echter geopteerd om te werken met relatieve spectroscopische factoren om de invloed van het gebruikte reactiemodel te verminderen. Het koppelen van een deeltje of een gat aan een stabiele, magische kern levert doorgaans een relatief duidelijke scheiding op tussen deze twee types van excitaties waardoor de bijna zuivere ééndeeltjes toestanden geïdentificeerd kunnen worden. Door een dergelijke studie uit te voeren op ^{67}Ni kan de zuiverheid van de geëxciteerde toestanden worden nagegaan om zo meer inzicht te krijgen in het stabiliserend effect van

المنارة للاستشارات

de $N = 40$ schilsluiting. Verder kunnen ook de posities van de neutronorbitalen bepaald worden om zo een schatting van de grootte van de $N = 40$ en 50 schilsluitingen te maken.

Proeven met exotische kernen zoals ^{66}Ni worden echter belemmerd door het feit dat deze kernen een korte levensduur hebben en snel vervallen naar een meer stabiele configuratie. Dit zorgt voor complicaties bij het uitvoeren van transferexperimenten aangezien de reactie in *inverse kinematica* dient te gebeuren omdat er geen trefschijf bestaande uit het instabiele ^{66}Ni geproduceerd kan worden. Daarom moeten de ^{66}Ni-isotopen aangemaakt worden, vervolgens tot een grote energie versneld worden en gericht worden op een trefschijf die deuterium bevat.

Voor dit experiment werden de ^{66}Ni isotopen geproduceerd aan de ISOLDE faciliteit te CERN, Genève. Hier wordt een primaire trefschijf bestaande uit uranium blootgesteld aan hoog-energetische protonen. Door interactie tussen deze protonen en uraniumkernen wordt door middel van *fissie* een breed spectrum van lichtere kernen gevormd. Via diffusie verlaten deze kernen de primaire trefschijf en werden naar de ionisatiebron geleid, waar ze door *resonante laser ionisatie* selectief geïoniseerd worden. Het laserlicht wordt afgestemd op het atomaire spectrum van ^{67}Ni om het alzo selectief te ioniseren. Deze ionen kunnen vervolgens uit de ionenbron onttrokken worden door het aanleggen van een potentiaalverschil (30 kV). Hierna wordt de bundel door een massascheider gestuurd zodat een selectie op massa kan gebeuren. Aangezien het naversnellen van deze laag-energetische bundel efficienter is voor ionen in een grote ladingstoestand worden de 1^+ ^{66}Ni ionen voor een bepaalde periode (30 ms) bestraald met een intense elektronenbundel tot een ladingstoestand van 16^+ bereikt was. Om dit proces optimaal te laten verlopen wordt de continue bundel eerst geaccumuleerd in REX-TRAP, waarna ze wordt doorgegeven aan REX-EBIS waar ze naar deze grote ladingstoestand gebracht worden. De laatste stap was de naversnelling met behulp van de lineaire REX-versneller, welke de ^{66}Ni bundel versnelt tot een energie van 2.95 MeV/u waarna ze op de reactie trefschijf gericht wordt.

Rond deze trefschijf bevinden zich twee types van detectoren. De silicium detectoren registreren de verstrooide deeltjes die het resultaat zijn van de interactie tussen bundel en trefschijf. Deze gesegmenteerde en positiegevoelige detectoren meten niet enkel de energie maar ook de richting van het gedetecteerde deeltje. Doordat de energie in twee stappen (d.w.z. twee verschillende silicium lagen) gemeten wordt, kan ook de aard van het deeltje bepaald worden doordat het energieverlies afhankelijk is van de ogenblikkelijke energie, massa en lading van het deeltje. Indien een proton gedetecteerd wordt, kan uit de gemeten energie en positie door gebruik te maken van het *behoud van energie* verder bepaald worden welke de excitatie energie van de uitgaande ^{67}Ni-kern is. Het tweede

المنارة للاستشارات

type detectoren is opgebouwd uit germanium en detecteert de γ straling die wordt uitgezonden wanneer een aangeslagen kern vervalt naar een lager gelegen energieniveau. Rond de reactiekamer bevinden zich daarom acht Miniball cluster detectoren die ieder bestaan uit drie germanium kristallen die ieder op hun beurt een zesvoudige segmentatie bezitten. Hierdoor bestaat het γ-detectie systeem uit 144 individuele segmenten, waarmee de richting van de uitgezonden γ straal bepaald kan worden. Aangezien de levensduur van de aangeslagen niveaus erg kort is ($\sim$ ps) kan deze straling met behulp van de Miniball detectoren waargenomen worden. Eerdere studies van het ^{67}Ni isotoop hebben echter een aangeslagen, *isomeer* toestand geïdentificeerd met een levensduur van 13.3 μs. Door de grote snelheid van de nikkelkernen kan de karakteristieke straling geassocieerd met het verval van deze toestand niet met de Miniball detectoren gezien worden. Omwille hiervan is een tweetal meter na de reactie trefschijf een verwijderbare folie geplaatst waarin de inkomende bundel wordt gestopt. Met een aparte germanium-detector kan vervolgens gezocht worden naar de specifieke, vertraagde overgangen horend bij deze isomeer. Door het maken van correlaties op een lange tijdschaal (120 μs in vergelijking met 1 μs voor γ stralen gedetecteerd in Miniball) kan alsnog de isomeer toestand geïdentificeerd worden (zie bv. Figuur 6.5 op p. 150).

Het combineren van zowel gesegmenteerde, positiegevoelige deeltjes- en γ-detectoren was noodzakelijk aangezien de energieresolutie van deeltjes onvoldoende was om individuele aangeslagen toestanden te kunnen onderscheiden (zie Figuur 6.7 en 6.8 op p. 152). Indien het excitatiespectrum gekend is, kon het karakteristieke vervalschema gebruikt worden en konden in de verdere analyse enkel protonen gebruikt worden die *in coïncidentie waren* met een gekende γ-straal. Verder bevatte het patroon van het γ verval ook informatie die nuttig was bij het toewijzen van een spin aan een aangeslagen toestand.

In eerste instantie werd daarom met behulp van de vergaarde data het excitatie- en γ-verval-spectrum van ^{67}Ni opgesteld. Hierbij werden 21 toestanden geïdentificeerd en 40 γ-overgangen geplaatst. Aangeslagen toestanden tot een excitatie-energie van 5708 keV, een energie die erg dicht bij de *neutronbindingsenergie* van 5808 keV ligt, werden in dit experiment waargenomen. Aangezien de kinetische energie van het resterend proton afneemt naarmate ^{67}Ni aangemaakt wordt met een grotere excitatie-energie, was het proton detectiebereik voor toestanden hoger gelegen dan 3620 keV te beperkt om een uitspraak te doen over de spin van deze toestanden.

Op basis van de gemeten hoekdistributies in combinatie met de verhoudingen in het karakteristieke γ verval konden de spins en relatieve spectroscopische factoren van zeven toestanden bepaald worden (zie Figs. 7.1, 7.2 en 7.3 op pp. 163, 167 en 168). Voor de grondtoestand en eerste twee aangeslagen toestanden werd reeds een spin gesuggereerd op basis van voornamelijk β verval

المنارة للاستشارات

en onelastisch reactiewerk (zie hiervoor Refs. [Wei99, Kou78, Gir88, Paw94, Geo02, Grz98, Zhu12, Mac03, Rik00]). Onze nieuwe data bevestigen deze voorstellen. Twee structuren met een sterk γ-verval naar de $9/2^+$ isomeer op 1007 keV werden waargenomen met excitatie-energieën van 2207 en 3277 keV. Beide toestanden werden geïdentificeerd als $5/2^+$ toestanden en de sterkte waarmee deze toestanden werden waargenomen duidt op het effect van het $\nu d_{5/2}$-orbitaal op de structuur van deze toestanden. De sterkst gevoede toestand wordt teruggevonden op een excitatie energie van 3621 keV. Echter, doordat deze toestand zwak gebonden is, zijn de verwachte hoekdistributie niet erg afhankelijk van de hoeveelheid overgedragen angulair moment. Het karakteristieke γ verval geeft de voorkeur aan een spin 1/2 interpretatie, maar er kan geen directe uitspraak over de pariteit worden gedaan.

Voor de presentatie van de gemeten relatieve spectroscopische factoren werd het $9/2^+$ niveau als referentie gebruikt, omwille van het feit dat uit één neutron transferreacties op lichtere nikkelkernen is gebleken dat dit niveau een erg zuivere één-deeltjes-configuratie heeft. De gemeten relatieve spectroscopische factoren tonen een waarde consistent met 1 voor de $1/2^-$ grond toestand en kleinere waarden voor de overige negatieve pariteitstoestanden op 694 keV (0.3, $5/2^-$) en 1724 keV (0.2, $3/2^-$). Het zuivere karakter van de grondtoestand werd reeds gesuggereerd daar de meting van het *magnetisch moment* van deze toestand in goede overeenstemming is met de verwachting voor een zuivere $\nu p_{1/2}$ configuratie (zie Ref. [Rik00]). Van de overige pf-orbitalen wordt aangenomen dat deze reeds aanzienlijk gevuld zijn in ^{66}Ni en de kleine relatieve spectroscopische factoren reflecteren deze aanname. De relatieve spectroscopische factoren van de twee $5/2^+$ toestanden op 2207 en 3277 keV, respectievelijk 0.25 en 0.28, duiden aan dat bijna 50% van de beschikbare $\nu d_{5/2}$ ééndeeltjes-sterkte bevat zit in deze twee toestanden. Het feit dat beide toestanden bijna identieke spectroscopische factoren bezitten duidt ook aan dat er een aanzienlijke menging optreedt tussen de zuivere ééndeeltjes- en meer collectieve, vervormde configuraties. Opvallend is de erg grote relatieve spectroscopische factor van het niveau op 3621 keV waarvoor een lage spinwaarde wordt verwacht op basis van het γ verval. Afhankelijk van spin van deze toestand bedraagt deze 1.1 ($1/2^+$) of 1.9 ($1/2^-$). Doordat deze laatste waarde niet fysisch is, heeft een $1/2^+$ spininterpretatie een lichte voorkeur. De overige toestanden met een energie lager dan 3621 keV worden zwak gevoed in de transferreactie en de beperkte statistiek laat niet toe om een uitspraak te doen over de spin van deze toestanden. Voor hoger gelegen toestanden is het gemeten bereik in de hoekdistributie te klein waardoor eveneens geen uitspraak gedaan kan worden over de spin.

Een vergelijking met de resultaten van één-neutron transferreacties op ^{58,60,62,64}Ni toont enkele trends (zie Figuur 8.1 op p. 174). Eerst en vooral is er de verwachte afname van één-deeltjes sterkte in de pf-orbitalen daar deze steeds

المنارة للاستشارات

meer gevuld raken naarmate er neutronen worden toegevoegd. Dit vertaalt zich ook in de afname van de excitatie-energie van het $9/2^+$ niveau, welke in elk isotoop als referentie wordt gebruikt om relatieve spectroscopische factoren te presenteren. Opvallend is ook de evolutie in de $\ell = 2$ toestanden op grote energie. De $\ell = 2$ één-deeltjessterkte is erg *gefragmenteerd* in de lichtere nikkelkernen, hoewel enkele van de laagstliggende $5/2^+$-toestanden een redelijke fractie van de één-deeltjessterkte bevatten (relatieve spectroscopische factor ≈ 0.1 - 0.3). Deze $\nu d_{5/2}$ één-deeltjessterkte concentreert zich echter meer in deze laagliggende $5/2^+$ toestanden naarmate het neutronnummer toeneemt, met een totale relatieve sterkte van ongeveer 50% in ^{67}Ni. Uit de globale systematiek blijkt ook dat er een duidelijke afscheiding is tussen de negatieve pariteits pf-toestanden op lage excitatie-energie en positieve pariteits sd-toestanden op grotere excitatie-energie. Vanuit dit oogpunt kunnen de geobserveerde toestanden in ^{67}Ni boven 2207 keV geïnterpreteerd worden als $\ell = 0$ of 2 toestanden. Dit argument ondersteunt ook weer de $1/2^+$ interpretatie van het niveau op 3621 keV, daar er geen sterke $\ell = 1$ toestanden zijn waargenomen in lichtere nikkelkernen. De *geïntegreerde werkzame doorsnedes* over het bereik waarin protonen kunnen worden waargenomen voor toestanden boven 3621 keV zijn identiek voor $\nu s_{1/2}$ en $\nu d_{5/2}$ configuraties. Hierdoor is het mogelijk een relatieve spectroscopische factor voor deze toestanden te bepalen, zonder dat de eigenlijke spin gekend is. Deze waarden beperken zich tot maximaal 0.16 en duiden nog steeds op aanzienlijke fragmentatie van de $\ell = 0$ en 2 ééndeeltjes-sterkte.

Een tweede gebied waar vergelijking mogelijk is, bevindt zich rond ^{90}Zr, waar de neutronen een gesloten $N = 50$ schil vormen en het Fermi niveau van de protonen zich rond $Z = 40$ bevindt (zie Figuur 8.10 op p. 189). Door te kijken naar de proton één-deeltjes-sterkte in de $N = 50$ *isotonen* kan deze systematiek vergeleken worden met de resultaten in het nikkelgebied. Voor de toestanden met negatieve pariteit (pf-orbitalen) en het $g_{9/2}$-niveau is er een grote gelijkenis tussen ^{67}Ni en zijn spiegelkern ^{89}Y. Zowel voor de positie als de relatieve spectroscopische factoren van deze toestanden is de overeenkomst erg goed. De fragmentatie van de $\ell = 2$ één-deeltjes sterkte is echter sterker in het ^{90}Zr-gebied en bevindt zich op een grotere excitatie-energie. De invloed van het $\pi d_{5/2}$-orbitaal is hierdoor niet nadrukkelijk aanwezig in de laagliggende $5/2^+$ toestanden. Uit de verdeling van de één-deeltjes sterkte in ^{89}Y wordt de grootte van de $Z = 50$ schilsluiting geschat op 3.9 MeV.

Twee problemen zijn aanwezig bij de bepaling van de grootte van de $N = 50$ schilsluiting. Voor de lichtere nikkelkernen, waar een grote fragmentatie van de sd-één-deeltjes-sterkte werd waargenomen, kan er voor de $\ell = 2$ toestanden geen onderscheid gemaakt worden tussen de spins $3/2^+$ en $5/2^+$. In het geval van ^{67}Ni is dit probleem ook aanwezig in combinatie met het feit dat er voor de meeste toestanden geen onderscheid gemaakt kan worden tussen $\ell = 0$

المنارة للاستشارات

en 2. Bovendien is het niet zeker dat de volledige $\nu d_{5/2}$ één-deeltjessterkte geobserveerd werd in ^{67}Ni. Om vooralsnog een schatting van de grootte van de $N = 50$ schilsluiting te kunnen maken wordt aangenomen dat i) in de lichtere nikkelkernen alle $\ell = 2$ toestanden een spin $5/2^+$ hebben en ii) dat voor ^{67}Ni alle geobserveerde toestanden hoger gelegen dan 3 MeV een $\ell = 2$ karakter hebben. Wanneer deze procedure wordt toegepast wordt een vrijwel constante grootte van 2.6 MeV voor de $N = 50$ schilsluiting bekomen. Deze schilsluiting is betrekkelijk kleiner dan de $Z = 50$ schilsluiting in ^{90}Zr, wat de sterkere invloed van het $\nu d_{5/2}$-orbitaal in het nikkelgebied kan verklaren. Tevens toont de indicatie van een constante $N = 50$ schilsluiting in $^{59-67}$Ni aan dat de neutronbezetting van het $\nu g_{9/2}$-orbitaal in ^{66}Ni beperkt is, aangezien de grootte van de $N = 50$ schilsluiting immers mede bepaald wordt door de bezetting van het $\nu g_{9/2}$-orbitaal.

Samenvattend werd het eerste één-neutron transferreactie-experiment in het neutron-rijke nikkel gebied succesvol uitgevoerd met behulp van de T-REX opstelling gekoppeld met de Miniball γ-detectoren. Er werd een duidelijke invloed van het $\nu d_{5/2}$-orbitaal, gelegen boven de $N = 50$ schilsluiting, waargenomen en dit liet toe een schatting te maken van de grootte van deze $N = 50$ schilsluiting nabij ^{68}Ni. De grootte van de $N = 50$ schilsluiting in ^{67}Ni bedraagt 2.6 MeV, en gedraagt zich constant ten opzichte van de lichtere nikkelisotopen. Hieruit kan worden afgeleid dat de bezetting van het $\nu g_{9/2}$-orbitaal in ^{66}Ni beperkt is.

Voor toekomstige studies is het aangewezen om enerzijds deze reactie te herhalen met geoptimaliseerde opstelling zoals bv. de *Helical Orbit Spectrometer* of HELIOS detector. Met deze detector is het mogelijk met een grote energieresolutie in een groter hoekbereik te meten. Hierdoor moet het mogelijk zijn de toestanden gelegen boven 3 MeV te karakterisren om zo de grootte van de $N = 50$ schilsluiting nauwkeuriger te bepalen. Ook het gebruik van de grotere bundelenergie beschikbaar met HIE-ISOLDE zorgt voor meer karakteristieke en uitgesproken angulaire distributies. Anderzijds is het interessant de evolutie van de $N = 50$ schilsluiting te volgen in zwaardere, meer neutronrijke nikkelkernen. Door de korte levensduur en lange diffusietijden van deze kernen zullen echter andere productietechnieken aangewend moeten worden, zoals bv. *in-vlucht* technieken. Tot slot zou een vergelijking tussen de gemeten resultaten en recente schillenmodelberekingen nieuwe en betere inzichten in de data kunnen bieden. De data rond de exacte positie van de één-deeltjes orbitalen in de buurt van ^{68}Ni kan ook gebruikt worden om via theoretische modellen nieuwe voorspellingen te maken aangaande de structuur van ^{78}Ni.

المنارة للاستشارات

Abbreviations

ANC	Asymptotic Normalization Coefficient
CM	Center of mass frame of reference
CRC	Coupled-Reaction Channel Approximation
CS	Closed Shell
DC	Doppler correction
DCO	Delayed coincidence tagging
DGF	Digital Gamma Finder (XIA)
DM	Doubly magic nucleus
DSSSD	Double sided silicon strip detectors
DWBA	Distorted-wave Born approximation
EBIS	Electron Beam Ion Source
GPS	General Purpose Separator
HF	Hartree-Fock
HO	Harmonic oscillator
HRS	High Resolution Separator
IF	In-Flight
ISOL	Isotope Separation On-Line
LAB	Laboratory frame of reference
LINAC	Linear accelerator
MBS	Multi-Branch System
PSA	Pulse-shape analysis

المنارة للاستشارات

PWBA	Plane-wave Born approximation
SE	Schrödinger equation
SEMF	Semi-empirical mass formula
SF	Spectroscopic factor
SH	Spherical Harmonics
SPANC	Single-particle asymptotic normalization factor
SPE	Single particle energy
TBME	Two-body matrix elements

المنارة للاستشارات

List of Symbols

b_{nLj}	Single-particle asymptotic normalization factor
$B(E2; J_i^\pi \rightarrow J_f^\pi)$	Reduced $E2$ transition probability between the initial state J_i^π to the final state J_f^π
c	Speed of light: c =2.99792458 m/s^2
C_{Lj}	Asymptotic normalization factor
$\frac{\mathrm{d}\sigma(\theta,\varphi)}{\mathrm{d}\Omega}$	Differential cross section for a nuclear reaction with polar coordinates θ and φ
e	Elementary charge: 1.602 10^{-19}C
$E(J_i^\pi)$	Excitation energy of the i^{th} state with spin and parity J^π
E_x	Energy of particle x
ϵ	Detection efficiency for detecting gamma rays, particles, ...
η	Sommerfeld parameter
$F_L(kR)$	Ricatti-Neumann functions
j_i	Incoming projectile flux, expressed in particles per seconds.
$f(\theta,\varphi$	Scattering function as a function of θ and φ
$G_L(kR)$	Ricatti-Bessel functions
$G^+(R,R\prime)$	Green's function used to solve inhomogeneous differential equations
$\hat{G}^+$	Integral operator of the Green's function
H	Hamiltonian
$H_L^{(\pm)}(kR)$	Ricatti-Haenkel functions
$\hbar$	Planck's constant: 1.055 Js
$\vec{T}$	Total isospin vector
J^π	State with spin J and parity π
$k_{i,f}$	Wave number of the initial or final wave
L	Angular momentum of a bound nucleon with respect to the binding core.
ℓ	Relative angular momentum between two colliding nuclei
L_z	z-projection of the angular momentum operator
m_e	Electron mass

المنارة للاستشارات

m_x	Mass of particle x
m_{AB}	Total mass of particles A and B ($m_{AB} = m_A + m_B$)
μ	Reduced mass of particles A and B: $\mu = m_A m_B / mAB$
N	(Harmonic) oscillatory shell number
n	Principal quantum number
N_A	Avogadro's constant ($6.022\ 10^{23}$ mol^{-1}
$N_{\alpha\prime\alpha}$	Overlap operator between basis states α and $\alpha\prime$
$\Delta\Omega$	Solid angle coverage
$\vec{p}_x$	Linear momentum vector of particle x
δ_L	Phase shift for partial wave L
$\Phi_{A:B}$	Overlap-function between nuclei A and B
π	Parity of a particular state
$P_L(\cos\theta)$	Legendre Polynomials
$\psi_\alpha(\vec{R}_x, \xi_p, \xi_t)$	Wave function of relative motion (in CM frame) for two particles in mass partition α with internal states defined by ξ_p and ξ_t
Q	Q value of a nuclear reaction
$\vec{q}$	Momentum transfer vector
$\vec{R}$	Relative position vector of two particles
$\vec{r}_x$	Position vector of particle x
R_c	Cut-off radius
ρ	Density of matter
$\mathbf{R}_L$	partial-wave R-matrix element
δS_{2n}	Difference in two neutron separation energy: $\delta S_{2n} = S_{2n}(Z,N) - S_{2n}(Z,$
$\vec{S}$	Position vector of the CM frame of reference of two particles
S_{Lj}	Spectroscopic factor of excited state with total spin j and angular momentum L
$\mathbf{S}_L$	Partial-wave S-matrix element
S_n(x)	Neutron separation energy: the amount of energy required to remove one neutron from nucleus x
$\Omega_\alpha(R)$	Source term in an inhomogeneous differential equation.
$\mathbf{T}_L$	Partial-wave T-matrix element
$\vec{v}_x$	Velocity vector of particle x
Φ	Wave function of the movement of the CM frame of reference
Ψ	Total wave function of a given system
ψ	Wave function of two colliding particles in the CM frame of reference
ξ	Internal coordinates of a nucleus
Y_{Lm}	Spherical harmonic functions with angular momentum L and z-projection m

المنارة للاستشارات

Contents

المنارة للاستشارات

المنارة للاستشارات

المنارة للاستشارات

المنارة للاستشارات

List of Figures

المنارة للاستشارات

المنارة للاستشارات

المنارة للاستشارات

المنارة للاستشارات

List of Tables

المنارة للاستشارات

المنارة للاستشارات

1

Structure of Atomic Nuclei

In this first chapter, the elementary features of atomic nuclei are discussed. Then the nuclear shell model, one of the basic models to describe nuclei, is introduced. Finally an overview of the current knowledge of the nuclear structure in the neighborhood of ^{68}Ni ($Z = 28, N = 40$) is discussed.

1.1 The atomic nucleus

All atomic nuclei in nature consist of two sorts of particles called *nucleons*[1], namely Z positively charged *protons* and N electrically neutral *neutrons*. Around this nucleus of $A = Z + N$ nucleons, a negatively-charged electron cloud is found, made up by Z electrons to create a global neutral atom. The chemical properties of the atom are due to the interactions of the electrons surrounding this atom with those of other atoms. Since the number of electrons surrounding a nucleus equals the number of protons in a neutral atom, these chemical properties are directly related to the proton number Z. Hence, the number of protons defines the *element*, independently of the number of neutrons. So far, elements up to and including 118 protons have been produced and studied. All elements are named like e.g. hydrogen, iron, nickel, lead and uranium. For a given element, nuclei can be formed with a varying number of neutrons without altering their chemical properties. These atoms are called the *isotopes* of a specific element.

[1] These nucleons are not fundamental particles and have an internal structure: they are composed out of three *quarks*, which in turn are fundamental particles.

المنارة للاستشارات

All nuclei found in nature were created either by *primordial nucleosynthesis* (mostly ^{1}H, ^{4}He and other elements up to ^{7}Li), *hydrogen burning*, *CNO cycles* in light stars (^{4}He) and *α-burning* in heavy stars (^{16}O, ^{20}Ne, ^{24}Mg, ^{28}Si and in very heavy stars all the way up to ^{56}Fe, the nucleus with the largest binding energy per nucleon). Heavier elements can be produced in low to intermediate mass (Asymptotic Giant Branch (AGB)) stars with a CO core by the *s-process*, involving neutron capture and subsequent β decay on the secondary Fe nuclei [Str06]. During supernovae explosions larger densities of neutrons lead to the *r-process*. Some stable nuclei found in nature can not be produced during the r- or s-processes, hinting to other production mechanisms. These are the *rp-process* and the *p-process*. The former occurs mostly in binary systems when stellar material rich in hydrogen is heated to high temperatures. The latter happens in the outer layers of core-collapsed supernovae and involves photo disintegration on previously created stable nuclei. More information on these stellar production mechanisms can be found in chapter 1 of [Tho09].

Not all combinations of protons and neutrons will result in a stable configuration. When individual nucleons bind and form a nucleus, energy is released. Due to the equivalence between mass and energy: $E = mc^2$, the mass of the resulting nucleus will be lower than the sum of its individual building blocks by an amount equal to the *binding energy* which can be experimentally determined through mass measurements [Bol87]:

$$B(A,Z) = \left(Zm_p + Nm_n - m_{A,Z}\right)c^2. \tag{1.1}$$

Here m_p and m_n are the proton and neutron mass respectively, while $m_{A,Z}$ is the total mass of the nucleus with Z protons and in total A nucleons. A theoretical expression, based on the *liquid drop model*, called the *semi-empirical mass formula* (SEMF) or *Bethe-Weizsäcker mass formula* has been found, with parameters fitted to the available experimental data:

$$B(A,Z) = a_V A - a_S A^{2/3} - a_C \frac{Z^2}{A^{1/3}} - a_A \frac{((A/2)-Z)^2}{A} + \delta(A,Z) \tag{1.2}$$

The terms in Eq. 1.2 are from left to right: the volume ($a_V = 15.8$ MeV), surface ($a_S = 18.3$ MeV), Coulomb ($a_C = 0.714$ MeV), asymmetry ($a_A = 23.2$ MeV) and pairing term ($\delta = +\frac{12}{A^{1/2}}$ MeV for even-even nuclei and $\delta = -\frac{12}{A^{1/2}}$ MeV for odd-odd nuclei). The Coulomb term tends to disfavor proton-rich nuclei as their mutual Coulomb repulsion lowers the binding energy. The asymmetry term[2] on the other hand prefers nuclei with an equal amount of protons and

[2]The justification for this term can be found in the fact that nucleons are fermions and due to the Pauli principle two fermions cannot occupy the same quantum state. When there is a large asymmetry between the number of protons and neutrons, one type of nucleons must be added to higher and higher energy levels, thus increasing the total energy of the nucleus and decreasing the binding energy.

المنارة للاستشارات

neutrons. For nuclei with $Z < 20$, the Coulomb term is not too strong and hence most stable nuclei have $Z \approx N$ in this mass region. For heavier elements more neutrons must be added in order to find a stable balance between the Coulomb and asymmetry term, leading to stability for nuclei with $N \approx 1.4Z$.

The nucleons in atomic nuclei obey the four fundamental forces of nature: the strong, electromagnetic, weak and gravitational interaction[3]. Under the influence of these first three types of interactions, unstable configurations can *decay* to a more stable nucleus. Radioactive decay can happen in various ways like e.g. α decay, β decay, electron capture and spontaneous fission [Kra87]. The strong interaction is essential in nuclei as it needs to overpower the repulsive electromagnetic interaction between the protons. However the exact behavior and properties of the strong nucleon-nucleon interaction are not known. Scattering data between free nucleons[4] have been used to model realistic nucleon-nucleon (and even three-nucleon) interaction potentials. Examples of such nucleon-nucleon interaction models are a.o. the Paris [Lac80], Bonn [Mac87] and Argonne [Wir95] potentials. These potentials can be used to calculate the structure and properties of nuclei from an *ab-initio* approach and this has been done for nuclei up to mass 13 [Nav07]. This limit for the calculations is set by current computing capabilities as the number of nucleon-nucleon(-nucleon) interactions increases rapidly when nucleons are added to the system [Var11].

1.2 The nuclear shell model

When looking at systematics of experimental observables over the entire nuclear landscape it can be seen that some specific numbers of nucleons show enhanced stability with respect to their neighbors. Fingerprints of increased stability can be identified when studying systematics of proton or neutron separation energies, $E(2_1^+)$ (the energy of the first excited 2^+ state) or $B(E2; 2_1^+ \rightarrow 0_{\text{gs}}^+)$ (reduced transition probability or indication of quadrupole collectivity in this transition) in even-even nuclei. These numbers, which are called *magic numbers* are experimentally observed to be 2, 8, 20, 28, 50, 82 and 126.

From a quantum mechanical point of view, one has to solve the Schrödinger equation (SE) of the A-nucleon system with the Hamiltonian:

$$H = \sum_{i=1}^{A} \frac{\mathbf{p}_i^2}{2m_i} + \sum_{i>j=1}^{A} V_{ij}(\mathbf{r}_i - \mathbf{r}_j) \tag{1.3}$$

[3]Listed here in order of decreasing relative strength

[4]This based either on fitting available neutron-proton scattering data for $T = 0$ states or neutron-proton or proton-proton data for $T = 1$ states.

المنارة للاستشارات

where the first term represents the total kinetic energy of all nucleons and the second part is the potential energy of the nucleons due to the interaction between them, modeled by a nucleon-nucleon potential (and additional Coulomb repulsion between protons). This nucleon-nucleon potential has a complicated structure as it depends on spin couplings and also contains tensor components. The main characteristics are its short range, charge independence and predominantly attractive behavior which becomes strongly repulsive when the distance between the nucleons involved approaches zero.

A basic assumption within the shell model[5] assumes that each nucleon will feel the average potential generated by all the other nucleons instead of all individual interactions separately. This is modeled as follows:

$$H = \underbrace{\sum_{i=1}^{A}\left[\frac{\mathbf{p}_i^2}{2m_i} + U(\mathbf{r}_i)\right]}_{H_0} + \underbrace{\left[\sum_{i>j=1}^{A} V_{ij}(\mathbf{r}_i - \mathbf{r}_j) - \sum_{i=1}^{A} U(\mathbf{r}_i)\right]}_{H_{\text{residual}}}. \tag{1.4}$$

The Hamiltonian is now split into two parts. The first part, H_0, describes the motion of each nucleon independently in an average mean field. The solutions should reproduce the nucleon single-particle energies (SPE (ϵ_j) in the vicinity of a doubly-magic nucleus (DM):

$$\epsilon_j = B(DM \pm 1; I = j) - B(DM; gs), \tag{1.5}$$

where B is the generalized binding energy for a given nucleus in a particular excited state j^π. H_{residual} will take into account the remaining details of the *residual* nucleon-nucleon interaction. The problem for nuclei in the vicinity of DM nuclei is now simplified as a nucleus can now be modeled as an inert, closed core surrounded by *valence* nucleons. In this scenario, the core is closed and the residual interactions are only applied to the limited number of valence nucleons. These interactions are not limited to nucleons as vacancies in a filled shell (*holes*) can be treated in the same way. Core polarization effects are included in these residual interactions because the core is in reality not perfectly inert and thus it will still interact with the valence nucleons. This is incorporated in the shell model by using *effective charges* for both neutrons and protons. These residual interactions are usually represented by the use of two-body matrix elements (TBME) obtained from the experimental properties of doubly-magic nuclei $\pm$ 1 and 2 nucleons.

The aim is to find a suitable potential $U(\mathbf{r}_i)$ which results in a small H_{residual} so it can be treated as a perturbation. Various types of mean field potentials can be used such as a Harmonic Oscillator (HO, see Figure 1.1) . This kind of potential

[5]For a more elaborate discussion on the nuclear shell model, see Refs. [Hey90, Sha04]

المنارة للاستشارات

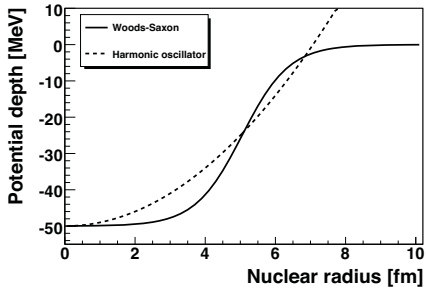

Figure 1.1: Comparison between the Harmonic oscillator potential (dashed line, no L^2 or $L \cdot s$ terms added) and the Woods-Saxon potential (solid line). Parameters: Potential depth: 50 MeV, nuclear radius $r_0 A^{1/3}$ with $r_0 = 1.25$ fm, diffuseness $a = 0.67$fm.

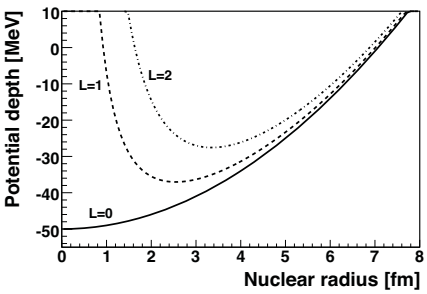

Figure 1.2: Effect of the centrifugal barrier (L^2 term) on the shape of the potential. For higher ℓ-values, the potential becomes repulsive at short distances, effectively pushing the nucleons to larger radii.

has the advantage that the SE can be solved analytically. However, it lacks the correct behavior for large distances as it keeps rising with increasing radius and thus neglects the short-range characteristic of the nucleon-nucleon interaction. Solving the SE with a HO potential leads to groups of degenerate energy levels which reproduce the experimental magic numbers reasonably well (see left hand side of Figure 1.3): 2, 8, 20, 40, 70 and 112, leading to the conclusion that a HO potential provides a good first order approximation. Each group of levels is labeled by the *oscillatory shell number* N and contains levels with *principal quantum number* n and angular momentum L satisfying $N = 2(n-1) + L$. The *parity* of a level $\pi = (-1)^L$ depends on the angular momentum of the orbital and alternates between positive and negative between these HO shells [Cas01].

An additional L^2 potential (where L is the angular momentum of the orbital, see above) is combined with the HO potential in order to flatten the potential and lifts the degeneracy in the solutions of a pure HO potential (see Figure 1.3). Alternatively, a Woods-Saxon potential can be used, which will be introduced in Section 2.4.7. Both potentials are drawn for comparison in Figure 1.1. For the HO with additional L^2 term, states with the highest angular momentum will have their radii shifted away from the center of the nucleus and decrease the most in energy. This is demonstrated in Figure 1.2 and resulting energy shifts are visible in Figure 1.3 [Kra87].

One final addition to the Hamiltonian is needed in order to successfully reproduce the experimental magic numbers. Agreement can be achieved by introducing a

المنارة للاستشارات

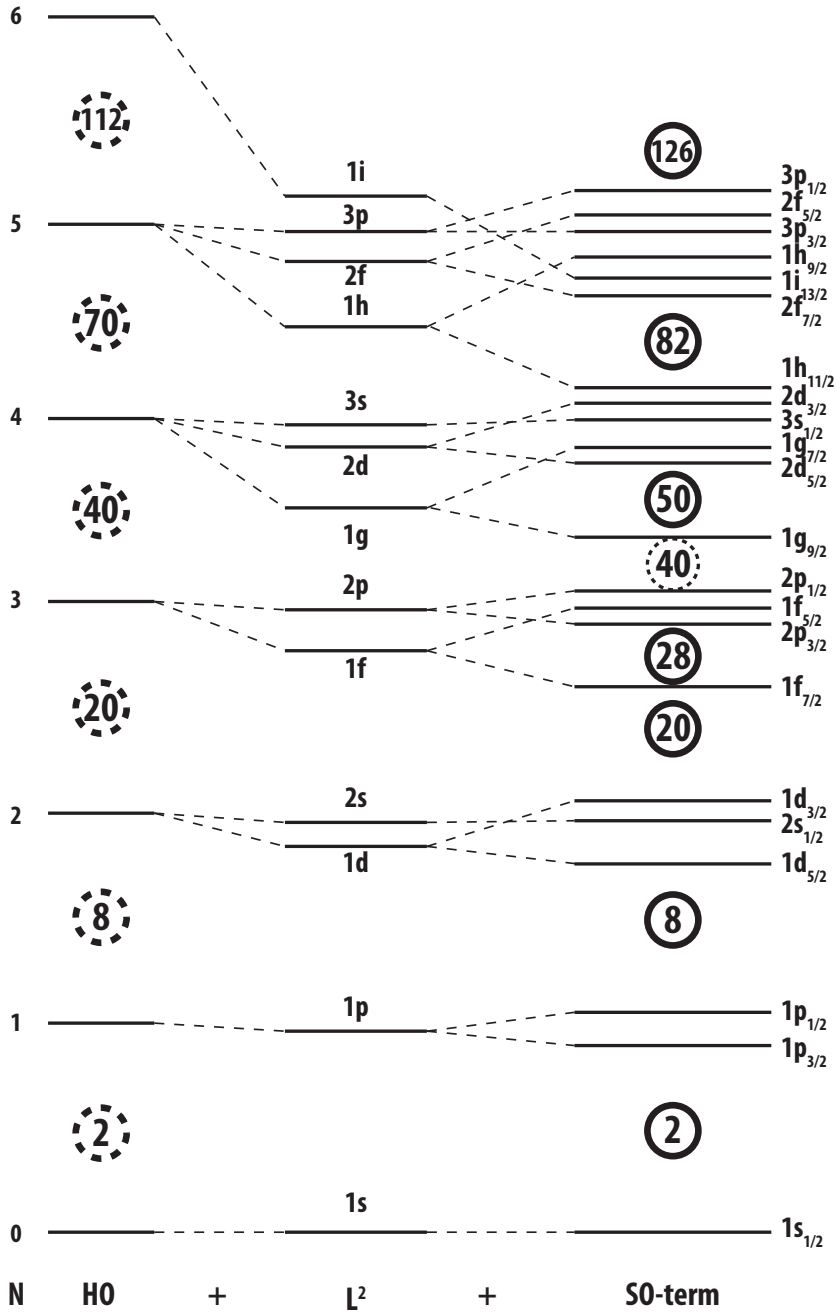

Figure 1.3: Overview of the influence of the different contributions to the Harmonic Oscillator potential on the relative splitting of the single-particle orbitals. From left to right: Pure Harmonic Oscillator potential, centrifugal barrier and spin-orbit potential.

المنارة للاستشارات

spin-orbit term. Because nucleons have an intrinsic spin of 1/2, the *total spin* of a nucleon when inserted into a specific orbital with angular momentum L will be $j = L \pm 1/2$. The spin-orbit interaction, which is an inherent quantum relativistic effect, will have a different effect on a nucleon if it is coupled in a parallel or anti-parallel way to the orbital angular momentum and this interaction will hence lift this degeneracy. This can be modeled by adding an interaction of the form $V_{L\cdot s} = -V_{Ls}\frac{\partial V(r)}{\partial r}\boldsymbol{L}\cdot\boldsymbol{s}$ with the derivative of a Woods-Saxon potential, leading to a surface peaked potential[6]. The minus sign indicates that parallel couplings are favored. From Figure 1.3 it is clear that a Harmonic Oscillator in combination with a L^2 and $L \cdot s$ interaction reproduces all known magic numbers and the shell structure of atomic nuclei [Kra87].

This work focuses on the neutron orbitals in the region around ^{68}Ni. As this isotope contains 40 neutrons, they form a closed Harmonic Oscillator subshell (see Figure 1.3). The $N = 40$ gap is formed by the separation between the negative-parity pf-orbitals below the gap and the unique positive-parity $\nu g_{9/2}$-orbital above the gap. Furthermore, the remaining positive-parity orbitals above the $N = 50$ gap are believed to be responsible for the onset of deformation and collectivity in this part of the chart of nuclei (see Section 1.2.5). From Figure 1.3 it is clear that both the $N = 40$ and 50 gaps are due to the SO splitting of the 1g orbital.

Self-consistent methods

Besides the historical introduction of the HO potential combined with a centrifugal and spin-orbit component, a microscopic, self-consistent method can be applied to find a central potential $U(r)$. This method requires the use of a nucleon-nucleon interaction $V_{NN}(\vec{r}_1, \vec{r}_2)$ combined with an initial guess of the central potential $U(r)$. Using this central potential one can calculate the ground state wave function by minimizing the system's energy and deduce the nuclear-matter density from this wave function: $\rho(\vec{r}) = \sum_j |\Psi_j(\vec{r})|^2$ where the sum includes all occupied orbits. Using this density, a new central field is found by $U(\vec{r}) = \int \rho(\vec{r\prime})V_{NN}(\vec{r}, \vec{r\prime})\mathrm{d}\vec{r\prime}$. These iterations are repeated until the solution converges. This method is referred to as the *Hartree-Fock* (HF) method [Hey90].

From a global and historical perspective, the foundations of the nuclear shell model can be traced to the early successes of the atomic shell model [Boh21]. The atomic shell model describes very well the configuration of electrons surrounding

[6] In case the SO interaction would not be surface peaked but present everywhere in the atomic nucleus, nucleons would experience a net force inside the nucleus which is not plausible [Cas01].

المنارة للاستشارات

an atomic nucleus based on the Coulomb interaction between the nucleus and the electrons and correctly predicts the existence of shells which are completely filled for elements with Z= 2, 10, 18, 36, 54 and 86: the noble gases He, Ne, Ar, Kr Xe and Rn. The contrast between the atomic and nuclear shell models lies in the fact that in the case of the atomic shell model the electrons move in a well defined, external Coulomb field[7], while in the case of the nuclear shell model the nucleons move around in a potential created by themselves.

1.2.1 The effect of nuclear shells

As nucleons are fermions they have a half-integer spin and when a composite system like an atomic nucleus is formed, quantum mechanics and more specifically the *Pauli Exclusion Principle* dictates that all fermions should have a different quantum state[8]. Within a level with total angular momentum j, one can place $2j + 1$ fermions with a different quantum state, namely the $z-$projection m_z. Without the Pauli Exclusion Principle all fermions would condensate in the lowest energy level.

Within the framework of the extreme independent particle model, in a given nucleus the Z protons and N neutrons will sequentially fill up all the available energy levels. This configuration defines the *ground state* of the nucleus. Due to the pairing interaction (see below), identical nucleons tend to form pairs with spin 0. For this reason orbitals which are completely filled have net spin of 0 and do not contribute to the total spin of the nucleus. The ground-state spin and parity of all even-even nuclei is therefore 0^+. *Excited states* of the nucleus can be formed by promoting one or more nucleons to higher-lying, empty orbitals and the energy required depends on the spacing between the orbitals involved. In the case of a *doubly-magic* nucleus both neutrons and protons fill up the available orbitals up to a shell gap. It will now require a large amount of energy to promote a particle or pair of particles over this energy gap to a higher lying orbital. On the other hand, in the mid-shell region, the nucleon pairs can easily scatter to available states which will substantially lower the $E(2_1^+)$ and enhance deformation.

The spin and parity of the excited states depend on the orbitals the uncoupled particles are placed in. As an example: consider the odd-odd ^{70}Cu nucleus, with an uncoupled $p_{3/2}$ proton and uncoupled $g_{9/2}$ neutron. The spins of both particles will quantum mechanically combine and this yields the $3^-, 4^-, 5^-$

[7]It should be noted that for many-electron systems also the electron-electron interaction is important. However, the atomic magic numbers can be easily reproduced using a single proton in a pure Coulomb potential.

[8]Neutrons and protons differ from each other due to the *isospin* quantum number and therefore a proton and neutron can occupy the same nuclear orbitals.

المنارة للاستشارات

and 6^- multiplet. Energywise, the order of these levels depends on the spatial overlap of both orbitals as described in Ref. [Cas01].

1.2.2 Calculations in the shell model

In nature, each nucleon within an atomic nucleus will interact with all the other nucleons. As including *all* nucleons in the calculation is unfeasible due to the enormous amount of nucleon-nucleon interactions, the problem is simplified within the shell model by modeling the nucleus as a combination of an inert core surrounded by a number of valence nucleons. It is common to select a doubly-magic nucleus to represent the core. Now only the residual interaction of the valence nucleons within the valence model space (i.e. the orbitals which are included in the calculation) has to be calculated. To correct for the fact that the core is not inert and still interacts with the valence nucleons, *effective two-body interactions* have to be used. Different approaches exist to describe these effective interactions:

- **Empirical interactions** are deduced from experimental data, more specifically from experimental binding energies in DM ± 1 and 2 and SPE in doubly-magic nuclei. This procedure can be applied to a single j shell and non-identical two-particle configurations ($j_1 \neq j_2$ coupled to spin J) with the restriction that only diagonal TBME can be obtained. For small model spaces a χ^2-fitting procedure can be applied to evaluate SPE and TBME using experimental data such as binding energies and excitation energies. The full spectroscopic strength of the j-orbitals under consideration might not be entirely contained in one specific state, leading to complications [Bru77].

- **Schematic interactions** assume that the χ^2-fitting can be simplified by using analytic functions containing a limited number of free parameters. The problem with this approach is that specific details of the interactions will be lost, resulting in deficiencies in energies and electromagnetic transition rates. Examples of schematic interactions include Yukawa, delta, Skyrme and Gogny type of forces and their results describe in general well global nuclear properties such as mass, radii and level densities but poorly reproduce detailed spectroscopic information like $B(E2)$-rates or spectroscopic factors [Bru77].
  By going "*beyond the mean field*" through the addition of long-range correlations, transition rates and excitation spectra can be obtained using these schematic interactions [Ben08].

المنارة للاستشارات

- **Realistic interactions** can be obtained from experimental nucleon-nucleon data using the Brueckner G-matrix formalism by fitting nucleon-nucleon potentials to the data [Dea04]. The repulsive force between nucleons at short distances is included in the G-matrix model and results in a well-behaved effective interaction. This model which assumes an inert core is an oversimplification because valence nucleons will interact with the core and will be prohibited to scatter to states occupied by the core nucleons. This introduces a mass dependence of the TBME, requiring a new calculation for each nucleus. Examples of calculations using realistic effective interactions in the nickel region include the GXPF1 interaction for the *pf*-shell ($1f_{7/2}, 2p_{3/2}, 1f_{5/2}, 2p_{1/2}$) [Hon02, Hon04], JJ4B [Lis04], JUN45 [Hon09] and the Oslo group [Hjo95] (all $2p_{3/2}, 1f_{5/2}, 2p_{1/2}, 1g_{9/2}$).

Using these TBME, one can solve the SE and obtain, besides the energy of the nuclear levels, the wave functions of states in the calculated nucleus. Despite the fact that a nuclear wave function is not an observable, it can be used to calculate experimental observables like energies, (relative) spectroscopic factors[9] $B(E2)$ values and magnetic moments.

A variety of codes capable of performing shell-model calculation is presently available like OXBASH (or the newer NuShellX [Cau99]), ANTOINE and NATHAN. The basic ingredients of a shell-model calculation hence require the choice of an appropriate core, valence space and interaction. The choice of core and valence space should not be too limited as this would lead to an oversimplification, nor too extended as this would lead to computational problems. In the case of shell model calculation in the neighborhood of ^{68}Ni, natural choices for the core nucleus are doubly-magic nuclei like ^{40}Ca, ^{48}Ca and ^{56}Ni. The valence spaces used almost always include the $pf_{5/2}g_{9/2}$ orbitals and recent calculations also include the $d_{5/2}$ orbital (using a ^{52}Ca core) [Cau02]. The concept of limiting both the number of valence nucleons and the valence space itself is called *truncation*. In this concept the core is closed and only the valence nucleons can move around within the defined valence space.

The result of a shell-model calculation provides a variety of information such as spin and parity of excited states, their energies, transition probabilities to other states and the composition of their wave functions. This last point is related to *configuration mixing* due to the residual interactions. A state with a given spin and parity can be created in a variety of ways. Under the influence of residual interactions, these different configurations mix, with the result that a particular configuration can be spread out over different states.

[9] Technically, absolute spectroscopic factors are no observables as the experimental values are highly model dependent. A comparison between shell-model calculations and experimental spectroscopic factors should therefore be done with care.

المنارة للاستشارات

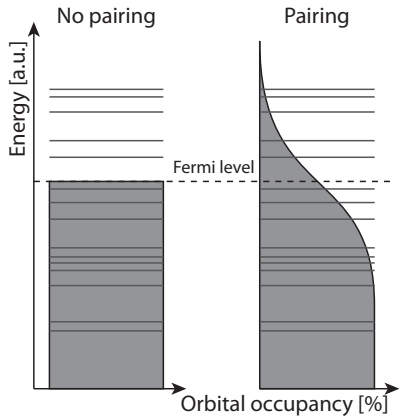

Figure 1.4: Illustration of the effect of the pairing interaction on the orbital occupancies near the Fermi surface. The gray zone represents the neutron occupancy: sequential filling up to a given orbital in the absence of pairing interaction, in contrast with a spread over partially filled orbitals near the Fermi surface due to pairing interaction.

1.2.3 Pairing interaction

Earlier it was mentioned that pairs of nucleons occupying the same orbital j tend to couple to a total spin $J = 0^+$. The driving mechanism behind this is the strongly attractive, short range *pairing interaction* defined by [Cas01]:

$$\left\langle j^2 J \left| V_{\text{pairing}} \right| j\prime^2 J \right\rangle = -G \left(j + \frac{1}{2} \right)^{\frac{1}{2}} \left(j\prime + \frac{1}{2} \right)^{\frac{1}{2}} \delta_{J0} \tag{1.6}$$

with $G = 17/A$ for protons and $G = 23/A$ for neutrons[10]. The pairing interaction is hence limited to $J = 0$ pairs but not restricted to *diagonal* matrix elements. For example it allows the off-diagonal scattering of a $J = 0$ pair from orbital j to $j\prime$ with equal strength. These nucleon pairs are scattered from levels slightly below the last one occupied (called *Fermi level*) to unoccupied orbitals above it. Pairs of nucleons in deeply bound orbitals are prohibited to scatter due to the Pauli principle. If the pairing interaction were a pure diagonal interaction, many different excited 0^+ states could be created, simply by promoting a pair of particles to a higher orbital, at the cost of roughly twice the energy separation of the orbitals involved. However, as off-diagonal scattering is incorporated in the pairing interaction, all these *pair scattered* configurations will mix and strongly

[10]The G-factor is slightly lower for protons due to Coulomb repulsion

المنارة للاستشارات

lower the coherent combination of these configurations. The orbital occupancy in the 0^+ ground-state wave function will be smeared out over orbitals near the Fermi level leading to many orbitals being partially occupied. This is illustrated in Figure 1.4.

The *fullness* V_j and *emptiness* U_j factors of a given orbital j with single-particle energy ϵ_j is given by

$$U_j = \frac{1}{\sqrt{2}}\left[1 + \frac{\epsilon_j - \lambda}{\sqrt{(\epsilon_j - \lambda)^2 + \Delta^2}}\right]^{\frac{1}{2}} \tag{1.7}$$

$$V_j = \frac{1}{\sqrt{2}}\left[1 - \frac{\epsilon_j - \lambda}{\sqrt{(\epsilon_j - \lambda)^2 + \Delta^2}}\right]^{\frac{1}{2}}. \tag{1.8}$$

Here, λ is the Fermi energy and Δ is the *gap parameter*, a measure for the width of the pairing gap, defined by

$$\Delta = G\sum_{i,j} U_j V_j. \tag{1.9}$$

1.2.4 Evolution of single-particle energies in exotic nuclei

The shell structure of atomic nuclei is not fixed over the entire chart of nuclei but depends on the mass number A, neutron excess $(N-Z)/A$ and shell occupation. The effect of the atomic mass A is reflected in the radial extension of the wave function and will cause a relative increase in binding for orbitals with high angular momentum [Gra04] (see e.g. Figure 3.8 in Ref. [Cas01]). A large neutron excess will lead to a softening of the neutron potential and cause high-spin states to increase in energy[11] [Dob94]. Furthermore the soft neutron skin will weaken the spin-orbit interaction as this depends on the spatial derivative of the Woods-Saxon potential. The effect of this spin-orbit interaction is stronger for high-L orbitals. The dependence of the shell structure on both A and $(N-Z)/A$ is rather weak and hence substantial changes are only expected for exotic nuclei with extreme N/Z ratios.

Single-particle energies also vary within a major shell and the driving force behind this is governed by the *monopole part* of the residual interaction[12]. This

[11] The larger diffuseness of the nucleon binding potential leads to a shape that is more similar to a Harmonic Oscillator potential. As can be seen in Figure 1.3 this increases the energy of high-L orbitals.

[12] For more information on the multipole expansion of the residual forces, see e.g. Refs. [Moi69, Sor08].

المنارة للاستشارات

monopole interaction expresses the effect of filling e.g. the neutron orbitals on the proton SPEs. The effect will be larger when the orbitals involved have similar wave functions, i.e. when there is a large overlap and hence strong interaction between neutrons and protons. The monopole interaction equals for a specific multiplet:

$$V^m_{jj\prime} = \sum_J (2J+1) \langle jj\prime J |V| jj\prime J\rangle / \sum_J (2J+1). \tag{1.10}$$

The connection between the SPE of a specific orbital j near two neighboring closed shells $CS1$ and $CS2$ is now given by

$$\epsilon^{CS1}_j = \epsilon^{CS2}_j + \sum_{j\prime} (2j\prime + 1 - \delta_{jj\prime}) V^m_{jj\prime} \tag{1.11}$$

where the sum contains all orbitals $j\prime$ which lie between the two closed shells under consideration. The Kronecker-δ is necessary to justify the Pauli Exclusion Principle (for identical nucleons). From this, the evolution of the energy separation between two orbits j_1 and j_2 can be extracted while filling an orbital $j\prime$:

$$\Delta\epsilon_{j_1,j_2} = V^m_{j_1 j\prime}(2j\prime + 1 - \delta_{j_1 j\prime}) - V^m_{j_2 j\prime}(2j\prime + 1 - \delta_{j_2 j\prime}). \tag{1.12}$$

The monopole interaction can be further decomposed into three main constituents: the central, spin-orbit and tensor part [Sor08]. In Figure 1.5, the effect of the tensor interaction on the πpf orbitals in the vicinity of ^{68}Ni due to the filling of the $\nu g_{9/2}$ orbital is presented. The tensor interaction has an attractive effect between orbitals with opposite spin-orbit couplings. E.g. the tensor force will be attractive between $\nu g_{9/2}$ and $\pi f_{5/2}$ ($j_{\uparrow\downarrow}$) orbitals, and repulsive between the $\nu g_{9/2}$ and $\pi f_{7/2}$ orbitals ($j_{\uparrow\uparrow}$)[13]. The effect of the tensor force indeed becomes stronger when the wave functions of the orbitals involved have a large overlap. The influence of filling the $\nu g_{9/2}$ orbital with neutrons will therefore be the strongest on the $\nu f_{5/2,7/2}$ orbitals compared to the νp orbitals. In Refs.[Ots10a, Sor08, Ots05] more information on the tensor interaction can be found.

It should be noted here that the monopole interaction between like nucleons is about two times weaker than the monopole interaction between unlike nucleons due to the Pauli Exclusion Principle. The strength of the two-body proton-neutron interaction decreases with the mass number and proposed values are ≈ 1 MeV for $A = 30$ and ≈ 300 keV for $A = 200$ [Sor08]. A correction to the monopole field between like nucleons has been suggested in the form of a three-body monopole force [Zuk03, Ots10b] and been applied to the neutron

[13]The symbols $j_{\uparrow\uparrow}$ and $j_{\uparrow\downarrow}$ indicate that both interacting orbitals have either the same spin-orbit alignment ($j_{\uparrow\uparrow}$) or opposite alignment ($j_{\uparrow\downarrow}$).

المنارة للاستشارات

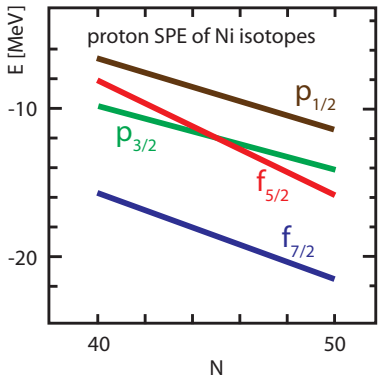

Figure 1.5: Effect of filling the $\nu g_{9/2}$ orbitals on the proton effective single-particle energies (monopole migration due to tensor interaction), leading to predicted orbital inversion around $N = 45$. Figure adapted from [Ots10a]

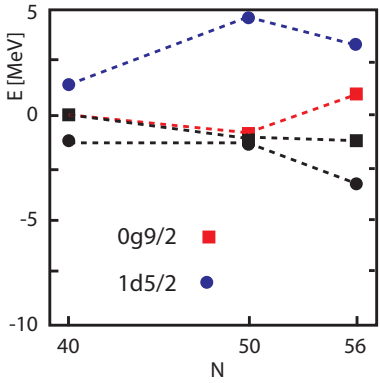

Figure 1.6: Three-body monopole force acting on the $\nu g_{9/2}$-$\nu d_{5/2}$ (relative) energy splitting as neutrons fill the $\nu g_{9/2}$-orbital (up to $N = 50$) and beyond in the nickel isotopes ($Z = 28$). Colored lines represent empirical interactions, black lines are obtained using a V_{lowk} [Sie12]. Figure adapted from [Sie12].

rich nickel region [Sie12]. This effect is illustrated in Figure 1.6 and will be discussed more extensively later on.

Based on the arguments above, existing shell closures may weaken and ones may arise when moving towards exotic nuclei due to strong monopole migration. A few example include the well established $N = 28$ shell closure (in stable nuclei) which vanishes in ^{42}Si [Bas07]. In the neutron-rich calcium chain a new magic number is expected to rise at $N = 34$ as ^{54}Ca is predicted to exhibit properties of a double-magic nucleus[Hon02].

Besides the monopole part of the residual interaction, also higher order terms are present which lead to correlations and configuration mixing. The *quadrupole* term plays an important role which is reflected in the fact that most even-even nuclei have a 2^+ state as the first excited state, resulting from broken nucleon pairs due to the quadrupole interaction [Cas01].

المنارة للاستشارات

1.2.5 Quadrupole collectivity

Within the framework of SU(3) symmetry, Zuker *et al.* pointed out that specific sequences of single-particle orbitals lead to collective behavior and deformation [Zuk95]. The exact SU(3) symmetry requires four protons (or holes) in one major shell and and four neutrons (or holes) in the same or another major shell. An exact diagonalisation of the Hamiltonian is not possible as the dimension is excessively large (on the order of 10^{40}). A simplification of the system to only neutrons or protons serves insight into the driving mechanism behind the development of collectivity. Exact calculations have shown that "*deformation and rotational features [..] are determined by the interplay of the quadrupole force with the central field, in the subspace of a major shell spanned by the sequence of* $\Delta j = 2$ *single-particle orbitals that comes lowest under the spin-orbit splitting*" [Zuk95].

An alternative view is that the energy cost of creating $np - nh$ states is compensated by the gain in correlation energy, leading to deformed states and development of quadrupole collectivity [Hey11]. This onset of collectivity results into a decrease of the $E(2_1^+)$ and an increase of $B(E2; 2_1^+ \rightarrow 0_{gs}^+)$ for even-even nuclei that can be experimentally investigated.

An example of such a sequence in the nickel region is the $\nu g_{9/2} d_{5/2} s_{1/2}$ combination above the $N = 40$ HO shell gap. The limitation of the exact SU(3) symmetry to a single major shell is called a *quasi-SU(3)* and is capable of explaining collective features when purely focusing on a single major shell. The $\nu g_{9/2} d_{5/2} s_{1/2}$-sequence is believed to be responsible for the observed swift onset of collectivity in the region below $Z = 28$. This will be discussed in Section 1.3.2.

1.3 The region around ^{68}Ni

In this section some known features in the neutron-rich nickel region are reviewed, including the importance of ^{68}Ni along the nickel chain. (d,p) studies on the stable ^{58,60,62,64}Ni isotopes are discussed and the spectroscopic data of ^{67}Ni are reviewed. The present status of experimental knowledge in the region below the nickel chain is also addressed.

المنارة للاستشارات

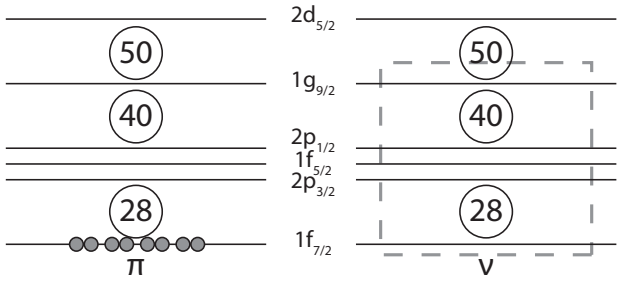

Figure 1.7: Valence space of the nickel isotopes. The dashed line on the neutron (ν) side shows the available orbitals occupied by neutrons in nickel isotopes that have been examined so far.

1.3.1 Systematics in the nickel isotopes ($Z = 28$)

A subdivision is made between the even- and odd-A nickel isotopes. The former will be used to point out the evolution of quadrupole collectivity in this isotope chain, while the discussion of the latter will focus on data from (d,p) experiments on stable nickel isotopes.

The common feature of the nickel isotopes is that the protons form a closed core with 28 protons filling the proton orbitals up to and including $\pi f_{7/2}$. $Z = 28$ is expected to form a firm closed shell for the light and stable nuclei but the shell closure is expected to weaken when neutrons start filling the $\nu g_{9/2}$ orbital due to the tensor interaction which acts repulsively on $\nu f_{7/2}$ and attractively on $\nu f_{5/2}$ (see also Figure 1.9). The consequences of these effects on the structure of ^{78}Ni will be discussed below.

Even-A nickel isotopes

At the extreme N/Z ratios of the nickel isotope chain two nuclei with presumed doubly magic character are expected to be found: $^{48}Ni_{20}$ and $^{78}Ni_{50}$. Figure 1.7 shows the available valence space which will be occupied by neutrons in the isotopes between these two extremes. From this figure, other interesting points along the nickel chain are expected at $^{56}Ni_{28}$ and $^{68}Ni_{40}$. The former due to the double $N = Z = 28$ shell closure and the latter due to the $N = 40$ HO shell closure. In Figure 1.8 the known information on the $E(2_1^+)$, $B(E2;2_1^+ \rightarrow 0_1^+)$ and δS_{2n} values is shown.

Limited information on $^{48}Ni_{20}$ is available: its half-life of $2.1^{+1.4}_{-0.4}$ ms [Bla00, Pom11] has been measured in combination with its two-proton radioactiv-

المنارة للاستشارات

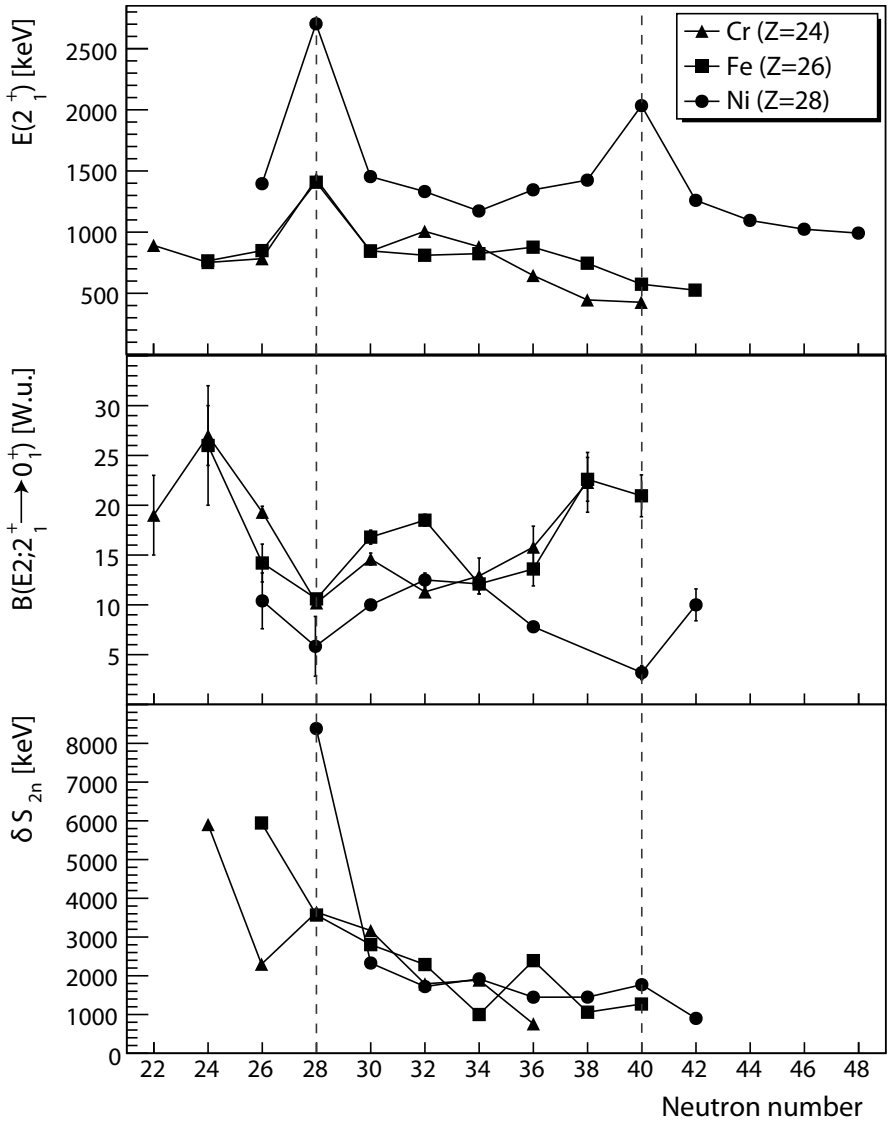

Figure 1.8: Systematics of E(2_1^+), $B(E2;2_1^+ \rightarrow 0_1^+)$-values and δS_{2n} in even-even isotopes of Cr, Fe and Ni. Data taken from [Sor02, Per06, Van07, Sei11, Bau12, Bre08, NND13].

المنارة للاستشارات

ity [Pom11]. Concerning $^{56}Ni_{28}$, Figure 1.8 shows a clear local maximum for $E(2_1^+)$, minimum for $B(E2;2_1^+ \rightarrow 0_{gs}^+)$ and δS_{2n} deviation, all consistent with a doubly-magic character for this nucleus. The $B(E2;2_1^+ \rightarrow 0_{gs}^+)$ value is slightly higher than expected, but this has been attributed to coherent 1p-1h quadrupole excitations ($1f_{7/2} \rightarrow 1f_{5/2}$ (also dipole) and $1f_{7/2} \rightarrow 2p_{3/2}$) across the $Z, N = 28$ gap for both protons and neutrons. Calculations using QMCD[14] reproduce this $B(E2)$ value and predict a 49% contribution of the doubly closed shell configuration to the ground-state wave function [Ots98]. This value is smaller than what one should expect for a solid closed configuration. More recent calculations show a double magic contribution of $\approx 60\%$ [Sie12]. This partial breakdown of the core due to dipole and quadrupole interactions between valence neutrons and protons is a consequence of strong proton-neutron correlations in $N = Z$ nuclei [Eng96].

The other extreme, $^{78}Ni_{50}$, on the neutron-rich, side forms a remarkable nucleus since it is not known whether the $N = 50$ shell closure, well established for nuclei near $Z = 40$, will survive under extreme N/Z-conditions [Pré04]. Recent mass measurements have indicated that, despite the fact that the $N = 50$ gap diminishes when approached from above ($Z \searrow 28$), the $N = 50$ shell gap persists in $^{78}Ni_{50}$. From a shell-model perspective several arguments have to be combined concerning the doubly-magic character of ^{78}Ni:

- The attractive $\pi f_{5/2}\nu g_{9/2}$ tensor force works more attractively on the $\nu g_{9/2}$ orbital than it does on the $\nu d_{5/2}$ orbital due to the specific details of this interaction [Sor08]. When protons are removed from ^{90}Zr (where the protons fill the pf-shell up to $Z = 40$ and neutrons occupy the $\nu g_{9/2}$ orbital leading to a well defined $N = 50$ shell gap) the residual tensor interaction will alter the effective single-particle energies of the neutron sdg-orbitals. The variation in the position of the $\nu g_{9/2}$ and $\nu d_{5/2}$ orbitals defines the size of the $N = 50$ shell gap. The strongest component of this tensor interaction is the $\pi f_{5/2}\nu g_{9/2}$ interaction. As protons are removed from the $\pi f_{5/2}$ orbital the effective energy of the $\nu g_{9/2}$ orbital will increase faster than the one of the $\nu d_{5/2}$ orbital, leading to a reduction of the shell gap.

- The large neutron excess might result in a more diffuse neutron surface which in turn can lead to a reduction of the SO splitting[15].

[14] Quantum Monte Carlo Diagonalization

[15] See e.g. Ref [Gau06] for an example of the reduction of SO splittings near $N = 28$ in exotic nuclei with extreme N/Z ratios.

المنارة للاستشارات

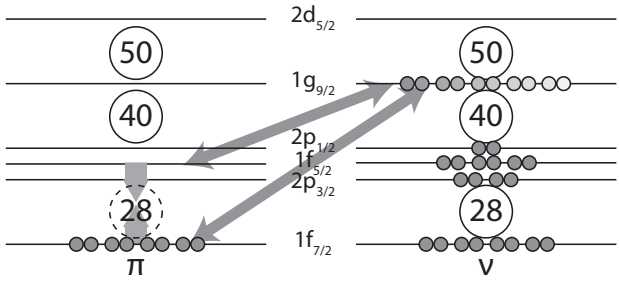

Figure 1.9: Reduction of the $Z = 28$ shell gap due to fg-tensor interaction when filling the $\nu g_{9/2}$ orbital.

- Recent calculations including three-body monopole forces[16] have estimated the evolution of the $N = 50$ shell gap as a function of the $\nu g_{9/2}$ occupancy (see Figure 1.6) [Sie12]. These calculations predict that the ≈ 1.7 MeV $N = 50$ shell gap near ^{68}Ni will increase up to 5 MeV in ^{78}Ni.
- When approaching ^{78}Ni$_{50}$ following the nickel chain, the $\pi f_{5/2}\nu g_{9/2}$ tensor interaction reduces the $Z = 28$ gap (see Figure 1.5) [Ots10a]. Evidence of this was found in the neutron-rich copper isotopes [Fra98] using Coulomb excitation [Ste08], where the excited $5/2_1^-$ state changes structure from a core-coupled collective state to a single-particle excitation when passing $N = 40$ and eventually becomes the ground state in ^{75}Cu$_{46}$ [Fla09]. The resulting reduction of the $Z = 28$ gap could facilitate proton excitations across the $Z = 28$ gap and hence introduce collectivity.

The interplay of all these phenomena questions the stabilizing effect of both the $Z = 28$ and $N = 50$ shell closures in ^{78}Ni$_{50}$ and hence its doubly-magic structure. Recent shell-model calculations have predicted a 79 % contribution of the doubly-closed configuration to the ground-state wave function, the highest one along the nickel chain [Sie12], with the 2_1^+ state at nearly 4 MeV. ^{78}Ni has been produced and its life time has been found to be 100^{+100}_{-60} ms [Hos05]. However, detailed spectroscopy of ^{78}Ni$_{50}$ is not (yet) possible due to its very exotic character and low production cross sections.

Assuming that the $N = 40$ gap is not too wide, the large density of the neutron orbitals between $N = 28$ and $N = 50$ would result in a smooth parabola-like[17]

[16] The mechanism behind the three-body force is the virtual excitation of a nucleon to a Δ-particle and subsequent de-excitation by scattering on a third nucleon. For more information see Refs. [Ots10b, Ots12].

[17] $B(E2;2_1^+ \rightarrow 0_1^+) \propto c(\pi\text{fp}, \nu\text{fpg})F(1-F)$ with $0 < F < 1$ the fractional filling of the shell and $c(\pi\text{fp}, \nu\text{fpg})$ the proton-neutron interaction between the available orbitals [Sor08].

المنارة للاستشارات

behavior of both $E(2_1^+)$ and $B(E2;2_1^+ \rightarrow 0_1^+)$ values, with the former reaching a minimum and the latter a maximum near mid-shell. From Figure 1.8 the opposite is evident as $E(2_1^+)$ peaks and $B(E2;2_1^+ \rightarrow 0_1^+)$ reaches a minimum at $N = 40$ [Sor02, Bre08]. This observation in combination with the fact that the first excited state in $^{68}Ni_{40}$ is a 0^+ rather than a 2^+ state [Ber82], led to an interpretation of a $N = 40$ HO shell closure [Bro95]. In contrast δS_{2n} systematics (Figure 1.8) do not reveal any irregularity at $N = 40$ as opposed to e.g. $N = 28$ [Rah07]. The measured $B(E2)$ value in $^{68}Ni_{40}$ is also considerably smaller with respect to $^{56}Ni_{28}$. This effect is attributed to the opposite parities of the pf orbitals below and $g_{9/2}$ orbital above the $N = 40$ gap. A 1p-1h configuration results in negative-parity states, requiring at least two particles to be promoted over the gap to create a positive-parity 2^+ state. As the quadrupole force is parity conserving, it cannot account for any contributions of chargeless neutron excitations to the $B(E2)$-value. Hence, all contributions to the $B(E2;2^+ \rightarrow 2_{gs}^+)$ must originate from proton excitations across the $Z = 28$ gap and hence due tot the breaking of the core. These proton excitations can be induced due to core polarization by neutrons occupying the $\nu g_{9/2}$ orbital. Shell model calculations have shown that 80% of the $B(E2)$-value is due to proton core excitations [Sor02] resulting from core polarizing effects of neutron pair scattering above the $N = 40$ gap. This mix of a doubly closed configuration ($\approx 50\%$ [Len10], $\approx 40\%$ [Cau02]) with *superfluid* neutron character gives most probably rise to an increased 2_1^+ energy, without causing distortions of the δS_{2n} [Len10]. Calculations by Langanke *et al.* have shown that the major part of the $E2$ strength resides at excitation energies of 5 to 6 MeV [Lan03].

Between $^{56}Ni_{28}$ and $^{68}Ni_{40}$, the systematics shown in Figure 1.8 do follow the parabolic seniority scheme trend. After $N = 40$, only the $B(E2)$ value in $^{70}Ni_{42}$ has been measured and a sharp increase in collectivity was found [Per06]. Systematics of the $E(2_1^+)$ show a decrease in excitation energy when neutrons are filling the $\nu g_{9/2}$ orbital and point towards an increase of collectivity. The seniority scheme (using proton-neutron interaction constant $c(\pi fp, \nu g)$) alone cannot explain the observed down-sloping trend and also the reduction of the $Z = 28$ gap due to the tensor force (see earlier). The increased monopole interaction between neutrons occupying the $\nu g_{9/2}$ orbital and πf orbitals is seen as a possible cause for the increased collectivity beyond $N = 40$ [Sor08]. The fact that $E(2_1^+)$ values decrease up to and including $^{76}Ni_{48}$ is also attributed to this assumed erosion of the $Z = 28$ shell gap [Sor08].

Odd-A nickel isotopes

The excitation energy spectra of odd-A nickel isotopes are governed by single neutron(-hole) states and multiplets arising from core-coupled structures.

المنارة للاستشارات

Measuring spectroscopic factors allows the position of neutron single-particle orbitals to be determined by calculating their center of gravity (see Eq. 2.22 in Section 2.3.2). Such studies have been performed in the nickel region in direct kinematics using enriched target foils of stable ^{58,60,62,64}Ni isotopes [Ful63, Ful64, Cos67, Anf70, Tur70, Cho73, Hut74, Wes91]. The information from these transfer reaction studies is summarized in Figure 8.2 (p. 175) and Figure 1.10, showing those states with substantial single-particle strength (the percentages indicate the amount of single-particle strength with respect to a pure configuration). The information as shown in Figure 1.10 is based on relative spectroscopic factors (see Section 2.4.12) with the relative spectroscopic factor of the $9/2^+_1$ state chosen as a reference state for each isotope. Discussing the structural evolution along the nickel chain in terms of relative spectroscopic factors eliminates the model dependencies related to analyzing one-nucleon transfer reactions as the information originates from different experiments performed by various authors.

The structure of the odd-A nickel isotopes between ^{59}Ni and ^{65}Ni below 2 MeV excitation energy can be characterized by the coexistence of two types of excitations: states with mainly single-particle character (large νpfg spectroscopic factors) and collective, core-coupled states, with the former mainly below 500 keV and the latter located around the 2^+_{core} energy (1-1.3 MeV). From an extreme shell model point of view (see Figure 1.7), one would expect a $5/2^-$ spin and parity for the ground state of ^{61,63}Ni. This is however not the case and the small ground-state spectroscopic factors measured in these isotopes indicate the influence of seniority > 1 configurations.

A similar situation occurs for the two $1/2^-$ states observed at low excitation energy. The $1/2^-_1$ state carries a large fraction of the $\nu p_{1/2}$ single-particle strength, except in ^{63}Ni where the absolute spectroscopic factor of the $1/2^-_1$ state is reduced by 50% while the total amount of observed $\nu p_{1/2}$ strength remains constant, again hinting to substantial mixing with $\nu f^3_{5/2}$ and core-coupled configurations.

The evolution of these different states throughout the nickel chain is also clearly visible, especially the two different $3/2^-$ states at low excitation energy. The state with the largest relative spectroscopic factor gradually increases in energy along the chain. The collective $3/2^-$ on the other hand follows the $E(2^+_{\text{core}})$ trend and carries a limited amount of $\nu p_{3/2}$ single-particle strength. As the pf orbitals get filled, the total amount of pf-single-particle strength also gradually decreases.

When focusing on the positive-parity states $5/2^+$ and $9/2^+$, a steep drop of the excitation energy with increasing neutron occupation is visible, mainly due to the increase in Fermi energy. The fact that the $\nu g_{9/2}$ energy is split between

المنارة للاستشارات

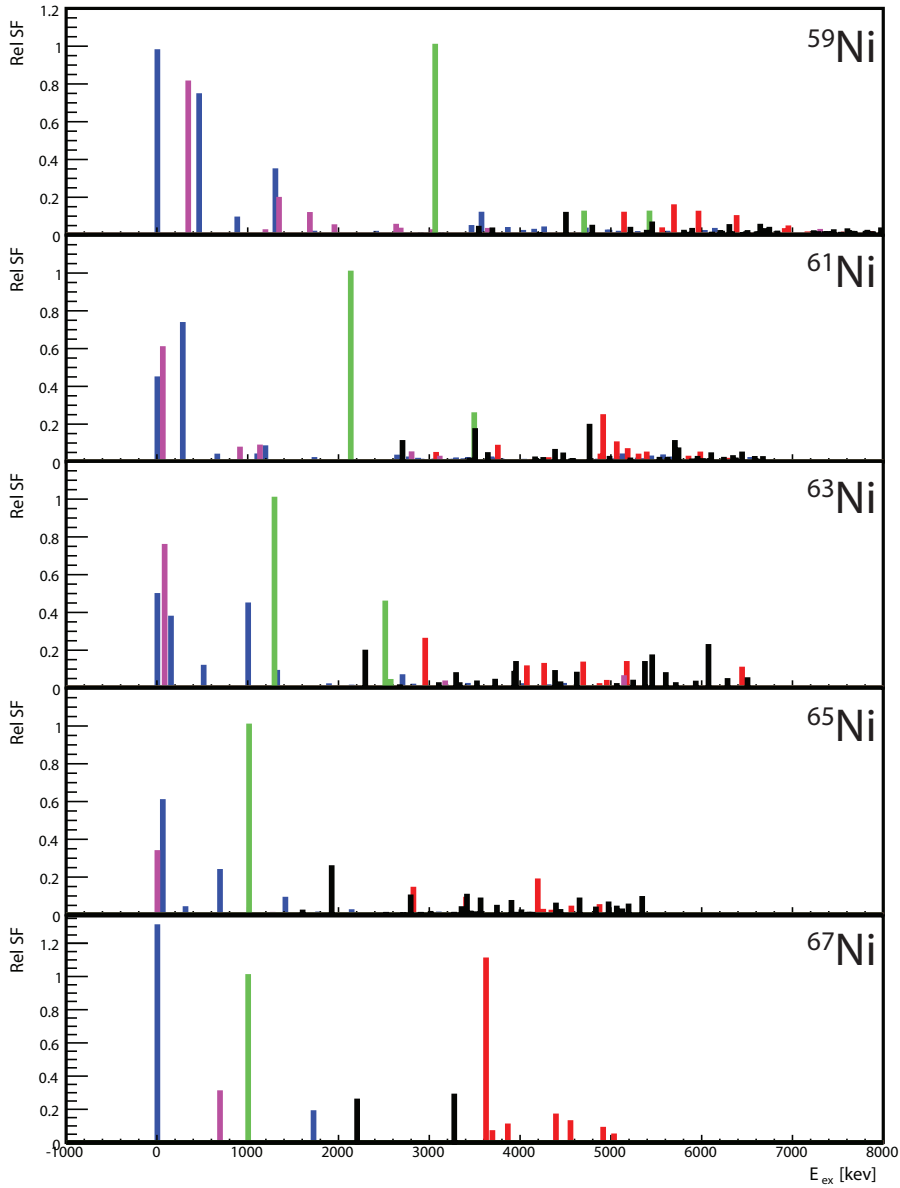

Figure 1.10: Evolution of the distribution of the single-particle strength (relative spectroscopic factors, $9/2^+_1$ as reference) in the odd-A nickel isotopes. Color code: red: $\ell = 0$, blue: $\ell = 1$, black: $\ell = 2$, purple: $\ell = 3$ and green: $\ell = 4$. Data on lighter isotopes from Refs. [Cho73, Ful64, Wes91, Cos67, Ful63, Anf70, Hut74, Tur70]. The bottom panel shows the measurements of ^{67}Ni and will be discussed later.

المنارة للاستشارات

two levels in ^{63}Ni might be due to a small amount of mixing with core-coupled octupole excitations (νpf $\otimes$ $3^-_{\rm core}$). This is plausible since the energy of the 3^-_1 state in the even-A nickel nuclei decreases from 4.4 MeV in ^{58}Ni to 3.5 MeV in ^{64}Ni. Two $5/2^+$ states are observed at low excitation energy, sharing in total up to 40% of the available νd$_{5/2}$ single-particle strength.

Recently, a consistent study of both (d,p) and (p,d) reactions on the stable even-A nickel isotopes allowed the direct application of the *sum-rule* method [Mac60] to extract neutron occupation numbers [Sch12]. These results will be reviewed in Chapter 8, but the reported $(2J+1)S$ values in Ref. [Sch13] can be compared to results from other (d,p)-reaction studies [Cho73, Ful64, Wes91, Cos67, Ful63, Anf70, Hut74, Tur70, NND13]. When absolute spectroscopic factors are compared, the results are in fair agreement for $\ell = 1$ and 3 states. However, the reported $2(J+1)$ values for the $9/2^+_1$ states in Ref. [Sch13] are smaller by a factor of at least two compared to the values reported by Ref. [NND13]. Therefore, comparing relative spectroscopic factors between Refs. [Sch13] and [NND13] is not possible.

^{67}Ni

As the proposed experiment focuses on the ^{66}Ni(d,p)^{67}Ni one-neutron transfer experiment, a summary is given about the present knowledge of ^{67}Ni, which, from an extreme shell model view, can be seen as a neutron hole coupled to a ^{68}Ni core. From β-decay studies, spins and parities of four states at 0, 694, 1007 and 2155 keV were tentatively assigned from log ft values [Wei99], while multi-nucleon transfer reactions [Kou78, Gir88] and quasi-inelastic scattering experiments [Grz98, Paw94, Mac03, Zhu12] identified a number of excited states with tentative spin assignments. All information available is summarized in Figure 1.11. In the deep-inelastic work of Ref. [Zhu12] high-spin states up to $21/2^-$ and $15/2^+$ built on top of the 1007 keV isomer were identified. This data will be discussed in more detail in Section 8.2.

The ground state was labeled with a $(1/2^-)$ spin and associated νp$^{-1}_{1/2}$ configuration as expected from shell-model calculations. This is also compatible with data from Ref. [Gir88] where the angular distribution fits with a $(1/2^-)$ interpretation. The measurement of the magnetic moment of the ground state was found to be close to the expected value for a pure νp$_{1/2}$ configuration, suggesting a nearly pure state [Rik00]. For the first observed excited state at 694 keV, a spin of $(5/2^-)$ was proposed based on the 4.6 log ft value measured in β decay [Wei99]. This is in contradiction with the extracted angular distribution in

المنارة للاستشارات

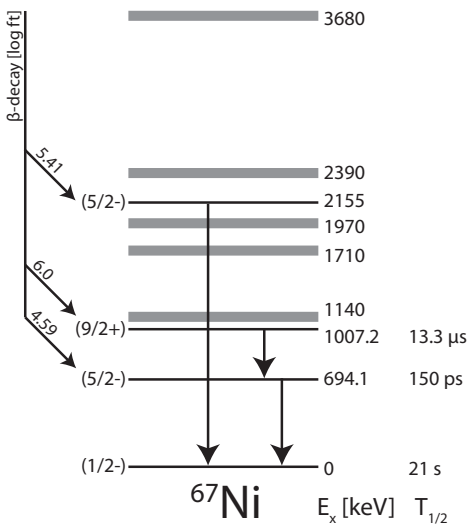

Figure 1.11: Level scheme as known at the time of the experiment. Data from Ref. [Zhu12] are not included here. Wide gray bars indicate levels observed in multi-nucleon transfer reactions with an energy resolution of typically ≈ 30 keV. The level at 1140 keV is most likely the 1007.2 keV isomeric state (see Figure 1.12). Combined data from [Wei99, Kou78, Gir88, Mac03, Grz98, Zhu12, Paw94].

the ^{70}Zn(^{14}C,^{17}O)^{67}Ni-reaction data[18] which favors a $(9/2^+)$ assignment [Gir88] (see Figure 1.12).

Both data sets also disagree on the spin of the 1007 keV state, for which a $(9/2^+)$ spin was proposed due to the forbidden β decay [Wei99], while Ref. [Gir88] proposes $(3/2^-)$. However, from Figure 1.12.A it can be seen that the 1.14 MeV state (corresponding to the 1007 keV state observed in the β-decay data) actually fits better with a $(9/2^+)$ spin and parity[19], questioning this interpretation[20]. Also, the isomeric decay of the 1007 keV state ($T_{1/2} = 13.3\mu$ s) [Grz98, Geo02] by two cascading γ rays of 313 and 694 keV is compatible with a $(9/2^+)\rightarrow(5/2^-)\rightarrow(1/2^-)$ sequence with a stretched quadrupole character [Zhu12] and the 313-keV $M2$ transition ($B(M2) = 0.05$ W.u.) leading to a μs-isomer. Further experimental data on the 1007-keV state comes from g-factor measurements [Geo02] providing a value of $\left|g(^{67m}\mathrm{Ni})\right| = 0.125(6)$. Shell model calculations (S3V [Sin92] and Oslo group interaction [Hjo95]) for a pure $\nu g_{9/2}$ configuration predict a value that is twice as large as the experimental value. This was attributed to $M1$ proton excitations across the $Z = 28$ gap which are not included in the calculations. From a two-state mixing scheme a contribution of 2% 1p-1h proton excitations to the wave function would result in the observed g-factor [Geo02].

[18] In Figure 1.12.A differences in excitation energy can be noticed, most probably due to a calibration offset.

[19] The dashed line is a copy from the fit for the 0.77 MeV state

[20] From Figure 1.12.B the separation between 0.77 MeV and 1.14 MeV is good, so it is unlikely that the angular distributions of both states are experimentally mixed.

المنارة للاستشارات

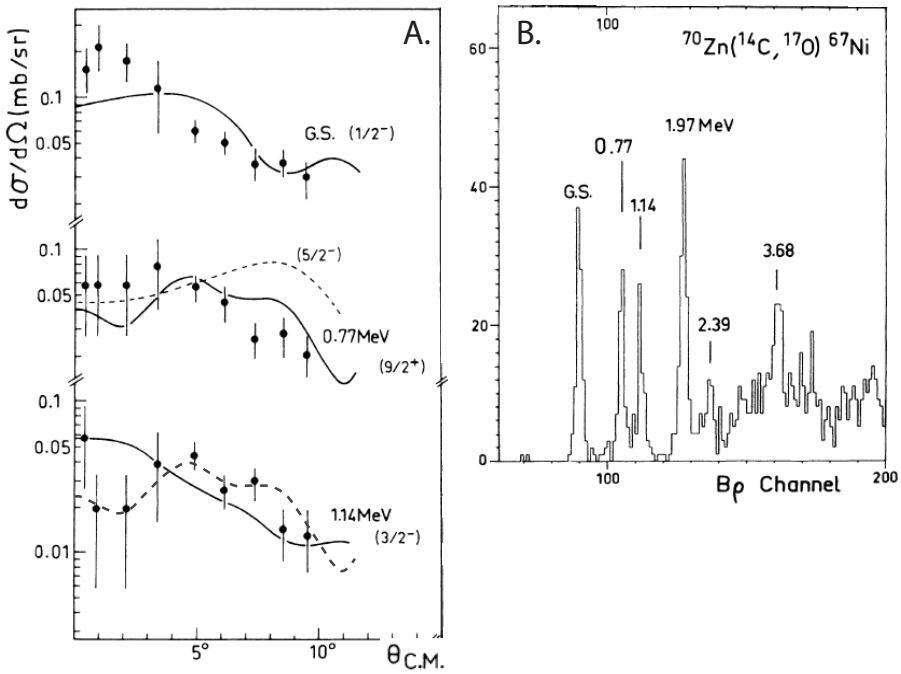

Figure 1.12: Figures from ^{70}Zn(^{14}C,^{17}O)^{67}Ni data taken from Ref. [Gir88]. A. Fits for three lowest states in ^{67}Ni with the $9/2^+$ distribution for 1.14 MeV copied from 0.77 MeV. B. Measured excitation spectrum.

At 2155 keV excitation energy, a second $(5/2^-)$ state was observed in β decay, interpreted as either a $\nu f_{5/2}^{-1} \otimes 0_2^+(^{68}\text{Ni})$ or $\nu p_{1/2} \otimes 2_1^+(^{68}\text{Ni})$. In Ref. [Wei99] the first coupling is put forward, but energywise the second coupling is more acceptable [Oro00].

Multi-nucleon transfer reactions on ^{70}Zn identified levels at 1140, 1710, 1970 , 2390 and 3680 keV [Gir88, Kou78], with tentative spin assignments of $3/2^-$ for levels at 1970 and 3680 keV. In Ref. [Gir88] it is however mentioned that the angular distributions for these states "*are not characteristic*".

1.3.2 Development of collectivity below $Z = 28$

In Figure 1.8, $E(2_1^+)$- and $B(E2;2_1^+ \rightarrow 0_1^+)$ values are also shown for Fe ($Z = 26$) and Cr ($Z = 24$) isotopes below the nickel chain. The main observation is that the $N = 28$ shell remains closed both in ^{54}Fe and ^{52}Cr. The

المنارة للاستشارات

stabilizing effect of the $N = 40$ HO shell closure however vanishes and a rapid development of collectivity can be observed in ^{62,64,66}Fe and ^{60,62,64}Cr [Rot11, Hot10, Lju10, Gad10, Pau09, Aoi09, Kan08, Sor03, Han99, Bau12]. This was initially triggered by the observation of the steep drop of $E(2_1^+)$ in $^{64,66}Fe_{38,40}$ [Han99], together with a recent determination of the $B(E2;2_1^+ \rightarrow 0_1^+)$ values from life time measurements and Coulomb excitation confirming the increase in collectivity [Lju10, Rot11, Van09].

Several reasons can be invoked for this onset of collectivity, with the first one being the repulsive tensor interaction between $\pi f_{7/2}$ and $\nu g_{9/2}$. As protons are removed from the $\pi f_{7/2}$ orbital, the $\nu g_{9/2}$ will shift down in energy, reducing the $N = 40$ gap and facilitating neutron excitations across the gap. The other reason lies in the (quasi-)SU(3) sequence spanned by the $\nu g_{9/2} d_{5/2} s_{1/2}$ orbitals above $N = 40$, which lead to collectivity and deformation (see Section 1.2.5 on p. 15).

To illustrate this second point, comparative SM calculations using a ^{48}Ca-core with active pf-shell plus $\nu g_{9/2}$ orbital and ^{52}Ca-core with active pf-shell plus the $\nu g_{9/2} d_{5/2}$-orbitals were performed [Cau02]. The agreement between both calculations for Fe isotopes is good up to and including $N = 36$, but beyond this point the inclusion of the $\nu d_{5/2}$ orbital is necessary to explain the increase in collectivity. In the case of Cr, the divergence between calculations using different neutron valence spaces already sets in at $N = 36$ [Sor03]. In conclusion, the reduction of the $Z = 28$ gap due to the tensor interaction alone cannot explain the onset of deformation in the iron and chromium region and the explicit inclusion of the νgds orbitals in shell-model calculations appears to be crucial.

1.4 Objectives and motivation

In the previous sections, the importance of the size of the $N = 50$ shell gap and, more generally, the positions of the single-particle neutron orbitals near ^{68}Ni for the structure in this mass region have been highlighted. According to nuclear theory the rapid development of quadrupole collectivity observed in the Fe and Cr isotopes is attributed to the quasi-SU(3) sequence spanned by the $\nu g_{9/2} d_{5/2}(s_{1/2})$ orbitals [Len10]. The positions of the positive-parity gds and negative-parity pf states and thus the size of the $N = 40$ and 50 gap are crucial because they influence the development of the quadrupole collectivity. However, due to the three-body monopole interaction [Ots10b], the $N = 50$ gap size will in turn depend on the occupancy of the $\nu g_{9/2}$ orbital itself [Sie12].

المنارة للاستشارات

Therefore the aim of the present work is to characterize the excited states in ^{67}Ni by studying this nucleus in a one-neutron transfer reaction, namely ^{66}Ni(d,p)^{67}Ni. Chapter 2 will describe how few-nucleon transfer reactions are sensitive to the single-particle character of the excited states and hence how information on the $N = 50$ gap size near ^{68}Ni can be inferred. This parameter can be used as input for current large-scale shell-model calculations in this region of the nuclear chart, as shown in Figure 1.6.

المنارة للاستشارات

المنارة للاستشارات

2

Reaction Theory

In this chapter, an overview of the reaction theories used to describe nuclear reactions with the emphasis on direct few-nucleon reactions is presented. Only the main line of thought is presented and the main formulas are highlighted. A more detailed derivation of these results can be found in Refs. [Tho09, Ber04, Gle04, Sat90]. The first part of this chapter deals with nuclear reactions from a phenomenological perspective by giving a few examples of various types of nuclear reactions. In the second part of the chapter, the quantum mechanical treatment of the scattering theory is discussed and the final part will illustrate the sensitivity of the proton angular distributions on various parameters for the ^{66}Ni(d,p) reaction studied here.

2.1 Nuclear reactions

As discussed in the previous chapter, a general nucleus ${}^{Z_A+N_A}_{Z_A}\mathrm{A}_{N_A}$ contains $Z_A + N_A$ nucleons, of which Z_A protons and N_A neutrons. In case such a nucleus is accelerated to a certain energy E_A in a laboratory and directed on a *target* nucleus ${}^{Z_B+N_B}_{Z_B}\mathrm{B}_{N_B}$, a nuclear reaction can occur. The accelerated nucleus is called the *projectile*. The general form of a nuclear reaction can be written as:

$$A + B \rightarrow C + D. \tag{2.1}$$

In this case A and B (*entrance channel*) are respectively the projectile and target, while C and D (*exit channel*) are called the *ejectile* and *recoil*. The combination

المنارة للاستشارات

of A, B, C and D is commonly referred to as a certain *mass partition*. Due to the relationship between mass and energy

$$E = mc^2 \tag{2.2}$$

the amount of energy released or required by the reaction can be calculated if the masses of all particles involved are known. This amount of energy is called the Q *value* of the reaction:

$$Q = (m_A + m_B - m_C - m_D)\, c^2. \tag{2.3}$$

In case the Q is positive, energy is released in the reaction as there is a reduction of the total mass of the system. Such reactions are called *exothermic*. Conversely, in case $Q < 0$ there is an increase in total mass of the system and hence a minimal amount of kinetic energy should be present to allow the reaction to take place. This amount of kinetic energy $-Q$ is called the *threshold energy* and the reaction is *endothermic*.

If one of the particles in the exit channel is produced in an excited state, the Q value will be lowered by this excitation energy. Hence excited states of the particles in the exit channel can be populated up to an excitation energy of $E + Q$, with E the available kinetic energy in the Center of Mass frame of reference (see Section 2.2). Hence, if the projectile energy is increased, both the number of excited states that can be populated in a certain partition as well as the number of possible partitions will increase.

2.1.1 Conservation laws

Nature does not allow all reactions to take place and all low-energy nuclear reactions are bound to obey a set of *conservation laws*:

- **Energy** and **Linear momentum**: Given a two-body reaction (as defined in Eq. 2.1), the laws of kinematics completely define the relative motion and energies of the particles in the exit channel. As discussed in the previous section, endothermic reaction require a minimal amount of kinetic energy to take place.
- **Charge**: The amount of charge is always conserved in any nuclear reaction. The total amount of charge in the entrance channel equals $Z_A + Z_B$ and this sum should be equal to $Z_C + Z_D$ i.e. the total charge in the exit channel. This means that nuclear reactions do not allow a neutron to transform into a proton or vice versa as this would alter the total charge in the exit channel.

المنارة للاستشارات

- **Mass number**: The total number of particles in the entrance and exit channel should also always be equal. In combination with conservation of charge this leads to the fact that during a nuclear reaction only an exchange or rearrangement of nucleons can happen and that no nucleons can be created or destroyed during this collision.
- **Angular momentum**: The total angular momentum (combination of intrinsic spin of the particles in the different channels and their relative angular momentum[1]) is conserved. In case of a one-neutron transfer reaction the neutron is initially bound with $L = 0$ to the proton, i.e. a $s_{1/2}$-wave. Assume that the neutron is transferred to e.g. a $L = 2$ state the relative angular momentum between the remaining proton and ^{67}Ni nucleus should also be $\ell = 2$. This point will be further illustrated later in this chapter.
- **Parity** is related to the previous point and can be used to determine spin and parity of states populated in reactions.
- **Isospin** is approximately conserved in reactions with light nuclei where the effect of the Coulomb force is small. In these reactions, the total isospin $\vec{T}$ is conserved and the population of states which do not conserve isospin is severely hindered. Examples of this can be found in the region near ^{12}C: The ^{14}C(^{3}H,p)^{12}C reaction only populates two $\vec{T} = 2$ levels in ^{12}C and population of the $\vec{T} = 0$ ground state is not observed [Ajz90]. This is in contrast with the ^{14}N(d,α)^{12}C reaction where different $\vec{T} = 0$ states are observed, including the ground state [Ajz85].

2.1.2 Types of nuclear reactions

Depending on the rearrangement of nucleons in or between the particles in the entrance channel, different types of nuclear reactions can be distinguished:

Elastic scattering

In this case there is no exchange of nucleons between the particles in the entrance channels, and all involved nuclei remain in their ground state and only their

[1]Throughout this text the concept of angular momentum will be used in different contexts. The symbols L and ℓ will be used to distinguish between two common uses: when referring to the angular momentum of a bound nucleon relative to its core the L symbol will be used. The relative angular momentum between nuclei before or after a collision will be referred to as ℓ.

المنارة للاستشارات

trajectories will be altered. The Q value for such a reaction is equal to 0 and Eq. 2.1 becomes

$$A + B \rightarrow A + B. \tag{2.4}$$

When this kind of reaction is studied using two nuclei, the interactions at work between A and B are the electromagnetic interaction (Coulomb force) and, for high energies, the strong force. High projectile energies are required to allow the nuclei A and B to approach each other close enough in order for the strong nuclear interaction to play a role. For this reason one often uses electrons to study elastic scattering which can be used to determine charge distributions. These leptons are not influenced by the strong interaction and can easily penetrate into the nucleus that is bombarded [Sic70].

Inelastic scattering

Still no exchange of nucleons occurs, but one of the incident nuclei gets excited to a more energetic state:

$$A + B \rightarrow A + B^*. \tag{2.5}$$

This notation indicates that after the reaction, the nucleus B is left in an excited state. An example of this is the study of nuclei by *Coulomb excitation*, where a nucleus is excited due to the changing electromagnetic fields. The rate at which a certain excited state is populated is related to the *quadrupole collectivity* of that state, expressed by a $B(E2)$ value [Ald75, Ald56, Van06, Bre13].

Transfer reaction

In this case one nucleon or a cluster of nucleons is transferred from one of the incident nuclei to the other one. For a one-neutron transfer reaction Eq. 2.1 becomes

$$A(= C + n) + B \rightarrow C + D(= B + n). \tag{2.6}$$

From this notation, it can be seen that the recoil nucleus is equal to the initial target with an additional neutron. Furthermore, nuclei C and D can also be populated in excited states, which will lead to a reduction in the available kinetic energy of the particles in the exit channel. In the case of a one-neutron transfer reaction Eq. 2.3 can be rewritten in terms of the neutron separation energies of nuclei A and D:

$$Q = \left(S_n(D) - S_n(A)\right) c^2 \tag{2.7}$$

where $S_n(x)$ is the neutron separation energy of nucleus x. An example of a transfer reaction is the ^{66}Ni(d,p)^{67}Ni one-neutron transfer reaction, which is

المنارة للاستشارات

the subject of this thesis. Since neutron separation energies are known for d (2224 keV) [Bra97] and ^{67}Ni (5808 keV), the Q value of the reaction is positive: $Q = 3586(3)$ keV [Kou78]. Due to conservation of angular momentum, the combination of the spins and parities of the nuclei in the exit channel will lead to a specific relative angular momentum between these particles. This will be explained in Section 2.4.8.

Capture reaction

When the incident energy is small, the nuclei in the entrance channel might form a composite configuration that lasts long enough to prevent an immediate escape back to the $A + B$ channel. These reactions often require the assistance of *resonances* in the composite nucleus (called *compound nucleus reaction*). After this capture, energy is released by particle or radiative emission:

$$A + B \rightarrow C^* \rightarrow C + \gamma. \tag{2.8}$$

Examples of capture reactions of importance for astrophysics are d(p,γ)^{3}He or ^{3}He(α,γ)^{7}Be (PP II chain) which occur in stars during hydrogen burning [Tho09].

Fusion-evaporation reaction

In the case of colliding heavy nuclei, a special kind of the capture reaction might happen. The two heavy nuclei can *fuse* together and create the compound nucleus in a highly excited state (the initial kinetic energy should be high enough to overcome the Coulomb barrier). Such a system very rapidly ($\approx 10^{-20}$s) releases energy by particle emission (evaporation) before γ decay takes over:

$$A + B \rightarrow C^* \rightarrow D^* + n + p \rightarrow D + \gamma. \tag{2.9}$$

Breakup reaction

In this final type of nuclear reactions one of the incident nuclei breaks up into multiple fragments:

$$A + B \rightarrow A + \sum B_i \tag{2.10}$$

where B_i is the i^{th} fragment of B. An example includes the break up of a deuteron into a proton and a neutron.

المنارة للاستشارات

2.1.3 Time and energy scales

The classification above is purely based on the eventual outcome of the reaction. However, these reactions can also be classified based on the time and energy scales involved.

Direct reactions

These are the fastest reactions which occur at high incident energy. The interaction between the particles in the entrance channel is limited to very few nucleons on the surface of the nuclei, leaving the underlying core unperturbed. These collisions have large impact parameters and are commonly referred to as *grazing collisions*. These reactions happen so fast that the final direction of the nuclei in the exit channel is heavily dependent on the initial direction of the incoming nuclei and hence the *angular distribution* of the remaining nuclei will have an outspoken shape. These reactions can be accurately described by one-step models such as DWBA (see Section 2.4.6) or CCBA.

Compound reactions

These are the slowest reactions and occur at low incident energy. If the incident projectile penetrates the target nucleus at low incident energy and small impact parameters (central collisions), it will spend a relatively long time in this target nucleus and will have the possibility to undergo many nucleon-nucleon collisions in the target. The incident kinetic energy will be divided among many nucleons in the target nucleus and the resulting system is a fusion of the incident nuclei. This compound system can further decay by either radiative emission or particle emission. In the case of the latter, a compound nucleus reaction might lead to the same result as a direct reaction, but the emitted particle will have lost all the information on how this state was formed and the resulting angular distribution will in general by isotropic.

2.2 Kinematics of nuclear reactions

The notation and derivation below are based on chapter 2 of [Tho09] and only non-relativistic kinematics are discussed[2]. Consider the notation in Eq. 2.1, where A and B are the two nuclei in the entrance channel with masses m_A,

[2]Relativistic kinematics can be found in chapter 2 of [Tho09]

المنارة للاستشارات

m_B and velocities $\vec{v}_A$, $\vec{v}_B$ in a fixed laboratory frame of reference (LAB). From this, we can write expressions for the energy and momentum of both nuclei: $E_A = \frac{1}{2} m_A v_A^2$, $\vec{p}_A = m_a \vec{v}_A$ and similar for nucleus B. During regular experiments, one of these two nuclei is the target nucleus B and generally at rest ($\vec{v}_B = 0$) and hence $E_B = 0$, $\vec{p}_B = 0$. We denote the positions of the nuclei A and B as $\vec{r}_A$ and $\vec{r}_B$. From symmetry reasons the dynamics of the reaction can be best described in the *center of mass frame of reference* (CM), which has its origin in the center of mass of nuclei A and B. Its coordinates $\vec{S}$ can be expressed in the LAB frame as:

$$\vec{S} = (m_A \vec{r}_A + m_B \vec{r}_B) / (m_A + m_B) \tag{2.11}$$

$$\vec{R} = \vec{r}_A - \vec{r}_B. \tag{2.12}$$

Eq. 2.12 gives the relative position vector of the colliding nuclei. Using

$$E_{\text{tot}} = \frac{1}{2} m_A v_A^2 + \frac{1}{2} m_B v_B^2 \tag{2.13}$$

in combination with Eq. 2.11 and 2.12, the expression for the total kinetic energy of the system can be rewritten as:

$$E_{\text{tot}} = \underbrace{\frac{1}{2} m_{AB} \dot{S}^2}_{\text{Center of mass motion}} + \underbrace{\frac{1}{2} \mu \dot{R}^2}_{\text{Relative motion}}. \tag{2.14}$$

Eq. 2.14 shows that the total kinetic energy of the system can be decomposed in the sum of the energy of motion of the center of mass (where $m_{AB} = (m_A + m_B)$) and the energy of relative motion (where μ denotes the *reduced mass*: $\mu = m_A m_B / m_{AB}$).

In the absence of external forces the motion of the center of mass will be constant and only the energy of relative motion will be relevant to describe the scattering of the nuclei. In the case of a stationary target in the LAB frame, the relation between the incoming projectile energy E_A and the energy of relative motion E simplifies to

$$E = \frac{1}{2} \mu \dot{R}^2 = m_B / m_{AB} E_A. \tag{2.15}$$

As will be shown in Section 2.4.2, all reaction models use the CM frame to perform their calculations. However, all experiment are performed in the LAB system and so relationships between the LAB and CM scattering angles (θ_{lab} and θ_{cm}) have to be established. Using trigonometry it is found that [Tho09]:

$$\tan \theta_{\text{lab}} = \frac{v\prime_C \sin \theta_{\text{cm}}}{\dot{S} + v\prime_C \cos \theta_{\text{cm}}} = \frac{\sin \theta_{\text{cm}}}{\rho + \cos \theta_{\text{cm}}} \tag{2.16}$$

المنارة للاستشارات

where $\rho = \dot{S}/v\prime_C$ and $v\prime_C$ denotes the velocity of C in the CM frame: $v\prime_C = v_C - \dot{S}$. An expression for ρ can be found using conservation of energy and linear momentum [Tho09]:

$$\rho = +\sqrt{\frac{m_A m_C}{m_B m_D}\frac{E}{Q+E}} \tag{2.17}$$

2.2.1 Direct versus inverse kinematics

As it can be seen in Eq. 2.15 the energy of the relative motion depends on the fraction of the mass of particle B, the stationary target nucleus, compared to the total mass in the incoming channel. Historically, targets of isotopically enriched materials were prepared and bombarded with energetic light projectile nuclei to induce reactions. By using light nuclei, nearly all the energy of the system will be contained in the CM energy of relative motion whereas the energy of the motion of the center of mass itself will be small because the center of mass will be nearly stationary at the target position. Hence, the relation between the scattering angles in CM and LAB frames of reference simplify to an elementary 1-to-1 relationship[3]. The kinematics involved in these types of reactions are called *direct kinematics*.

For unstable nuclei, on the other hand, it is in general not possible to prepare suitable targets and perform nuclear reactions in direct kinematics. By swapping the projectile and target nuclei, thus by preparing a target composed of light nuclei and accelerating the radioactive isotopes, this problem can be overcome. The downside is that now most energy will be contained in the motion of the center of mass rather than in the energy of relative motion (see Eq. 2.15). Hence high incoming projectile energies are necessary to provide a suitable CM energy. This type of kinematics is called *inverse kinematics*.

Also the angular dependence of the energy of the resulting ejectile C will behave differently in direct or inverse kinematics[4]. In Figure 2.1 a comparison is made between direct and inverse kinematics for the ^{66}Ni(d,p) reaction. The angular dependence of the energy of the outgoing proton in direct kinematics is very small and the separation between the lines representing different excitation energies of ^{67}Ni equals this amount of excitation energy. In inverse kinematics the situation is clearly different and a strong dependence on the scattering

[3] I.e. Eq. 2.17 becomes nearly 0 and from Eq. 2.16: $\tan\theta_{lab} \approx \tan\theta_{cm}$

[4] The kinematics of the heavy nucleus under investigation on the other hand will not change significantly after the reaction. In case of direct kinematics, it will remain nearly stationary, while in inverse kinematics the heavy projectile will travel straight on, still carrying the majority of the initial incoming energy.

المنارة للاستشارات

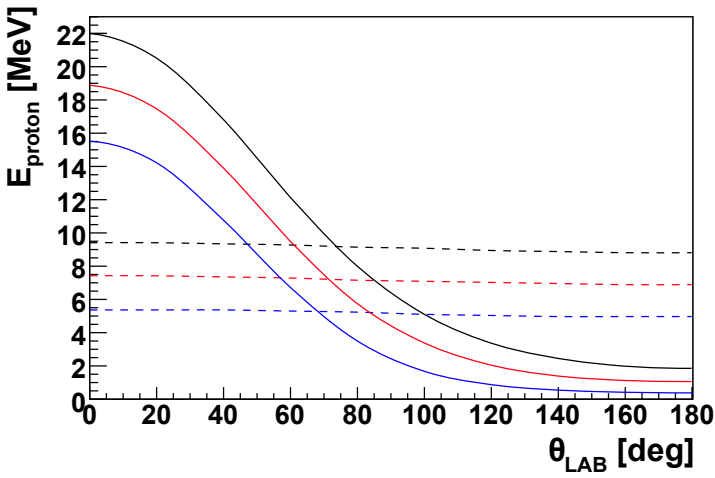

Figure 2.1: Comparison between direct and inverse kinematics for the ^{66}Ni(d,p) reaction with an incoming beam energy of 2.9 MeV/u. The solid lines represent the inverse kinematics, the dashed lines the direct kinematics. Three different excitation energies (of ^{67}Ni) are presented: black for 0 MeV, red for 2 MeV and blue for 4 MeV.

angle can be seen. Furthermore, considerable kinematical compression occurs for large LAB (and hence small CM) angles as the kinematical lines come close together at these large angles. Due to the strong angular dependence in forward directed angles, not only good energy resolution but also adequate positional resolution has to be obtained for the detection of the outgoing protons in order to distinguish excited states. Another factor that was not considered here is the beam spot size, which can distort the kinematical picture more severely[5] in inverse kinematics as opposed to direct kinematics.

2.3 Information from direct nuclear reactions

A direct nuclear reaction generally involves the transfer of a nucleon or cluster of nucleons from one of the nuclei involved in the collision to the other. As was mentioned on page 32, the newly formed nucleus can be populated either in its ground state or in an excited state. The nature of a direct reaction, which is a fast, peripheral reaction, implies that only few nucleons are involved and

[5]This is due to the combination of angular dependence of the ejectile energy and position resolution.

المنارة للاستشارات

many particle rearrangements do not occur. Therefore, excited states with predominantly collective character are not or very weakly populated in direct nuclear reactions.

In Section 2.4.8, it will be discussed that the specific *angular distribution* or *differential scattering cross section* of the ejectiles after a direct nuclear reaction, depends strongly on the spin and parity of the state that was populated in the reaction. Measuring the angular distribution and energy of these ejectile hence yields valuable information on the spin and parity of the excited states. The energy of the ejectile can be used to determine the excitation energy of the state that was populated (see e.g. Figure 2.1) and the angular distribution can be compared with model calculations to infer information on the spin and parity of this state.

2.3.1 Differential cross sections

The *differential cross section of a reaction* $\frac{\mathrm{d}\sigma(\theta,\varphi)}{\mathrm{d}\Omega}$, where θ is the polar angle with respect to the beam axis and φ measures the azimuthal angle, is related to the angular distribution of the remaining ejectile. Its value is usually expressed in *barns* [b] or *millibarns* [mb][6] per steradian [srad]. If a particle detector is installed to measure ejectiles under certain polar angles θ and φ, then the rate of detected ejectiles will depend on

- The size of the detector. This value is expressed as a *solid angle* $\Delta\Omega$ given in *steradians*[7].
- The rate of incoming projectiles denoted as the incoming flux j_i [s^{-1}].
- The differential cross section for this particular setup and reaction: $\frac{\mathrm{d}\sigma(\theta,\varphi)}{\mathrm{d}\Omega}$.
- The number of target nuclei N_t the projectiles can interact with [cm^{-2}]. For a given thickness d this is $N_t = \frac{\rho d}{A} N_A$, with ρ the density, A the targets mass number and N_A *Avogadro's constant*.
- The detection efficiency ϵ, which can depend on the angle of detection: $\epsilon(\theta)$.

[6] 1 mb = 10^{-3} b = 10^{-31} m^2 = 0.1 fm^2

[7] The total solid angle of all space around a single point equals 4π srad

المنارة للاستشارات

This leads to a detection rate of reaction ejectiles $\frac{\mathrm{d}N}{\mathrm{d}t}$ of[8]

$$\frac{\mathrm{d}N}{\mathrm{d}t} = j_i N_t \epsilon(\theta) \frac{\mathrm{d}\sigma(\theta,\varphi)}{\mathrm{d}\Omega} \Delta\Omega \tag{2.18}$$

and hence one can experimentally measure the differential cross section for populating a specific state by measuring the rate of detection under various angles:

$$\frac{\mathrm{d}\sigma(\theta,\varphi)}{\mathrm{d}\Omega} = \frac{\frac{\mathrm{d}N}{\mathrm{d}t}}{j_i n \Delta\Omega \epsilon(\theta)}. \tag{2.19}$$

The total cross section for a certain reaction can be found by integrating the differential cross section over all solid angles:

$$\sigma_{\mathrm{tot}} = \int \frac{\mathrm{d}\sigma(\theta,\varphi)}{\mathrm{d}\Omega} \mathrm{d}\Omega = \int_0^{\pi} \int_0^{2\pi} \frac{\mathrm{d}\sigma(\theta,\varphi)}{\mathrm{d}\Omega} \mathrm{d}\varphi 2\pi \sin\theta \mathrm{d}\theta. \tag{2.20}$$

2.3.2 Spectroscopic factors

Dedicated DWBA codes will compute, given a specific single-particle configuration, the differential cross section to populate that state. These calculations are performed assuming a pure single-particle configuration. The methods and their sensitivity to different single-particle states will be discussed in Section 2.4.8. However, the states that are populated in direct nuclear reactions are in general not pure configurations due to configuration mixing with collective modes and multi-particle rearrangement configurations. The direct reaction process is only sensitive to the single-particle part of the bound-state wave function and therefore the measured absolute differential cross section will have to be scaled down with respect to the calculated one:

$$\frac{d\sigma_{\mathrm{exp}}(\theta,\varphi)}{d\Omega} = S_{Lj} \frac{d\sigma_{\mathrm{DWBA}}(\theta,\varphi)}{d\Omega}. \tag{2.21}$$

Direct reactions hence offer a valuable tool as the *spectroscopic factor* (SF) S_{Lj} can be directly obtained by scaling the calculated differential cross section to the measured one. This SF can also be compared with shell-model calculations and is related to the *single-particle purity* of a state.

From the quantum mechanical treatment later in this chapter it follows that the experimental SF is equivalent to the norm of the overlap function ($I^B_{An} = \langle \Theta_A | \Theta_B \rangle$, with $\Theta_{A,B}$ the wave functions of the nuclei A and B) of

[8] Here it is assumed that the detector has a small surface and that the differential cross section does not vary considerably with changing θ and φ. To incorporate these feature the product $\frac{\mathrm{d}\sigma(\theta,\varphi)}{\mathrm{d}\Omega}\Delta\Omega$ in Eq. 2.18 should be replaced by $\int_{\mathrm{Detector}} \frac{\mathrm{d}\sigma(\theta,\varphi)}{\mathrm{d}\Omega}\mathrm{d}\Omega$.

المنارة للاستشارات

the nucleus before and after the transfer reaction: SF $= \langle I^B_{An} | I^B_{An} \rangle$. If the transferred nucleon is placed in a given orbital with total spin j without altering the underlying core then the overlap function can be written as $I^B_{An} = \langle \Theta_A | \Theta_A \otimes \phi_{Lj} \rangle$, with ϕ_{Lj} the bound-state single-particle wave function of the transferred neutron. As the core is untouched, the evaluation of this matrix element is the single-particle wave function ϕ_{Lj} itself. For a pure configuration this leads to a SF of 1. In case of mixed configurations, the SF will depend on the *coefficient of fractional parentage* (CFP) of the pure configuration and lead to a SF smaller than 1. This shows the connection and equivalence between spectroscopic factors from an experimental and quantum mechanical point of view.

In general the single-particle strength of an orbital will be spread out over a number of excited states due to configuration mixing, but, by determining the *center of gravity* or *centroid* of the single-particle strength, one can deduce the energy of this single-particle orbit. This is done by a weighted sum of the excitation energies with the spectroscopic factor as weighting factor:

$$\epsilon_{\mathrm{sp},Lj} = \frac{\sum_k S_{Lj,k} E_k}{\sum_k S_{Lj,k}}. \tag{2.22}$$

There are however problems when absolute spectroscopic factors are quoted as they depend on 1- the optical model potentials used, 2- the correctness of DWBA approximation used and 3- the geometry of the single-particle potential parameters [Muk05]. This issue can be overcome by quoting *relative spectroscopic factors* or *asymptotic normalization coefficients* (ANC). Furthermore, for direct reactions at low energy, the reaction will only be sensitive to the tail of the wave functions involved, while the SF is the norm of the overlap function of the nucleus before and after the transfer reaction and is hence evaluated over the whole nuclear volume. Since low-energy nuclear reactions are not sensitive to the nuclear interior, absolute SFs may not be extracted reliably and hence ANCs or relative spectroscopic factors should be used instead. The comparison between spectroscopic factors and ANCs will be quantified in Section 2.4.12.

المنارة للاستشارات

2.4 Scattering theory

2.4.1 General approach

In order to solve a general scattering problem, one has to solve the *Schrödinger equation* (SE) of the system describing the colliding nuclei A and B:

$$\left[-\frac{\hbar^2}{2m_A}\nabla^2_{\vec{r}_A} - \frac{\hbar^2}{2m_B}\nabla^2_{\vec{r}_B} + V(\vec{r}_a - \vec{r}_B)\right]\Psi(\vec{r}_A, \vec{r}_B) = E_{tot}\Psi(\vec{r}_A, \vec{r}_B). \quad (2.23)$$

The first two terms of the Hamiltonian between square brackets represent the kinetic energy of the two colliding particles and the last term is the interaction potential between them. This general form can be transformed to the CM frame of reference by using Eq. 2.14 and this leads to:

$$\left[-\frac{\hbar^2}{2m_{AB}}\nabla^2_{\vec{S}} - \frac{\hbar^2}{2\mu}\nabla^2_{\vec{R}} + V(\vec{R})\right]\Psi(\vec{S}, \vec{R}) = E_{tot}\Psi(\vec{S}, \vec{R}). \quad (2.24)$$

If one assumes that the total wave function $\Psi(\vec{S}, \vec{R})$ can be split into two parts with the first part representing the motion of the CM and the second part representing the relative motion of the nuclei in the CM frame: $\Psi(\vec{S}, \vec{R}) = \Phi(\vec{S})\psi(\vec{R})$, Eq. 2.24 can be split into two separate equations[9]:

$$-\frac{\hbar^2}{2m_{AB}}\nabla^2_{\vec{S}}\Phi(\vec{S}) = (E_{tot} - E)\Phi(\vec{S}) \quad (2.25)$$

$$\left[-\frac{\hbar^2}{2\mu}\nabla^2_{\vec{R}} + V(\vec{R})\right]\psi(\vec{R}) = E\psi(\vec{R}) \quad (2.26)$$

where Eq. 2.25 represents the SE for the motion of the CM in the LAB frame, while Eq. 2.26 describes the relative motion of the colliding nuclei. As Eq. 2.25 does not depend on the interaction potential between A and B, its form is very simple and can be solved directly. The resulting wave function is a plane wave: $\Phi(\vec{S}) \propto \exp(\mathrm{i}\vec{K}\cdot\vec{S})$ with wave number $\vec{K}$ satisfying $E_{\mathrm{tot}} - E = \hbar^2K^2/2m_{AB}$.

The physics information of the reaction is contained in Eq. 2.26 but this equation can not be solved directly. The reason for this is that the interaction potential $V(\vec{R})$ is in general not a simple function. Eq. 2.26 only has analytical solutions for a few simple potentials like the Coulomb potential ($1/r$ behavior) and when the potential equals zero (free space).

[9]This can be justified if one assumes that the interaction $V(\vec{R})$ only depends on the relative separation between A and B and not on the absolute coordinates.

المنارة للاستشارات

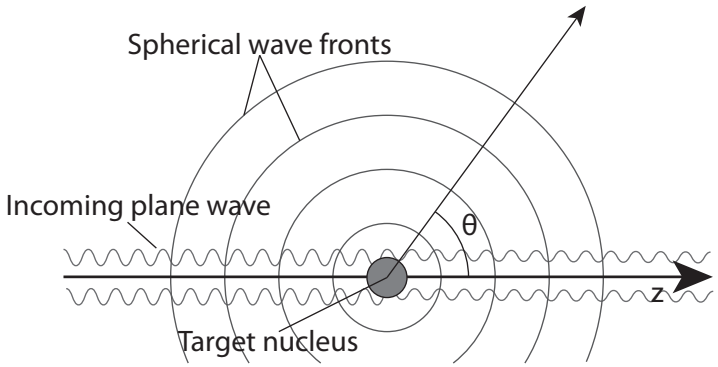

Figure 2.2: Schematic depiction of the reaction principle where a plane wave scatters on a target nucleus. The spherical wave fronts reflect the scattered beam, while the reduced amplitude of the outgoing plane wave reflects the probability of an undisturbed passage.

The general form of the wave function $\psi(\vec{R})$ can be split into two parts. The first part is the contribution from the incoming, undisturbed beam. If the CM frame is oriented with its z-axis along the incoming beam direction, this part of the wave function can be written as $\psi^{\text{beam}} = Ae^{\mathrm{i}k_i z}$, which is a simple plain wave with wave number[10] k_i and A being proportional to the incident flux. The scattered particles can be described asymptotically by spherical waves in order to conserve the outgoing flux: $\psi^{\text{scattered}} = Af(\theta,\phi)\frac{e^{ik_f R}}{R}$. The function $f(\theta,\phi)$ describes the angular distribution of the scattered particles, as well as the strength of the reaction. Hence, the total wave function of relative motion can be written for large R as (see also Figure 2.2):

$$\psi^{\text{total}}(R,\theta,\phi) = Ae^{\mathrm{i}k_i z} + Af(\theta,\phi)\frac{e^{\mathrm{i}k_f R}}{R}. \tag{2.27}$$

As the flux is proportional to the squared norm of the wave function, it follows that:

$$\frac{\mathrm{d}\sigma(\theta,\varphi)}{\mathrm{d}\Omega} = \frac{v_f}{v_i}\left[f(\theta,\phi)\right]^2. \tag{2.28}$$

The goal of various theories is to solve Eq. 2.24 and hence find an expression for $f(\theta,\phi)$. One way to do so is by using the *partial wave expansion* and will be illustrated first for elastic scattering.

[10]The subscript i refers to the initial wave number. Depending on the outcome of the reaction, the relative motion might be different and hence the relative motion will be described by a different wave number k_f.

المنارة للاستشارات

2.4.2 Partial wave expansion

Assuming that the interaction is spherically symmetric, one can take advantage of this symmetry and convert Eq. 2.26 from the Cartesian $\vec{R}$ to spherical coordinates R, θ, ϕ. It is found that Eq. 2.26 becomes

$$-\frac{\hbar^2}{2\mu}\left[\frac{1}{R^2}\frac{\partial}{\partial R}\left(R^2\frac{\partial}{\partial R}\right) - \frac{L^2}{\hbar^2 R^2} + V(R)\right]\psi(R,\theta,\phi) = E\psi(R,\theta,\phi) \quad (2.29)$$

where L^2 is the *angular momentum operator*[11]. The combination of Eq. 2.29 with a spherical symmetric interaction potential results in a Hamiltonian which commutes with both L^2 and L_z (the projection of the angular momentum on the z-axis). Therefore the solutions of Eq. 2.29 can be expressed as linear combinations of the eigenstates of H, L^2 and L_z. By separation of variables we can write these eigenfunctions as:

$$\psi_{kLm}(\vec{R}) = R_L(k,R)Y_{Lm}(\theta,\phi) \quad (2.30)$$

with R_L the solutions of the radial equation and Y_{Lm} the Spherical Harmonics[12] (SH) as solutions of the spherical part of the SE (Eq. 2.30). k, finally, indicates the relative linear momentum: $k = \sqrt{2\mu E/\hbar^2}$. For convenience Eq. 2.29 is usually rewritten using the substitutions: $R_L(k,R) = \frac{u_L(k,R)}{kR}$, $\rho = kR$ and $U(\rho) = \frac{V(\rho/k)}{E}$ as [Ber04]

$$\left[\frac{\mathrm{d}^2}{\mathrm{d}\rho^2} + 1 - \frac{L(L+1)}{\rho^2}\right]u_L(k,\rho) = U(\rho)u_L(k,\rho). \quad (2.31)$$

This equation has to be solved, depending on the type of the potential $U(\rho)$. We distinguish two types of interaction: 1- finite range potentials (including the special case of a potential equal to zero) which can be used to model the short-range strong interaction between nuclei and 2- the Coulomb potential which has a $1/r$ behavior extending up to infinity. General solutions of Eq. 2.31 can be obtained by combining the solutions of the finite range and Coulomb interaction separately, and match them at the *cut-off radius* R_c, which is larger than the range of the finite potentials. First, the results in case of free particles are discussed, which can be generalized for a finite range interaction potential.

[11] $L^2 = -\frac{\hbar^2}{\sin^2\theta}\left[\frac{\partial}{\partial\theta}\left(\sin\theta\frac{\partial}{\partial\theta} + \frac{\partial^2}{\partial\phi^2}\right)\right]$

[12] The spherical harmonics are also related tot the *Legendre polynomials* $P_L(\cos\theta)$ through the relation $Y_l^0(\theta,\phi) = [(2L+1)/4\pi]^{1/2} P_L(\cos\theta)$. As central potentials commute with the angular momentum operators L^2 and L_z, it is often easier to use these Legendre polynomials. In the subsequent parts of the text relations are mostly expressed in terms of $P_L(\cos\theta)$.

المنارة للاستشارات

Free particles

In the case of a particle in free space the potential $V = 0$ for all R. The solutions of Eq. 2.31 (where the right-hand side equals 0 in the case of free particles[13]) can then be expressed as linear combinations of *spherical Ricatti-Bessel* (G_L in Eq. 2.32) and *spherical Ricatti-Neumann functions* (F_L in Eq. 2.32) [Ber04]. For large ρ these are both damped ($1/\rho$) oscillating functions, while for $\rho \to 0$ the Ricatti-Bessel functions are regular and the Ricatti-Neumann functions are irregular at the origin[14].

Also (complex) linear combinations of these functions are solutions of the SE and in one particular case these are called the *Ricatti-Haenkel functions* and are defined as

$$H_L^{(\pm)}(kR) = G_L(kR) \pm \mathrm{i}F_L(kR) \tag{2.32}$$

where $H_L^{(+)}$ represents outgoing and $H_L^{(-)}$ incoming spherical waves as their asymptotic behavior equals $H_L^{(\pm)}(kR \to \infty) \propto \exp \pm \mathrm{i}(kR - L\pi/2)$.

The expression for a plane wave $\exp(\mathrm{i}kz)$ can also be expanded as a sum of partial waves and it can be proven that [Mer70]:

$$e^{\mathrm{i}kz} = \sum_{L=0}^{\infty} (2L+1)\mathrm{i}^L P_L(\cos\theta)\frac{1}{kR}F_L(kR). \tag{2.33}$$

This leads in combination with Eq. 2.32 to:

$$e^{\mathrm{i}kz} = \sum_{L=0}^{\infty} (2L+1)\mathrm{i}^L P_L(\cos\theta)\frac{1}{kR}\frac{\mathrm{i}}{2}\left[H_L^-(kR) - H_L^+(kR)\right] \tag{2.34}$$

which describes a plane wave arriving at the target and leaving it undisturbed.

Non-zero finite potential

For a short-range potential (i.e. a potential that is non-zero up to a radius $R = R_N$) as arbitrarily shown in Figure 2.3 the problem can be split into two Regions I and II. In Region I, where the potential is non-zero, the wave function $u_L^I(kR)$ depends on the shape and depth of the potential and has to be solved using numerical methods. In Region II, the particle moves again as a free particle and hence the wave function will satisfy the Ricatti-Bessel

[13] In this case Eq. 2.31 is called the *Ricatti-Bessel equation*

[14] More properties of these functions can be found in [Ber04] and references therein

المنارة للاستشارات

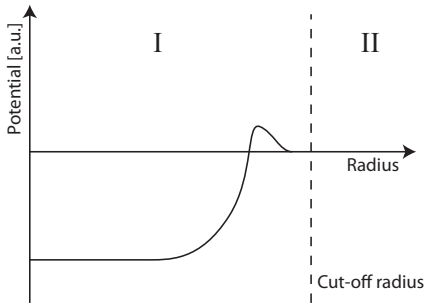

Figure 2.3: Definition of cut-off radius and integration zones I and II used for finite potentials. In this example an arbitrary potential is used.

equation. Solutions of Eq. 2.32 are not directly applicable in Region II, but these can be rewritten in a more general form:

$$u_L^{II}(k,R) = \alpha_L \left[H_L^-(kR) - \mathbf{S}_L H_L^+(kR)\right] \tag{2.35}$$

with α_L as an overall normalization factor and $\mathbf{S}_L$, the *partial-wave S-matrix element*, which includes the effects of the potential. The laws of quantum mechanics require the wave function and its derivative to be continuous at all times. This is done using the *inverse logarithmic derivative*, which is also sometimes called the *partial-wave R-matrix element*:

$$\mathbf{R}_L^{II} = \frac{1}{\alpha_L} \frac{H_L^-(kR_c) - \mathbf{S}_L H_L^+(kR_c)}{H_L^-{}'(kR_c) - \mathbf{S}_L H_L^+{}'(kR_c)}. \tag{2.36}$$

From the numerical integration of the wave function in Region I, the logarithmic derivative at $R = R_c$ in this region ($\mathbf{R}_L^I$) is known. As $\mathbf{R}_L^I$ and all quantities except $\mathbf{S}_L$ in Eq. 2.36 are known, requiring that $\mathbf{R}_L^I = \mathbf{R}_L^{II}$ leads to a value for $\mathbf{S}_L$ for each partial wave. From $\mathbf{S}_L$ one defines the quantity δ_L as

$$\mathbf{S}_L = \mathrm{e}^{2\mathrm{i}\delta_L}. \tag{2.37}$$

δ_L is called the *phase shift*, which is clear when looking at the asymptotic behavior of Eq. 2.35: $u_L(k, R \to \infty) \propto e^{i\delta_L} \sin(kR - L\pi/2 + \delta_L)$, with $\alpha_L{}' = \alpha_L / \cos\delta_L$. In case δ_L is positive, the oscillations are shifted towards smaller values of R. This is the case for attractive potentials as these potentials *pull the wave function towards the origin*. On the other hand, negative values of δ_L, occurring for repulsive potentials, shift the wave function towards larger R, representing the repulsive character of these potentials.

Instead of $\mathbf{S}_L$, also the *partial-wave T-matrix element* $\mathbf{T}_L$ is used and is defined as $\mathbf{S}_L = 1 + 2\mathrm{i}\mathbf{T}_L$. The T-matrix elements will prove their use in Section 2.4.5.

المنارة للاستشارات

Finally, the full scattering wave function can be written in the partial-wave expansion as:

$$\psi(R,\theta) = \sum_{L=0}^{\infty} (2L+1)\mathrm{i}^L P_L(\cos\theta)\frac{1}{kR}u_L^{II}(k,R) \tag{2.38}$$

with $u_L^{II}(k,R)$ the radial functions as given in Eq. 2.35 with $\alpha_L = i/2$ [Tho09]. Also a relation between $\mathbf{S}_L$ and the scattering function $f(\theta)$ exists and one can show that [Tho09]:

$$f(\theta) = \frac{1}{2ik}\sum_{L=0}^{\infty}(2L+1)P_L(\cos\theta)(\mathbf{S}_L - 1). \tag{2.39}$$

Coulomb potential

Due to the nature of the Coulomb interaction, which reaches up to infinity, the method used in the previous section cannot be applied here. The explicit form of the Coulomb potential between two point charges Z_1 and Z_2, which are separated by a distance R is equal to

$$V_c(R) = \frac{Z_1 Z_2 e^2}{R} \tag{2.40}$$

where e is the unit of charge. The SE of Eq. 2.26 with $V = V_c$ can be solved analytically and the resulting wave function depends on the dimensionless *Sommerfeld parameter* η, which depends on the charge of the two nuclei and their relative velocity:

$$\eta = \frac{Z_1 Z_2 e^2}{\hbar v} = \frac{Z_1 Z_2 e^2}{\hbar}\left(\frac{\mu}{2E}\right)^{1/2}. \tag{2.41}$$

The resulting wave function can be written in partial-wave expansion as

$$\psi_c(\vec{k},\vec{R}) = \sum_{L=0}^{\infty}(2L+1)\mathrm{i}^L P_L(\cos\theta)\frac{1}{kR}F_L(\eta,kR). \tag{2.42}$$

This result is very similar to the solution for a finite-range potential presented in Eq. 2.38. The functions $F_L(\eta,kr)$ are called the *regular Coulomb functions* and in fact the Spherical Ricatti-Bessel functions (Eq. 2.32) are a special case of the regular Coulomb functions, namely those with $\eta = 0$. The asymptotic form of $F_L(\eta,kR)$ is:

$$F_L(\eta,kR) \propto \sin(kR - L\pi/2 + \sigma_L(\eta) - \eta\ln(2kR)) \tag{2.43}$$

المنارة للاستشارات

where $\sigma_L(\eta)$ is the Coulomb phase shift[15]. From this, one can find an expression for the scattering amplitude $f_c(\theta)$:

$$f_c(\theta) = -\frac{\eta}{2k\sin^2(\theta/2)} \exp\left[-i\eta \ln(\sin^2(\theta/2)) + 2i\sigma_0(\eta)\right]. \tag{2.44}$$

More interesting is the squared norm of this scattering function which gives an expression for the point-Coulomb cross section or the *Rutherford cross section*. This result is the same as the cross section obtained using classical mechanics:

$$\sigma_{\text{Ruth}} = |f_c(\theta)|^2 = \frac{\eta^2}{4k^2\sin^4(\theta/2)}. \tag{2.45}$$

Global solution

The general structure of the scattering wave function can be found by combining the results from the previous sections. The first step is to define the general phase shift for each partial wave due to the total potential $V(r)$ which is the sum of both the Coulomb potential $V_c(r)$ and the short-range nuclear potential $V_n(r)$:

$$\delta_L = \sigma_L(\eta) + \delta_L^n. \tag{2.46}$$

In order to find the Coulomb-distorted nuclear phase shift δ_L^n (or $\mathbf{S}_L^n$), the same reasoning as developed for the Coulomb interaction can be used. This results in a generalization of Eq. 2.35, now using Coulomb functions with $\eta \neq 0$ instead of the Haenkel functions:

$$u_L^{II}(k,R) = \alpha_L \left[H_L^-(\eta,kR) - \mathbf{S}_L^n H_L^+(\eta,kR)\right]. \tag{2.47}$$

By generalizing Eq. 2.39, the dependence of the general scattering amplitude $f_{nc}(\theta)$ on the nuclear and Coulomb phase shift can be found:

$$e^{2i\delta_L} - 1 = (e^{2i\sigma_L(\eta)} - 1) + e^{2i\sigma_L(\eta)}(e^{2i\delta_L^n} - 1). \tag{2.48}$$

Hence, the total scattering amplitude $f_{nc}(\theta)$ will be a combination of two scattering amplitudes: one pure point-Coulomb scattering amplitude $f_c(\theta)$ and additional *Coulomb-distorted* nuclear-scattering amplitude $f_n(\theta)$, which is no longer due to the short-range nuclear forces alone:

$$f_{nc}(\theta) = f_c(\theta) + f_n(\theta) \tag{2.49}$$

$$f_n(\theta) = \frac{1}{2ik}\sum_{L=0}^{\infty}(2L+1)P_L(\cos\theta)e^{2i\sigma_L(\eta)}(\mathbf{S}_L^n - 1). \tag{2.50}$$

[15] An explicit expression for the Coulomb phase shift is $\sigma_L(\eta) = \arg\Gamma(1+L+i\eta)$

المنارة للاستشارات

The total scattering cross section is equal to the squared norm of Eq. 2.49. Hence interference effects between the nuclear and Coulomb scattering amplitude can either constructively or destructively modify the scattering cross section:

$$\sigma(\theta) = |f_{nc}(\theta)|^2 = |f_c(\theta) + f_n(\theta)|^2 . \tag{2.51}$$

Optical potentials

The elastic scattering model described in the previous sections, treats the interaction between the projectile and target nuclei as an average interaction. However, in reality each nucleon of the projectile will interact with each individual nucleon of the target. In order to fit the model calculations to experimental data, it is often found that better results are obtained when besides a real-valued potential, also a *negative imaginary* part is introduced: $V_{\text{tot}}(r) = V(r) + iW(r)$, with $W(r)$ a negative potential. The main reason for this is that beside elastic scattering, which is the main component of the global wave function, also other reaction channels are open (see Section 2.1.2). In these reactions, the exit channel differs from the entrance channel and hence flux has to be removed from the elastic-scattering channel. Using the continuity equation [Tho09]

$$\nabla \cdot \vec{j}(\vec{R}, t) + \frac{\partial \rho(\vec{R}, t)}{\partial t} = 0 \tag{2.52}$$

with $\vec{j}(\vec{R}, t) = \vec{v}\,|\psi|^2$ as the *nuclear flux* and $\rho(\vec{R}, t) = |\psi|^2$ the nuclear density. One can evaluate the second term in Eq. 2.52 and find an equivalent expression:

$$\nabla \cdot \vec{j}(\vec{R}, t) = \frac{\mathrm{i}}{\hbar}\left[\delta(\vec{R} - \vec{R}_i)H - H^{\dagger}\delta(\vec{R} - \vec{R}_i)\right] \tag{2.53}$$

with $\vec{R}_i$ referring to the internal coordinates of the Hamiltonian. In case this Hamiltonian H has a complex component, the rate of loss of flux can be calculated:

$$\frac{\partial\,|\psi|^2}{\partial t} = -\nabla \cdot \vec{j}(\vec{R}, t) + \frac{2}{\hbar} W\,|\psi|^2 . \tag{2.54}$$

From this it follows that in case W is negative, flux is removed and W is referred to as an *absorptive* potential. In general, potentials which contain both real and imaginary parts are called *optical potentials*.

When introducing complex potentials the general solutions of the previous sections remain valid, but it will affect the phase shifts δ_L which will become complex as well. Moreover their moduli $|\mathbf{S}_L|^2$ will not be equal to 1 and in the case of absorptive potentials: $|\mathbf{S}_L|^2 < 1$.

المنارة للاستشارات

2.4.3 Multi-channel scattering

The results discussed in Section 2.4.2 only describe the elastic scattering of two nuclei under the influence of both the Coulomb repulsion and a nuclear interaction. However, depending on the energy of the projectile, elastic scattering is not the only process that might occur. Examples of the different outcomes of the collision between ^{66}Ni and ^{2}H are amongst others ^{67}Ni + p, ^{67}Cu + n or the breakup of ^{2}H. Besides these different *mass partitions*, the residual nucleus (^{67}Ni or ^{67}Cu in the previous examples) can be produced in an excited state. We will refer to the internal state or wave function of the projectile as $\phi^{xp}_{I_p\pi_p}(\xi_p)$ where x denotes the mass partition, p the state, I_p the spin and π_p the parity of the state of the projectile. The internal coordinates are described by ξ_p. A similar definition is used for the target-like nucleus: $\phi^{xt}_{I_t\pi_t}(\xi_t)$.

In case these two nuclei have relative angular momentum ℓ, the three angular momenta $\ell, \vec{I}_p$ and $\vec{I}_t$ have to be coupled to a total angular momentum $\vec{I}_{\text{tot}}$. There are two different schemes to couple these angular momenta, schematically compared in Figure 2.4.

- **S-basis**: In the S-basis, one first couples the intrinsic spins $\vec{I}_p$ and $\vec{I}_t$ to a intermediate *channel spin* $\vec{S}$, in a second step this channel spin is coupled to the angular momentum ℓ to $\vec{J}_{\text{tot}}$. This basis is most often used in compound-nucleus reactions as there is typically little channel-spin mixing in these resonances.
- **J-basis**: In the J-basis, the first coupling is between the intrinsic spin of the projectile $\vec{I}_p$ and the relative angular momentum ℓ resulting in the total projectile $\vec{J}_p$. In the second step this $\vec{J}_p$ is coupled to the intrinsic spin of the target which gives $\vec{J}_{\text{tot}}$. The advantage of this basis is that spin-orbit forces for the projectile are diagonal and hence this scheme is mostly used for direct reactions.

The set of all quantum numbers for a specific reaction[16] in the J-basis is $\{xpt, LI_pJ_pI_t\}$, abbreviated by α, denotes a specific partial-wave channel. The radial wave function of the relative motion for this partial wave will be written as $\psi_\alpha(\vec{R}_x, \xi_p, \xi_t)$ (instead of $u_L(R)$) and the total system wave function is now denoted by $\Psi(\vec{R}_x, \xi_p, \xi_t)$. $\vec{R}_x, \xi_p, \xi_t)$ is a sum over all partitions which are the

[16]This means: specific mass partition where the outgoing particles are in a defined state.

المنارة للاستشارات

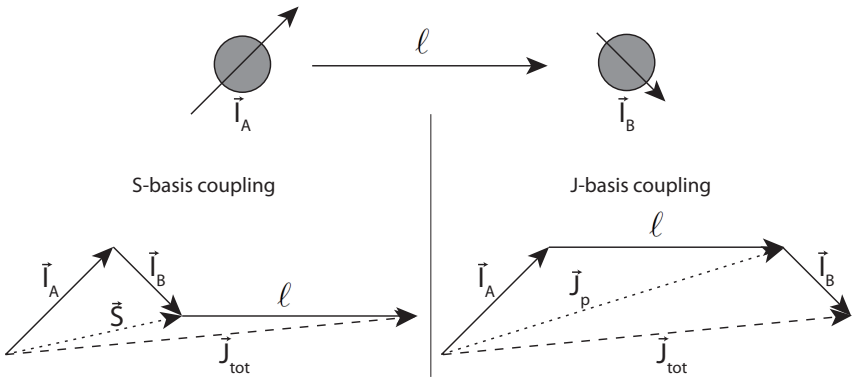

Figure 2.4: Comparison of the two different coupling schemes: S-basis (left) and J-basis (right). Classically these two schemes result in the same final coupling vector $\vec{J}_{\rm tot}$.

product of the internal states and their relative motion[17]:

$$\Psi^{M_{\rm tot}}_{xJ_{\rm tot}}(\vec{R}_x,\xi_p,\xi_t) = \sum_\alpha \left[\left[{\rm i}^L Y_L(\vec{R}_x)\otimes\phi^{xp}_{I_p}(\xi_p)\right]_{J_p}\otimes\phi^{xt}_{I_t}(\xi_t)\right]_{J_{\rm tot},M_{\rm tot}} \frac{\psi^{J_{\rm tot}}_\alpha(\vec{R}_x)}{R_x}. \tag{2.55}$$

This defines the relative motion of the two nuclei in partition x with total angular momentum $J_{\rm tot}$ and projection $M_{\rm tot}$. Also for the external part ($R_x > R_c$) the radial wave function (Eq. 2.47) can be generalized to depend on the entrance channel α_i and is given by[18]:

$$\psi^{J_{\rm tot}\pi}_{\alpha\alpha_i}(\vec{R}_x) = \frac{\rm i}{2}\left[H^-_{L_i}(\eta_\alpha,k_\alpha R_x)\delta_{\alpha\alpha_i} - \mathbf{S}^{J_{\rm tot}\pi}_{\alpha\alpha_i}H^+_L(\eta_\alpha,k_\alpha R_x)\right] \tag{2.56}$$

$$= F_{L_i}(\eta_\alpha,k_\alpha R_x)\delta_{\alpha\alpha_i} + \mathbf{T}^{J_{\rm tot}\pi}_{\alpha\alpha_i}H^+_L(\eta_\alpha,k_\alpha R_x) \tag{2.57}$$

Here $\pi = (-1)^L\pi_{xp}\pi_{xt}$ is the total parity of the partial wave with relative angular momentum L and α_i denotes the incoming channel[19]. The factors

[17] A similar expression can be found for the S-basis, but this is not discussed here.

[18] This expression now contains the generalized Haenkel functions $H^\pm_L(\eta_\alpha,k_\alpha R_x)$ which are related to the Haenkel functions introduced in Eq. 2.32. The Haenkel functions introduced in Eq. 2.32 are in fact a special case of the general Haenkel functions, namely those with $\eta = 0$.

[19] The $\delta_{\alpha\alpha_i}$ term ensures that for non-elastic channels only outgoing Coulomb functions are present.

المنارة للاستشارات

$\mathbf{S}^{J_{\rm tot}\pi}_{\alpha\alpha_i}$ give the amplitude of the outgoing wave in channel α that originates from the incoming channel α_i and form now a full matrix.

2.4.4 Coupled equations

Eq. 2.55 contains the channel wave functions $\psi^{J_{\rm tot}}_\alpha(\vec{R}_x)$. In order to find these wave functions, the set of coupled equations which they satisfy must be constructed, starting from the SE of the whole system: $[H-E]\,\Psi^{M_{\rm tot}}_{J_{\rm tot}\pi}=0$. H is the total Hamiltonian and includes internal parts, kinetic energy and the interaction, which we assume here to be described by central potentials:

$$H = H_{xp}(\xi_p) + H_{xt}(\xi_t) + T_x(R_x) + V_x(R_x,\xi_p,\xi_t). \tag{2.58}$$

The first two contributions determine the internal wave functions of the nuclei in this mass partition: $\phi^{xp}_{I_p}(\xi_p)$ and $\phi^{xt}_{I_t}(\xi_t)$, each with eigenvalues ϵ_p and ϵ_t in Eq. 2.55. One can then find[20]

$$\sum_\alpha [H-E]\,|\alpha; J_{\rm tot}\pi\rangle \frac{\psi^{J_{\rm tot}}_\alpha(R_x)}{R_x} = 0. \tag{2.59}$$

By projecting on one of the basis states, one arrives at the set of coupled-channels equations:

$$\sum_\alpha R_{x\prime}\,\langle\alpha\prime\,|H-E|\,\alpha\rangle\,R_x^{-1}\psi^{J_{\rm tot}}_\alpha = 0 \tag{2.60}$$

$$\sum_\alpha (H-E)_{\alpha\prime\alpha}\,\psi^{J_{\rm tot}}_\alpha = 0 \tag{2.61}$$

with for each $\alpha\prime$ a separate equation.

The Hamiltonian matrix element $\langle\alpha\prime\,|H-E|\,\alpha\rangle$ can be evaluated in two ways: one with H acting on the right side, the *prior*-form: $H=H_{xp}+H_{xt}+T_x+V_x$ and one acting on the left side: $H=H_{x\prime p}+H_{x\prime t}+T_{x\prime}+V_{x\prime}$, the *post*-form. In the prior-form the evaluation of the matrix element becomes:

$$\begin{aligned}
(H-E)_{\alpha\prime\alpha} &= R_{x\prime}\,\langle\alpha\prime\,|T_x+V_x-E_{xpt}|\,\alpha\rangle\,R_x^{-1} &(2.62)\\
&= R_{x\prime}\,\langle\alpha\prime|\alpha\rangle\,R_x^{-1}\,[T_{xL}-E_{xpt}] + R_{x\prime}\,\langle\alpha\prime\,|V_x|\,\alpha\rangle\,R_x^{-1} &(2.63)\\
&\equiv N_{\alpha\prime\alpha}\,[T_{xL}(R_x)-E_{xpt}] + V^{\rm prior}_{\alpha\prime\alpha} &(2.64)
\end{aligned}$$

[20] The section between the outer square brackets in Eq. 2.55 is now abbreviated as $|\alpha; J_{tot}\pi\rangle$.

المنارة للاستشارات

Here $N_{\alpha\prime\alpha}$ is the overlap operator between the two basis states $\alpha\prime$ and α, and $E_{xpt} = E - \epsilon_{xp} - \epsilon_{xt}$. For reactions within one mass partition ($x\prime = x$), this overlap operator is diagonal: $N_{\alpha\prime\alpha} = \delta\alpha\prime\alpha$. Hence, reactions within a partition will have to be dealt with differently than reaction between different mass partitions. One can now, using these definitions, rewrite Eq. 2.61 as:

$$\left[T_{xL}(R_x) - Expt\right]\psi_{\alpha}^{J_{\rm tot}}(R_x) + \sum_{\alpha\prime} V_{\alpha\alpha\prime}^{\rm prior}\psi_{\alpha\prime}^{J_{\rm tot}}(R_{x\prime}) + \sum_{\alpha\prime, x\neq x} N_{\alpha\alpha\prime}\left[T_{x\prime L} - E_{x\prime p\prime t\prime}\right]\psi_{\alpha\prime}^{J_{\rm tot}}(R_{x\prime}) = 0 \tag{2.65}$$

where the last summation includes the non-orthogonal terms, which are particularly important in transfer reactions. A similar reasoning can also be followed using the post-form of the interaction.

2.4.5 Integral form

The **S**−matrix elements introduced above depend on the boundary conditions for differential equations. A different way of calculating them may be done using an integral form. By rewriting the SE, one finds the inhomogeneous equation:

$$\left[E_{xpt} - T_{xL}(R) - V_c(R)\right]\psi_{\alpha}(R) = \sum_{\alpha\prime}\langle|V|\rangle\psi_{\alpha\prime}(R\prime) = \Omega_{\alpha}(R) \tag{2.66}$$

where the term abbreviated as $\Omega_{\alpha}(R)$ is called a *source term*.

This equation can be solved using the formalism of the *Green's function* $G^{+}(R, R\prime)$[21]. One can write the solutions as:

$$\psi_{\alpha}(R) = \delta_{\alpha\alpha\prime}F_{\alpha}(R) + \frac{2\mu_x}{\hbar^2}\int G^{+}(R, R\prime)\Omega_{\alpha}(R\prime)dR\prime \tag{2.67}$$

$$\psi_{\alpha} = \phi + \hat{G}^{+}\Omega_{\alpha} \tag{2.68}$$

$$\psi_{\alpha} = \phi + \hat{G}^{+}V\psi_{\alpha} \tag{2.69}$$

where Eq. 2.68 is a more compact notation in case of elastic scattering. Here $\hat{G}^{+}$ is the Green's integral operator that has the kernel function $2\mu_x/\hbar^2 G^{+}(R, R\prime)$. In terms of Coulomb potential U_c and the kinetic energy operator $\hat{T}$, the Green's

[21] For a formal definition of the Green's function: see [Tho09]

المنارة للاستشارات

	Schrödinger equation	Lippmann-Schwinger	Asymptotic behavior
Free	$[E-T]\,\psi = 0$	$\hat{G}_0^+ = [E-T]^{-1}$	$\psi = F$
Distorted	$[E-T-U_1]\,\chi = 0$	$\chi = \psi + \hat{G}_0^+ U_1 \chi$	$\chi \to \psi + \mathbf{T}^{(1)} H^+$
Full	$[E-T-U_2-U_1]\,\phi = 0$	$\phi = \psi + \hat{G}_0^+ (U_1+U_2)\phi$	$\phi \to \psi + \mathbf{T}^{(1+2)} H^+$

Table 2.1: Overview of the Lippmann-Schwinger equations using the two potential formalism.

operator can also be written as

$$\hat{G}^+ = \left[E - \hat{T} - U_c\right]^{-1}. \tag{2.70}$$

In the solutions of Eqs. 2.68 and 2.69 of which the latter is called a partial-wave *Lippmann-Schwinger equation*, ϕ is referring to the homogeneous solution ($\Omega_\alpha = 0$) and is only present in the elastic channel. Using this notation, the T-matrix in Eq. 2.57 becomes

$$\mathbf{T} = -\frac{2\mu}{\hbar^2 k} \left\langle \psi^{(-)} \left| V \right| \phi \right\rangle \equiv -\frac{2\mu}{\hbar^2 k} \int \psi(R) V(R) \phi(R) dR \tag{2.71}$$

with the $(-)$ symbol denoting complex conjugation.

Two-potential formula

Suppose that the channel interaction $V(R)$ can be split into two parts $U_1(R)$ and $U_2(R)$. We can then use U_1 as the main distorting interaction and U_2 as the remaining potential containing details of the interaction. Eq. 2.71 will now also contain these two terms and we define again ψ as the solution for the free field, χ for U_1 only and ϕ the full solution.

In Table 2.1 the T-matrix element $\mathbf{T}^{(1)}$ describes the scattering due to U_1 alone: $\mathbf{T}^{(1)} = \frac{2\mu}{\hbar^2 k} \left\langle \psi^{(-)} \left| U_1 \right| \chi \right\rangle$. Similarly one can find an expression for $\mathbf{T}^{(1+2)}$, which is also affected by U_2 [Tho09]:

$$-\frac{\hbar^2 k}{2\mu} \mathbf{T}^{(1+2)} = \left\langle \phi^{(-)} \left| U_1 \right| \chi \right\rangle + \left\langle \chi^{(-)} \left| U_2 \right| \phi \right\rangle \tag{2.72}$$

This equation is called the *two-potential formula* and is an exact solution for both real and complex potentials.

2.4.6 Born approximation

In the case of only one potential $U(R)$ it is possible to find the exact solution for χ using the Lippmann-Schwinger equation $\chi = \psi + \hat{G}_0^+ U_1 \chi$. The problem is

المنارة للاستشارات

however that χ appears both in the left and right side of this equation, resulting in an implicit relationship. Therefore one can construct the *Born series* by iteration:

$$\chi = \psi + \hat{G}_0^+ U \left[\psi + \hat{G}_0^+ U \left[\psi + \hat{G}_0^+ U \left[\ldots\right]\right]\right] \tag{2.73}$$

$$= \psi + \hat{G}_0^+ U\psi + \hat{G}_0^+ U\hat{G}_0^+ U\psi + \hat{G}_0^+ U\hat{G}_0^+ U\hat{G}_0^+ U\psi + \ldots \tag{2.74}$$

And using Eq. 2.71 one also finds the equivalent expression:

$$\mathbf{T} = -\frac{2\mu}{\hbar k}\left[\left\langle \psi^{(-)}\left|U\right|\psi\right\rangle + \left\langle \psi^{(-)}\left|U\hat{G}_0^+ U\right|\psi\right\rangle + \ldots\right]. \tag{2.75}$$

If the potential U is weak, the higher-order terms will become less and less important and therefore the series can be cut at some point while still retaining sufficient precision. If only the first term of Eq. 2.75 is kept, this approximation is called the *plane-wave Born approximation* (PWBA)[22]:

$$\mathbf{T}^{\mathrm{PWBA}} = -\frac{2\mu}{\hbar^2 k}\left\langle \psi^{(-)}\left|U\right|\psi\right\rangle. \tag{2.76}$$

One can also evaluate the scattering amplitude in this approximation by using:

$$f^{\mathrm{PWBA}}(\theta) = -\frac{\mu}{2\pi\hbar^2}\int d\vec{R} e^{-\mathrm{i}\vec{q}\cdot\vec{R}} U(\vec{R}) \tag{2.77}$$

with $\vec{q}$ the momentum transfer. Hence the scattering amplitude is simply proportional to the *Fourier transform* of the potential.

In the case of two potentials, a similar Born series can be constructed for the T-matrix element $\mathbf{T}^{(1+2)}$ as was done in Eq. 2.75:

$$\mathbf{T}^{(1+2)} = \mathbf{T}^{(1)} - \frac{2\mu}{\hbar k}\left[\left\langle \chi^{(-)}\left|U_2\right|\chi\right\rangle + \left\langle \chi^{(-)}\left|U_2\hat{G}_0^+ U_2\right|\chi\right\rangle + \ldots\right]. \tag{2.78}$$

If U_2 is weak, this series will converge soon. There is no requirement on the magnitude of U_1 here. If this series is truncated after the first term:

$$\mathbf{T}^{\mathrm{DWBA}} = \mathbf{T}^{(1)} - \frac{2\mu}{\hbar}k\left\langle \chi^{(-)}\left|U_2\right|\chi\right\rangle, \tag{2.79}$$

we call this the distorted-wave Born approximation (DWBA) as it uses the wave functions χ which include the effects of the distortion potential U_1, in the evaluation of the matrix elements. It is very useful for exit channels when the

[22] This approximation is only valid for weak potentials such as in electron-nucleus scattering at high energies.

المنارة للاستشارات

potential U_1 is chosen to be a central potential which in itself cannot cause the transition to this exit channel. This leads to $\mathbf{T}^{(1)}$ and the T-matrix element for the transition from the incoming channel α_i to the exit channel α becomes:

$$\mathbf{T}^{\mathrm{DWBA}}_{\alpha\alpha_i} = -\frac{2\mu_\alpha}{\hbar k_\alpha}\left\langle \chi^{(-)}_\alpha \left| U_2 \right| \chi_{\alpha_i} \right\rangle \tag{2.80}$$

$$= -\frac{2\mu_\alpha}{\hbar k_\alpha}\left\langle \chi^{(-)}_\alpha \left| R_x \left\langle \alpha \left| H - E \right| \alpha_i \right\rangle R^{-1}_{x_i} \right| \chi_{\alpha_i} \right\rangle . \tag{2.81}$$

In this last equation, the formalism developed in Section 2.4.4 was used to obtain an expression for the DWBA T-matrix element for transfer between different mass partitions. The inner matrix element is integrated over the internal coordinates with the Hamiltonian H written either in prior or post form. Using for example the post form one finds:

$$\mathbf{T}^{\mathrm{DWBA,post}}_{\alpha\alpha_i} = -\frac{2\mu_\alpha}{\hbar k_\alpha}\left\langle \chi^{(-)}_\alpha \left| \left[T_{xL} + U_\alpha - E_{xpt}\right] \hat{N}_{\alpha\alpha_i} + \hat{V}^x_{\alpha\alpha_i} \right| \chi_{\alpha_i} \right\rangle$$

$$= -\frac{2\mu_\alpha}{\hbar k_\alpha}\left\langle \chi^{(-)}_\alpha \left| \hat{V}^x_{\alpha\alpha_i} \right| \chi_{\alpha_i} \right\rangle . \tag{2.82}$$

This form is particularly simple as the non-orthogonality terms $\hat{N}_{\alpha\alpha_i}$ disappear for inelastic scattering and reactions to different mass partitions.

2.4.7 Reaction mechanisms

The conclusion of the previous sections is that details of the reaction mechanisms depend on the potentials used to describe the interaction between nuclei.

The general interaction between two spherical nuclei is mostly described by an attractive well with a radius slightly larger than the nuclear radius which then becomes zero in a smooth but sudden way. The most common form for such a well is given by the *Woods-Saxon potential*:

$$V(R) = -\frac{V_r}{1 + \exp(\frac{R - R_r}{a_r})}. \tag{2.83}$$

Typical values for the depth V_r are $40 - 50$ MeV (in case nucleons are used as projectiles) and a diffuseness a_r of 0.6 fm. The value of R_r is given by $R_r = r_r(A_1^{1/3} + A_2^{1/3})$ and thus proportional to the sum of the radii of the nuclei involved, multiplied with r_r which is typically $1.20 - 1.25$ fm. The absorptive

المنارة للاستشارات

imaginary potential $W(R)$ has the same form but its depth will be shallower (typically $10-20$ MeV) and will reach farther than the normal nuclear potential (i.e. $R_W > R_r$) to reflect absorption at the nuclear surface.

For charged nuclei, the Coulomb interaction introduced in Eq. 2.40 should be included[23].

Ideally, all the model parameters are obtained from scattering data at relevant energies, but also models can be used. The dependence of the depth of the real potential on the laboratory energy is of the order of $\partial V_r/\partial E \approx -0.3$ MeV for laboratory energies up to 20 MeV but tends to decrease less rapidly at higher energies.

Finally also *spin-orbit* potentials are included to couple the nuclear spin to the relative angular motion. This potential is of the form:

$$V_{so} = \mathcal{F}_1^{\mathrm{so}}(R) 2\vec{L}\cdot\vec{s}. \tag{2.84}$$

Using the J-basis one can easily evaluate the $\left\langle (Ls)J \left| 2\vec{L}\cdot\vec{s} \right| (Ls)J \right\rangle$-matrix elements, which are $+L$ for parallel and $-L-1$ for anti-parallel couplings. The form of the factor $\mathcal{F}_1^{\mathrm{so}}(R)$ is taken in analogy with the spin-orbit term for electrons in atoms [Tho26]:

$$\mathcal{F}_1^{\mathrm{so}}(R) = \left(\frac{\hbar}{m_\pi c}\right)^2 \frac{1}{R}\frac{\mathrm{d}}{\mathrm{d}R}\frac{V_{so}}{1+\exp\left(\frac{R-R_{so}}{a_{so}}\right)} \tag{2.85}$$

where $(\hbar/m_\pi c)^2 = 2.00$ fm^2. The value of V_{so} is about $5-8$ MeV for nucleons.

Global Optical Potentials

Experimental data using a specific projectile incident on a variety of targets at different energies can be used to fit the optical potentials parameters. The model parameters will in general vary smoothly with energy and mass of the target[24] and hence interpolations as well as extrapolations can be performed to determine optical potential parameters for a specific reaction. A collection of fitted data that provides this information is called a *global optical potential*. Examples of global optical potentials relevant for the reaction studied here can be found in e.g. [Per74, Kon03, Loh74, Per63].

[23] In the case where one penetrates in the nucleus, Eq. 2.40 has to be modified: $V_{Coul} = Z_p Z_t e^2 \left(\frac{3}{2} - \frac{R^2}{2R_{Coul}^2}\right)\frac{1}{R_{Coul}}$, with $R_{Coul} = r_{coul}A^{1/3}$.

[24] This section is written from the point of view of a light projectile incident on a heavy target.

المنارة للاستشارات

Single-nucleon binding potentials

A transfer reaction depends on how the transferred nucleon was bound to its original core and how it will be bound to the target after the transfer. If the interaction of this nucleon with both cores is described in an averaged way, the same type of potentials can be used as in the optical model, i.e. a Woods-Saxon potential combined with a spin-orbit interaction but without imaginary components. This is identical to the discussion in Section 1.2 and also these nuclear levels can be characterized by the set of quantum numbers nLj. The individual wave functions of these nucleons ϕ^m_{Lsj} are given by:

$$\phi^m_{Lsj} = [Y_L(\hat{r}) \otimes X_s]_{jm} \, u_{Lsj}(r)/r \tag{2.86}$$

with X_s denoting the intrinsic spin of the nucleon. The asymptotic behavior of the radial part of these wave functions behaves as:

$$u_{Lsj}(R) =_{r>R_n} C_L W_{-\eta,L+\frac{1}{2}}(-2k_I r) \rightarrow C_L e^{-k_I r} \tag{2.87}$$

where $W_{-\eta,L+\frac{1}{2}}(-2k_I r)$ are the Whittaker functions [Tho09].

The spin-orbit potential, which is a surface-peaked potential, might play an important role in peripheral transfer reactions. Due to its influence in the region close to the nuclear surface it will introduce differences in the cross section for parallel and anti-parallel spin-orbit couplings (e.g. the $\nu p_{1/2}$ and $\nu p_{3/2}$ orbitals). Neutrons placed in orbitals with a parallel spin-orbit coupling (like $\nu p_{3/2}$, $\nu d_{5/2}$ and $\nu g_{9/2}$) will have a larger probability to be found near the nuclear surface due to the attractive SO potential. This will lead to an increase of the reaction cross section as low-energy transfer reactions probe the tail of the nuclear wave functions. In general to radius of the SO interaction is chosen to be smaller than the radius of the Woods-Saxon binding potential ($r_0 = 1.25$ fm versus $r_{SO} = 1.05 - 1.10$ fm) as the Woods-Saxon acts as a mean-field potential. This situation is derived from the optical model potential parameters where r_{SO} is also smaller than r_0. Evidence for the reduced r_{SO} in the optical model potentials was found from the analysis of scattering data using polarized beams [Gre66b, Gol66, Gre66a], where fits using smaller SO radii provided better agreement with the experimental data. Concerning the bound state potentials in the shell model it can be shown that the reduced values of r_{SO} arise naturally from the Brueckner many-body theory [Spr67].

Coupling potentials for transfer reactions

The final ingredient necessary to describe the transfer are the off-diagonal potentials that couple different partial waves within a multi-channel set. For a

المنارة للاستشارات

transfer reaction this involves the three-body Hamiltonian:

$$H = T_r + T_R + V_p(r) + V_t(r\prime) + U_{c\prime c}(R_c). \tag{2.88}$$

In Eq. 2.88, r refers to the relative coordinate of the transferred nucleon with respect to the projectile core, while R refers to the difference in projectile-target positions. The primed versions relate to the situation after the transfer and hence $r\prime$ is the relative position of the transferred nucleon with respect to the target in the case of transfer from projectile to target. Finally, $U_{c\prime c}(R_c)$ is the *core-core potential*.

In a similar way as was done in Section 2.4.4 (page 51) we can rewrite this Hamiltonian in the prior and post form:

$$\begin{aligned} H &= T_R + U_i(R) + H_p(r) + \mathcal{V}_i(R, r) && (2.89)\\ &= T_{R\prime} + U_f(R\prime) + H_t(r\prime) + \mathcal{V}_f(R\prime, r\prime). && (2.90) \end{aligned}$$

Here the potentials $U_{i,f}(r)$ are the entrance (i) and exit (f) diagonal potentials and $\mathcal{V}_{i,f}(R, r)$ represent the *interaction terms* which cause the transition of the nucleon from one core to the other. These potentials have the following form:

$$\begin{aligned} \mathcal{V}_i &= V_t(r\prime) + U_{c\prime c}(R_c) - U_i(R) && (2.91)\\ \mathcal{V}_f &= V_p(r) + U_{c\prime c}(R_c) - U_f(R\prime). && (2.92) \end{aligned}$$

The first part of these interaction terms is the binding potential $V_{p,t}$. The two last terms are called the *remnant terms*.

The general strategy is now to calculate the distorted waves $\chi_{i,f}$ in the entrance and exit channel using the scattering potentials $U_{i,f}$ in combination with the method resulting from Eq. 2.74. With these wave-functions the T-matrix is calculated in either the prior or post description (Eq. 2.82) using the interaction terms discussed above.

2.4.8 Scattering amplitudes in transfer reactions

In the case of a transfer reaction one can rewrite Eq. 2.82 in either prior or post form[25]:

$$\mathbf{T}^{\text{exact}}_{\text{post}} = \left\langle \chi_f^{(-)}(R_f)\Phi_{I_A:I_B}(r_f)\,|V_p(r) + U_{c\prime c} - U_f(R\prime)|\,\Psi^{\text{exact}} \right\rangle. \tag{2.93}$$

[25] As was discussed in Section 2.4.4, the prior and post formalism should lead to the same result.

المنارة للاستشارات

In the framework of DWBA theory, the exact solutions of the scattering problem Ψ^{exact} are replaced by a distorted wave multiplied by a corresponding bound state:

$$\mathbf{T}_{\text{post}}^{\text{DWBA}} = \left\langle \chi_f^{(-)}(R_f)\Phi_{I_A:I_B}(r_f)\,|\mathcal{V}|\,\Phi_{I_b:I_a}(r_i)\chi_i(R_i)\right\rangle . \tag{2.94}$$

The functions $\Phi_{I_A:I_B}(r_f)$ and $\Phi_{I_b:I_a}(r_i)$ are called *overlap functions* and are usually described by single-particle states calculated using a Wood-Saxon potential (see page 57). They describe the wave function of the transferred nucleon or cluster when it is bound to one of the cores.

In order to further evaluate the T-matrix elements in Eq. 2.94, the remnant terms are usually neglected. The interaction potential $\mathcal{V}$ reduces in this case to $V_p(r)$ i.e. the binding potential for the deuteron. When we also require the interaction to have a range of approximately zero, the so-called *zero-range approximation*, we arrive at $V_p\phi_d(r_i) = D_0\delta(r_f - r_i)$ with $D_0 \approx -122.5$ MeV fm$^{3/2}$. Eq. 2.94 now reduces to:

$$\begin{aligned}\mathbf{T}_{\text{post, ZR}}^{\text{DWBA}} &= D_0 \int e^{\mathrm{i}\vec{q}\cdot\vec{R}}\Phi_{I_A:I_B}(\vec{r})d\vec{R} \\ &= \sum_{L=0}^{\infty} \mathrm{i}^L(2L+1)\int \frac{F_L(0,qR)}{qR}P_L(\cos(\theta))\Phi_{I_A:I_B}(\vec{r})d\vec{R}. \end{aligned}\tag{2.95}$$

In this expression $\vec{q}$ represents the momentum transfer which increases with scattering angle as $q^2 = p_i^2 + p_f^2 - 2p_ip_f\cos\theta$, with $p_{i,f}$ the linear momentum of the incoming and outgoing particles. Consider how the T-matrix elements for the transfer to a specific bound state are calculated. The angular part of the integral ensures that only these L-values appearing in the bound state wave function $\Phi_{I_A:I_B}$ are summed, i.e. only the value in case of a bound state: $L = L_B$.

Once the T-matrix elements are calculated, the scattering amplitudes $f(\theta)$ can be obtained using Eq. 2.39 and the fact that $\mathbf{S}_L = \frac{1}{2}\mathrm{i}\mathbf{T}_L$.

With this information, one can now calculate the differential cross-section for a certain reaction. This is most conveniently done in three steps:

1. Obtain optical potentials from either fitting the potentials to available scattering data or use global optical potentials evaluated at the correct incident energies.

2. Calculate the single-particle wave functions of the transferred nucleon or cluster. This is usually done with standard diffuseness and radius

المنارة للاستشارات

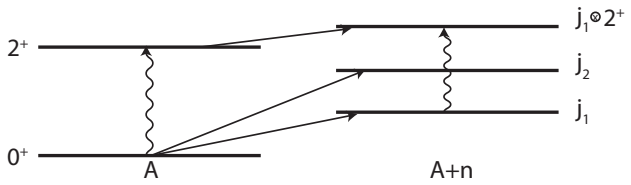

Figure 2.5: Schematic view of higher-order transfer reactions. The first two states in the A+n system can be directly reached in a transfer reaction. The highest state requires a two-step process and the different paths are indicated here.

parameters, while the depth of the potential is scaled to reproduce the correct binding energy.

3. Calculate the differential cross sections using DWBA, either in prior or post formalism which should give the same results. This cross section can be directly compared with the data.

The process of this calculation is performed using available computer codes like FRESCO [Tho88] and DWUCK [Ros71]. In this work, all calculations have been performed using FRESCO.

2.4.9 Higher-order reactions

One of the key concepts and assumptions in the DWBA framework outlined here is that the transferred particle is placed in a dedicated orbital without altering the underlying core. However, this does not have to be *a priori* true. Considering the picture shown in Figure 2.5, the first two states in the A+n system (A is assumed to be an even-even nucleus) are idealized single-particle-like states and can be directly populated in the one-neutron transfer reaction. The third state is e.g. a core-coupled state, coupling the odd neutron in orbital j_1 to a 2^+ core-excitation. Such a configuration can not be directly reached and requires a two-step process by either first exciting the core to a 2^+ state and a subsequent transfer to the orbital j_1 or the other way around.

The formalism incorporating such transfer mechanisms is called the *coupled-reaction channel approximation* (CRC). Details on the development of this formalism are not discussed here but can be found in e.g. Refs [Gle04, Tho09]. The main ingredient is that the optical potentials used to calculate the T-matrix element in Eq. 2.71 will no longer depend only on the relative coordinates of the nuclei involved alone, but also on their internal coordinates so to allow

المنارة للاستشارات

for inelastic scattering [Gle04]. The differential cross section of the scattered protons will no longer depend on the square of $f(\theta)$, but be proportional to

$$\frac{\mathrm{d}\sigma}{\mathrm{d}\Omega} \propto |f_{\mathrm{direct}}(\theta) + f_{\mathrm{indirect}}(\theta)|^2 \tag{2.96}$$

due to configuration mixing. Depending on the relative phases of both scattering amplitudes, the resulting cross section can be influenced by constructive and destructive interference of these components.

Comparative studies have been performed focusing on the choice of the reaction model, e.g. in Refs. [Ros75, Sch72, Asc72, Asc74], primarily aiming on reaction studies in the rare-earth region at high incident energies. Here the combination of strongly deformed nuclei with highly collective structures and high relative velocity of the colliding particles leads to non-negligible contributions from higher-order processes. In some cases an enhancement of the cross section by a factor of two was observed. The general rule dictates that these higher-order processes become more outspoken for collective, deformed nuclei and high incident energies. For spherical medium to heavy mass nuclei at low bombarding energy, the differences between DWBA and CCBA calculations are limited. Therefore the reaction model used to analyze the ^{66}Ni(d,p)^{67}Ni transfer reaction experiment is DWBA.

2.4.10 Deuteron breakup and nonlocality

Two additional phenomena have to be considered when calculating transfer reaction cross sections for (d,p) reactions. Firstly, the breakup of the deuteron, which is only bound by 2.225 MeV, can influence the reaction mechanism. The adiabatic approximation (ADWA) models this by replacing the deuteron-target optical potential by the sum of the proton/neutron-target potential evaluated at half the center of mass energy [Joh70]. In this way, the proton and deuteron interact independently with the target and share the available energy. Both zero-range (ZR-ADWA) [Joh70] and finite-range (FR-ADWA) [Joh74] versions of this approximation have been developed and a more complete overview can be found in Ref. [Nun11].

The importance of deuteron breakup increases when the CM energy exceeds greatly the energy needed to excite the deuteron to the continuum [Tho09] which reaches up to 10 MeV. Hence, CM energies much larger than 20 MeV require the adiabatic approximation to accurately include the effect of deuteron breakup on the calculated differential cross sections [Tho09]. The small CM energy in the present experiment (5.67 MeV) justifies the use of DWBA over ADWA.

المنارة للاستشارات

The second phenomenon that could influence the calculated differential cross sections is the effect of the nonlocality of the nucleon-nucleus interaction [Tim13]. The proposed method in Ref. [Tim13] incorporates nonlocality and three-body degrees of freedom in a consistent way. Starting from the adiabatic approximation developed by Johnson and Tandy ([Joh74]), the nucleon-nucleus potentials used are instead evaluated for an energy larger by ≈ 40 MeV than half the deuteron energy. This extra energy models the kinetic energy of the proton and neutron present during the reaction and incorporates both nonlocality and breakup in the local potential used during the calculation. The resulting deuteron-nucleus potential is more shallow and enhances the predicted cross sections, thus lowering absolute spectroscopic factors. Additionally, the effect is ℓ-transfer dependent and causes differences in relative spectroscopic factors as well.

The effect of this method was evaluated for the present ^{66}Ni(d,p)^{67}Ni experiment. Variations in the magnitude of the cross section were observed, but the shape of the cross section was not affected. The maximum change in relative spectroscopic factors was less than 10% and does not change the results within the quoted error bars.

2.4.11 Classical view of the angular distributions

From a classical point of view, by using the expression $L = Rq$, an intuitive picture of the origin of the proton angular distributions can be drawn. For peripheral reactions, the transfer will take place at the nuclear surface $R \approx R_C$. Hence when transferring the neutron to a state with given angular momentum L, a minimum of linear momentum has to be transferred. As L increases, so will q, and this shifts the peak in the angular distribution to larger θ_{CM} values (recall that $q^2 = p_i^2 + p_f^2 - 2p_i p_f \cos\theta$). Examples of this can be found in Figure 2.7.

The calculated and observed differential cross sections exhibit an oscillatory pattern which can also be described by classical arguments. The principle is schematically presented in Figure 2.6. The incoming particle can scatter on two places on the target nucleus and still have the same final direction. These two places are on the opposite sides of the nucleus as shown in Figure 2.6. Due to the *wave-particle duality principle*, particles will also exhibit wave characteristics and vice versa. In this case the (incoming) particles will have a wave length[26] λ associated with them, just as light, depending on their energy and mass. As the lower path is 2δ longer than the upper path in Figure 2.6, these two paths

[26]In the case of transfer, the energy and mass of the particles change during the process of transfer and hence the wave length of the outgoing particle will change depending on the reaction kinematics.

المنارة للاستشارات

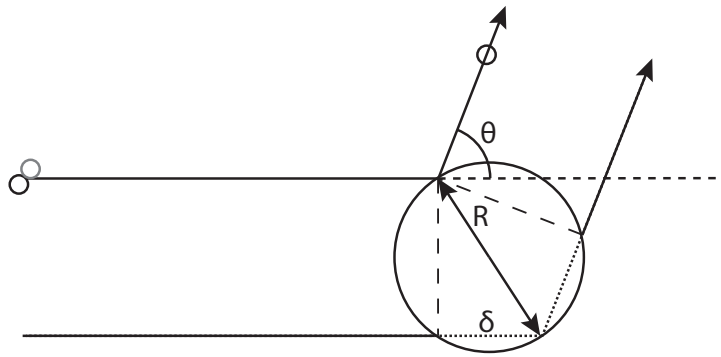

Figure 2.6: Schematic picture of the classical view of transfer reactions. See text for more details.

will cause an *interference* spectrum to arise when they recombine (Fraunhofer diffraction). *Constructive inference* will be observed when the path length difference 2δ is equal to an integer multiple of the outgoing particle wave length ($2\delta = n\lambda_{\text{out}}$). *Destructive interference* will arise when both outgoing waves have a phase difference of half a wave length or $180°$($2\delta = \left(n + \frac{1}{2}\right)\lambda_{\text{out}}$). This phenomenon is the same as the interference patterns observed in e.g. Young's two-slits experiment.

As will be demonstrated in Section 2.5.3, the interference pattern will become more outspoken for higher beam energies. This is due to the fact that for higher incoming beam energies, the initial (and hence also final) wave length of the particles is smaller. Hence, shorter path length differences 2δ and thus smaller angular variations in the direction of the outgoing proton will lead to faster oscillation in the interference pattern. Furthermore, for incident energies near the Coulomb barrier, the Coulomb field acts as a diverging lens (Fresnel diffraction) [Ful75].

2.4.12 Spectroscopic factors and ANC's

In Section 2.3.2, it was argued that experimental absolute spectroscopic factors as introduced in Eq. 2.21 depend on the optical-model potentials used as well as on the geometry of the single-particle binding potential. Also, for low-energy transfer reactions, the reaction probes only the tail of the wave function, rather than being sensitive to the total wave function. This feature is a key motivation for the definition and use of the asymptotic normalization coefficient (ANC).

المنارة للاستشارات

When considering the asymptotic behavior of the overlap function $\Phi_{I_A:I_B}$ introduced in Eq. 2.93 (Section 2.4.8) it should be noted that this behavior should be identical to the one of a single-particle wave function with the same quantum numbers. Namely, for large r:

$$\Phi^{Lj}_{I_A:I_B}(r) \overset{r>R_C}{\approx} C_{Lj} i\kappa h_L(i\kappa r) \tag{2.97}$$

with $\kappa = \sqrt{2\mu_{An}\epsilon_{An}}$ where μ_{An} is the reduced mass of the A+neutron system and ϵ_{An} is the binding energy of the system. Finally, the scaling constant C_{lj} is the ANC. The single-particle wave function has by definition a similar asymptotic behavior:

$$\varphi_{nLj}(r) \overset{r>R_c}{\approx} b_{nLj} i\kappa h_L(i\kappa r) \tag{2.98}$$

with n the principal quantum number. Here the scaling factor is referred to as the *single-particle asymptotic normalization factor* or SPANC. As both the overlap function and single-particle wave function have the same asymptotic behavior C_{Lj} and b_{nLj} are proportional to each other:

$$C_{Lj} = K_{nLj} b_{nLj}. \tag{2.99}$$

If one now assumes that this proportionality is valid for all values of r one has:

$$\Phi^{Lj}_{I_A:I_B}(r) = K_{nLj}\varphi_{nLj}(r). \tag{2.100}$$

As $\varphi_{nLj}(r)$ is normalized to unity, one arrives, by taking the norm on both sides of Eq. 2.100:

$$S_{Lj} = K^2_{nLj} = \frac{C^2_{Lj}}{b^2_{nLj}} \tag{2.101}$$

or that the ANC is the product of the SF and SPANC. Both the SF and SPANC are dependent on the geometrical properties of the potentials, but the ANC is not [Muk05]. On the other hand, the ANCs do not have an explicit structure dependence and are hence hard to interpret.

2.5 Calculations for ^{66}Ni(d,p)^{67}Ni

In this section some calculations and predictions for the one-neutron transfer reaction ^{66}Ni(d,p)^{67}Ni at $E_{\mathrm{CM}} = 5.67$ MeV will be presented. The influence of various parameters like angular-momentum transfer, incident energy, incoming and outgoing potentials, will be presented.

المنارة للاستشارات

2.5.1 Angular momentum transfer sensitivity

Eq. 2.95 shows that in the evaluation of the T-matrix element only one term of the sum over all possible angular momenta will remain, namely that value of ℓ which equals the total angular momentum transferred by the transferred nucleon. This will force the angular distribution of the remaining proton to have a shape which depends on the amount of transferred angular momentum. The magnitude of the cross section will also depend on ℓ due to *momentum matching*. Ideal momentum matching occurs when the amount of transferred momentum equals the initial momentum of the transferred neutron [Fes74]:

$$\left| \frac{A}{A+1} k_f - k_i \right| \approx \sqrt{\frac{2m}{\hbar^2} |\epsilon_n|} \tag{2.102}$$

with $\epsilon_n = 2.246$ MeV, the binding energy of the deuteron [Bra97]. When both sides of this equation are multiplied by R ($qR = L$) it is clear that this limits the amount of transferred (angular) momentum to low values in the case of (d,p) reactions. In contrast for e.g. (^{4}He,^{3}He) transfer reactions, where the binding energy of the neutron is higher and hence higher angular momentum transfer is favored while low ℓ-transfer reactions are mismatched at all angles reducing the magnitude of the cross-section.

In Figure 2.7, differential cross section calculations for the ground state of ^{67}Ni are shown assuming different configurations and thus also different angular momentum transfers. Only $j = \ell + 1/2$ couplings are included, representing orbitals in the neighborhood of the $N = 40$ gap: $2s_{1/2}(\ell = 0), 1p_{3/2}(\ell = 1), 0d_{5/2}(\ell = 2), 0f_{7/2}(\ell = 3), 0g_{9/2}(\ell = 4)$ and $0h_{11/2}(\ell = 5)$. The optical model parameters used are taken from [Han06, Per63] and shown in Table 2.2. In this table, the potentials V denote real potentials, while W refer to imaginary potentials, as introduced in Section 2.4.2. The subscript v means volume potential (WS-potential), s refers to surface potentials and *so* finally is short for spin-orbit potential.

The evolution of the first maximum of the angular distributions in Figure 2.7 is evident: the differential cross-section clearly peaks for $\theta_{\mathrm{CM}} = 0^\circ$ in case of $\ell = 0$ transfer and shifts to larger angles for higher ℓ-transfer reactions. For higher values of angular momentum transfer the peak in the distribution becomes less pronounced.

From Figure 2.7, it is also clear that the *total reaction cross-section* becomes substantially smaller with an increasing amount of transfer angular momentum, due to poor ℓ-matching conditions when a large amount of angular momentum has to be transferred (see Eq. 2.102).

المنارة للاستشارات

Partition	Optical Potentials					
^{66}Ni-d	V_v [MeV]	r_v [fm]	a_v [fm]	W_v [MeV]	r_v [fm]	a_v [fm]
[An06]	94.9	1.14	0.8	1.5	1.37	0.5
	W_s [MeV]	r_s [fm]	a_s [fm]	V_{so} [MeV]	r_{so} [fm]	a_{so} [fm]
	10.7	1.37	0.8	3.6	0.97	1.0
^{67}Ni-p	V_v [MeV]	r_v [fm]	a_v [fm]	W_v [MeV]	r_v [fm]	a_v [fm]
[Per63]	55.4	1.26	0.7	0.0	0.0	0.0
	W_s [MeV]	r_s [fm]	a_s [fm]	V_{so} [MeV]	r_{so} [fm]	a_{so} [fm]
	13.5	1.26	0.5	7.5	1.26	0.5
system	Nucleon binding potentials					
n to p	V [MeV]	r [fm]	a [fm]			
	50	1.25	0.65			
n to ^{66}Ni	V [MeV]	r [fm]	a [fm]			
	71	1.25	0.65			

Table 2.2: Optical model parameters and nucleon binding potentials used for the calculation of the differential cross section for (d,p) ground state to the ground state op ^{67}Ni. ^{66}Ni-d potentials taken from [Han06] with $E_{\mathrm{CM}} = 5.67$ MeV and ^{67}Ni-p potentials from [Per63] with $E_{\mathrm{CM}} = 9.31$ MeV.

2.5.2 Q value dependence

The Q value of the reaction strongly influences the magnitude of the differential cross-section for the reaction. As the Q value from Eq. 2.3 can also be rewritten as $Q = S_n(^{67}\mathrm{Ni}^*) - S_n(\mathrm{d})$ it is obvious that the Q value of a reaction can be modified in two ways: either by producing ^{67}Ni in different excited states, which leads to an artificial reduction of $S_n(^{67}\mathrm{Ni})$, or by changing the target nucleus. The one-neutron transfer reactions (d,p) and (^{4}He,^{3}He) have very different S_n values for the target particles: $S_n(\mathrm{d}) = 2.2$ MeV and $S_n(^4\mathrm{He}) = 20.6$MeV [Aud97, Aul97]. Hence the (^{4}He,^{3}He) reaction will have a strongly negative Q value (-15.6 MeV) and lead to strongly reduced cross sections. A third possibility for the one-neutron transfer reaction is the (t,d) reaction and has a Q value of -449 keV and will have the enhanced cross sections in the vicinity of the ground state. Q matching occurs when the Q value for a reaction to a particular state equals 0. Under this condition, the binding energy of the transferred neutron does not change which facilitates the transfer. Despite the influence of Q matching on the magnitude of the reaction cross section also the spectroscopic factors of the states that are populated have to be considered. In case of strong fragmentation of the available single-particle strength (and thus small spectroscopic factors) in the vicinity of the Q matching energy level, no outspoken or strong reaction cross section populating specific states are to be expected.

المنارة للاستشارات

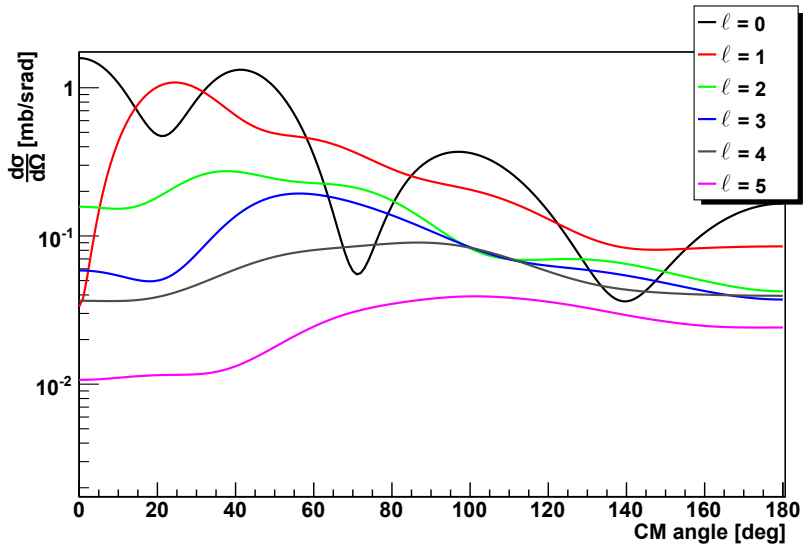

Figure 2.7: Different differential cross-sections for ^{66}Ni(d,p)^{67}Ni transfer reaction at 2.95 MeV/u. ^{67}Ni is produced in its ground state and differential cross-sections assuming various amounts of angular momenta transfer have been plotted. For all ℓ-transfers $J = L + s$ was used. Optical potentials and nucleon binding potentials from Table 2.2.

In the case of ^{66}Ni(d,p)^{67}Ni, the S_n value of ^{67}Ni is 5.8 MeV and hence Q *matching* occurs around an excitation energy of 3.583 MeV [Aud03]. In Figure 2.8, the angular distribution for ℓ =0, 2 and 4 is shown for different excitation energies ($E_{\text{ex}} = 0, 1.5, 3.583$ and 5 MeV in ^{67}Ni). The general observations are that better Q matching indeed leads to an enhanced cross section. The blue dotted lines in Figure 2.8 represent the calculations for ^{67}Ni produced with an excitation energy of 3.583 MeV, i.e. leading to perfect Q matching. The integrated cross-sections reach their maximum value for all amounts of transferred angular momentum at this excitation energy. However, the oscillatory behavior becomes less pronounced, making the amount of ℓ-transfer harder to identify. This last remark is mainly due to the fact that at these high excitation energies, the neutron binding potentials becomes shallow, leading to less pronounced single-particle wave functions which in turn affect the shape of the angular distributions. This effect is even stronger in the purple dotted and dashed curve, representing calculations for $E_{\text{ex}} = 5$ MeV [Coo82, Vin70].

المنارة للاستشارات

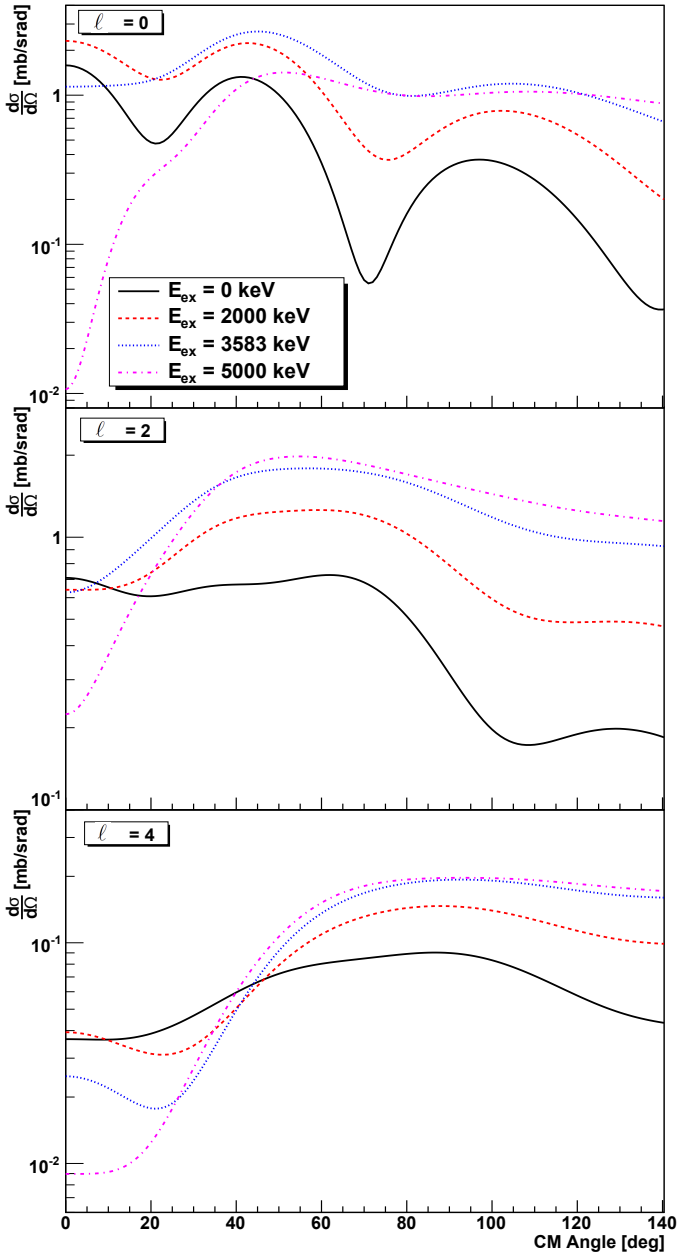

Figure 2.8: Differential cross-sections for ^{66}Ni(d,p)^{67}Ni transfer reaction at 2.95 MeV/u for different excitation energies assuming $\ell = 0$, 2 or 4. The differential cross sections are calculated for excitation energies of 0 (ground state), 2.0, 3.583 and 5 MeV. The Optical Model potentials used can be found in Table 2.2.

المنارة للاستشارات

2.5.3 Beam-energy dependence

When the incoming energy of the projectile is changed, also due to Eq. 2.15 the energy available in the CM frame of reference will change. New reaction channels will open as the available energy for the reaction is equal to $E + Q$. The larger amount of energy available in the CM frame of reference will also lead to a higher relative momentum of the colliding particles which will change the term qR in Eq. 2.95. As the Coulomb functions behave asymptotic as $\propto \sin(qR)$, this will result in stronger oscillations and hence lead to an increased ℓ-transfer sensitivity.

It should also be noted that since the incoming beam energy is increased, the optical model potentials should be adjusted. For this comparison global optical model potentials from [An06] (^{66}Ni-d) and [Kon03] (^{67}Ni-p) are used for beam energies of 3 (current maximum REX-ISOLDE beam energy), 5 and 10 MeV (both available with HIE-ISOLDE). The potentials from Ref. [An06] are valid for the Z-range $[6 - 92]$, A-range $[12 - 238]$ and E-range $[1 - 200]$ MeV and [Kon03] is valid for Z-values between $[13 - 83]$, A-range $[27 - 209]$ and E-range $[0 - 200]$ MeV. The real volume parts decrease with increasing CM energy and the imaginary volume part will become larger. The imaginary surface part will decrease because the reactions will become less peripheral and start to probe the inside of the target nucleus. The potentials used can be found in Table 2.3.

The results of the DWBA calculations for these different beam energies in the case of $\ell = 0$, 2 or 4 can be seen in Figure 2.9. In the case of $\ell = 0$, the differences between 3 and 5 MeV/u can be found in a faster oscillation pattern and an enhanced amplitude difference between the first minimum and maximum (at $\theta = 0°$). The oscillatory pattern obtained for 10 MeV/u is less clear but the pronounced maximum of the differential cross-section for $\theta = 0°$ remains the dominant feature. For $\ell = 2$ the differential cross-sections for 5 and 10 MeV/u have clearly pronounced minima and maxima, while the one for 3 MeV/u behaves more smoothly. This trend is even more obvious for the calculations assuming $\ell = 4$.

Besides the dependence of the ℓ-transfer sensitivity on the incoming beam energy, the magnitude of the cross section will also change as can be seen in Figure 2.9. This is due to momentum matching conditions described in Section 2.5.1. As the beam energy increase, so will the amount of transferred moment q and this will favor transfer reactions where a higher amount of angular-momentum transfer is involved.

المنارة للاستشارات

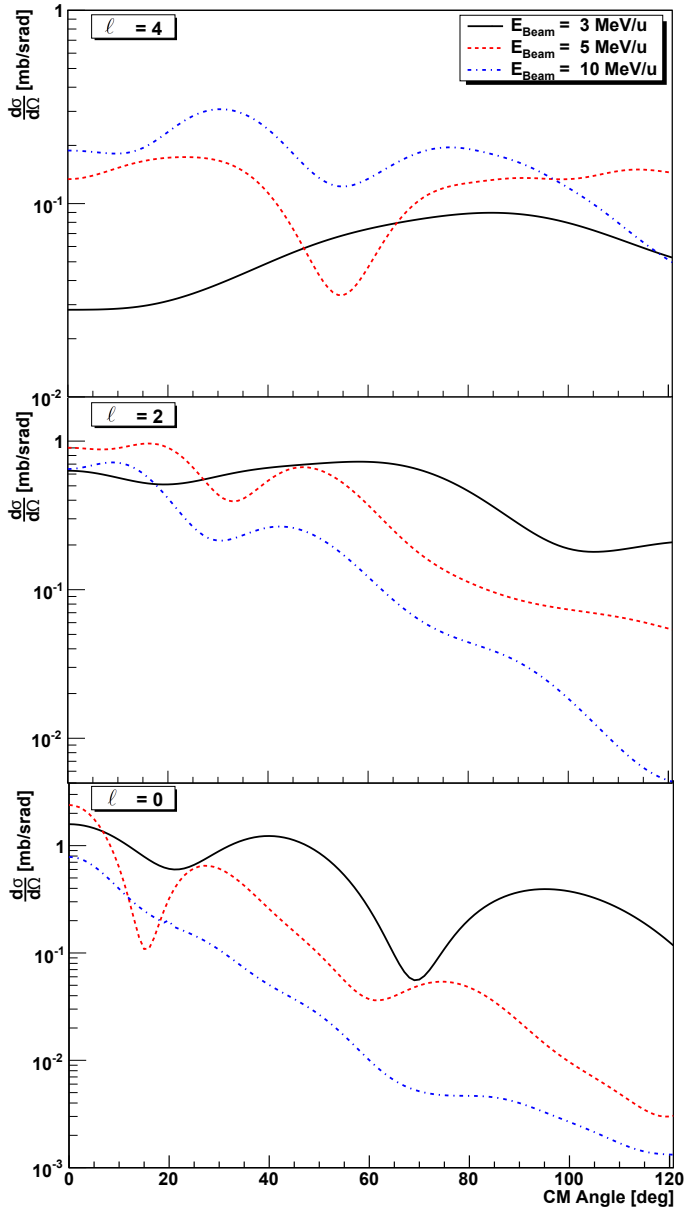

Figure 2.9: Differential cross-sections for ^{66}Ni(d,p)^{67}Ni transfer reaction for ^{66}Ni beam energies of 3, 5 and 10 MeV/u. ^{67}Ni is produced in its ground state and differential cross-sections assuming $\ell = 0$, 2 and 4 have been plotted. For all ℓ-transfers $J = L + s$ was used. Optical potentials and nucleon binding potentials can be found in Table 2.3.

المنارة للاستشارات

	^{66}Ni-d		
Beam energy [MeV/u]	V_v [MeV]	W_v [MeV]	W_s [MeV]
3	94.9	1.5	10.7
5	93.9	1.7	10.5
10	91.5	2.3	10.2
	^{67}Ni-p		
	V_v [MeV]	W_v [MeV]	W_s [MeV]
3	60.8	0.7	8.8
5	59.2	1.0	9.1
10	55.3	2.0	8.4

Table 2.3: Overview of the depths of the various potentials for different beam energies taken from [An06]. Radii, diffusenesses and SO-potentials are identical for all energies and can be found in Table 2.2

2.5.4 Optical-model parameters dependence

In literature, different sets of global optical model potential compilations exist and the choice of the used potentials will affect both the shape and magnitude of the calculated differential cross-sections. In this section, differential transfer and elastic cross-sections are calculated for different sets of optical model potentials and compared. For the d-^{66}Ni-system three different collections of potentials were used from [Loh74, An06, Han06]. Likewise, for the p-^{67}Ni-system potentials from five compilations can be used [Per63, Kon03, Mor07, Li08][27]. Instead of comparing all 15 possible combinations directly, first the influence of the prior (d-^{66}Ni) potential is discussed by choosing a fixed post potential. The same can be done inversely by fixing the prior potential and repeat the calculation with different post potentials.

Incoming potential dependence

Three sets of GOMPS are available for the incoming ^{66}Ni-d channel [Loh74, An06, Han06]. For ℓ-transfer values between 0 and 4 the characteristic angular distributions have been plotted in Figure 2.10. The GOMPs by Yinlu Han *et al.* consistently provide higher cross sections than the compilations from Haixia *et al.* and Lohr *et al.*, a feature that can be attributed in the different Coulomb radii used in these different sets.

[27] [Mor07] provides two compilations.

المنارة للاستشارات

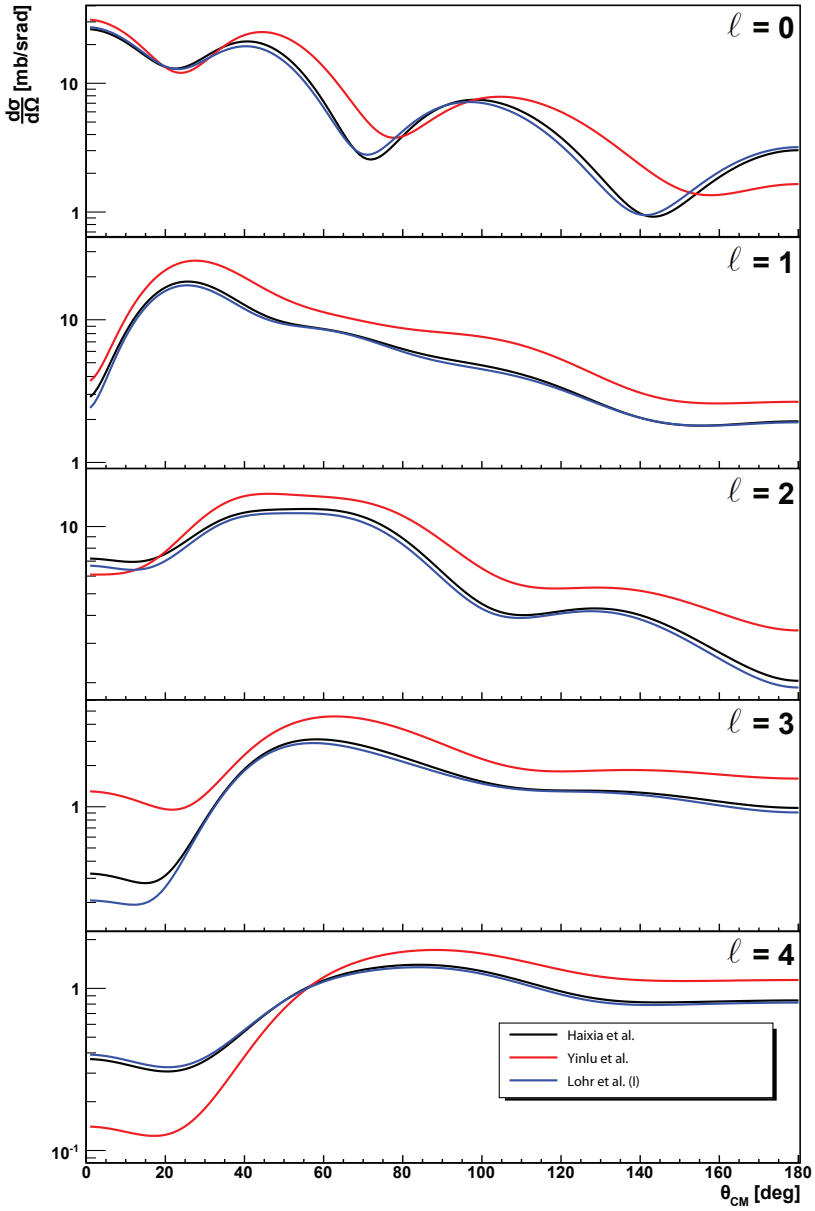

Figure 2.10: Dependence of the angular distribution on the incoming potential parameters.

المنارة للاستشارات

Outgoing potential dependence

For the dependence on the outgoing optical-model parameters five sets of potentials [Per63, Kon03, Mor07, Li08] were compared in Figure 2.11. These can be divided into two groups: one group including a real volume potential ([Per63, Kon03]) and the second group without a real volume part ([Mor07, Li08]). From Figure 2.11, it can be seen that except for $\ell = 0$ transfer, the overall behavior and magnitude of the cross section is similar. For angles close to $\theta_{\mathrm{CM}} = 0$ degrees substantial differences between the different sets can be seen. The identification of the first maximum is not altered by the choice of potential meaning that ℓ assignments are not depending on the potentials used. As the potentials of Refs. [Per63, Kon03] do include a real volume potential this set is preferred over the set without a real volume part [Mor07, Li08]. For this reason, the compilation by Koning [Kon03] was used in the DWBA calculations.

2.5.5 Effect of SO coupling

The role of the SO term in transfer reactions was discussed in section 2.4.7. In the case of the ^{66}Ni(d,p) reaction, the effect of the (non-)inclusion of the SO interaction is shown in Figure 2.12 where the differential cross section for a state at 3621 keV assuming a $\nu g_{9/2}$ configuration[28] is shown assuming different values for r_{SO}. In the case when r_{SO} equals 1.05 fm no distinction can be made between the calculations including and excluding the SO interaction. The effect of a SO interaction with $r_{SO} = 1.10$ fm is visible as a slightly enhanced cross section is calculated ($\approx 10\%$ enhancement). Choosing identical values of r_0 and r_{SO} of 1.25 fm leads to a clear increase of the cross section. For physical acceptable values of r_{SO} no strong effect of the SO interaction is to be expected, showing that the reaction is indeed peripheral.

[28] The $\nu g_{9/2}$ orbital was chosen as the effect of the SO interaction increases with the angular momentum of the orbital under consideration. The effects visible in Figure 2.12 are hence the largest effects to be expected.

المنارة للاستشارات

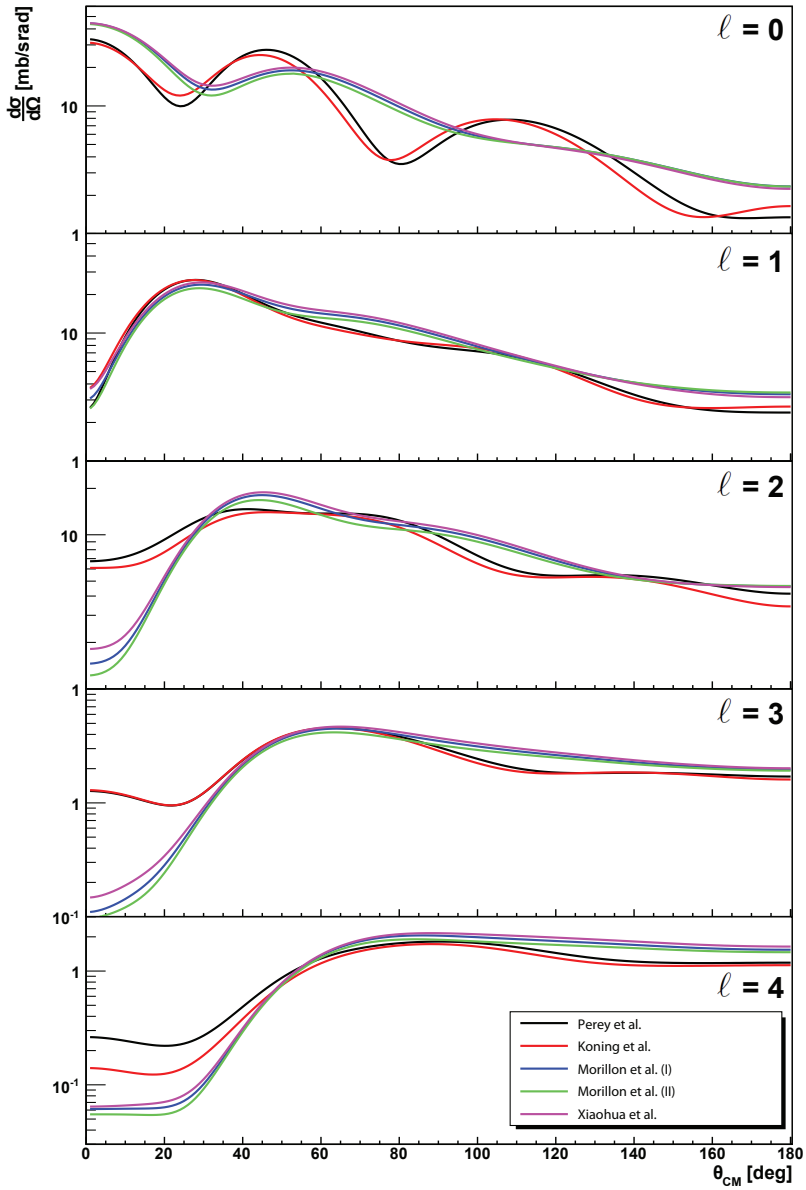

Figure 2.11: Dependence of the angular distribution on the outgoing potential parameters.

المنارة للاستشارات

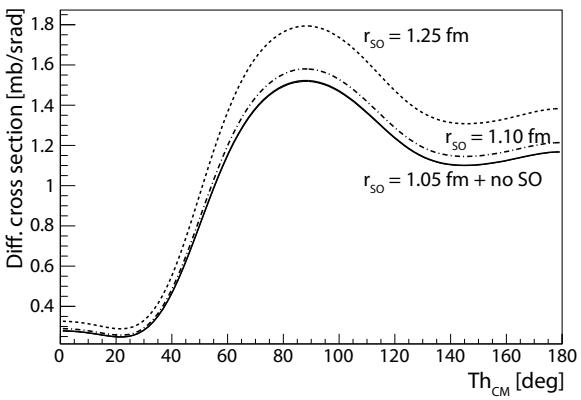

Figure 2.12: Effect of inclusion of the SO interaction on the differential cross section for a $\nu g_{9/2}$ orbital at 3621 keV excitation energy. The solid line represents the calculation without SO interaction and calculation including the SO interaction with a radius $r_{SO} = 1.05fm$.

المنارة للاستشارات

المنارة للاستشارات

3

Experimental Setup

In this chapter the methods used to produce, manipulate and accelerate the unstable ^{66}Ni isotopes as to perform nuclear reactions and finally to detect the reaction products are discussed. Further also the data structure and analysis procedures are outlined.

3.1 Beam production

As the isotope of interest ^{66}Ni is unstable with a half-life of 54.6 hours [Joh56], it is not possible to perform a nuclear reaction study of this isotope in direct kinematics; by preparing a sample of ^{66}Ni and bombarding it with light nuclei. As outlined in Section 2.2.1, these studies have to be performed in inverse kinematics. This requires the production and acceleration of ^{66}Ni in a dedicated facility: the REX-ISOLDE radioactive ion beam facility in CERN, Geneva. Here a variety of isotopes is produced using one of the main production techniques available, namely by the *Isotope Separation On-Line* (ISOL).

Besides ISOL, a second widely used technique exists to produce beams of exotic isotopes: the In-Flight (IF) method [Mor04]. This technique takes advantages of the high energy of the primary heavy-ion beam which is directed on a thin reaction target to induce *projectile fragmentation* causing the projectiles to break up into smaller residues, or reaction products from heavy-ion fusion evaporation (depending on the collision energy). To separate the isotopes of interest from the primary beam and other reaction products a combination of electromagnetic

المنارة للاستشارات

fields and energy degraders is necessary. The big advantage of the IF technique is the fact that the process is not affected by chemical properties of the element under investigation. Also isotopes with short life times can be studied in this way. Examples of IF facilities include NSCL (Michigan, USA), RIKEN (Tokyo, Japan) and GANIL (Caen, France).

Isotope Separation On-Line uses a target in which the incident beam induces reactions such as fission, spallation, fusion and fragmentation [Huy04, Dup07]. The variety of produced species will thermalize in the target or a catcher. The choice of both target and incident primary beam should be optimized in order to have high production cross sections of the isotope of interest along with a low background from contamination. After diffusion from the target volume, the isotopes of interest should be selectively ionized, extracted and sent to the experiment. Due to the diffusion of the isotopes out of the target matrix, the ISOL technique does (in contrast to IF) depend on the chemical properties of these elements. The ion-optical properties like emittance, energy resolution and timing structure of these beams on the other hand are of excellent quality.

When performing experiments with radioactive beams the following conditions should be optimized:

1. **Production rate** should be as high as possible. This rate ultimately depends on the production cross section for a specific primary beam-target combination and the energy of the primary beam. The initial primary beam intensity also has to be optimized to provide the highest production rates but low enough as not to damage the target system.

2. **Efficiency** of extraction, ionization and transport to the dedicated experiments has to be optimal to minimize losses of the produced isotopes.

3. **Fast**. Depending on the half-life of the isotope of interest, the system should be fast as to reduce the losses due to decay of the produced isotopes to a minimum. IF facilities allow elements with half-lives as small as several μs to be studied, while at ISOL facilities, depending on the physical and chemical properties of the isotope of interest, isotopes with the shortest possible half-lives of several ms can be produced.

4. **Selectivity** should be maximal to reduce unwanted background from contaminants produced in the target (or originating from the target itself).

In the following paragraphs the ISOL technique will be summarized as the ^{66}Ni beam was produced using this technique.

The primary beam used to produce ^{66}Ni at ISOLDE is provided by the PS-Booster accelerator of the CERN accelerator complex, which is shown in

المنارة للاستشارات

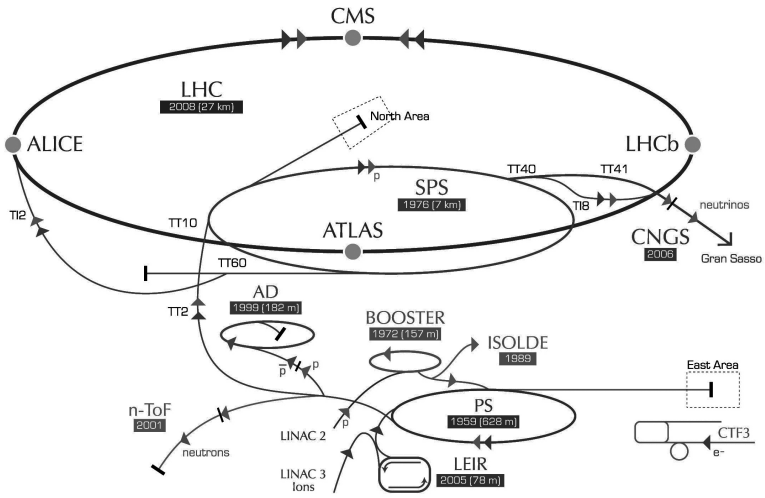

Figure 3.1: Overview of the CERN accelerator complex. Taken from [CER12].

Figure 3.1. This accelerator delivers 1.4-GeV protons to ISOLDE; it consists of four coupled synchrotrons operating with a 1.2-s period. Bunches of protons are either delivered to ISOLDE or to other CERN accelerators. This pattern is called the *proton supercycle* and generally encompasses between 20 and 40 pulses of up to 3 10^{13} protons per pulse. These protons are directed on a ∼50-mg/cm^2 $^{238}UC_x$ target and induce fission. Cross sections for this reaction in inverse kinematics have been measured for the comparable energy of 1AGeV [Ber03] and these results are shown for nickel and gallium, which is expected to be a potential contaminant, in Figure 3.2. From this figure it is expected that both ^{66}Ni and ^{66}Ga are produced in equal amounts.

All fission products are thermalized in the target, diffuse[1] out of the target material and effuse[2] towards the ion source, which consists of a heated cylindrical cavity. In order to optimize the diffusion time, both the target and transfer line are heated to a temperature around 2000 °C by an electrical current as to avoid the sticking of atoms to the wall of the target container and transfer line.

The chemical properties of nickel result in a slow release from the target matrix. This is evident from Figure 3.3 where the count rate of elastically

[1]Diffusion is the spontaneous spreading of particles, heat, momentum. Diffusion can be modeled by Brownian movement.

[2]Effusion is the process where individual atoms or molecules move through a hole without colliding with other molecules. This can occur when the hole is smaller than their mean free path.

المنارة للاستشارات

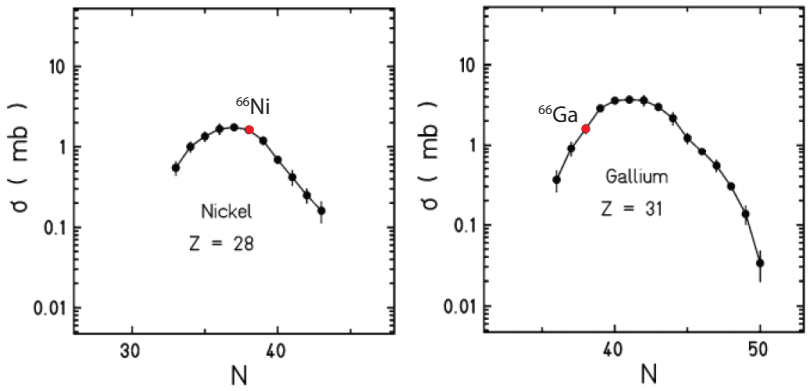

Figure 3.2: Fission cross section for ^{238}U+p at 1AGeV for different isotopes of nickel and gallium. Data taken from [Ber03].

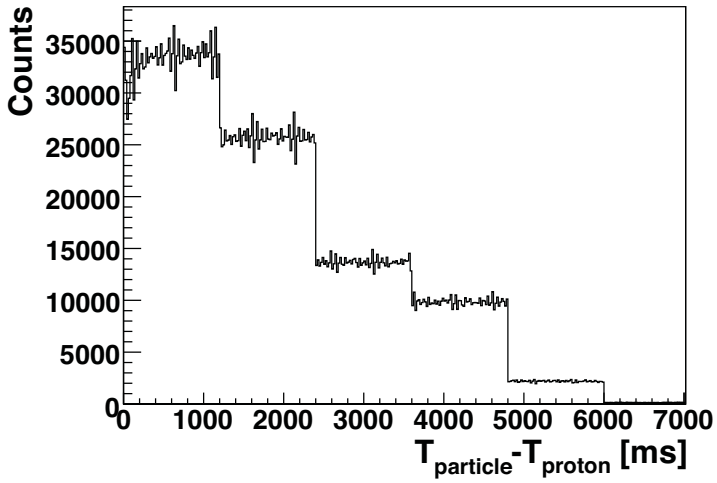

Figure 3.3: Rate of detected deuterons from the secondary target (after particle identification) in the T-REX array as a function of time elapsed since the last proton impact on the primary production target. The blocked structure is due to irregular spacings in the supercycle. See text for additional comments.

المنارة للاستشارات

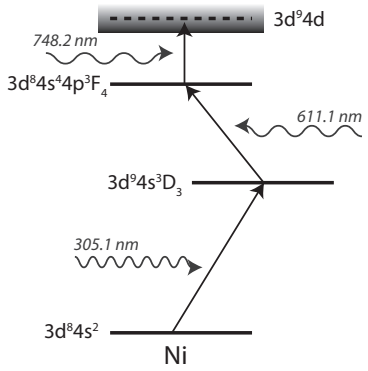

Figure 3.4: Ionization scheme used by RILIS to perform resonant laser ionization.

scattered deuterons from the secondary target is shown as function of the time elapsed since the proton impact on the production target. The block-like structure, with widths of 1.2 seconds, is the result of the irregular structure of the supercycle (i.e. order of proton pulses delivered to ISOLDE, see below). There is no evidence for a particular time structure (i.e. exponential decay, see e.g. Refs [Van06, Bre08, Bre13]) in these blocks themselves, pointing to the rather constant release from the target. This is also evident as data could still be collected even when the target had not been irradiated for several hours. The release of gallium, which is known to be fast [Van06], was not observed here, pointing already to a high degree of beam purity.

3.1.1 RILIS

The produced elements are transported through the transfer line and delivered to the ion source or *hot cavity* in order to (selectively) ionize the elements of interest. At the ISOLDE facility three types of ion sources are available: *resonant laser ionization*, *surface ionization* and a *plasma-ion source*. For this experiment only the first two methods are relevant and will be discussed here.

Resonant laser ionization is performed by taking advantage of the known electronic level scheme of a given element. Usually two or three laser beams with tuned wave lengths are combined to perform this resonant ionization process. The system is driven by two copper-vapor lasers (18-ns pulses at 11 kHz) and are used to pump three dye lasers, delivering laser beams within a 530-850 nm wave length range. By using nonlinear beta-barium bromate (BBO) frequencies can be doubled or tripled to reach wave lengths in the 214-415 nm range, essential for

المنارة للاستشارات

elements with an ionization potential of more than 8 eV [Cat04]. In the case of nickel the three-step process: $3d^8 4s^2 \rightarrow 3d^9 4s^3 D_3 \rightarrow 3d^8 4s^4 4p^3 F_4 \rightarrow 3d^9 4d(\rightarrow$ continuum) is used with corresponding wave lengths $\lambda_1 = 305.1$ nm, $\lambda_2 = 611.1$ nm and $\lambda_3 = 748.2$ nm (see Figure 3.4). This method is element selective as the laser beams wave lengths are tuned to match the known transitions of the element of interest. For other elements these wave lengths are out of resonance. The efficiency for the ionization of nickel is around 6% [Cat04].

Surface ionization does not play a role for nickel due to its high ionization potential of 7.64 eV, but the high temperature of the hot ionization cavity is able to surface ionize elements with low ionization potentials. The element with lowest ionization potential in the neighborhood of nickel is gallium (ionization potential of 6 eV). The amount of surface ionized gallium depends on the temperature of the target and transfer line, which has therefore to be chosen to provide a good balance between mobility of the element of interest and contamination from surface ionization.

The level of contamination can be monitored by periodically measuring with lasers ON (in resonance, nickel and contaminants in the beam) and with lasers OFF (off resonance, only contaminants in the beam). This comparison provides the purity level of the beam. In this experiment almost no particles are detected during measurements with lasers OFF, leading to purity level of at least 99%.

3.1.2 Mass selection

After the ionization, the resulting ions are moved away from the ion source by an extraction electrode at 30 kV[3] and guided to one of the two available mass separators at ISOLDE. These are the General Purpose Separator (GPS) and High Resolution Separator (HRS) . The nominal mass resolving powers of these separators are $M/\Delta M = 2400$ for GPS and 10000 for HRS [Jon93]. The GPS consists of a double focusing H-magnet with a bending angle of 70° and is capable of distributing three different masses within a 15% mass range at the same time. The HRS has two bending C-magnets (90° and 60°) and delivers one mass. For this experiment the GPS separator is used.

[3]Due to the pulsed character of the incoming proton beam and consequential high amount of ionized air particles a high load was created on this extraction voltage. Therefore the extraction voltage was reduced to 0 V in a time span from 35 μs before to 6 ms after proton impact.

المنارة للاستشارات

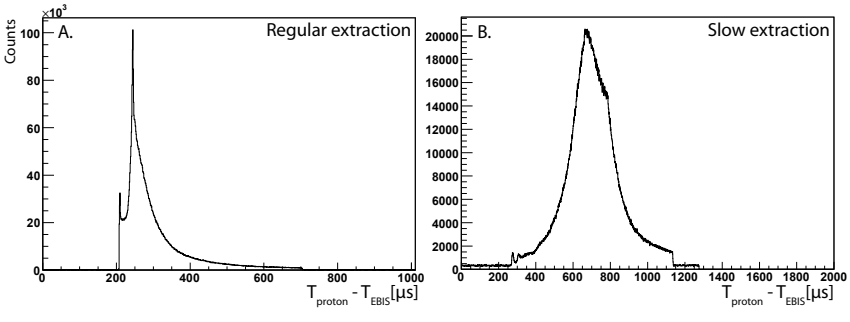

Figure 3.5: Release profiles from REX-EBIS with A. regular extraction and B. slow extraction. Detection time with respect to the initial release from REX-EBIS.

3.1.3 REX-ISOLDE

In order to perform the ^{66}Ni(d,p) reaction study one needs an energetic beam of ^{66}Ni. It is therefore necessary to efficiently accelerate the continuous 30-kV ^{66}Ni beam. At ISOLDE this is done by the REX (Radioactive Experiment) post-accelerator which is a linear accelerator (LINAC). This type of accelerator works more efficiently when highly charged ions are provided rather than the 1^+ ions delivered by one of the separators. This higher charge is reached by irradiating the ions for a specific time with an energetic electron beam in REX-EBIS (Electron Beam Ion Source). First the ^{66}Ni beam is prepared by bunching it into packages in REX-TRAP which were then handed over to REX-EBIS and charge bred for a given time. An extensive overview of the technical specifications and operating details of the REX-ISOLDE post-accelerator can be found in e.g. chapter 3 of [Van06].

For the ^{66}Ni(d,p) experiment the irradiation time of REX-EBIS is set to 28.5 ms, which leads to an optimized 16^+ charge breeding efficiency. The whole REX-system is synchronized and works in a 30-ms operating cycle (28.5 ms for breeding with an additional 1.5 ms for transportation of the ions between the different elements of REX), with a *duty cycle* of 10%, meaning RF-power is provided for 10% of the time between consecutive EBIS pulses, with a maximum repetition rate of 50 Hz. Hence, ions are collected and cooled in REX-TRAP for 30 ms before being transported to EBIS. After charge breeding for 28.5 ms they are transmitted to the REX accelerator and accelerated to an energy of at most 3 MeV/A.

An important parameter which influences the experiment is the rate at which

المنارة للاستشارات

the exit potential of REX-EBIS drops as well as the potential gradient. These parameters greatly influence the instantaneous projectile rate at the reaction setup. A slow drop of the exit potential allows the ions with the highest kinetic energy to be extracted first and hence a more gradual release profile can be achieved. The difference between regular and slow extraction is shown in Figure 3.5.A where a clear peak in the release is visible around 250 μs. The slow extraction (Figure 3.5.B) offers a way to spread the available beam more evenly within the beam ON window, leading to better noise control of the particle detectors (see Section 3.2.2), more accurate particle reconstruction and less dead time due to a lower instantaneous rate. It should be noted that the comparison in Figure 3.5 is a qualitative rather than quantitative comparison as both release profiles were obtained during different measuring times. Slow extraction was achieved in the present experiment by fixing the drop time of the exit potential at 720 μs.

3.1.4 Beam time structure

From Figure 3.3 it is evident that the release of nickel isotopes from the primary target is slow and constant over a long time period (hours). Figure 3.6 shows how this continuous beam coming from the primary target is bunched in the REX-TRAP system and how the TRAP-EBIS-LINAC are synchronized. Besides this, also two *reference times*[4] are indicated. The first one being the *T1* reference, the impact of the primary proton beam on the production target. The information from this timing signal is used e.g. in Figure 3.3 to demonstrate the release from the target after proton impact. The second reference time is the moment when particles are released from EBIS and is used in Figure 3.5 to show the difference between regular and slow extraction from EBIS.

The bottom panel of Figure 3.6 shows how the release from EBIS triggers the data acquisition system to start gathering data for a period of 1.2 ms. The first particles arrive at the setup around 200 μs after this EBIS trigger and the beam is cut, depending on the length and synchronization of the RFQ pulse, after $\approx$ 1 ms. After this *beam ON window* the data acquisition's buffers are read out (duration of a few ms) and the data is digitally stored (see Section 3.3). After this read-out a second measuring window (with length equal to the beam ON window) is opened called the *beam OFF window*. Data collected within this window originates purely from background radiation. These data are also read out after the data collection window is closed.

[4]Also a third reference time was present but not indicated in Figure 3.6. This reference time is the start of a new supercycle.

المنارة للاستشارات

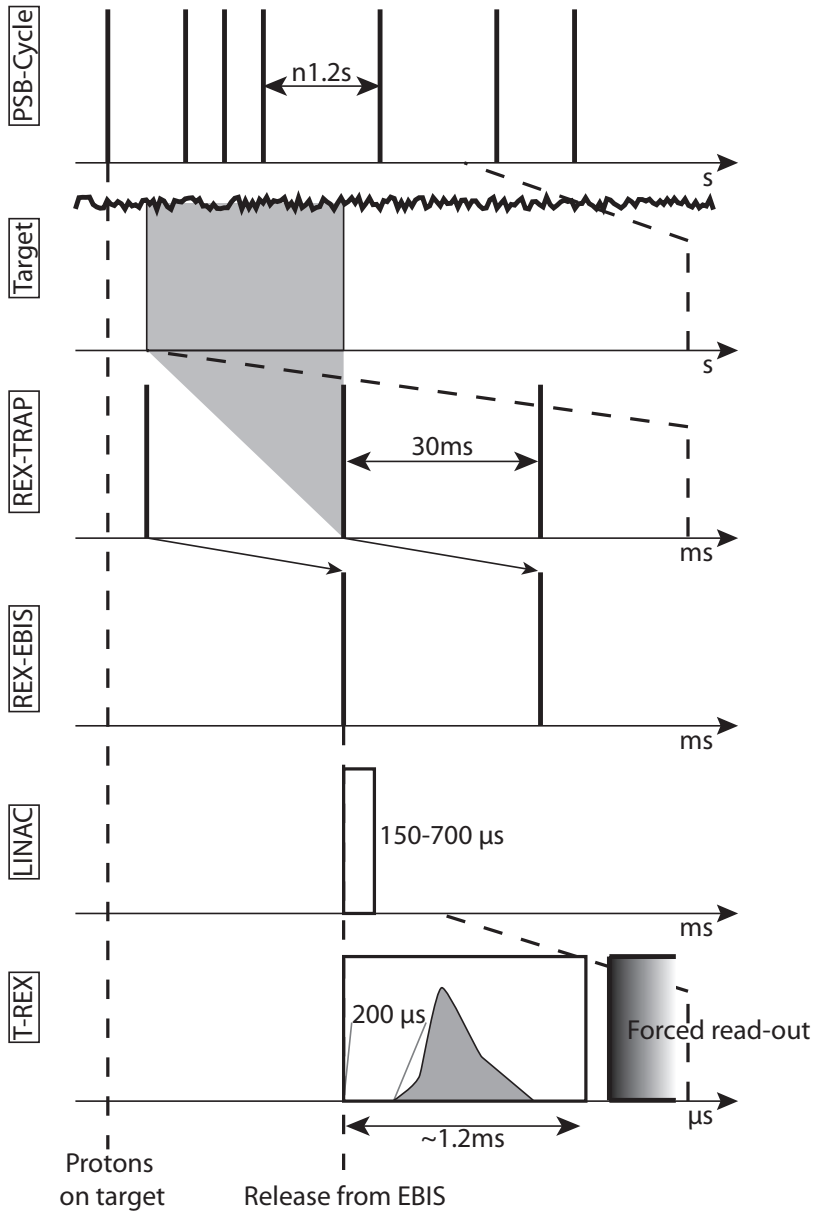

Figure 3.6: Time structure of the post-accelerated beam at REX-ISOLDE from the initial proton beam to the profile of the particles arriving at the scattering chamber. The nano-structure of the beam is not indicated in this figure.

المنارة للاستشارات

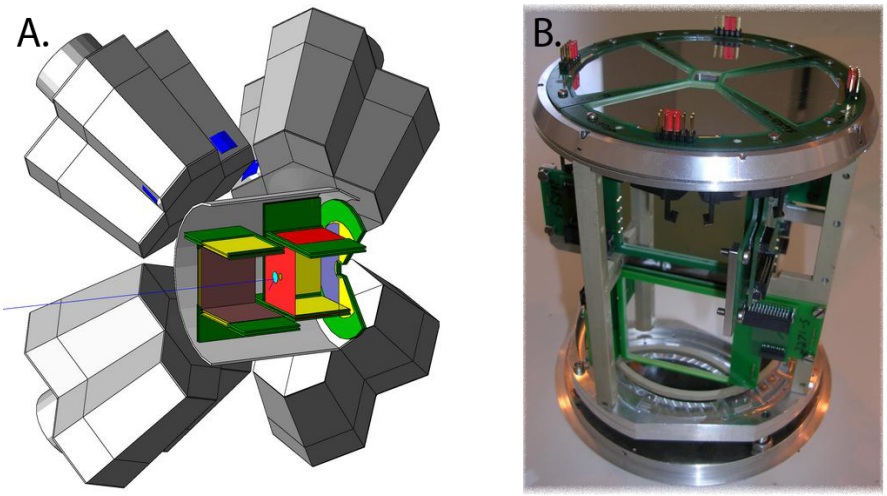

Figure 3.7: A. Drawing of the reaction chamber and four surrounding Miniball cluster detectors, T-REX array is partly shown. B. Picture of the dismounted T-REX array (backward direction on top).

Using the REX-cycle parameters for this given experiment, data with beam on target are recorded for 1.2 ms $\times$ 33 Hz = 39.6 ms/s or 4% of the time. The advantage of this *pulsed beam* is that the background can be efficiently suppressed as data are only taken during beam-on-target periods. A potential downside is that for high beam intensities the *instantaneous beam intensity* can lead to a high count rate in the particle detectors and consequently considerable dead time.

3.2 Detection arrays

Three kinds of detectors are used to collect the data resulting from the nuclear reactions. Particles resulting from elastic scattering and transfer reactions are recorded by the *T-REX particle detection array* (Section 3.2.2), placed inside the *reaction chamber*. Surrounding the reaction chamber eight *Miniball cluster detectors* are placed, registering γ rays following the decay of excited states populated during transfer reactions (Section 3.2.3). Finally, a *delayed coincidence setup* is placed 2 meters downstream the beam line in order to perform spectroscopy of isomeric states (Section 3.2.4). In the following sections these arrays and the reaction chamber will be reviewed.

المنارة للاستشارات

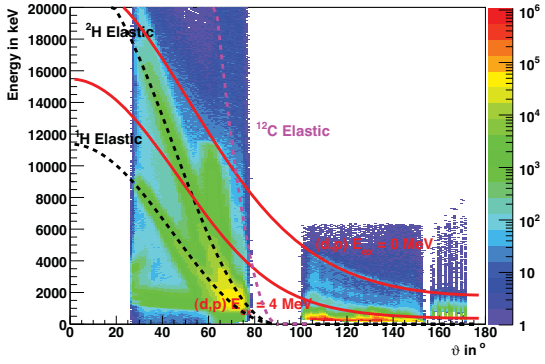

Figure 3.8: Full energy of all detected particles in the T-REX array with respect to detection angle. Expected kinematical signatures are also presented.

3.2.1 Reaction chamber

The reaction chamber is mounted on the beam line behind the REX accelerator and has a cylindrical shape, partly shown in Figure 3.7.A. The reaction target is mounted on the target ladder which is inserted through a hole in the bottom and positioned in the center of the chamber. Up to four targets can be mounted on this target ladder and the desired one is selected by adjusting the magnetically coupled feed-through [Bil12]. The geometry of the chamber is compact as to allow a close configuration of the surrounding Miniball detector in order to maximize detection efficiency [Bil12].

A deuterated polyethylene (CD_2) target with thickness of 100 $\mu g/cm^2$ is used as reaction target, the target characterization is discussed in Section 6.4.3.

3.2.2 T-REX Particle detectors

Principle

The particles that are registered by the silicon particle detectors are not only protons emitted after a transfer reaction. Also recoils due to elastic scattering of ^{66}Ni on ^{2}H,^{12}C and ^{1}H (the target used is not purely composed out of ^{2}H) are detected in the silicon array. Furthermore electrons emitted in the β decay of radioactive species implanted in the scattering chamber form a background in the particle spectrum. Figure 3.8 shows the full energy spectrum of all particles detected in the scattering chamber with respect to the detection angle, along

المنارة للاستشارات

with the expected kinematical signatures. In the forward direction transfer protons and elastic deuterons overlap in a large angular range and no direct separation between the two is possible. The common technique applied to distinguish between different types of particles is to use the particle-specific, energy-dependent energy loss in a given material. The energy loss is due to interaction between the charge of the particle and the electrons present in the target material. The *stopping power* $S(E) = -\mathrm{d}E/\mathrm{d}x$ of a given particle in a specific matter is described by the *Bethe-Bloch formula* [Kra87]:

$$S(E) = -\frac{\mathrm{d}E}{\mathrm{d}x} = \frac{4\pi}{m_e c^2}\frac{nz^2}{\beta^2}\left(\frac{e^2}{4\pi\epsilon_0}\right)^2\left[\ln\left(\frac{2m_e c^2\beta^2}{I\left(1-\beta^2\right)}\right) - \beta^2\right]. \tag{3.1}$$

In Eq. 3.1 v is the velocity of the particle, $\beta = v/c$, x the distance traveled, z the charge, m_e the electron mass, n the electron density[5], I the mean excitation potential of the material[6] and ϵ_0 the permittivity of vacuum. For non-relativistic energies (i.e. $\beta << 1$) Eq. 3.1 reduces to

$$S(E) = -\frac{\mathrm{d}E}{\mathrm{d}x} = \frac{4\pi n z^2}{m_e v^2}\left(\frac{e^2}{4\pi\epsilon_0}\right)^2\left[\ln\left(\frac{2m_e v^2}{I}\right)\right]. \tag{3.2}$$

As Eq. (3.2) is a function of v^2, using the relation $v^2 = 2E/m$, the Bethe-Bloch formula incorporates a direct mass dependence for particles with equal energies.

By using two layers of silicon to detect particles, the first one to measure the energy loss over a known distance and the second one to measure the remaining energy of the particle, the type of particle can be determined. Such a configuration is called a ΔE-E-*telescope*.

Design

The ΔE-E-telescopes used in the T-REX setup[7] have an active area of 50 mm × 50 mm and are build up of two layers of silicon. A picture of the detectors is shown in Figure 3.7.B. The ΔE part has a thickness of 140 μm and the $\mathrm{E_{rest}}$ thickness measures 1 mm. The ΔE part of the detector is segmented in the form of 16 position-sensitive strips, oriented perpendicular to the beam direction. The position sensitivity is obtained as the front side of the ΔE detector is covered with resistive material, reducing the signal strength depending on the position of the hit. On the back side, the full energy signal is recovered and the (calibrated) ratio of these two signals provides the position of the hit.

[5] $n = \frac{N_A Z \rho}{M_u}$ with Z the atomic number of the target material and M_u the molar mass and ρ the density of the material.

[6] $I \approx (10\mathrm{eV})Z$ or taken from tables [Sta12]

[7] Micron position-sensitive detector, X1 type [Sem12]

المنارة للاستشارات

The E_{rest} detectors have the same active area as the ΔE part and no segmentation is applied here. The separation between ΔE and E_{rest} parts of the telescope is 2.2 mm [Bil12].

Eight quadrants of this type of ΔE-E_{rest}-telescope are mounted in the scattering chamber, four in the forward direction, covering an angular range between 30°and 75°and four in the backward direction, covering angles between 105°and 150°. The worst position resolution in θ_{LAB} is found in the strips the closest to 90° and measures $\approx 5.5°$ [Bil12].

Elastic scattering is the dominant reaction process and in order to protect the silicon detectors from the high rate of elastically scattered particles, a Mylar foil of 12 μm thickness is mounted in 2 mm in front of the forward ΔE-E telescopes. The elastic scattering is strongest for angles close to 90°in the LAB and the Mylar foil stops most elastic ^{2}H and ^{12}C.

Extreme angles are covered by two circular-shaped double-sided silicon strip detectors (DSSSD) [Ost02] and a E_{rest} detector (in forward detection for particle identification and in backward direction for electron vetoing). The DSSSD is segmented into 16 angular rings (front side) and 24 radial strips (back side)[8]. In the present experiment only a DSSSD in the backward direction is available. The whole configuration of DSSSD and circular E_{rest} detector behind it is also referred to as CD (circular disc) detector.

Calibration

A quadruple α-source (^{148}Gd ($E_\alpha = 3271$ keV), ^{239}Pu ($E_\alpha = 5245$ keV), ^{241}Am ($E_\alpha = 5638$ keV) and ^{244}Cm ($E_\alpha = 5902$ keV)) is used to calibrate the ΔE part of the barrel array and DSSSD. This is a straightforward procedure for the DSSSD and backward-directed quadrant of the barrel, but corrections should be applied for the forward barrel, due to energy losses in the Mylar foil. The energy-loss calculation software SRIM [Zie10] is used to calculate the energy losses in the Mylar foil.

In a first step the position signals from the individual strips are calibrated. After threshold determination, the ratio $\text{channel}_{strip}/\text{channel}_{back,\Delta E}$ is calibrated to range between 0 and 1. Finally, the full energy signal of the ΔE part is calibrated to reproduce the correct full energies as the α particles were all stopped in the ΔE part. A dependence of the full ΔE energy on the position of the hit is also observed during this calibration process (see Figure 3.9) due to capacitive coupling between these two layers of the ΔE detector. An energy correction is

[8]The number of channels for the back side is reduced to 12 as the radial strips are coupled two-by-two for read-out

المنارة للاستشارات

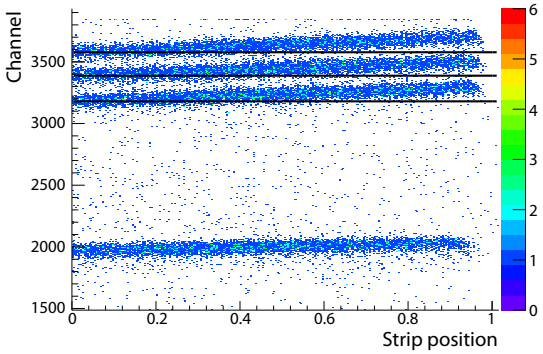

Figure 3.9: Position dependence of the full energy signal from the back of the ΔE detectors. The solid lines are fixed to the centroid at position 0.

applied using the expression

$$E_{\text{corrected}} = \frac{E_{\text{calibrated}}}{[1 - (0.5 - \text{Position})\, A]}. \tag{3.3}$$

The tilt-factor A is found to be 0.035.

Calibration of the E_{rest} detectors is only necessary in the forward direction as particles in the backward direction are stopped in the ΔE part of the telescope. The E_{rest} detector here has the function to veto electrons and an accurate energy calibration is not essential. No mono-energetic source that provided particles penetrating into the E_{rest} detector is available at ISOLDE. The method used to calibrate the E_{rest} detector employs a ^{152}Eu source and relies on Si-Miniball coincidences using the 1408 keV γ line where the 1408 keV γ ray undergoes Compton scattering the T-REX array prior to being detected by Miniball (see Figure 8 in Ref. [Bil12]) [Wim09]. As the available data using a ^{152}Eu source combined with biased T-REX detectors taken during this experiment is limited, calibration values from a previous experiment (using the same electronics settings) were used [Joh09].

Detection of δ electrons

In Section 3.1.3 the need for slow extraction was discussed as beam-induced noise is observed in the backward barrel ΔE detectors. The signal of the detector reflects the release profile of the particles from EBIS as shown in Figure 3.5.A. The amount of noise is directly proportional to the thickness of the target used and saturates completely when the beam is impinging directly on the target

المنارة للاستشارات

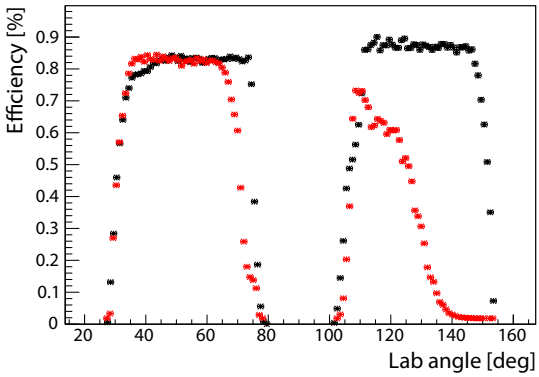

Figure 3.10: Efficiency for proton detection and correct propagation in the analysis procedure. Black dots for ^{66}Ni in its ground state, red dots for an excitation energy of 3863 keV.

ladder. The origin of this noise is believed to stem from δ electrons [Ste57] which are the result of the electromagnetic interaction between the energetic projectile and a target material causing ionization of the target[9]. Systematic studies of this effect have shown relationships between the total electron yield γ_T, energy loss of impinging ions in the target foil and initial projectile energy [Rot98].

Slow extraction, in combination with a reduced proton current (1 μA) on the primary production target is necessary to control the noise level in the backward barrel quadrant. The remaining noise triggers the need for increased thresholds of these quadrants, which in combination with the kinematics of the transfer protons (Figure 2.1) results in a substantial reduction of the detectable angular range for highly excited states.

Efficiency

Simulations are required to evaluate the efficiency of the silicon array. For this reason the setup has been entered into the GEANT4 simulation package [Ago03] and the simulation is performed under the same conditions as the experiment itself. A flat angular distribution of the emitted protons is assumed and two

[9]In later experiments using REX-postaccelerated beams in this mass region, the beam induced noise could be significantly lowered by applying a positive bias voltage to the target ladder as to prevent the electrons from escaping [Wim09, Els13, Müc11]. This supports the statement that the detected noise originates from δ electrons. At the time of the ^{66}Ni(d,p) experiment no bias voltage could be applied to the target ladder due to technical difficulties and safety issues.

المنارة للاستشارات

versions of the simulated events are saved: one set containing *all simulated* events and a different set containing *all detected* events. The former set is analyzed to provide the reference numbers of counts for each angle, while the data stored in the latter are converted to have the same structure as the actual data taken in the experiment. These files are analyzed as if they were actual data files. In this way effects from the high thresholds in the backward direction and losses due to faulty particle identification in the forward direction are included in the efficiency. The total number of counts in each angular bin after this analysis is compared with the number of simulated events in the same angular range to provide the efficiency. The efficiency is determined for all excitation energies observed as the proton kinematics depend on the excitation energy (see Figure 2.1).

Two examples are given in Figure 3.10, the black dots show the efficiency for the protons emitted after ^{67}Ni is produced in its ground state. The efficiency is constant for the backward barrel and nearly constant for the forward barrel. The little reduction for small scattering angles is due to the fact that protons start to punch through the E_{rest} detector due to the high kinetic energy which leads to a decreased efficiency. The efficiency of the forward barrel is slightly lower than backward barrel due to losses in the particle identification process which is applied in the forward barrel[10]. The red dots represent protons associated with an excitation energy of 3863 keV in ^{67}Ni. The backward barrel shows a rapid decrease in efficiency due to the combination of the small proton kinetic energy and high thresholds for detection[11]. As these threshold are different for each quadrant this decrease occurs in steps.

3.2.3 Miniball γ detectors

γ rays emitted by the recoiling nuclei after a transfer product is produced in an excited state are in general emitted *in flight*. Due to the high velocity of these nuclei ($v \approx 0.085$c) the effective wave length and energy of the emitted radiation is affected by a Doppler shift depending on the direction of the γ ray. This imposes requirements on the γ-detection system which are: 1- high detection efficiency 2- optimal solid angle coverage and 3- high granularity (or position sensitivity).

The Miniball γ-detection array [Ebe01, War13], which consists of 8 cluster detectors of 3 hyper pure germanium crystals each sixfold electronically

[10]Particle identification is not applied in the backward direction as only protons can be detected here due to the kinematics of the reaction. The E_{rest} detector is used only to veto electrons.

[11]The high detection thresholds are necessary to minimize the influence of the δ electrons.

المنارة للاستشارات

segmented is placed in close geometry around the reaction chamber to optimize the solid-angle coverage and total detection efficiency. Its high level of segmentation (144 segments) allows for sufficient position sensitivity to properly correct for Doppler shifts.

The germanium crystals have a hexagonal end cap with the outer electrode being electronically segmented. The high voltage (3500-4500 V) is applied to the central core. These seven signals are preamplified twice: first by the cold preamplifiers directly on top of the crystal and a second time by the warm preamplifiers [War13]. Cooling of the germanium crystals is done by a *cold finger* in contact with a liquid nitrogen (LN2) dewar.

A frame constructed out of flexible aluminum arms surrounds the reaction chamber and is used to mount the Miniball cluster detectors. The flexible arms allow the polar angles (θ, φ) of the cluster to be varied with respect to the beam axis. Furthermore the internal rotation α and target-cluster distance d can be changed.

The core of a crystal collects the signal of the full energy deposited in the crystal, while the segments electrodes only observe the portion of energy deposited in that particular segment. The energy resolution of the core signal ($\approx 2.2 - 2.3$ keV) is also better than the energy resolution of the segments (≈ 3 keV). The core signal is hence used for energy determination and timing, while the segments are used for position information.

Compton scattering can result in the deposition of energy in multiple segments and crystals of the array. In the case where only one crystal fires but multiple segments collected a fraction of the energy, the segment with the maximal energy deposition is selected as primary interaction point. When hits are observed *within multiple crystals of the same cluster* and within the *add-back time window* of 250 ns then the core energies are summed and the segment with the highest energy is again selected as primary interaction point. This process is called *add-back* correction and is applied to all clusters individually. As add-back is a software procedure, it is applied during the analysis (see Section 3.4).

Calibration

The ranges of the digital gamma finders (DGFs, see Section 3.3) are set to be able to register γ-ray energies up to an energy of 8 MeV[12]. Several standard sources are used for calibrating the Miniball clusters like ^{152}Eu, ^{207}Bi and ^{60}Co, providing calibration transitions up to 1770 keV. For the calibration of the

[12]The ranges of all clusters except one are set to a range of 8 MeV. Due to efficiency complications, only the data from these seven clusters are used during the analysis.

المنارة للاستشارات

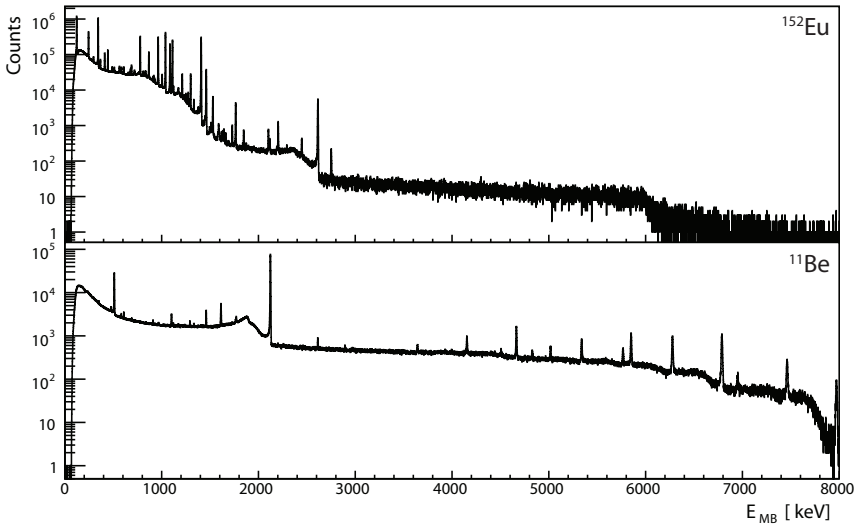

Figure 3.11: ^{152}Eu (source) and ^{11}Be (stopped beam) spectra at the center of Miniball, used for calibration and efficiency determination.

high-energy region of the detectable range, data collected during a previous experiment (stopped ^{11}Be ($T_{1/2}$ = 13.76 s) beam, IS430) [Joh09] are used both for energy calibration and efficiency determination (see Figure 3.11).

Efficiency

A relative efficiency curve is obtained using the absolute intensities and known branching ratios [Mey90, Vas05, Mil82], listed in Table 3.1. The absolute photo peak efficiency curve is subsequently obtained by using known γ-γ-coincidences between different gamma rays. Couples that are used to determine the *anchor points* of the efficiency curve were: for ^{11}Be: 2124 keV-4666 keV and 2124 keV-5847 keV; for ^{152}Eu: 121 keV-244 keV, 344 keV-788 keV, 121 keV-964 keV and 121 keV-1112 keV; and for ^{207}Bi: 1770 keV-569 keV and 897 keV-1440 keV. The three relative efficiency curves are scaled to reproduce the correct absolute efficiency for the anchor points and are combined into one global efficiency curve. A combination of two functions is used to fit this global efficiency and it is given by

$$\epsilon(E_\gamma) = \exp\left[\sum_{i=0}^{3} A_i \left(\ln(E_\gamma/200)\right)^i + B_i \left(\ln(E_\gamma/1000)\right)^i\right]. \qquad (3.4)$$

المنارة للاستشارات

^{152}Eu		^{207}Bi		^{11}Be	
E_γ [keV]	I_γ [%]	E_γ [keV]	I_γ [%]	E_γ [keV]	I_γ [%]
121.78	25.58 (6)	569.	8.2 (2)	2124.4	35.45
244.69	7.583 (19)	897.	7.2 (3)	2895.3	0.079
344.28	26.5 (4)	1442.	5.1 (2)	4665.9	1.84
367.79	0.861 (5)	1770.	4.78 (2)	5018.9	0.47
411.12	2.234 (4)			5851.5	2.13
443.97	3.15 (3)			6789.9	4.37
688.67	0.876 (8)			7974.7	1.85
778.9	12.94 (2)				
867.34	4.25 (2)				
964.08	14.74 (2)				
1085.87	10.45 (2)				
1112.07	13.64 (2)				
1212.95	1.422 (6)				
1299.14	1.623 (8)				
1408.01	21.01 (2)				

Table 3.1: Branching ratios of the transitions used in the decay of ^{152}Eu, ^{207}Bi and ^{11}Be to determine the efficiency curve of Miniball.

Low energy		High energy	
A_0	2.432	B_0	1.766
A_1	-0.106	B_1	-0.474
A_2	-0.61	B_2	-0.19
A_3	0.05	B_3	-0.05

Table 3.2: Parameters used in Eq. 3.4 to describe the global efficiency curve of Miniball for this experiment.

This gives a function controlling the different behavior for low and high γ-ray energies. The coefficients used are given in Table 3.2 and the photo-peak efficiency for a 1 MeV γ ray is 5.85 %. The global curve can be found in Figure 3.12.

Note: both the relative and absolute efficiency curve are obtained using data processed including the add-back procedure.

Positioning

An accurate position determination of the cluster positions is necessary to perform a reliable Doppler correction (DC). The positions are determined by

المنارة للاستشارات

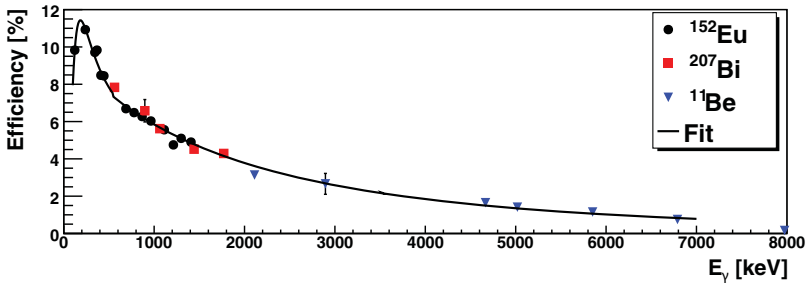

Figure 3.12: Efficiency curve for Miniball, containing the experimental data points for ^{152}Eu, ^{207}Bi and ^{11}Be. Fitted curve from Eq. 3.4, using parameters from Table 3.2 is also shown.

measuring the Doppler shift of a known transition seen in a nuclear reaction with known incoming velocity of the projectile. Here the ^{22}Ne(d,p)^{23}Ne reaction followed by the emission of a 1016.95-keV γ ray is used. As the projectile is much heavier than the target nucleus both in ^{22}Ne(d,p) and ^{66}Ni(d,p), the recoil does not deviate considerably from its trajectory after the reaction. As a consequence no sensitivity on the azimuthal angle φ[13] of the detectors was achievable, nor necessary.

The detected core energy is plotted for each segment that served as the primary interaction point after add-back. The measured centroid energy is Doppler corrected using the known β (v/c) of the beam to find the best θ of that segment. These angles are used to Doppler correct the final data. The expression for Doppler correction was given by

$$E_{\mathrm{DC}} = E_{\mathrm{detected}} \frac{(1 - \beta \cos(\theta_{\mathrm{segment}}))}{\sqrt{1 - \beta^2}}. \tag{3.5}$$

Eq. 3.5 depends on the velocity of the beam through β. If the initial energy and energy loss of the ^{22}Ne projectiles are not precisely known, an offset of the obtained θ angles is observed. This can be compensated by varying the β of the ^{66}Ni projectiles to minimize the FWHM of the Doppler-corrected transitions. In the analysis of the ^{66}Ni(d,p) data an *effective* β value of 0.085 is used, resulting in a relative energy resolution of 1% across the whole energy range of Miniball (as a reference: an intrinsic relative energy resolution of 0.5% is found from source runs). This β value of 0.085 is slightly higher than the β of 0.078 which is calculated from the known beam energy of 2.95 MeV/u.

[13]The coordinate system used for all detectors involved around the target is a spherical coordinate system using the beam direction as z-axis (polar angle θ reference) and the x-axis is directed towards the ceiling (azimuthal angles φ reference).

المنارة للاستشارات

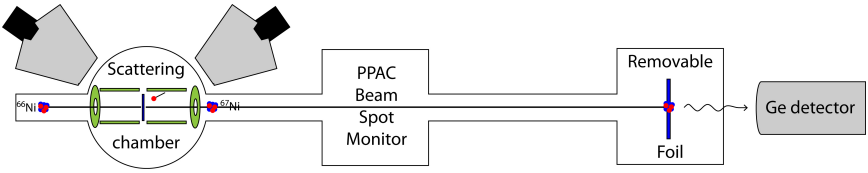

Figure 3.13: Schematic depiction of the delayed coincidence setup. See text for additional information.

3.2.4 Delayed coincidence tagging setup

In Section 1.3.1 the known features of the 1007-keV 13.3-μs isomer have been discussed. Due to the half-life of this state it is not possible to use prompt proton-γ coincidences to extract an angular distribution for this state. Therefore a *delayed coincidence* setup and technique (DCT) is developed. Two meters downstream the beam line a removable aluminum foil holder is installed in a separate chamber (see Figure 3.13). Directly next to the chamber a coaxial germanium detector is placed to detect the delayed γ decay. The idea is to monitor all radiation near the DCT chamber and to make coincidence on a long time scale (≈ 100 μs) with protons detected in the T-REX array. The practical implementation into the software will be outlined in Section 3.4.

The limited dimensions of the DCT chamber allow the chamber to be quickly vented and pumped during the foil-changing cycle. ^{66}Ni only undergoes β decay to the ground state of ^{66}Cu which does not contribute to the background observed by the DCT. In contrast, the β decay of ^{66}Cu to ^{66}Zn does have γ rays following the decay, which provide the main source of radiative background in the DCT spectrum. Due to the relative long half-life of ^{66}Ni of 54.6 hours, the intensity of the background radiation grows with time. Simulations have shown that for beam intensities of around 1 10^6 pps (the expected beam intensity), an 8 hour foil changing cycle is necessary to limit the background [Dar09]. Towards the end of the experiment this cycle time is increased to 12 hours.

For energy calibration and efficiency determination ^{152}Eu and ^{60}Co sources are used. The ^{152}Eu source is used for setting up the relative efficiency curve and energy calibration; and the sum peak technique using the ^{60}Co source provides the scaling for the absolute efficiency curve. The analytic expression used for the efficiency curve is similar to Eq. 3.4 used for the Miniball clusters. The total photo peak efficiencies for the two transitions of interest are $\epsilon_{\mathrm{int},313} = 7.4\%$ and $\epsilon_{\mathrm{int},694} = 4.4\%$.

المنارة للاستشارات

Transmission efficiency

The total photo peak efficiency can not be directly used to correct the amount of observed delayed coincidences for efficiency as this assumes that *all projectiles are collected on the aluminum foil without any spread (i.e. point source)*. As the primary ^{66}Ni beam is focused at the target position the resulting secondary ^{67}Ni nuclei will be focused roughly in the same manner. This leads to divergence downstream and part of the ^{66,67}Ni beam is not collected on the aluminum collection foil. Also trajectory changes due to elastic scattering and straggling result in additional divergence and lead to collection losses. The beam is hence collected over a large area of the aluminum foil and not concentrated in one point like the sources used. Losses due to in-flight decay are negligible as the transit time of ≈ 70 ns is small compared to the half-life of 13.3 μs. Therefore an internally consistent method is used to determine the global DCT efficiency.

The method that is used relies on the *top-feeding* of the isomer and makes a comparison between the number of top-feeding proton-γ events observed in Miniball and the number of 313 keV and 694 keV counts in DCT with these events. The former number is $\propto \epsilon_{\mathrm{MB},\gamma_{\mathrm{top}}}$, while the latter is $\propto \epsilon_{\mathrm{MB},\gamma_{\mathrm{top}}}\ \epsilon_{\mathrm{transmission}}\ \epsilon_{\mathrm{photo\ peak},313/694}$. By taking the ratio of these two quantities, the dependence on $\epsilon_{\mathrm{MB},\gamma_{\mathrm{top}}}$ vanishes and a value $\propto \epsilon_{\mathrm{transmission}}\ \epsilon_{\mathrm{photo\ peak},313/694}$ remains. As $\epsilon_{\mathrm{photo\ peak},313/694}$ is known from source runs, the transmission efficiency can be obtained and hence also the global, absolute DCT efficiency: $\epsilon_{\mathrm{DCT},313/694} = \epsilon_{\mathrm{transmission}}\ \epsilon_{\mathrm{photo\ peak},313/694}$. Top-feeding transitions that are used for this method can be identified from Figure 5.3.A showing the prompt Miniball radiation in delayed coincidence with either 313 keV or 694 keV. The prompt Miniball transitions used for this method are 1201 keV, 1330 keV and 2270 keV. The results of this analysis are shown in Table 3.3. The width of the delayed coincidence window was 40 μs, which equals three half-lifes of the 1007 keV isomer or 82.5% of all decays. This is taken into account in the results presented in Table 3.3. An average transmission efficiency of 53 ± 6 % was found from these results, with the main contribution to the error bar originating from the absolute photo peak efficiencies. The proton-γ-DCT spectra used can be found in Appendix A (pp. 202 (1201 keV), 205 (1330 keV) and 218 (2270 keV)).

3.3 Data acquisition & structure

The signal processing and data collection for experiments using T-REX in combination with Miniball is split into two parts: the analog signal processing of the signals from the silicon T-REX array and the direct digitization of the

المنارة للاستشارات

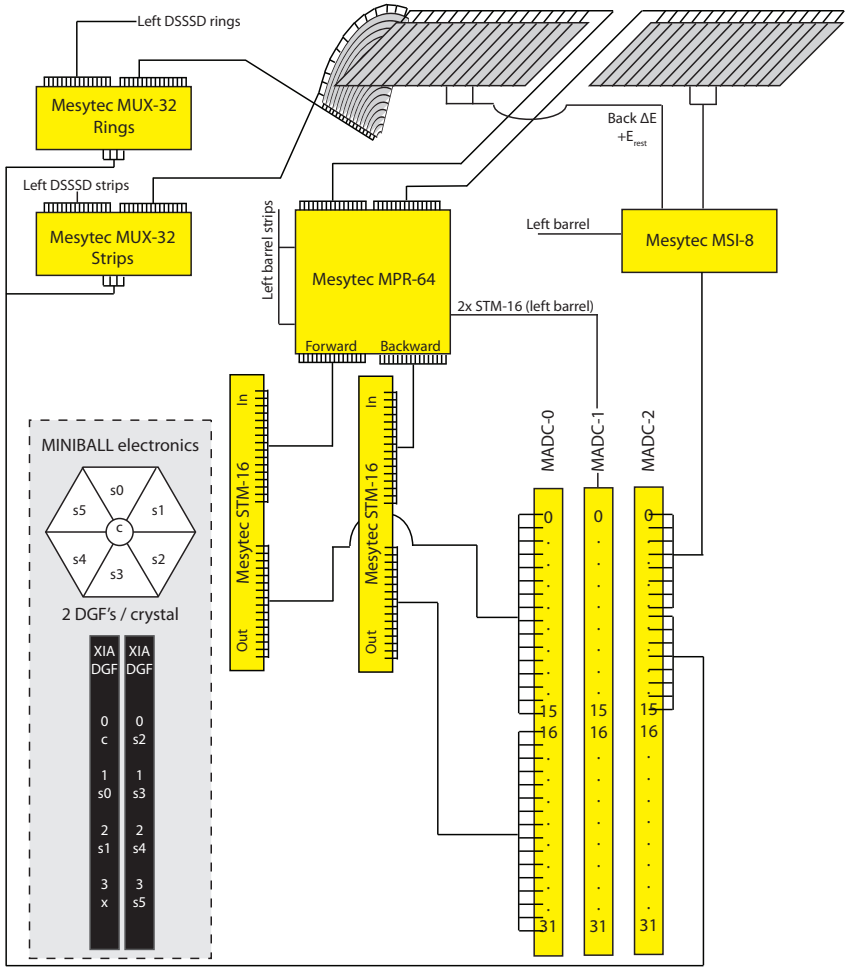

Figure 3.14: Arrangement of electronic modules used to process signals from the T-REX array limited here to the Top-Left trigger group. Only the top quadrant and modules necessary to process its channels are depicted here. For the whole Top-Left trigger group additional modules are required unless mentioned otherwise. The same lay-out was repeated for the Bottom-Right trigger group. See text for information.

المنارة للاستشارات

	ϵ_{DCT} [%]	
Gate energy [keV]	313 keV	694 keV
1198	4.4 (5)	1.7 (5)
1330	4.0 (8)	2.8 (7)
2270	4.6 (8)	1.8 (7)
Weighted average	4.4 (2)	2.0 (2)
Transmission efficiency	**59 (8)**	**46 (9)**

Table 3.3: Global efficiency of the DCT efficiency and transmission efficiency to the DCT setup.

γ-signals detected by Miniball. The structure and lay-out of the modules used is schematically shown in Figure 3.14.

The digital electronics used for processing the γ signals from the Miniball cluster detectors consists of XIA's Digital Gamma Finders (DGF) [Com12] CAMAC modules. For each crystal, seven signals have to be handled: one full energy core signal and six segments. In total $8 \times 3 \times 7 = 168$ channels have to be processed. Two DGF modules are used for each Miniball crystal: the first one handles the core signal and two segments, the remaining four segment channels are connected to the second DGF. This is done to divide the load evenly over both modules. The core channel serves as a trigger to read out the remaining seven channels. The DGFs also has an internal amplifier, with programmable gain and offset, used to shape the incoming signal which was only handled by Miniball's preamplifiers. A 40 MHz sampling 16-bit ADC using a fast filter for timing, pile-up rejection, trigger generation and a slow filter for energy determination digitalize the data [War13]. XIA DGFs also provides the possibility to perform pulse-shape analysis (PSA) to improve the position resolution of the detected γ rays. However, this feature has not been used during Miniball experiments. After digitization, the data are buffered until a read-out is forced. Time stamping of the events is provided by a dedicated module (*master clock*) synchronizing all the internal 40 MHz clocks (25 ns resolution). Besides the 48 DGF modules used by Miniball, also 6 additional DGF modules are used. One is dedicated to the delayed coincidence-detector, one is used to save Super cycle, T1 (proton impact) and EBIS time stamps and the final four modules were previously used as digital time stamp generators of the analog particle detection system. With the implementation of the new Mesytec MADC-32 modules in 2009, these time stamping DGFs became obsolete and are not used any longer.

T-REX signals are handled by a set of Mesytec modules. Depending on the type of signal, a different set of modules is used. The division separates signals from the DSSSD, strip signals of the barrel detectors and the remaining signals from

المنارة للاستشارات

the unsegmented detectors like backside of the ΔE-detectors and E_{rest} signal. The difference between these groups lies in the preamplification and amplification process. Eventually all shaped signals are used as input of Mesytec MADC-32 modules [Mes12a] using 12-bit conversion (1.6 μs) and inclusion of sliding scale. Events are written to the buffer (8k 32-bit words) and processed when prompted with a forced read-out. Internal time-stamping is also performed in these modules with the same resolution (40 MHz, 25 ns) as the XIA DGFs. The MADC clocks are also synchronized by the DGF master clock. The trigger conditions will be discussed later in this section. The four quadrants of the T-REX array are divided into two *trigger groups*: Top-Left and Bottom-Right. This division is based on the fact that in the event of (elastic) scattering both particles are detected in different trigger groups.

Multiplexing is applied to signals of the DSSSD detector using Mesytec MUX-32 modules [Mes12c]. These modules have a 32-channel input and are capable of preamplifying and amplifying two simultaneous events. The amount of incoming signals is reduced from 32 to 4: an energy signal and a signal indicating the input channel for the primary and secondary hit [Mes12c]. Two MUX-32 modules are used for each trigger group: one for the angular rings and a second one for the radial strips. The eight output signals from these two modules serve as input on MADC-2 (see Figure 3.14). The signals from the E_{rest} part of the CD detector are not multiplexed but directly connected to MADC-2 after shaping[14].

For each trigger group the 64 barrel strip channels (16 for each quadrant as a distinction is made between the forward and backward strips) are preamplified using a Mesytec MPR-64 module, also providing the bias voltage which is applied on the common side of the strips [Bil12]. These preamplified signals are shaped by four Mesytec STM-16 modules, one for each quadrant. The 32 shaped signals of the two top quadrants are grouped in one MADC, and a second MADC is used for the 32 signals from the left quadrants.

The eight signals of the unsegmented parts of the barrel detector are first preamplified and shaped by a Mesytec MSI-8 module which have an integrated timing filter amplifier and applied bias voltage for the detectors [Mes12b]. This module has 16 output channels: 8 timing signals and 8 shaped energy signals of the detectors which are digitalized by MADC-32s.

Timing signals from the barrel ΔE, E_{rest} and CD detector (both triggers from MUX-32 modules and E_{rest} part of the CD) are combined in a logical OR-module to create a common OR for the whole trigger group, triggering the three MADCs.

As outlined in the definition of the beam ON window (p. 84), the DGF and

[14]This is not shown in Figure 3.14

المنارة للاستشارات

MADC buffers start to fill during a predefined time interval when a bunch of particles is extracted from the EBIS after which a read-out is forced. The main difference between the buffer filling in the DGFs and MADCs lies in the fact that the DGFs (γ rays) collect data without requiring a trigger. This is not the case for the MADC where at least one of the specific signals has to be above threshold (see above). The handling of the data read-out is done by the MARABOU software [Lut00] using MBS data structures.

3.4 Software analysis procedure

The raw data files saved by MARABOU are processed in three steps by ROOT5.16 based analysis software. In short these three steps are 1- unpacking the MBS data and creating correlated events 2- calibration of these events and application of noise filtering 3- kinematical reconstruction by transforming the detected signals into particles and γ rays.

3.4.1 Event building

In this first step the raw data files are transformed to the ROOT data types. The MBS structure (Multi-Branch System) of the data groups all signals detected before a forced read-out into a single MBS event. One MBS event hence corresponds to a single beam ON or OFF window. The MBS event contains multiple *MBS subevents* which encompass data from a single MADC or DGF module. Depending on the type of module the 16- or 32-bit data are decoded and saved in a uniform ROOT format. After the whole MBS event is decoded, the actual events are created. MADC subevents (corresponding to particles) are used as primary event generators and sorted according to their time stamp. MADC hits that occur within a predefined coincidence window, in this case $|\Delta T| < 0.5$ μs are grouped together (into what is called a BuiltEvent). In a second stage, also DGF subevents are either added to existing BuiltEvents or new BuiltEvents are added to the time line if no coincidence is found.

For the DCT, the coincidence window is extended to a total width of 120 μs. The reference point is the time stamp of an MADC subevent and the window spans from -40 μs to +80 μs ($T_{\mathrm{DCT}} - T_{\mathrm{MADC}}$). γ rays detected in DCT can be assigned to multiple BuiltEvents, while γ rays detected in Miniball are added to a single BuiltEvent. The reason to assign the DCT γ rays to multiple BuiltEvents is that at this point no identification can be made of the signals detected by the MADCs.

المنارة للاستشارات

The BuiltEvents are saved as separate entries of a ROOT tree.

3.4.2 Calibration

The uncalibrated information stored in the tree generated after the first sorting step is filtered and calibrated. For each BuiltEvent a new object called CalibratedEvent is created, containing information of Miniball clusters (coming from DGF subevents), barrel and CD events (from the MADCs).

Threshold checks are performed for all signals and the signals are calibrated when above threshold. For the barrel detectors, the ΔE signal has to be above threshold if this data are to be processed. The most energetic strips are identified and define which strip registered the hit as well as the position along the strip (within the range between 0 and 1)[15]. If above threshold, also the E_{rest} signal is calibrated and added to the event. In the same way, information from the CD detector is de-multiplexed and calibrated. For DGF-subevents a distinction is made between DGFs handling Miniball data and the DGF of the DCT setup.

3.4.3 Kinematical reconstruction

In the final stage of the analysis software the calibrated signals stored in the CalibratedEvents objects are transformed to the physical entities Particles and Gammas. A gamma is created from the calibrated DGF information. The add-back procedure for Miniball γ's is applied here as outlined on p. 93 and the segment ID of the most energetic segment is used to determine the direction of the detected γ ray. The timing signal of the detected γ rays is also corrected for the *walk* of the DGFs. This correction has the biggest influence on low-energy γ rays.

For barrel and CD events a particle identification is performed and the procedure applied depends on which quadrant registered a hit. In case of the forward barrel both transfer products and elastic scattered particles can be detected. The ΔE-E_{rest}-signature of the detected particle is compared with a kinematical calculation to determine its kind. An example of the separation between deuterons and protons in the forward barrel detector can be found in Figure 5.5 on p. 133. The 3D-position of the hit is deduced from the strip number and position along the strip, and translated into spherical coordinates θ and φ.

[15]For multiplicity 1 the assignment is straightforward. For multiplicity 2 a distinction is made between hits in neighboring strips and hits in non-neighboring strips. In case of the former, the barrel event is accepted and a half integer strip number is assigned to the hit. For the latter the event is generally discarded unless the weakest position channel has a calibrated position smaller than 0.05.

المنارة للاستشارات

After particle and position determination the *energy losses* of the particle in both the Mylar foil and target are calculated. This is done by calculating the range for this kind of particle in the material (given its known energy), adding the effective thickness[16] to this range and calculate the amount of energy required to achieve this range.

After this step the data are in a suitable format to create the relevant spectra, histograms and angular distributions of the protons. In order to rely on proton-γ-coincidences the specific time structure of these coincidences has to be considered. For γ's detected by Miniball, the proton-γ-time difference is shown in Figure 5.1 (p. 128) and clearly shows the *prompt* peak of γ's due to a transfer reaction. The constant plateau left and right is due to *random* background radiation. The time behavior of the DCT technique is shown in Figure 5.2 (p. 129) and defines the 40 μs wide *delayed* and *random-delayed* windows. For a discussion of the observed half-life of the isomer, see p. 110 of Chapter 4 and p. 128 of Chapter 5.

[16] This differs from the actual thickness of the material as the particle will enter the material under a given angle depending on its direction.

المنارة للاستشارات

4

Paper I: Identification of the deformation-driving $\nu d_{5/2}$ orbital in $^{67}_{28}$Ni$_{39}$

Paper submitted for publication in
Physical Review Letters

المنارة للاستشارات

المنارة للاستشارات

J. Diriken,[1,2] N. Patronis,[1,3], A.N. Andreyev,[1,4,5] S. Antalic,[6] V. 20,[7] A. Blazhev,[8] I.G. Darby,[1] H. De Witte,[1] J. Eberth,[8] J. Elseviers,[1] V.N. Fedosseev,[9] F. Flavigny,[1] Ch. Fransen,[8] G. Georgiev,[10] R. Gernhauser,[7] H. Hess,[8] M. Huyse,[1] J. Jolie,[8] Th. Kröll,[7] R. Krücken,[7] R. Lutter,[11] B.A. Marsh, [9], T. Mertzimekis,[12] D. Muecher,[7] R. Orlandi,[1,13] A. Pakou,[2] R. Raabe,[1] G. Randisi,[1] P. Reiter,[8] T. Roger,[1] M. Seidlitz,[8] M. Seliverstov,[1,9] C. Sotty,[10] H. Tornqvist,[14] J. Van De Walle,[14] P. Van Duppen,[1] D. Voulot,[9] N. Warr,[8], F. Wenander,[9] and K. Wimmer[7,15]

[1] *Instituut voor Kern- en Stralingsfysica, KU Leuven, Celestijnenlaan 200D, B-3001 Leuven, Belgium*
[2] *SCK•CEN, Boeretang 200, B-2400 Mol, Belgium*
[3] *Department of Physics and HINP, The University of Ioannina, 45110 Ioannina, Greece*
[4] *Department of Physics, University of York, YO10 5DD*
[5] *Advanced Science Research Center, Japan Atomic Energy Agency (JAEA), Tokai-mura, 319-1195, Japan*
[6] *Department of Nuclear Physics and Biophysics, Comenius University, 84248 Bratislava, Slovakia*
[7] *Physik Department E12, Technische Universität München, D-85748 Garching, Germany*
[8] *IKP, University of Cologne, D-50937 Cologne, Germany*
[9] *AB Department, CERN 1211, Geneva 23, Switzerland*
[10] *CSNSM, CNRS/IN2P3, Universite Paris-Sud 11, UMR8609, F-91405 ORSAY-Campus, France*
[11] *Fakultät für Physik, Ludwig-Maximilians-Universität München, D-85748 Garching,* [12] *INP, NCSR "Demokritos", GR-15310, Ag. Paraskevi/Athens, Greece*
Germany
[13] *School of Engineering, University of the West of Scotland, Paisley, PA1 2BE, United Kingdom, and the Scottish Universities Physics Alliance (SUPA)*
[14] *PH Department, CERN 1211, Geneva 23, Switzerland*
[15] *Department of Physics, Central Michigan University, Mount Pleasant, Michigan 48859, USA*

المنارة للاستشارات

Abstract:

Background: The $\nu g_{9/2}, d_{5/2}, s_{1/2}$ orbitals are assumed to be responsible for the swift onset of collectivity observed in the region below ^{68}Ni. Especially the single-particle energies and strength of these orbitals separated by the $g_{9/2}$-sd ($N = 50$) shell gap have a strong influence.
Purpose: Determine the single-particle $\nu g_{9/2}$ and $\nu d_{5/2}$ strength distribution near ^{68}Ni ($Z = 28, N = 40$) by studying ^{67}Ni.
Method: A one-neutron transfer reaction ^{66}Ni(d,p) study in inverse kinematics employing a post-accelerated RIB is performed at the REX-ISOLDE facility. A combination of Miniball, T-REX and a newly developed delayed correlation technique as to investigate μs-isomers was used.
Results: Identification of positive-parity states with substantial $\nu g_{9/2}$ (1007 keV) and $\nu d_{5/2}$ (2207 keV and 3277 keV) single-particle strengths up to an excitation energy of 5.8 MeV.
Conclusions: 50% of the $\nu d_{5/2}$ single-particle strength relative to the $\nu g_{9/2}$-orbital is concentrated in and shared between the first two observed $5/2^+$ levels. The estimated $N = 50$ shell gap size is found to be 2.6 MeV. The results are compared with similar studies in the region around $^{90}_{40}Zr_{50}$.

المنارة للاستشارات

In spite of extended studies of deformed atomic nuclei, questions remain about the microscopic origin of deformation. It is well-established that most nuclei with a magic proton and neutron number have a spherical character while nuclei situated far away from these so called doubly closed shell nuclei are deformed. However, already three decades ago, a so-called "island of inversion" has been discovered around the magic number $N = 20$ where, unexpectedly, semi-magic nuclei appear to be deformed in their ground state due to strong quadrupole correlations between $\Delta j = 2$ orbitals, in this case within the pf-shell [1,2].

The region of the nuclear chart below the doubly (semi) magic nucleus ^{68}Ni ($Z = 28$, $N = 40$) is also characterized by a swift onset of collectivity [3,4]. This is suggested to arise from the combination of the small size of the $N = 40$ shell gap and of the presence of the $\nu g_{9/2}$-$d_{5/2}$-$s_{1/2}$ orbitals above this gap which should strongly enhance quadrupole collectivity [5]. Large-scale shell model calculations have shown that the inclusion of the $\nu d_{5/2}$-orbital in the model space is indeed necessary to reproduce the collective features of nuclei in this region [5,6]. The contribution of the $\nu g_{9/2}$-$d_{5/2}$ quadrupole collectivity depends on the single-particle energies of these orbitals (sensitive to three-body monopole forces [7]) and on the occupancy of the $\nu g_{9/2}$ orbital (see Fig. 3 in Ref. [8]). From this perspective, the distribution of the positive-parity $\nu g_{9/2}$, $d_{5/2}$, $s_{1/2}$ single-particle strength at $N = 40$ (^{68}Ni) serves as an anchor point to validate shell-model calculations and the assumption itself.

One-neutron transfer reactions into the direct neighbors of ^{68}Ni are excellent tools to probe the size of shell gaps and test the single-particle character of the neutron orbitals. Due to the lack of stable isotopes in this mass region the use of energetic, radioactive ion beams (RIBs) are needed to perform these studies. In this letter, we report on the one-neutron transfer reaction using a post-accelerated RIB (^{66}Ni, $T_{1/2} = 54.6$ h) to study the ^{66}Ni(d,p)^{67}Ni reaction in inverse kinematics (Q value = 3.58 MeV). The combination of a pure RIB, a highly-segmented silicon and an efficient γ-ray detector array was crucial to perform these measurements and the strategy followed was similar to e.g. Ref [9].

Spectroscopic information on ^{67}Ni is available from previous experiments however firm spin assignments were missing [10-17]. Data from β decay provided tentative spin assignments for the lowest excited states [10], while deep inelastic and multi-nucleon transfer reactions identified the position of higher excited states [11-14]. The g factor of the 13.3 μs [15] isomeric $(9/2^+)$ state at 1007 keV was found to be smaller by a factor of two than expected for a pure $1g_{9/2}$ configuration [16].

The 99% pure ^{66}Ni beam was produced at the REX-ISOLDE facility using the RILIS ion source [18], post-accelerated to 2.95 MeV/u by REX [19] and

المنارة للاستشارات

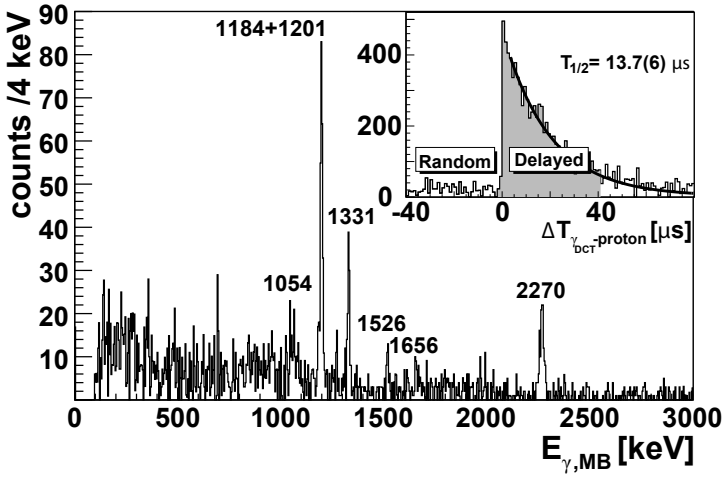

Figure 4.1: Miniball γ-ray spectrum, in prompt coincidence with a proton detected in T-REX and in delayed coincidence (120 μs time window) with either a 313 or 694 keV γ transition. The inset shows the time difference between a prompt proton - Miniball γ-ray event and a delayed 313 keV γ-ray transition. The half life deduced from an exponential fit is 13.7 (6) μs, in agreement with the previously observed values of 13.3 (2) μs [15] and 13 (1) μs [16] for the 1007 keV isomer in ^{67}Ni.

directed onto a deuterated polyethylene target located in the center of T-REX silicon array, resulting in a center-of-mass (CM) energy of 5.67 MeV and average intensity of $4.1 \cdot 10^6$ pps. A combination of the T-REX position sensitive particle detection array [20] and Miniball (MB) γ-ray detectors [21] was used to register the reaction products and γ radiation. The protons were detected in the T-REX array resulting in a total energy resolution of the order of 1.3 MeV (FWHM), mainly determined by the combination of proton kinematics and position resolution.

In order to investigate the 13.3 μs isomeric state (1007 keV) in ^{67}Ni, a delayed-coincidence setup was developed. The reaction products and the beam were stopped in a thick aluminum foil 2 meters downstream the target. The characteristic 313 and 694 keV transitions depopulating the isomer (see Fig. 4.1 and 4.2) were detected in a germanium detector positioned in close geometry to the beam stopper. Delayed correlations in a 120 μs time window between protons detected by T-REX, prompt gammas in Miniball and delayed isomeric transitions could be studied in this way despite the strong radioactive decay background (Fig. 4.1).

المنارة للاستشارات

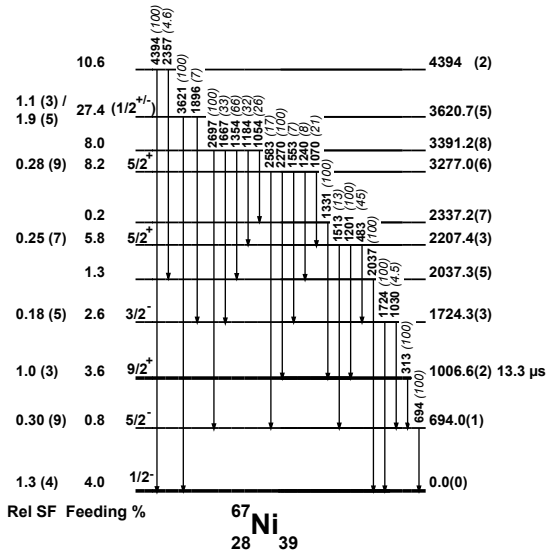

Figure 4.2: Partial level scheme of ^{67}Ni; all levels below 2 MeV observed in this study are shown. Above 2 MeV the partial level scheme includes the levels with a feeding probability $> 5\%$ and the levels involved in their gamma decay. Relative spectroscopic factors (Rel SF) with respect to the $9/2^+$ state are also given. The remaining (d,p)-strength is distributed among other states up to 5.7 MeV in excitation energy and will be discussed in Ref. [22]. In total 17 levels of which 7 are shown between 2.0 and 5.8 were identified and characterized by their gamma decay. For clarity, excited states identified in Ref. [14] are omitted.

Using the available information from prompt γ-γ coincidences, detected proton position and energy, and delayed coincidence data, an improved level scheme was constructed. Part of the deduced level scheme is shown in Fig. 4.2. An illustrative figure depicting the quality of the data is shown in Fig. 4.3. The inset of Fig. 4.3 shows the feeding pattern of ^{67}Ni based on measured proton intensities and kinematics (gray area) and on the measured γ-ray intensities and their position in the level scheme (black line). Both curves have been integral-normalized up to 5.4 MeV excitation energy to exclude the influence of the elastically-scattered protons visible at 6.4 MeV. The good agreement between the feeding pattern in ^{67}Ni deduced from the proton kinematics from T-REX and γ spectra from Miniball supports the reliability of the analysis method used and demonstrates the need for proton-γ coincidences to extract proton angular distributions from excited states.

Angular distributions of the detected protons could be extracted for various

المنارة للاستشارات

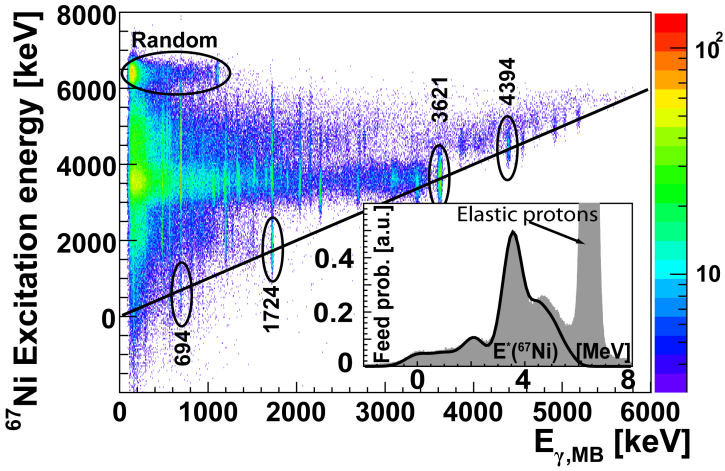

Figure 4.3: (Color online) Excitation energy in ^{67}Ni deduced from proton kinematics with respect to coincident Doppler-corrected γ rays in Miniball. Events on the solid, diagonal line indicate the population of an excited state followed by a ground state transition (examples are indicated with the γ-ray energy in keV). The events above 6 MeV excitation energy are random coincidences with elastically scattered protons. Inset: gray area: Experimental feeding probability of ^{67}Ni, deduced from the detected proton kinematics and intensities. Black line: Excitation curve reconstructed from efficiency-corrected intensities γ rays, their position in the level scheme and folded with the experimental energy resolution (see Fig. 4.2). An additional 4% feeding probability to the ground state was included to match the low-energy part of the spectrum with the gray area.

states by requiring strict conditions on proton kinematics (and thus the excitation energy in ^{67}Ni within $\pm$ 300 keV) and coincident γ rays. The obtained angular distributions were compared with DWBA calculations from FRESCO [23] using global optical model potentials from Refs. [24,25]. Examples of fits for states at 0, 1007, 2207 and 3277 keV are presented in Fig. 4.4 using different ℓ transfers. The obtained scaling factors were used to deduce relative spectroscopic factors (Rel SF in Fig. 4.2) with respect to the 1007 keV $9/2^+$ isomer.

The ground state of ^{67}Ni had previously a tentative $(1/2^-)$ assignment based on allowed β decay to the ^{67}Cu ground state $3/2^-$ [26], quasi-elastic transfer reactions on ^{70}Zn [12] and shell model predictions. From our DWBA analysis (Fig. 4.4.A) a $\ell = 1$ assignment is indeed favored, supporting the $1/2^-$

المنارة للاستشارات

spin assignment and $\nu p_{1/2}^{-1}$ shell model interpretation. The high relative spectroscopic factor hints to a pure configuration compatible with magnetic moment measurements [15].

The first excited state at 694 keV is weakly populated and fits equally well the $\ell = 1$, 2 and 3 momentum transfer. Based on the log ft value of the allowed β decay from the $(7/2^-)$ ground state of ^{67}Co, a $\nu f_{5/2}^{-1}$ configuration was proposed [10]. The stretched quadrupole character of the 694 keV transition [14] together with the short life time (150(4) ps) [27] and the ground state spin assignment fix the spin and parity to $5/2^-$ which is compatible with an $\ell = 3$ transfer.

Transfer to the state at 1007 keV was determined using the delayed coincidence technique and is compatible with $\ell = 3$ or 4 transfer (Fig. 4.4.B). However, the isomeric 313-694 keV decay sequence of the 1007 keV state has been shown to have a stretched quadrupole character [14]. The 13.3 μs half life of the 313 keV γ line calls for a $M2$ transition which fixes, in combination with the absence of a ground state transition, the spin of this state to $9/2^+$.

The proton angular distribution of the 1724 keV level is in agreement with an $\ell = 1$ transfer. A spin and parity assignment of $3/2^-$ is favored due to the small γ branch to the $5/2^-$ state at 694 keV and the strong top-feeding from the $5/2^+$ level at 2207 keV (see below).

The proton angular distribution of the excited state at 2207 keV fits well with $\ell = 2$ and to a lesser extent $\ell = 1$ (Fig. 4.4.C). However $\ell = 1$ is excluded because of the strong, prompt γ-ray transition towards the $9/2^+$ state at 1007 keV. The absence of a direct γ decay to the $1/2^-$ ground state further supports a $5/2^+$ spin assignment.

The same arguments also hold for the 3277 keV state (Fig. 4.4.D), whose proton angular distribution is best described by $\ell = 1$ or 2, combined with the characteristic gamma decay leads to a $5/2^+$ assignment.

As θ_{CM} angles close to 0° are not covered, $\ell = 0$ states cannot be identified unambiguously. The state at 3621 keV fits $\ell = 1$ and 2 equally well, but $\ell = 0$ cannot be entirely discarded. From the γ-decay pattern a low spin assignment is preferred due to the strong branch to the $1/2^-$ ground state and $3/2^-$ 1724 keV state. From the systematics of (d,p) reaction on lighter nickel isotopes [28,29], strong $\ell = 0$ population of $1/2^+$ states was observed while no states with $\ell = 1$ momentum transfer were populated. This would be compatible with a $(1/2^+)$ assignment.

The other observed states were weakly populated and no information on the spin could be extracted. Based on the observations in the lighter nickel

المنارة للاستشارات

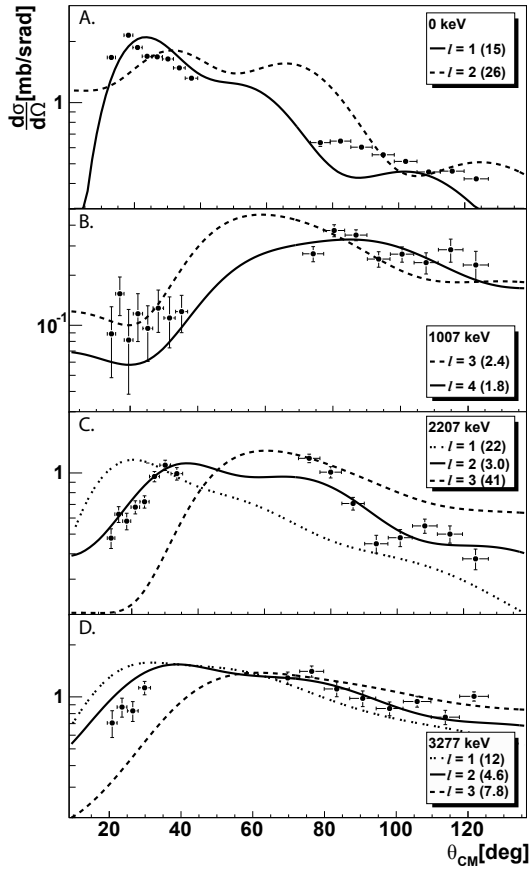

Figure 4.4: Angular distributions and DWBA calculations (best fits only) for states with energies of 0, 1007, 2207 and 3277 keV. The reduced χ^2 values of the fits are quoted between parentheses.

isotopes [28,29] we assume that feeding to states above 3277 keV is of $\ell = 0$ or 2 character.

As expected, the reduction of the relative spectroscopic factors of the negative parity p3/2 and f5/2 neutron orbitals when going towards heavier nickel isotopes continues in ^{67}Ni with the exception of the $1/2^-$ state that receives similar strength compared to the $9/2^+$ state. Concerning the positive-parity states, however one notices that half of the $\nu d_{5/2}$ strength (relative to the $\nu g_{9/2}$ strength) is divided over the first two $5/2^+$ states at 2207 keV and 3277 keV. A similar phenomenon is observed in the lighter nickel isotopes albeit with lower

المنارة للاستشارات

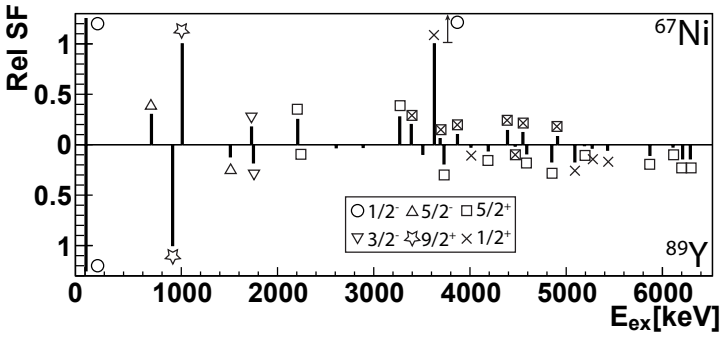

Figure 4.5: Distribution of single-particle strength in ^{67}Ni (top) and ^{89}Y (bottom). Relative SF with respect to $9/2^+_1$ are shown. States that could not be characterized in ^{67}Ni have a double label ($1/2^+$ and $5/2^+$). Data for ^{89}Y taken from [30].

strength: 31%, 27%, 23% and 34% in ^{59,61,63,65}Ni respectively [28,29]. The difference between the weighted average energy (using the rel SF's as individual weights) of the $5/2^+$ relative to the $9/2^+$ levels in $^{59-65}$Ni has a rather constant value around 2.6 MeV. The same value is obtained for ^{67}Ni assuming that all levels not characterized by spin above 3 MeV are $\ell = 2$ transfer. This value is slightly larger than the difference in effective single-particle energy between $g_{9/2}$ and $d_{5/2}$ (≈ 1.7 MeV) and hence the size of the $N = 50$ energy gap at ^{68}Ni obtained from recent shell-model calculations using empirical interaction [8]. As the influence of the $N = 40$ shell gap swiftly disappears when moving towards lower Z values, one expects a strong influence of quadrupole correlations in the (s)dg orbitals as observed through the enhanced collectivity in the Fe and Cr nuclei at $N = 40$ [5,31,32]. The weighted average of the energy of the $\nu s_{1/2}$ configuration follows closely the one of the $\nu d_{5/2}$ orbital, but it is striking that in contrast to the lighter nickel isotopes where the $1/2^+$ single particle strength is spread over several states, in ^{67}Ni most of the strength is concentrated in one ($1/2^+$) state at 3621 keV. The origin of this feature is currently not understood.

It is finally illustrative to compare the structure of doubly closed (semi-magic) ^{68}Ni ($N = 40$) and ^{90}Zr ($Z = 40$) as they exhibit a very similar excitation spectrum [33]. Single-proton transfer data from ^{88}Sr(^{3}He,d)^{89}Y [30] can be compared to our data (see Fig. 4.5). Despite the agreement for the $1/2^-, 3/2^-$ and $9/2^+$ states below 2 MeV, the structure of the positive-parity (s)d-states is very different as the $\ell = 0$, 2 strength is more fragmented and resides at higher energy in ^{89}Y. A low-lying $5/2^+$ state at 2222 keV in ^{89}Y has been identified [34] but it is only very weakly observed in the available (^{3}He,d)-data [30]. This comparison indicates a much more pronounced $Z = 50$ gap in ^{90}Zr compared to

المنارة للاستشارات

the $N = 50$ gap near ^{68}Ni and stresses the difference in the structure of these doubly closed shell nuclei in spite of their similar excitation spectrum.

In conclusion, the ^{66}Ni(d,p)^{67}Ni one-neutron transfer reaction has been studied for the first time using a post-accelerated RIB to investigate positive-parity states beyond the $N = 40$ and 50 gaps in ^{68}Ni. The combination of an efficient particle and gamma detection array formed a key ingredient for this experiment. Compared to the $\nu g_{9/2}$ strength, more then 50% of the $\nu d_{5/2}$ strength is concentrated in two relatively low-lying states while the relative $\nu s_{1/2}$ strength appears to be situated in one state only. The weighted average of the energy of the $\nu d_{5/2}$ configuration relative to the $g_{9/2}$ configuration is slightly larger than calculated by recent shell-model calculations. However, its low value as compared to the 5 MeV at ^{78}Ni should allow enhanced quadrupole collectivity from the $g_{9/2}$-ds neutron orbitals to play a key role in the heavy chromium isotopes around $N = 40$. It will be important to extend these studies using the higher beam energies available from HIE-ISOLDE to investigate the strength distribution of the neutron sdg orbitals when moving towards ^{78}Ni.

Acknowledgments

This work has been funded by FWO-Vlaanderen (Belgium), by GOA/2010/010 (BOF KU Leuven), by the Interuniversity Attraction Poles Programme initiated by the Belgian Science Policy Office (BriX network P7/12), by the European Commission within the Seventh Framework Programme through I3-ENSAR (contract no. RII3-CT-2010-262010), by a grant from the European Research Council (ERC-2011-AdG-291561-HELIOS), by the Slovak Research and Development Agency (No. APVV-0105-10), by BMBF under contracts 06KY9136I, 05P12PKFNE, 06MT7178 and 06MT9156 and the Maier-Leibnitz-Laboratorium, Garching.

[1] C. Thibault *et al.*, Phys. Rev. C **12**, 644 (1975).
[2] A. P. Zuker, J. Retamosa, A. Poves, and E. Caurier, Phys. Rev. C **52**, R1741 (1995).
[3] J. Ljungvall *et al.*, Phys. Rev. C **81**, 061301 (2010).
[4] A. Gade *et al.*, Phys. Rev. C **81**, 051304 (2010).
[5] S. M. Lenzi, F. Nowacki, A. Poves, and K. Sieja, Phys. Rev. C **82**, 054301 (2010).
[6] E. Caurier, F. Nowacki, and A. Poves, Eur. Phys. J. A **15**, 145 (2002).
[7] T. Otsuka, T. Suzuki, J. D. Holt, A. Schwenk, and Y. Akaishi, Phys. Rev. Lett. **105**, 032501 (2010).

المنارة للاستشارات

[8] K. Sieja and F. Nowacki, Phys. Rev. C **85**, 051301 (2012).
[9] M. Seeger *et al.*, Nucl. Phys. A **539**, 223 (1992).
[10] L. Weissman *et al.*, Phys. Rev. C **59**, 2004 (1999).
[11] R. T. Kouzes, D. Mueller, and C. Yu, Phys. Rev. C **18**, 1587 (1978).
[12] M. Girod, P. Dessagne, M. Bernas, M. Langevin, F. Pougheon, and P. Roussel, Phys. Rev. C **37**, 2600 (1988).
[13] T. Pawlat *et al.*, Nucl. Phys. A **574**, 623 (1994).
[14] S. Zhu *et al.*, Phys. Rev. C **85**, 034336 (2012).
[15] R. Grzywacz *et al.*, Phys. Rev. Lett. **81**, 766 (1998).
[16] G. Georgiev *et al.*, J. Phys. G: Nucl. Part. Phys. **28**, 2993 (2002).
[17] J. Rikovska *et al.*, Phys. Rev. Lett. **85**, 1392 (2000).
[18] V. Fedoseyev *et al.*, Hyperfine Interact. **127**, 409 (2000).
[19] D. Voulot *et al.*, Nucl. Instrum. Meth. B **226**, 4103 (2008).
[20] V. Bildstein *et al.*, Eur. Phys. J. A **48**, 85 (2012).
[21] N. Warr *et al.*, (2013), to be published.
[22] J. Diriken *et al.*, (2013), to be published.
[23] I. J. Thompson, Comput. Phys. Rep. **7**, 167 (1988).
[24] Y. Han, Y. Shi, and Q. Shen, Phys. Rev. C **74**, 044615 (2006).
[25] A. Koning and J. Delaroche, Nucl. Phys. A **713**, 231 (2003).
[26] E. Runte *et al.*, Nucl. Phys. A **441**, 237 (1985).
[27] H. Mach *et al.*, Nucl. Phys. A **719**, C213 (2003).
[28] T. Anfinsen *et al.*, Nucl. Phys. A **157**, 561 (1970).
[29] R. Fulmer *et al.*, Phys. Rev. **133**, B955 (1964).
[30] G. Vourvopoulos *et al.*, Nucl. Phys. A **174**, 581 (1971).
[31] W. Rother *et al.*, Phys. Rev. Lett. **106**, 022502 (2011).
[32] O. Sorlin *et al.*, Euro. Phys. J. A **16**, 55 (2003).
[33] D. Pauwels *et al.*, Phys. Rev. C **86**, 064318 (2012).
[34] J. Melssen *et al.*, Nucl. Phys. A **376**, 183 (1982).

المنارة للاستشارات

المنارة للاستشارات

5

Paper II: Study of the ^{66}Ni(d,p)^{67}Ni one-neutron transfer reaction

Paper submitted for publication in
Physical Review C

المنارة للاستشارات

المنارة للاستشارات

J. Diriken,[1,2] N. Patronis,[1,3], A.N. Andreyev,[1,4,5] S. Antalic,[6] V. 20,[7] A. Blazhev,[8] I.G. Darby,[1] H. De Witte,[1] J. Eberth,[8] J. Elseviers,[1] V.N. Fedosseev,[9] F. Flavigny,[1] Ch. Fransen,[8] G. Georgiev,[10] R. Gernhauser,[7] H. Hess,[8] M. Huyse,[1] J. Jolie,[8] Th. Kröll,[7] R. Krücken,[7] R. Lutter,[11] B.A. Marsh, [9], T. Mertzimekis,[12] D. Muecher,[7] R. Orlandi,[1,13] A. Pakou,[2] R. Raabe,[1] G. Randisi,[1] P. Reiter,[8] T. Roger,[1] M. Seidlitz,[8] M. Seliverstov,[1,9] C. Sotty,[10] H. Tornqvist,[14] J. Van De Walle,[14] P. Van Duppen,[1] D. Voulot,[9] N. Warr,[8], F. Wenander,[9] and K. Wimmer[7,15]

[1] *Instituut voor Kern- en Stralingsfysica, KU Leuven, Celestijnenlaan 200D, B-3001 Leuven, Belgium*
[2] *SCK•CEN, Boeretang 200, B-2400 Mol, Belgium*
[3] *Department of Physics and HINP, The University of Ioannina, 45110 Ioannina, Greece*
[4] *Department of Physics, University of York, YO10 5DD*
[5] *Advanced Science Research Center, Japan Atomic Energy Agency (JAEA), Tokai-mura, 319-1195, Japan*
[6] *Department of Nuclear Physics and Biophysics, Comenius University, 84248 Bratislava, Slovakia*
[7] *Physik Department E12, Technische Universität München, D-85748 Garching, Germany*
[8] *IKP, University of Cologne, D-50937 Cologne, Germany*
[9] *AB Department, CERN 1211, Geneva 23, Switzerland*
[10] *CSNSM, CNRS/IN2P3, Universite Paris-Sud 11, UMR8609, F-91405 ORSAY-Campus, France*
[11] *Fakultät für Physik, Ludwig-Maximilians-Universität München, D-85748 Garching,* [12] *INP, NCSR "Demokritos", GR-15310, Ag. Paraskevi/Athens, Greece*
Germany
[13] *School of Engineering, University of the West of Scotland, Paisley, PA1 2BE, United Kingdom, and the Scottish Universities Physics Alliance (SUPA)*
[14] *PH Department, CERN 1211, Geneva 23, Switzerland*
[15] *Department of Physics, Central Michigan University, Mount Pleasant, Michigan 48859, USA*

المنارة للاستشارات

Abstract:

The quasi-SU(3) sequence of the positive parity $\nu g_{9/2}, d_{5/2}, s_{1/2}$ orbitals above the $N = 40$ shell gap are assumed to induce strong quadrupole collectivity in the neutron rich Fe ($Z = 26$) and Cr ($Z = 24$) isotopes below the nickel region. The position of these single-particle orbitals influences the amount of collectivity through the size of the $N = 50$ gap separating the $\nu g_{9/2}$-orbital from the remainder of the sd-shell. In this work the $N = 50$ shell gap is probed and characterized in the neighborhood of ^{68}Ni ($Z = 28$, $N = 40$) by investigating the neutron single-particle states of ^{67}Ni through the ^{66}Ni(d,p)^{67}Ni one-neutron transfer reaction at 3 MeV/A in inverse kinematics performed at the REX-ISOLDE facility. A combination of the Miniball γ-array and T-REX particle-detection setup was used. A delayed coincidence technique was developed to perform direct spectroscopy of the 13.3-μs isomer at 1007 keV in ^{67}Ni. Excited states up to an excitation energy of 5.8 MeV have been populated. The results show the identification of strongly populated $\nu g_{9/2}$ (1007 keV) and $\nu d_{5/2}$ (2207 keV and 3277 keV) positive parity neutron states. Negative parity (νpf) states have been observed at low excitation energy. The extracted relative spectroscopic factors show that the $\nu d_{5/2}$ single-particle strength is mostly split over two excited states at 2207 and 3277 keV, hinting towards the influence of this orbital on the structure in this mass region.

Note: *The version of this paper as printed here does not include the sections containing the results and discussion. A more elaborate discussion of these items can be found in chapters 7 and 8.*

المنارة للاستشارات

Introduction

While ^{68}Ni ($Z = 28$ and $N = 40$) exhibits properties of a doubly-closed shell nucleus [1-4], recent experiments point to the swift onset of collectivity in the region below the neutron-rich nickel isotopes ($Z = 28$) between the $N = 40$ and $N = 50$ shell gaps [5-16]. One of the first observations was the β decay of neutron-rich Mn isotopes which revealed a sharp decrease of the 2_1^+ energies in ^{64,66,68}Fe ($Z = 26$) [5,6] and later in the neutron rich Cr isotopes ($Z = 24$) [7]. The discovery of a μs-isomer in ^{67}Fe proved to be compatible with enhanced deformation in this nucleus [8]. Recently, $B(E2; 2_1^+ \rightarrow 0_1^+)$ values were measured for neutron-rich Fe and Cr isotopes using lifetime measurements [9-11] and Coulomb excitation [12,13], which confirmed the increase in collectivity when approaching $N = 40$. Other experiments like deep-inelastic scattering [14-16] supported these previous findings.

The main reasons for this enhanced collectivity are believed to be a combination of the reduction of rather shallow $N = 40$ shell gap due to the repulsive $\pi f_{7/2}\nu g_{9/2}$ tensor interaction when protons are removed [17] and the presence of the $\nu g_{9/2}$-$d_{5/2}$-$s_{1/2}$ orbital sequence directly above this gap which strongly enhances quadrupole collectivity [18,19]. The latter is supported by the fact that large-scale shell model calculations that do not include the $\nu d_{5/2}$ orbital in their valence space fail to reproduce the experimental trends [20]. In contrast, recent calculations encompassing enlarged valence spaces including the $\nu d_{5/2}$ orbital provide better agreement with the experimental data [19,21]. Note that in the calculations of Ref. [19] the quadrupole-quadrupole interaction of the $\nu g_{9/2}$, $d_{5/2}$ orbitals is increased by 20% to correct for the absence of the $\nu s_{1/2}$ orbital in the valence space. The effect of the quadrupole coherence generated by this quasi-SU(3) sequence (Δj=2) containing the $\nu g_{9/2} d_{5/2}(s_{1/2})$ partners depends on their relative energy separation, and thus on the $N = 50$ gap size. Recent calculations have shown that this particular gap size depends, due to three-body monopole forces [22], on the occupancy of the $\nu g_{9/2}$ orbital itself (see Fig. 3 in Ref. [23]). These calculations suggest that the $N = 50$ shell gap is established when the $\nu g_{9/2}$ orbital gets filled with neutrons and thus when approaching ^{78}Ni (estimated gap size $\approx$ 5 MeV), hinting to a robust shell closure for the latter [23]. Near the $N = 40$ nucleus ^{68}Ni the $N = 50$ shell gap is considerably weaker which can lead to enhanced quadrupole collectivity.

The calculations in Ref. [19] assume that the $N = 50$ has a similar evolution as observed in the Zr isotopes [24] in combination with an estimated $N = 50$ gap size of 5 MeV in ^{78}Ni. Experimental input on the size of the $N = 50$ shell gap near ^{68}Ni would provide valuable information for these large-scale shell model calculations as it can serve as an anchor point for the gap size evolution [19].

المنارة للاستشارات

Calculations using three-body forces and information from the Zr-chain provided an estimated $N = 50$ gap size of 1.5-2 MeV near $N = 40$ [19,23,24].

^{68}Ni forms a peculiarity amongst the less exotic nickel isotopes as experimental data suggesting conflicting pictures is available for this nucleus. $B(E2)$-measurements revealed a clear local minimum in the $B(E2; 2_1^+ \rightarrow 0_1^+)$-systematic and a maximum in the excitation energy of this 2_1^+ state [1-4]. This suggested fingerprint of magicity, along with the existence of μs-isomers in this region [25], is in contradiction with mass measurements, where S_{2n} systematics do not reveal an irregularity at $N = 40$ [26,27]. This anomaly has been attributed to the parity change between the pf-shell below and gd-orbitals above the $N = 40$ Harmonic Oscillator shell gap, requiring at least two neutrons to be excited to form a 2^+ state. From an extreme single-particle shell model perspective ^{67}Ni can be described as a one-neutron hole coupled to ^{68}Ni and hence its excitation spectrum is expected to contain a considerable amount of neutron single-particle strength at low energy, mainly from the empty orbitals and hole states from the filled orbitals.

Spectroscopic information on ^{67}Ni is available from a range of experiments [28-34]. Data from β decay provided tentative spin assignments and proposed configurations for the lowest excited states up to and including the $9/2^+$ isomer [28]. Deep inelastic and multi-nucleon transfer reactions identified the position of higher lying excited states [29-32] and in some cases tentative spin assignments were proposed [30,32]. In the most recent deep-inelastic study in Ref. [32] yrast states up to 5.3 MeV were identified all built on top of the 1007 keV isomer. The magnetic moment of the ground state has been measured and its value of $0.601\mu_N$ differs by only 6% from the expected Schmidt value, hinting towards a very pure $\nu p_{1/2}$ ground state configuration [33]. Finally, the measurement of the g factor of the 13.3 μs [25] isomeric $9/2^+$ state at 1007 keV provided a value smaller by a factor of two than expected for a $1g_{9/2}$ configuration [34]. This reduction was attributed to a 2% admixture of proton 1p-1h $M1$-excitations ($f_{7/2}^{-1} f_{5/2}^{1}$) across the $Z = 28$ gap that would strongly affect the g factor [34].

One-neutron transfer reactions into both ^{67,69}Ni are a powerful tool to probe the stability of the $N = 40$ subshell closure, test the single-particle character of excited nuclear states, extract the centers of gravity of the neutron orbitals of interest and determine the size of shell gaps.

In this paper we present the results of a study of ^{67}Ni by a ^{66}Ni(d,p)-reaction (Q-value: 3.580 MeV [29]), favoring transfer with low ℓ-values. The obtained experimental angular distributions are compared with DWBA calculations, allowing spin and parity assignments and relative spectroscopic factors to be reported.

المنارة للاستشارات

The main findings of this work have already been published in Ref. [35] and in this paper the details of the analysis will be presented. In section 5 details about the experimental setup and measuring conditions are summarized and the newly developed delayed coincidence technique is discussed. The analysis of the data is presented in section 5 leading to the results reported in chapter 7. In chapter 8 the obtained results are compared with systematics in the lighter nickel isotopes and proton single-particle systematics in the $N = 50$ isotones near ^{90}Zr.

Experimental setup

Beam production and manipulation

The radioactive ^{66}Ni beam ($T_{1/2} = 54.6$ h [36]) was produced at the ISOLDE facility in CERN by bombarding a 50 g/cm^2 UC_x target with pulses of 1.4 GeV protons at an intensity of $\sim 6\ 10^{12}$ protons per pulse (average current of 1 μA). The interval between these pulses was always a multiple of 1.2 seconds. The target matrix was heated to a temperature of $\sim$ 2000 °C in order to optimize diffusion and effusion times through the tungsten transfer line towards the ionization cavity. Here the nickel isotopes were selectively ionized in a three-step resonant laser ionization process ($\lambda_1 = 305.1$ nm, $\lambda_2 = 611.1$ nm, $\lambda_3 = 748.2$ nm) using the RILIS laser ion source [37,38]. Elements with low ionization potentials could be surfaced ionized due to the high temperature of the system and cause contaminants such as gallium ($Z = 31$, IP = 6.0 eV) to appear in the beam. The level of contamination was checked by comparing data with the RILIS lasers ON (data containing both nickel and contaminants in the beam) with data in laser OFF mode (only contaminants). From this comparison a beam purity of at least 99% ^{66}Ni was obtained.

The positively charged nickel beam was extracted from the ion source by applying a 30 kV electrostatic potential and was subsequently sent through the General Purpose Separator, resulting in a continuous ^{66}Ni beam which was injected in REXTRAP [39]. In this Penning trap the continuous beam was accumulated during 30 ms and cooled by interactions with the buffer gas present (usually Ne or Ar). This bunch of ions was thereafter transferred to REX-EBIS, the Electron Beam Ion Source, where the ions were brought to a high charge state (16^+). The time necessary to reach this charge state (28 ms) was optimized for the isotope of interest and equaled the trapping time in REXTRAP in order to synchronize the system.

المنارة للاستشارات

The bunch of highly charged isotopes was extracted from EBIS and send through an A/q separator in order to select one specific ^{66}Ni charge state without contamination from the residual gas ions [40]. For this experiment, the slow extraction technique from EBIS (i.e. a smooth drop of the trapping potential) was used in order to maximize the spread of the available ions within the 800 μs bunch window.

Next, the beam was accelerated to a maximum energy of 3 MeV/A by the REX accelerator, which consists of a low-energy RFQ (max 300 keV/A) and a high-energy section (0.8 - 3.0 MeV/A) containing three 7-gap resonators and one 9-gap resonator [41], before being delivered to the experimental setup. The final energy depends on the A/q of the beam and was 2.95 MeV/A in this case. The global transmission efficiency of REX (including trapping and charge breeding) was of the order of $5 - 10\%$.

A 100 μg/cm^2 thick CD_2 target was placed in the center of the scattering chamber. The target purity was found to be 88% based on the ratio of elastically scattered protons and deuterons.

Detection arrays and signal handling

The scattering chamber was surrounded by two sets of detection arrays: the T-REX charged-particle detection setup [42] and the Miniball (MB) γ-array [43,44].

The T-REX charged-particle detection setup consisted of eight silicon ΔE-E telescopes (ΔE thickness: 140 μm, E thickness: 1000 μm), four in both the forward and backward direction, covering an angular range from 27° to 78° in the forward and 103° to 152° in the backward direction [42]. Each telescope consisted of 16 position sensitive strips oriented perpendicular to the beam direction, to allow position determination of detected particles. Calibration of the ΔE detectors was done using a quadruple α-source (^{148}Gd, ^{239}Pu, ^{241}Am and ^{244}Cm) and T-REX-Miniball coincidences were used to calibrate the E_{rest} detector. During the calibration process it was found that the full energy signal of the ΔE detector depends on the position of the hit along the strip. All full energy signals were hence corrected for this problem with parameters extracted from the measurement with the α-source. The energy resolution of particles detected by the ΔE-E telescopes was determined by the combination of intrinsic detector resolution, position uncertainty, beam spot size, energy losses and angular dependence of the particle kinematics and was of the order of 1300 keV. When using α-sources typical energy resolutions of 55 keV were achieved. The forward quadrants were shielded by a 12 μm Mylar foil to reduce the amount of incident elastically scattered particles at laboratory angles greater than 70° where the incident rate was high and kinetic energy of the particles low due to

المنارة للاستشارات

the reaction taking place in inverse kinematics. The influence of the Mylar foil on the detected energy of protons resulting from a (d,p)-reaction is discussed in section 5. The particle detectors were divided in two trigger groups (top-left and bottom-right), with as trigger condition either a hit in the ΔE or E-part in one of the quadrants of the trigger group. The 64 channels of the position sensitive strips were divided over two Mesytec MADC-32 modules (with internal time stamping) while the remaining signals (full ΔE energy and E energy) are all connected to a separate MADC-32.

During the experiment a significant increase of noise was noticed in the backward quadrants of T-REX, directly proportional to the instantaneous beam intensity and target thickness. The combination of the slow extraction from REX-EBIS (see section 5) and a reduction in beam intensity were necessary to control this problem, which was most likely to be caused by random summing of δ-electrons created by the heavy ion beam interacting with the CD_2 target or target holder material [45].

In order to detect the γ rays that were emitted after the population of ^{67}Ni in an excited state, eight Miniball cluster detectors were positioned around the scattering chamber [43]. Each Miniball cluster was composed of three hyper-pure germanium crystals, which were sixfold electrically segmented. The high granularity of the Miniball array allowed for a precise determination of the direction of the detected γ rays, which was necessary to perform a Doppler correction of the detected γ-ray energy. This was needed as the decaying nuclei travel at speeds around 0.08c while emitting γ rays, leading to Doppler shifts of the emitted wave lengths. The position of all clusters was determined by analyzing data from ^{22}Ne(d,p) reactions with known incoming energy by investigating the Doppler shift of the 1017 keV line in each segment. The signals from the Miniball array were digitally handled by a series of Digital Gamma Finder (DGF) modules, with an energy range of nearly 8 MeV. Energy calibration and efficiency determination were done using ^{152}Eu and ^{207}Bi sources. For the high energy part of the spectrum, data from the β decay of a stopped ^{11}Be beam ($T_{1/2} = 13.76$ s), including transitions up to 7.97 MeV, were used [46]. The total photo peak efficiency for 1 MeV gamma transitions was found to be 5.9 %. As the energy resolution of the detected protons in T-REX was insufficient to disentangle individual excited states purely based on proton kinematics, proton-γ-coincidences were necessary in order to obtain angular distributions. A similar strategy has been used on one-nucleon transfer reactions on stable nuclei to extract angular distributions for unresolved levels, like e.g. ^{64}Zn(d,^{3}Heγ) and ^{64}Ni(d,^{3}Heγ) [47,48].

Data was acquired during the 800 μs beam ON window, when a bunch of isotopes was being accelerated by REX. After this window is closed, the obtained data was read out and another 800 μs beam OFF window was started, encompassing

المنارة للاستشارات

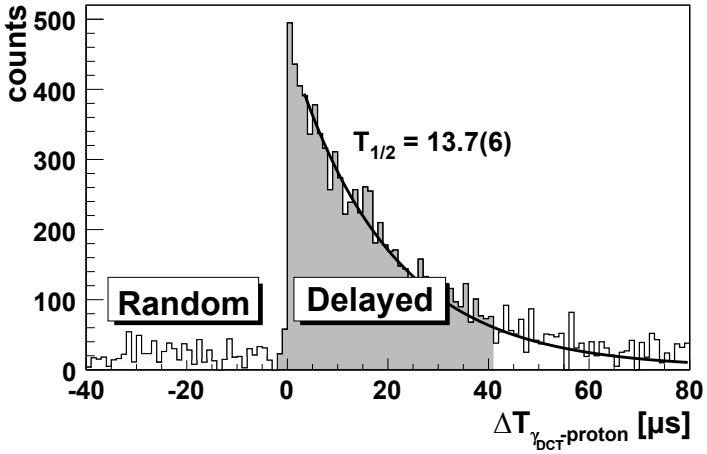

Figure 5.1: Proton-γ time difference in the delayed coincidence detector for the 313 keV delayed transition detected in the delayed coincidence germanium detector, background subtracted. Definitions of time windows are indicated. In the text these time windows are referred to as *delayed* and *random-delayed*. An exponential fit is applied to the time structure providing a halflife of 13.7 $\pm$ 0.6 μs.

natural background and β-decay radiation of isotopes stopped in the scattering chamber. All detected signals were directly timestamped by internal clocks running at 40 MHz.

Delayed coincidence technique

In section 5 the currently available experimental data concerning the 1007 keV 13.3 μs isomer in ^{67}Ni was discussed. As this state lacks prompt γ radiation in its decay, proton-γ-coincidences with Miniball could not be used to produce angular distributions based on γ gates. For this purpose a Delayed Coincidence (DCT) technique was developed encompassing a thick, removable aluminum foil used to stop the incoming beam and a dedicated coaxial germanium detector with the purpose to detect the isomeric, delayed transitions of 313 and 694 keV that followed the population of the 1007 keV isomer or states decaying via this isomer. The aluminum foil was positioned 2 meters downstream of the target position and renewed every 8 hours in order to limit the background originating from accumulated β decay. The coincidence window between gammas detected in the delayed coincidence chamber and particles detected by T-REX was

المنارة للاستشارات

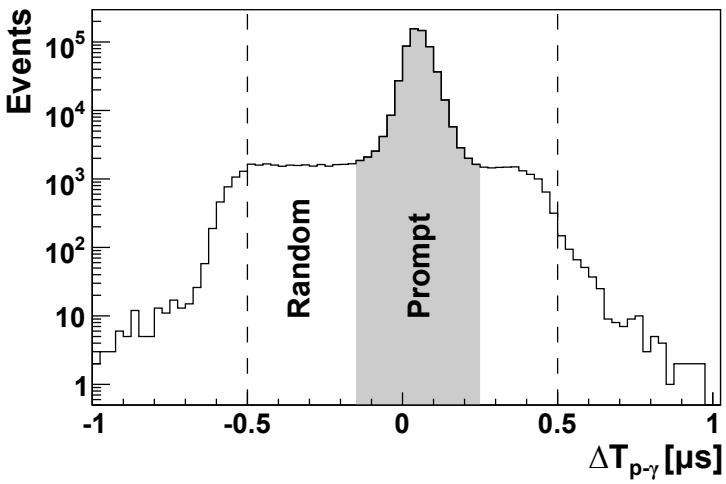

Figure 5.2: Proton-γ time difference between γ-rays detected in Miniball and protons detected by T-REX. The gray region defines the *prompt* proton-γ time window, other events are referred to as *random* coincidences. The width of the prompt window is determined by the timing resolution of the low energy γ-rays after the walk-correction.

asymmetrically set to 120 μs, ranging from -40 μs to 80 μs with the particle time stamp as the reference point. The relation between the proton and gamma time stamps is shown in Fig. 5.1 for the 313 keV transition (left and right background next to the 313 keV transition is subtracted) and shows the definition of the *delayed* and *random-delayed* windows, which are both 40 μs long. The delayed coincidence time window hence accounts for 87.5% of the isomeric transitions. As a comparison, the time relation between gammas detected in Miniball and protons detected in T-REX is given in Fig. 5.2, showing the more narrow coincidence window. In case of Miniball-T-REX coincidences the detected radiation is either *prompt* or *random* as defined in Fig. 5.2.

As the time of flight between the reaction target and the delayed coincidence setup was of the order of 80 ns, losses due to in-flight-γ-decay were negligible. The exponential shape has a fitted half-life of 13.7 (6) μs which is in good agreement with the previously measured values of 13.3 (2) μs (Ref. [25]) and 13 (1) μs (Ref. [34]) and confirms the weighted average of 13.3 (2) μs [25].

The efficiency of the delayed coincidence detection setup was determined in two steps: using a ^{152}Eu source at the aluminum foil's position (absolute photo peak efficiency using a point source) and also by using the reaction data itself

المنارة للاستشارات

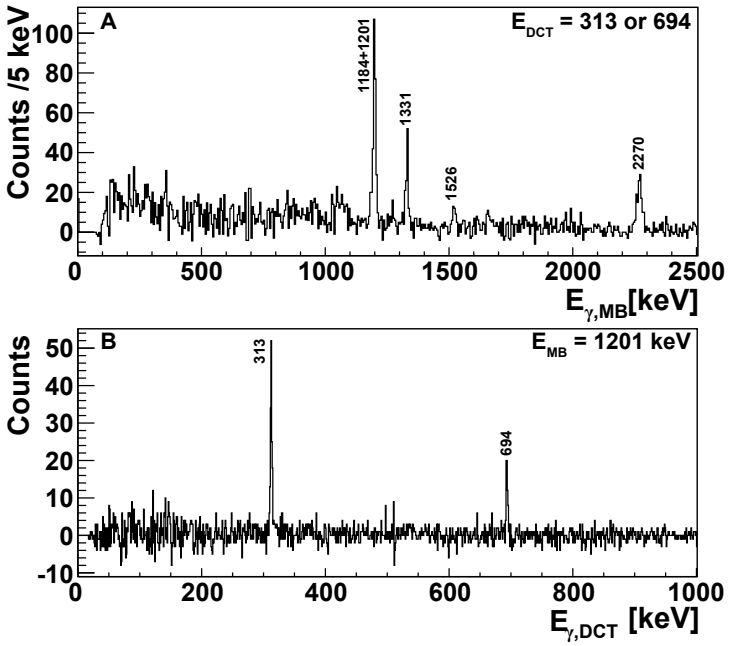

Figure 5.3: A. Doppler corrected γ-ray spectrum in Miniball, in delayed coincidence with either 313 keV or 694 keV. Random-delayed events (see Fig. 5.1) and the Delayed coincident background have been subtracted. B. Delayed coincidence spectrum requiring a prompt proton-1201 keV event in Miniball. This spectrum was used to determine the delayed coincidence efficiency. See text for more information.

by comparing the intensities of the prompt γ transitions arriving on top of the isomer with the intensity of the 313 keV and 694 keV in delayed coincidence with these events. The second step also includes the effect of a non point-like source and the transmission efficiency between the reaction target and the delayed coincidence setup. By comparing the results from both steps this transmission efficiency could be determined. As an example, Fig. 5.3.A shows the prompt Miniball radiation in delayed coincidence with either 313 keV or 694 keV, which allowed the identification of transitions arriving on top of the 1007 keV isomer. Fig. 5.3.B shows the inverse situation as the delayed coincidence spectrum is shown, requiring a prompt 1201 keV transition in Miniball. One can compare the 1201 keV intensity in Fig. 5.4 depending on the gate photo peak efficiency of Miniball ($\sim \epsilon_{\mathrm{MB},1201}$) with the intensity of either 313 or 694 keV in Fig 5.3.B which is proportional to the product of the delayed coincidence detector photo

المنارة للاستشارات

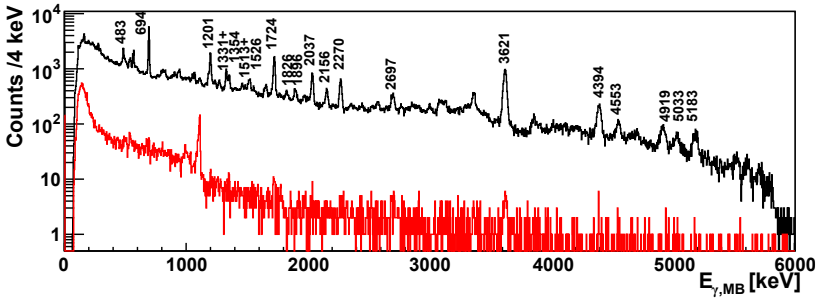

Figure 5.4: (Color Online) Doppler corrected Miniball γ-ray spectra, prompt proton coincident (black) and random proton coincident (red). See Fig. 5.2 for definition of Miniball timing windows. In the prompt spectrum most lines belonging to the γ-decay of ^{67}Ni can be clearly identified, while only traces of the most intense lines remain in the random spectrum together with a broadened β-decay line around 1039 keV (^{66}Cu $\rightarrow$ ^{66}Zn).

Table 5.1: Overview of the efficiency of the delayed coincidence setup for the two delayed transitions of interest with energies of 313 and 694 keV. The first row includes the absolute photo peak efficiency for the germanium detector obtained from source data. Further the global efficiency, determined using three prompt T-REX-Miniball gates, are given. The weighted averages of these different gates (line 4) are used in the analysis of the data. Finally, the transmission efficiency from the comparison between the absolute photo peak efficiency with the global efficiency is shown. This transmission efficiency also incorporates the fact that the spread of ions on the stopper foil is not a point source.

Gate [keV]	313 keV	694 keV
Source	7.4 (2)	4.4 (2)
1201	4.4 (5)	1.7 (5)
1331	4.6 (8)	1.8 (7)
2270	4.0 (8)	2.8 (7)
Global	4.4 (6)	2.0 (4)
Transmission	59 (8)	46 (9)

peak efficiency, gate photo peak efficiency of Miniball and the transmission efficiency ($\sim$ $\epsilon_{\mathrm{DCT,313\ or\ 694}}$ $\epsilon_{\mathrm{MB,1201}}$ $\epsilon_{\mathrm{Trans}}$). As all parameters except the transmission efficiency were known from source data, the transmission efficiency could be determined. An overview of these efficiencies is given in Table 5.1, leading to an average transmission efficiency of 53 (6)%.

المنارة للاستشارات

Analysis

Data structure

The event-by-event structure of the data allowed the construction of particle-γ-coincidences by placing a 1 μs coincidence window around the timestamps of the detected signals. The effective particle-γ_{MB} time structure within these events is shown in Fig. 5.2, indicating that the majority of the γ-rays detected within 1 μs of a proton is indeed prompt radiation resulting from transfer reactions. Events outside of the $\pm$0.5 μs time window were due to higher multiplicity events and shifts due to the walk-correction applied to the time stamps of low energy γ rays. The data in the random window of Fig. 5.4 were scaled based on the integrals of γ rays originating from β decay in the prompt and random window. The prompt nature of the radiation is also evident from Fig. 5.4 where the corresponding γ spectra are shown for both prompt and random proton-γ timing coincidences. The data in the random spectrum is limited and only contains a doubly-humped structure around 1039 keV, the dominant transition in the β decay of ^{66}Cu (note that no γ-rays are emitted in the β decay of ^{66}Ni) [49], which is due to the Doppler correction procedure. Also traces of the most intense prompt transitions, Compton background of the 1039 keV transition and radiation from the REX-accelerator are observed.

After the event building and calibration of the raw, detected signals, the kinematic reconstruction of the events was performed. In the case of the γ rays detected by Miniball the *add-back*-procedure was performed by summing γ-ray energies detected within the same cluster. The segment in which the highest energy was deposited is chosen as the primary interaction point and provided the direction used for Doppler correction.

In the case of γ rays detected in the delayed coincidence setup, the 120 μs wide coincidence windows were applied. Delayed coincident γ-rays could in principle be assigned to several particles within the 120 μs time window. However, the data showed that 95 % of the delayed coincident gamma rays were uniquely assigned to a single proton.

Particle identification is performed based on their ΔE-E signature for particles detected in the forward direction ($\theta_{LAB} < 90^{\circ}$). Fig. 5.5 illustrates the separation between identified deuterons and protons in one strip of the forward ΔE-E telescope. In the backward direction all protons are stopped in the ΔE detector and hence the $\mathrm{E_{rest}}$-detector serves as a veto to filter out electrons.

Energy corrections were applied to the detected particles for energy losses in the Mylar foil (only forward direction) and target (all directions). These corrections

المنارة للاستشارات

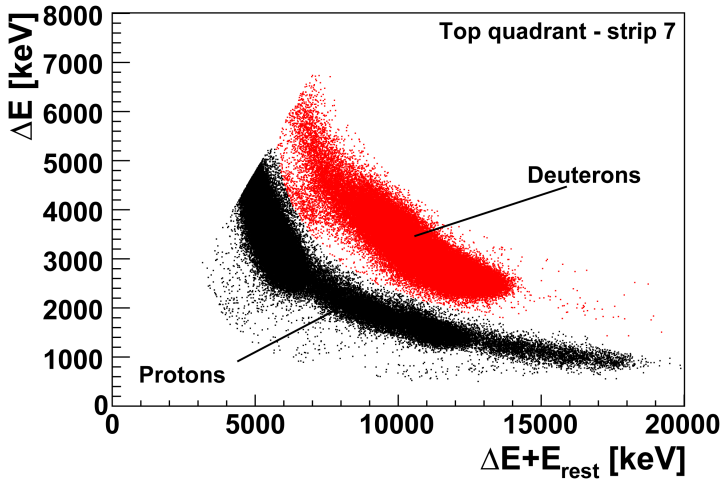

Figure 5.5: (Color online) Measured ΔE-E signature in strip 7 (θ_{LAB} between 42° and 48°) of the barrel detector. Particles that are stopped in the ΔE part of T-REX are rejected and not shown in this figure. The separation between particles identified as deuterons (red) and protons (black) is indicated.

were obtained by calculating the range of the detected particles in e.g. the Mylar foil based on the detected energy, adding the effective thickness of the Mylar foil to this calculated range and finally calculating the energy needed to obtain this combined range. Finally, based on the proton kinematics (energy and position of the detected proton), the corresponding excitation energy of ^{67}Ni was calculated based on the missing mass method.

^{67}Ni Level scheme

In order to construct the level scheme, information from (proton-)$\gamma\gamma$ coincidences, (proton-)DCT-γ-coincidences (see Fig. 5.3) and coincident initial excitation energy (from the missing mass method) has been combined. An instructive figure combining data from Doppler corrected γ-ray energy in Miniball and initial excitation energy is shown in Fig. 5.6, which can be used as a first guide to construct the level scheme and determine the decaying γ transitions. Events situated on the solid line correspond to transfer reactions that populate a specific excited state which subsequently decay with the emission of a γ ray directly to the ground state. Already from this figure one clearly identifies substantial feeding of excited states at 1724 and 3621 keV.

المنارة للاستشارات

The most detailed information can be obtained from the combination of proton-$\gamma\gamma$ coincidences and the corresponding incoming excitation energies. An example is given in Fig. 5.7.A, where proton-$\gamma\gamma$ coincidences are shown with a gate on the 1724 keV transition. Two strong transitions are clearly visible. The order of the 483, 1724 and 1896 keV γ rays can be determined by plotting the incoming excitation energy of ^{67}Ni deduced from the missing mass method for each of these transitions. The spectrum for 1724 keV shows multiple peaks, with the one at lowest energy around 1900 keV. The other gates have their first peak at higher energies, revealing that 1724 keV is a ground state transition. These two other transitions are placed directly on top of the 1724 keV transition as the position of the first peak in their excitation energy spectrum matches the sum of 1724 keV and the γ-ray gate energies, defining two states at 2207 and 3621 keV.

Repeating this analysis for all possible γ gates allowed to create the level and decay scheme of ^{67}Ni shown in Fig. 5.8. As a consistency check a comparison was made between the experimental excitation spectrum (or feeding probability) deduced from all detected protons in singles and a reconstruction based on the proposed level scheme (Fig. 5.8) and measured γ-ray intensities. This comparison is presented in Fig. 5.9. The normalization of both feeding probabilities was based on the integrals of both curves up to an energy of 5400 keV in order to exclude the influence of the elastic proton peak at 6.4 MeV. In the reconstructed curve the ground state feeding was left as a free variable and a 4% contribution was found. For each state a Gaussian distribution with FWHM of 800 keV (obtained from the experiment data) was used. The good overall agreement between the excitation spectrum obtained from proton energies alone and the reconstructed curve based on γ-intensities supports the proposed level scheme and the procedure to rely on proton-γ-coincidences to extract angular distributions.

A final note should be made on the region above 4 MeV excitation energy. When looking to γ-rays originating from this excitation energy in ^{67}Ni, some direct ground state transitions can be seen, as well as most of the γ rays found at low excitation energy in the level scheme (e.g. 694, 1201 and 1724 keV), but in Fig. 5.6 transitions connecting these highly excited states with those at lower excitation energy are not observed. This might be due to the high level density at high excitation energy and the high variety of possible decay paths. (d,p)-experiments on lighter nickel isotopes at comparable center of mass (CM) energies have shown that at high excitation energy a large number of states are populated with rather small cross sections, supporting this statement [50-56]. The reconstructed curve in Fig. 5.9 for excitation energies higher than 4 MeV was corrected for this missed top-feeding by comparing the intensities of the γ rays placed in the low energy part of the level scheme with the direct ground

المنارة للاستشارات

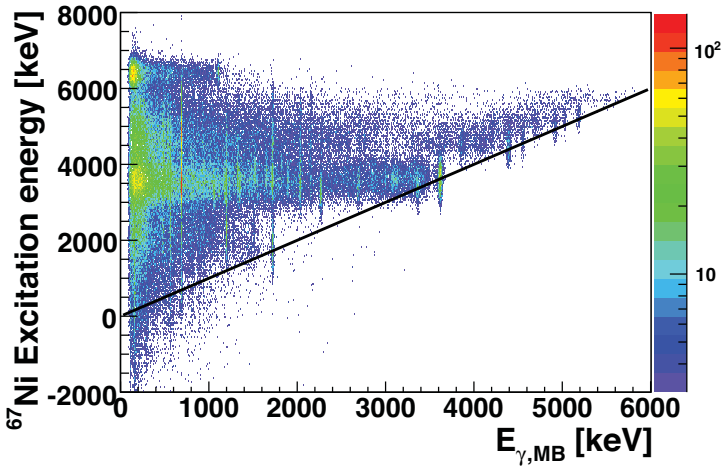

Figure 5.6: (Color online) Doppler corrected energy of γ rays with respect to the original excitation energy of ^{67}Ni, deduced from proton kinematics. Events on the solid line correspond to direct ground state γ transitions after the transfer reaction.

state decay. From this analysis the total amount of missed γ-ray intensity was found to be 50% of the total intensity.

In Fig. 5.6 a strong signal above 6 MeV excitation energy can be seen, mostly random coincidences with low energy γ rays and 1039 keV (^{66}Cu β decay). This 6.4 MeV excitation energy signature corresponds to elastically scattered protons (impurities in the target), which are in random coincidence with background radiation. This strong signature is also visible in Fig. 5.9 at 6.4 MeV excitation energy.

Normalization

In order to normalize the obtained angular distributions and obtain absolute cross sections, the beam intensity must be known. Here we used elastically scattered deuterons to determine the beam intensity by scaling the differential elastic cross section to the experimental data as $N = It\frac{\mathrm{d}\sigma}{\mathrm{d}\Omega}\Delta\Omega\frac{\rho d}{A}N_A P_d \epsilon_D$, with I the average beam intensity, t the measuring time, $\frac{\mathrm{d}\sigma}{\mathrm{d}\Omega}$ the differential cross section, $\frac{\rho d}{A}N_A$ the number of target nuclei, P_d the target purity and ϵ_D the efficiency for detecting deuterons, including losses in the particle identification.

المنارة للاستشارات

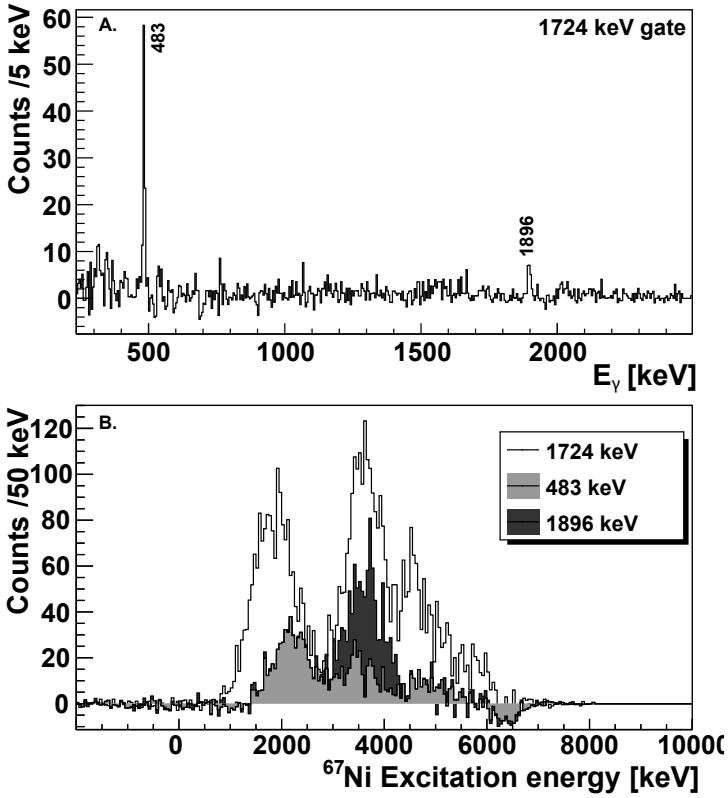

Figure 5.7: A. Proton-γ-γ coincidences for the 1724 keV transition. The strongest coincidences at 483 keV and 1896 keV are clearly visible. B. Corresponding incoming excitation energies in ^{67}Ni deduced from coincident proton kinematics for 1724 keV and coincident γ rays, efficiency corrected. See text for more information.

المنارة للاستشارات

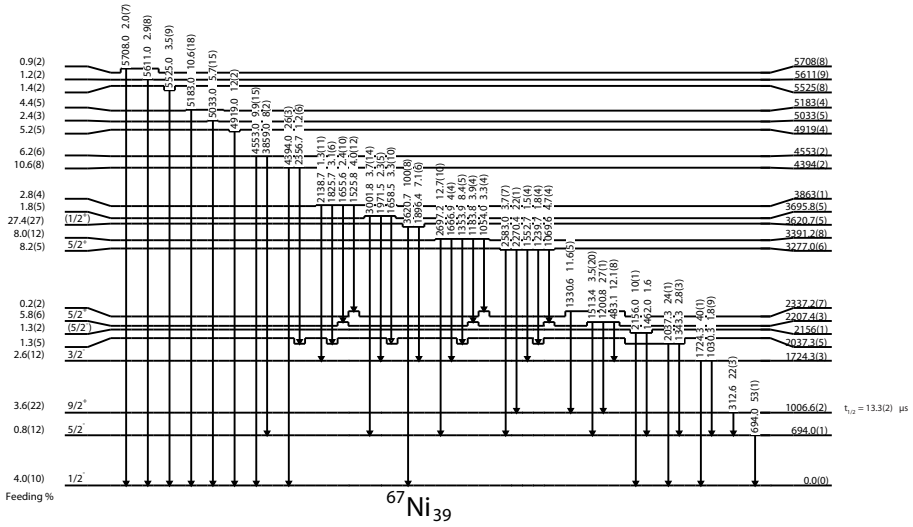

Figure 5.8: Level scheme constructed from the available (d,p)-data. Gamma and level energies are given in keV. Gamma-ray intensities relative to the 3621 keV transition.

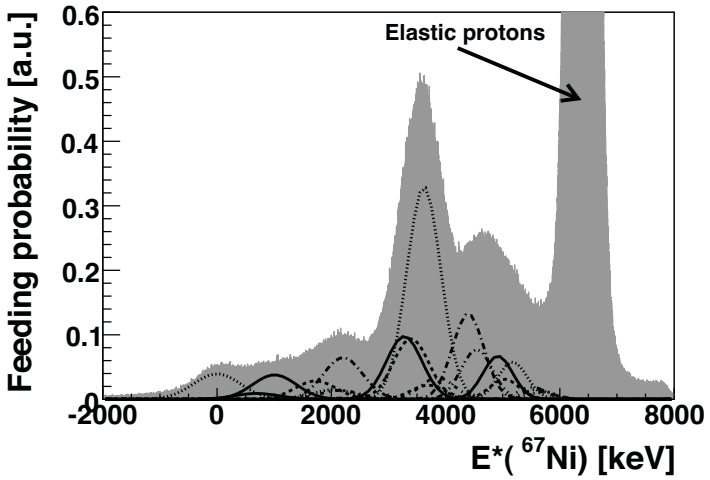

Figure 5.9: Experimental excitation spectrum deduced from proton kinematics in singles (gray area) compared with a reconstructed feeding probability based on the proposed level scheme and γ-ray intensities (black line). Individual contributions have been drawn for completeness.

المنارة للاستشارات

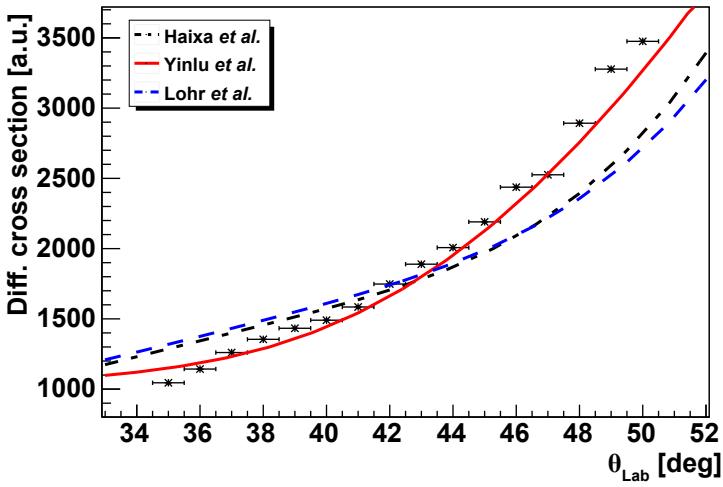

Figure 5.10: (Color online) Angular distribution of elastically scattered deuterons. The DWBA calculations using optical potential paramaters from Refs. [60,61,62] are shown as the three lines.

This last angle-dependent parameter is obtained from GEANT4 simulations [58]. All these quantities except the average beam intensity are known. As the detection range for deuterons was limited from 35° to 50°, it was not possible to fit the optical potentials to the data and hence Global Optical Model Potentials (GOMPs) have been used. Fig. 5.10 shows the comparison of three differential cross section calculated with the program FRESCO [59] using different GOMPs available from literature [60,61,62], with the GOMP from Ref. [62] giving the best agreement due to the larger Coulomb radius. The most important optical model potential parameters used are summarized in Table 5.2. A total beam intensity of 4.1(3) 10^6 pps was found using this analysis.

By normalizing the transfer data to the elastic scattering of deuterons, uncertainties in physical properties of the target can be neglected as both data sets are obtained under the same conditions and do not depend on the properties of the target.

DWBA analysis

The transfer reaction angular distributions were calculated using the DWBA code FRESCO [59], with potentials for the incoming channel from Ref. [62]. As

المنارة للاستشارات

Table 5.2: Overview of the optical model parameters used in the DWBA analysis taken from GOMP's in Refs. [62] (incoming channel) and [63] (outgoing channel).

Channel	V [MeV]	r [fm]	a [fm]	W [MeV]	r_w [fm]	a_w [fm]	W_d [MeV]	r_d [fm]	a_d [fm]	r_c [fm]
$d + {}^{66}$Ni	83.4	1.17	0.81	0.7	1.33	0.47	13.9	1.563	0.7	1.35
	V [MeV]	r [fm]	a [fm]	W_d [MeV]	r_d [fm]	a_d [fm]	V_{so} [MeV]	r_{so} [fm]	a_{so} [fm]	r_c [fm]
$p + {}^{67}$Ni	56.7	1.20	0.67	8.33	1.28	0.48	5.72	1.03	0.59	1.25

the range of identified elastically scattered protons is insufficient to fit the optical model potentials to the data, four sets of GOMPs available from literature can be used to describe the outgoing channel [63-66]. The main difference between these sets is that the former two GOMPs include a real volume part, while the latter two don't. In this analysis the GOMPs from Ref. [63] were used, however the shape of the angular distributions does not vary significantly between the different sets of potentials, while variations in the magnitude of the differential cross section are limited to 10%. An overview of the optical model potential parameters used can be found in Table 5.2. In order to calculate the wave functions of the neutron bound in ^{67}Ni, a Woods-Saxon potential was used with the standard parameters $r = 1.25$ fm and $a = 0.65$ fm. The depth of this potential is scaled in order to reproduce the correct binding energy.

The low center of mass energy of the reaction (5.67 MeV) justifies the use of DWBA over ADWA as the influence of deuteron breakup is negligible at this CM energy [67]. The influence of nonlocality in the reaction as discussed in Ref. [68] was assessed and limited influence on the calculated differential cross sections was found. The variations in the extracted relative spectroscopic factors due to this nonlocality were found to be of the order of 10% at most and do not change the results within the quoted error bars.

As the absolute scaling factors between the calculated cross sections and the experimental data at energies near the Coulomb barrier depend both on the optical model potentials and geometry of the single-particle binding potentials, absolute spectroscopic factors cannot be quoted reliably [69]. Therefore only relative spectroscopic factors (with respect to the 1007 keV isomer originating from the $\nu g_{9/2}$-orbital) and ANCs will be reported here. Calculations for all populated states were performed assuming pure configurations (spectroscopic factor = 1) ranging between $s_{1/2}$ and $g_{9/2}$.

From the experimental data angular distributions were obtained by requiring double gates on excitation energy (proton kinematics) and coincident γ-ray energy, similar to the analysis in Ref. [48]. The width of excitation energy was set to 600 keV in order to reduce possible distortion due to γ feeding from

المنارة للاستشارات

higher lying levels. By using this width only 70% of all events is included as the FWHM of these peaks in the excitation energy spectra is about 700 keV. In case of a small separation between excited states, connected by an intense γ-ray transition (e.g. 1724 and 2207 keV, connected by the 483 keV transition), the contribution of the 2207 keV state was explicitly subtracted by combining spectra from different gates. Angular distributions are obtained in the laboratory frame-of-reference in 5° bins, all individually efficiency corrected, with coefficients obtained from GEANT4 simulations [42,57]. Depending on the γ-decay pattern, multiple γ gates could be used to obtain an angular distribution for a specific state. In this case, the angular distributions were created for all these possible gates, including individual corrections for γ-detection efficiency, before creating the global angular distribution from the weighted average. If applicable delayed coincidence data were included for states decaying via the isomeric state at 1007 keV. Only for the ground state a single gate on excitation energy was used due to the lack of (delayed) coincident γ rays.

[1] O. Sorlin et al., Phys. Rev. Lett. 88, 092501 (2002).
[2] N. Bree et al., Phys. Rev. C 78, 047301 (2008).
[3] R. Broda et al., Phys. Rev. Lett. 74, 868 (1995).
[4] O. Perru et al., Phys. Rev. Lett. 96, 232501 (2006).
[5] M. Hannawald et al., Phys. Rev. Lett. 82, 1391 (1999).
[6] J. M. Daugas et al., Phys. Rev. C 83, 054312 (2011).
[7] O. Sorlin et al., Eur. Phys. J. A 16, 55 (2003).
[8] M. Sawicka et al., Eur. Phys. J. A 16, 51 (2003).
[9] J. Ljungvall et al., Phys. Rev. C 81, 061301 (2010).
[10] W. Rother et al., Phys. Rev. Lett. 106, 022502 (2011).
[11] C. Fransen et al., J. Phys.: Conf. Ser. 312 (2011).
[12] J. Van de Walle et al., Euro. Phys. J. A 42, 401 (2009).
[13] T. Baugher et al., Phys. Rev. C 86, 011305 (2012).
[14] A. Gade et al., Phys. Rev. C 81, 051304 (2010).
[15] N. Hotteling, Phys. Rev. C 82, 044305 (2010).
[16] S. Lunardi et al., Phys. Rev. C 76, 034303 (2007).
[17] T. Otsuka, T. Suzuki, R. Fujimoto, H. Grawe, and Y. Akaishi, Phys. Rev. Lett. 95, 232502 (2005).
[18] A. P. Zuker, J. Retamosa, A. Poves, and E. Caurier, Phys. Rev. C 52, R1741 (1995).
[19] S. M. Lenzi, F. Nowacki, A. Poves, and K. Sieja, Phys. Rev. C 82, 054301 (2010).
[20] E. Caurier, F. Nowacki, and A. Poves, Eur. Phys. J. A 15, 145 (2002).
[21] A. Poves, E. Caurier, F. Nowacki, and K. Sieja, Phys. Scr. 2012, 014030

المنارة للاستشارات

(2012).
[22] T. Otsuka, T. Suzuki, J. D. Holt, A. Schwenk, and Y. Akaishi, Phys. Rev. Lett. 105, 032501 (2010).
[23] K. Sieja and F. Nowacki, Phys. Rev. C 85, 051301 (2012).
[24] J. Duflo and A. P. Zuker, Phys. Rev. C 59, R2347 (1999).
[25] R. Grzywacz et al., Phys. Rev. Lett. 81, 766 (1998).
[26] S. Rahaman et al., Eur. Phys. J. A 34, 5 (2007).
[27] R. Ferrer et al., Phys. Rev. C 81, 044318 (2010).
[28] L. Weissman et al., Phys. Rev. C 59, 2004 (1999).
[29] R. T. Kouzes, D. Mueller, and C. Yu, Phys. Rev. C 18, 1587 (1978).
[30] M. Girod, P. Dessagne, M. Bernas, M. Langevin, F. Pougheon, and P. Roussel, Phys. Rev. C 37, 2600 (1988).
[31] T. Pawlat et al., Nucl. Phys. A 574, 623 (1994).
[32] S. Zhu et al., Phys. Rev. C 85, 034336 (2012).
[33] J. Rikovska et al., Phys. Rev. Lett. 85, 1392 (2000).
[34] G. Georgiev et al., J. Phys. G: Nucl. Part. Phys. 28, 2993 (2002).
[35] J. Diriken et al., (2012), submitted to Phys. Rev. Lett.
[36] N. R. Johnson, R. K. Sheline, and R. Wolfgang, Phys. Rev. 102, 831 (1956).
[37] V. Fedoseyev et al., Hyperfine Interact. 127, 409 (2000).
[38] A. Jokinen et al., Nucl. Instrum. Meth. B 126, 95 (1997).
[39] F. Ames, G. Bollen, P. Delahaye, F. O., G. Huber, O. Kester, K. Reisinger, and P. Schmidt, Nucl. Instrum. Meth. A 538, 17 (2005).
[40] R. Rao, O. Kester, T. Sieber, D. Habs, and K. Rudolph, Nucl. Instrum. Meth. A 427, 170 (1999).
[41] T. Sieber, Nucl. Instrum. Meth. A 701, 656 (2002).
[42] V. Bildstein et al., Eur. Phys. J. A 48, 85 (2012).
[43] N. Warr et al., (2013), to be published.
[44] J. Eberth et al., in AIP. Conf. Proc., Vol. 656 (2003) pp. 349-356.
[45] E. J. Sternglass, Phys. Rev. 108, 1 (1957).
[46] D. J. Millener, D. E. Alburger, E. K. Warburton, and D. H. Wilkinson, Phys. Rev. C 26, 1167 (1982).
[47] M. Seeger, T. Kihm, K. Knöpfle, U. Schmidt-Rohr, J. Hebenstreit, D. Paul, and P. V. Rossen, Nucl. Phys. A 533, 1 (1991).
[48] M. Seeger et al., Nucl. Phys. A 539, 223 (1992).
[49] H. Miyahara, K. Hara, C. Mori, Y. Kasugai, and K. Kawade, Nucl. Inst. Meth. A 324, 219 (1993).
[50] M. Chowdhury and H. S. Gupta, Nucl. Phys. A 205, 454 (1973).
[51] R. Fulmer et al., Phys. Rev. 133, B955 (1964).
[52] E. Wesolowski et al., J. Phys. G Nucl. Partic. 17, 955 (1991).
[53] E. Cosman et al., Phys. Rev. 163, 1134 (1967).
[54] R. H. Fulmer and A. L. McCarthy, Phys. Rev. 131, 2133 (1963).

المنارة للاستشارات

[55] T. Anfinsen et al., Nucl. Phys. A 157, 561 (1970).
[56] G. Huttlin et al., Nucl. Phys. A 227, 389 (1974).
[57] I. Turkiewicz et al., Nucl. Phys. A 143, 641 (1970).
[58] S. Agostinelli et al., Nucl. Instr. Meth. A 506, 250 (2003).
[59] I. J. Thompson, Comput. Phys. Rep. 7, 167 (1988).
[60] J. Lohr and W. Haeberli, Nucl. Phys. A 232, 381 (1974).
[61] Haixia An and Chonghai Cai, Phys. Rev. C 73, 054605 (2006).
[62] Y. Han, Y. Shi, and Q. Shen, Phys. Rev. C 74, 044615 (2006).
[63] A. Koning and J. Delaroche, Nucl. Phys. A 713, 231 (2003).
[64] F. G. Perey, Phys. Rev. 131, 745 (1963).
[65] B. Morillon and P. Romain, Phys. Rev. C 76, 044601 (2007).
[66] Xiaohua li and Chonghai Cai, Nucl. Phys. A 801, 43 (2008).
[67] N. B. Nguyen, F. M. Nunes, and R. C. Johnson, Phys. Rev. C 82, 014611 (2010).
[68] N. K. Timofeyuk and R. C. Johnson, Phys. Rev. Lett. 110, 112501 (2013).
[69] A. M. Mukhamedzhanov and F. M. Nunes, Phys. Rev. C 72, 017602 (2005).

المنارة للاستشارات

6

Analysis

The main line followed in the analysis of the data is discussed on pp. 132-140 of Chapter 5, as part of the paper submitted for publication in *Physical Review C*. In this chapter a more elaborate discussion of the analysis will be presented, mainly focusing on the determination of the level scheme (Figure 5.8 on p. 137) and feeding probability curve (Figure 4.3 on p. 112). Extraction of the angular distributions and a description of the input files for the DWBA code FRESCO will also be given.

6.1 Level scheme

Figure 1.11 (p. 24) shows the initial knowledge of the level scheme of ^{67}Ni, including three observed γ rays of 313, 694 and 2155 keV [Wei99]. When comparing the known information from Figure 1.11 with the Doppler corrected γ-ray spectrum from the (d,p) experiment in Figure 6.1, the richness of the obtained data becomes clear because numerous transitions can be identified. Transitions up to an energy of 5800 keV were observed, an energy that corresponds with the neutron separation energy in ^{67}Ni. This is an indication that a wide variety of different excited states were populated in the transfer reaction.

By taking advantage of the event-by-event structure of the data, specific coincidence spectra could be created. Some of the most convenient spectra are for instance

المنارة للاستشارات

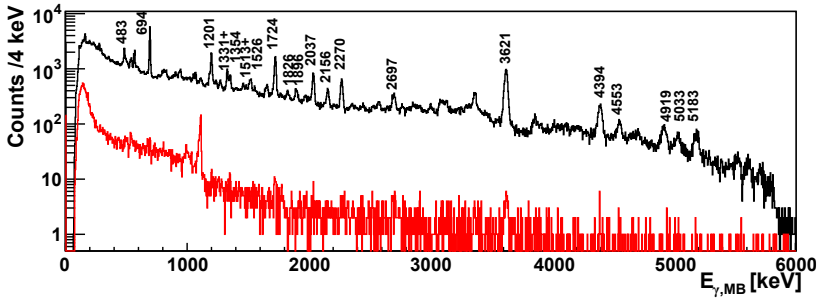

Figure 6.1: Doppler corrected γ-ray spectrum, proton gated, prompt (black) and random (gray).

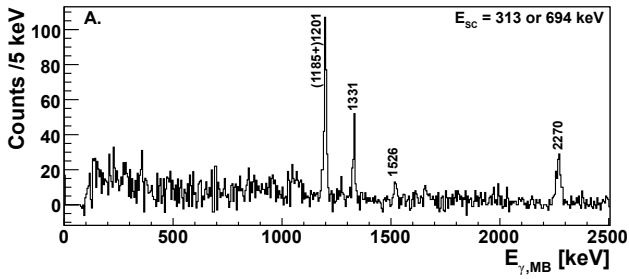

Figure 6.2: Doppler corrected γ-ray spectrum, proton gated and Delayed coincident with either the 313 of 694 keV transition. Random subtracted.

- γ-γ **coincidences** in Miniball. By plotting γ's observed in prompt coincidence with a predefined gate (γ_{gate}) in Miniball, information on the γ-decay scheme can be deduced. An additional prompt proton-γ_{gate} coincidence can be imposed to purify the spectra.
- The **delayed coincidence** spectrum in the γ detector at the delayed coincidence chamber when a specific γ_{gate} is observed in Miniball (in prompt coincidence with a proton observed in T-REX). In this way transitions that feed the isomer can be identified.
- Based on the kinematics of a proton in prompt coincidence with a γ_{gate} the **excitation energy of ^{67}Ni** after the transfer reaction can be deduced (see Figure 2.1). In this way the order of certain transitions can be deduced (an example will be given below). In the discussion below this kind of spectrum will be referred to as *coincident excitation energy spectrum*. Also the inverse conditions can be applied: by plotting all γ rays that are in prompt coincidence with a proton corresponding to a given initial

المنارة للاستشارات

excitation energy of ^{67}Ni, the γ rays (and γ cascades) originating from that region of the excitation scheme can be identified.

Not all coincidences will be discussed here, except for a few peculiarities and instructional examples.

By starting from the known level structure of ^{67}Ni, additional new states can be identified by identifying prompt γ-γ-coincidences with the 694 keV line or searching for prompt proton-γ-coincidences that also have a DCT with 313 and 694 keV. The latter transitions can be identified from Figure 6.2, showing prompt γ transitions in Miniball that are also DCT with 313 or 694 keV. The transitions of 1201 and 2270 keV define two new excited states at 2207 and 3277 keV. The 1201 keV transition is labeled (1185+)1201 keV because the 1185 and 1201 keV transitions can not be completely disentangled and specific gating shows a mutual coincidence. The order of these γ rays can be deduced from the ^{67}Ni excitation energy spectrum (see pp. 201 and 202). From the 1185 keV DCT spectrum (p. 201) the amount of delayed coincident events is very limited and hence the influence of this transition in Figure 6.2 should be minimal. The existence of these levels at 2207 and 3277 keV can be proven from the ^{67}Ni excitation energy spectrum coincident with these transitions because they show a first peak around the energies mentioned (see pp. 202 and 218). The two other transitions (1330 and 1526 keV) labeled in Figure 6.2 are also mutual coincident (see pp. 205 and 209), with the 1330 keV coming directly on top of the 1007 keV isomer based on intensity balances and other coincidences.

Intense ground-state transitions can be identified by examining the coincident excitation-energy spectra for prompt transition observed in Miniball. When the (first) peak in this spectrum equals the γ-ray energy, then this transition has to be a ground state transition. Examples of such transitions include 694, 1724, 3620 keV (see pp. 199, 212 and 220) and most of the high-energy transitions. The information from proton-γ_{MB} coincidences in Miniball is combined in Figure 6.3, which can be used as a first guide to identify excited states and place γ rays. Here events on the diagonal line represent events in which ^{67}Ni is populated in an excited state and subsequently decays directly to the ground state. This strategy has also been used in the past, even for one-nucleon transfer reactions in direct kinematics using stable nuclei, when individual excited states could not be resolved. An example can be found in the ^{64}Zn(d,^{3}He)- and ^{64}Ni(d,^{3}He)-reaction work of Refs. [See91, See92] where the energy resolution of the particles was 170 keV.

The coincident excitation-energy spectra are very useful to determine the order of γ rays in the level scheme. Consider e.g. the γ_{gate} of 1724 keV (p. 212), prompt coincident with 483 and 1896 keV. Figure 5.7.B (p. 136) shows the different coincident excitation energies. From this it can be concluded that

المنارة للاستشارات

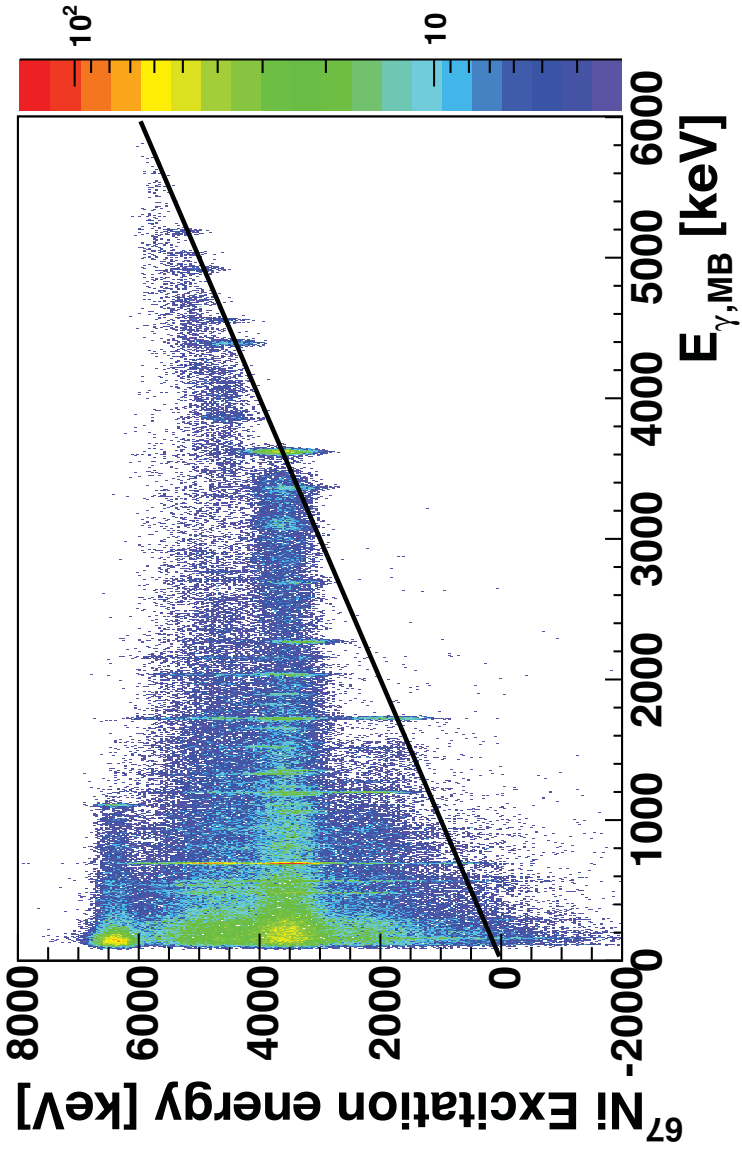

Figure 6.3: Excitation energy in ^{67}Ni with respect to coincident γ-ray energies. Events on the line depict direct ground state decays after population of that specific state.

المنارة للاستشارات

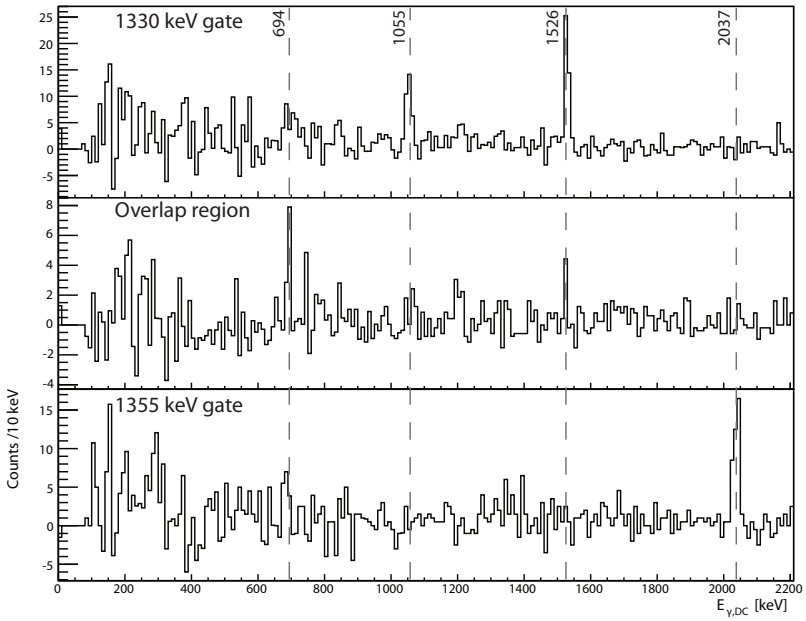

Figure 6.4: Detailed scan of the proton-γ-γ-coincidences for the 1330-1355 keV doublet and overlap region. Prompt minus random, background subtracted. The evolution of the prominent peaks can be tracked throughout the triplet. As the applied energy gates do not have equal widths absolute γ-ray intensities cannot be directly compared. The strong signal of the 694 keV transition (which is absent in the top and bottom panel) supports the existence of the 1343-keV transition.

the 1724 keV line is a ground-state transition, while the two other transitions come right on top of this state, defining levels at 2207 and 3621 keV. As can be seen from Figure 5.7.B, more top-feeding transitions are expected since these most intense transitions do not account for the full top feeding of the 1724 keV state and especially the region above 4 MeV is poorly explained. Other weaker coincidences with 1553, 1661 and 2139 keV leading to additional top-feeding have been identified. These transitions are not the main branches in the γ-decay of the states they de-excite, but the weak peaks in the proton-γ-γ-spectrum at the corresponding energy differences justify their position in the level scheme.

A special note has to be made concerning the apparent doublet at 1330-1355 keV. A careful scan of the proton-γ-γ-coincidences in this region is shown in Figure 6.4. The top panel includes most of the 1330 keV peak as γ_{gate} and the bottom one shows coincidences for the 1355 keV transition. The spectrum in

المنارة للاستشارات

the middle is gated on the overlapping region of the two peaks. The difference between gates on 1330 and 1355 keV is clear, but the evolution of the 694 keV transition shows that this doublet is actually a triplet as the relative intensity of the 694 keV transition peaks in the middle spectrum. A second argument originates from the fact that the 1330 keV has DCT-events and is logically placed directly on top of the isomer. As a consequence a prompt 694-1330 keV coincidence is not possible.

The coincidence spectra for the 1513-1526 keV doublet also show some of these problems (see pp. 208 and 209). The left part of the doublet (1513 keV) contains a strong 694 keV transition, while traces of DCT can be found for the 1526 keV member of the doublet. Besides this it also has a strong coincidence with 1330 keV, which is placed directly on top of the isomer. However, still a considerable amount of 694 keV coincidences can be observed. Since no trace can be found from the 1643 keV (2337-694 keV) γ ray which is necessary to see this coincidence, the observed 694 keV intensity is most likely due to 1513 keV γs within the 1526 kev γ-gate window. Furthermore the coincidence excitation energy spectrum shows traces of events originating from the ≈ 2 MeV region, which is consistent with the similar spectrum for 1330 keV.

Based on the observed proton-γ-γ-coincidences, observation of DCT-events and ^{67}Ni excitation energy spectrum corresponding to observed γ_{gate}'s, the level scheme is expanded. All observed coincidences and DCT-transitions are tabulated in Table 6.1 and the updated version of the level scheme is shown in Figure 5.8.

6.2 Delayed coincidence analysis

Figure 6.5 illustrates the selectivity of the Delayed coincidence technique and displays the increasing peak-to-background ratio of the delayed transitions when more stringent conditions are imposed. The top panel (A) shows the unrestricted, particle and proton coincident DCT spectra, already indicating an increasing peak-to-background ratio for the delayed transitions, while for other transitions (mostly from β decay) this ratio remains constant. When isolating the delayed and random-delayed parts of proton coincident DCT spectrum (see Figure 6.6 for time window definitions), both spectra in Figure 6.5.B are identical except for the pronounced 313 and 694 keV intensities in the delayed spectrum. When subtracting both spectra in Figure 6.5.B, only the pure delayed transitions remain (see Figure 6.5.C). The signal at 1039 keV in Figure 6.5.C is an artifact due to the subtraction of the dominant peak from the ^{66}Cu β decay. The intensity of the 313-694 keV sum peak at 1007 keV has a large

المنارة للاستشارات

E_γ	Counts	Error	Rel. int.	Error	Coincident γ's [keV]	DCT
483	4087	154	16.6	1.0	1070, 1185, 1526, 1724	N
694	11312	151	54.0	0.9	1343, 1461, 1512, 2696, (2926), 3000	N
1030						N
1055	450	74	2.6	0.4	1330	(N)
1070	641	76	3.7	0.4		N
1185	728	70	4.4	0.4	483, 1199, (1724)	(N)
1201	4576	109	27.9	0.7	1185, 1656	Y
1240	358	78	2.2	0.5	694, (1343), 2035	N
1275	670	77	4.2	0.5	-	N
1330*	1823	83	11.8	0.5	1525	Y
1343*	378	49	2.5	0.3	694, 1826	N
1353*	1197	75	7.8	0.5	2037	N
1460						
1513					694, 1185	Y
1526					(694), 1330	Y
1553	175	52	1.2	0.4	1724	N
1650	932	84	6.9	0.6	483, 1201, 1724, 2037	(N)
1724	5567	112	42.6	1.1	483, 1553, 1667, 1896, 1972, 2139	N
1826	555	73	4.4	0.6	2037	N
1896	923	77	7.6	0.7	1724	N
1972	267	62	2.3	0.5	1724	N
2037	2708	86	23.6	0.9	(1240), 1353, (1650), 1826	N
2156	1135	81	10.4	0.8		N
2270	2258	81	21.5	1.0		Y
2356	194	61	1.9	0.6		N
2583	440	69	4.7	0.8	694	N
2697	1153	79	13.0	1.0		N
3362	1077	73	15.3	1.5		N
3620	6442	98	100.0	8.3		N
3859	684	70	11.6	1.6		N
4392	1492	66	29.7	3.5		N
4553	573	53	12.0	1.8		N
4919	562	49	13.1	2.0		N
5033	275	40	6.7	1.3		N
5183	427	40	10.8	1.8		N
5525	127	25	3.5	0.9		N
5611	120	21	3.4	0.9		N
5708	46	20	1.4	0.6		N

Table 6.1: Overview of the γ-rays observed in Figure 6.1, intensities (absolute and relative to the 3620 keV transition) and coincident γ-rays. * indicates doublets and triplets, see text for more information.

المنارة للاستشارات

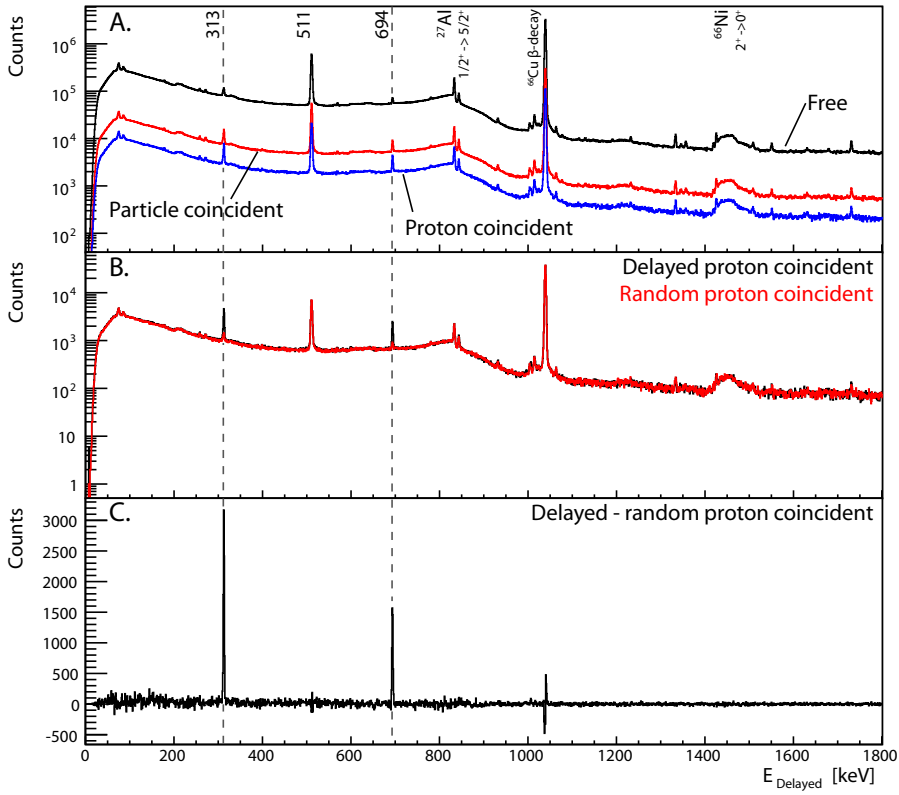

Figure 6.5: Delayed coincidence spectra. A. Unrestricted DCT spectrum (black), particle coincident (red) and proton coincident (blue), timing condition: $\Delta T = [-40, 80]$ μs. B. Delayed proton coincident (black), random proton coincident (red), time normalized (40μs windows). C. Delayed minus random spectrum. The signal at 1039 keV (^{67}Cu β decay) in C. is an artifact due to subtraction of this high-intensity decay line.

uncertainty due to the proximity of two background transitions with energies of 1003 and 1013 keV. The extracted values are tabulated in Table 6.2. Using the sum peak technique [Kim03] to determine the absolute photo peak efficiency of the DCT detector, values similar to the ones mentioned in Section 3.2.4 were found: $\epsilon_{313\text{ keV}} = 7(1)\%$ and $\epsilon_{694\text{ keV}} = 3.7(6)\%$. Also from Figure 6.5 it is clear that besides the 313 and 694 keV delayed transitions no other (μs-)isomers are identified in ^{67}Ni.

In Figure 6.5 two peculiar transitions are observed: a broad structure around

المنارة للاستشارات

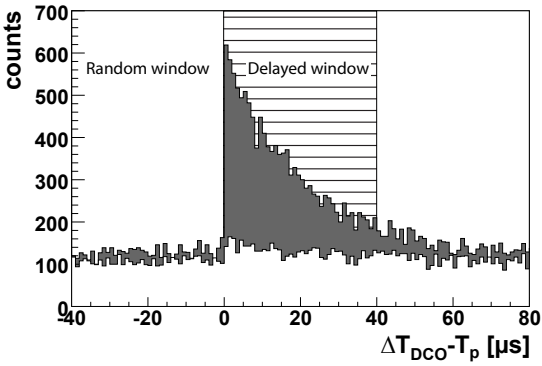

Figure 6.6: Time structure of DCT events. Proton and 313 keV DCT gated. Gray area is time structure for 313 keV peak, white area is the sum of left and right background.

E_γ [keV]	Integral
313	8600 (100)
694	4790 (70)
1007	320 (50)

Table 6.2: Intensities in the delayed transitions (and sum peak) obtained from spectrum Figure 6.5.C.

1445 keV and a sharp transition at 844 keV. These transitions originate from Coulomb excitation of the incoming ^{66}Ni beam scattering on ^{27}Al in the stopper foil. The half-life of the 844 keV $1/2^+ \rightarrow 5/2^+$ transition in ^{27}Al is 35 ps [NND13], while the half-life of the 1425 keV $2^+ \rightarrow 0^+$ transition in ^{66}Ni measures 0.8 ps [Sor02]. The faster $2^+ \rightarrow 0^+$ transition in ^{66}Ni causes the 1425 keV γ ray to be emitted while decelerating in the aluminum foil. Hence the observed γ-ray energy is Doppler shifted to higher energies. Because of its longer half-life, the 844 keV $1/2^+ \rightarrow 5/2^+$ transition in ^{27}Al is slower and is on average emitted when ^{27}Al is already stopped, resulting in a sharp peak in the γ-ray spectrum.

6.3 Feeding pattern

Based on proton kinematics observed in singles (not requiring any γ coincidence) it is possible to reproduce the experimental feeding probability curve. This experimental curve is shown both in Figs. 6.7 and 6.8 as the gray area. The

المنارة للاستشارات

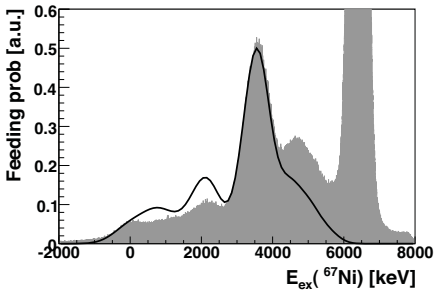

Figure 6.7: Experimental ^{67}Ni feeding probability based on proton kinematics in singles (gray area) and curve based on extended ^{67}Ni level scheme and γ-ray intensities.

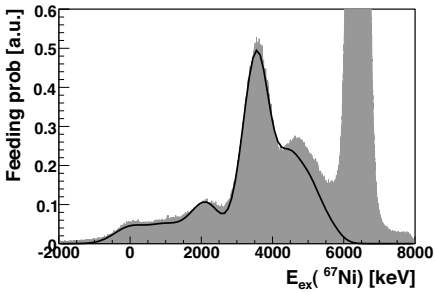

Figure 6.8: Experimental ^{67}Ni feeding probability based on proton kinematics in singles (gray area) and curve based on extended ^{67}Ni level scheme and γ-ray intensities, corrected for high energy top-feeding. See text for additional comments.

reconstructed feeding probability of a specific state was calculated by summing all decaying γ-intensities from a given state and subtracting all top-feeding transitions based on the improved level scheme (Figure 5.8) and measured γ-ray intensities (Table 6.1). The feeding probabilities of all excited states are subsequently folded with a Gaussian function (FWHM of 800 keV[1]) and summed. The line drawn in Figure 6.7 is the superposition of all these gaussians. The integral of the experimental feeding probability has been normalized to the integral of the reconstructed curve (black line) up to an excitation energy of 5400 keV to exclude the influence of the peak due to elastically scattered protons which appears between 6000 and 7000 keV. Despite the fact that the 3.5 MeV region was accurately reproduced, the feeding at low excitation energies was clearly overestimated, while a substantial amount of feeding in the 4+ MeV region was unaccounted for.

When looking specifically to γ rays originating from this high excitation energy region, two sets of γ rays are observed: high energy γ rays, often direct ground state transitions, but also known transitions in the lower part of the level scheme e.g. 694, 1724, 1200 and 2037 keV (see Figure 6.9). However, no new γ rays connecting these highly excited states with the known structure up to 3.6 MeV

[1]This value was based on the coincident excitation energy spectrum of the 3621 keV transition shown on p. 220. Based on GEANT4 simulations an energy dependence of the FWHM was introduced which increased for smaller excitation energies to a value of 1060 keV for the ground state. The source of this energy dependence is the dependence of the proton kinematics on the excitation energy (see Figure 2.1)

المنارة للاستشارات

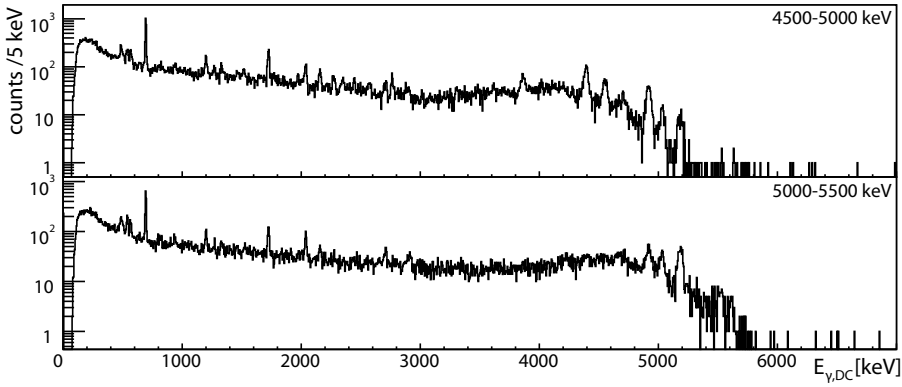

Figure 6.9: γ-ray spectrum, Doppler corrected, for ^{67}Ni excitation energy cuts of 4500-5000 keV (top) and 5000-5500 keV (bottom). See text for discussion.

are observed. Also (proton-)γ-γ-coincidences with an additional restriction on the incoming excitation energy do not reveal the missing transitions. This effect is caused by a combination of two factors:

- The high density of levels at this excitation energy. This is consistent with reaction work on lighter nickel isotopes described in Refs. [Cho73, Ful64, Wes91, Cos67, Ful63, Anf70, Hut74, Tur70] and will be discussed in more detail in the next chapter. It is expected that sdg-single-particle strength will be fragmented in small portions over a large number of states at these excitation energies, leading to small integrals of the characteristic γ-decay transitions.
- Numerous decay paths are in principle possible for these highly excited states, depending on their spin.

The combination of these two factors might lead to the fact that these connecting transitions can not be resolved from the background. This is also evident when scanning through the coincident ^{67}Ni excitation energy spectra for all known transitions in the level scheme (these spectra can be found in Appendix A). For the known, intense transitions at low excitation energy (e.g. 694, 1724, ... keV) it can be seen that a substantial amount of this intensity originates from highly excited states in ^{67}Ni. No strong transitions could be identified in this way that originate purely from these highly excited states.

The reconstructed excitation curve in Figure 6.8 is corrected for this *missed γ-ray intensity* by comparing the intensity observed in the known transitions at

المنارة للاستشارات

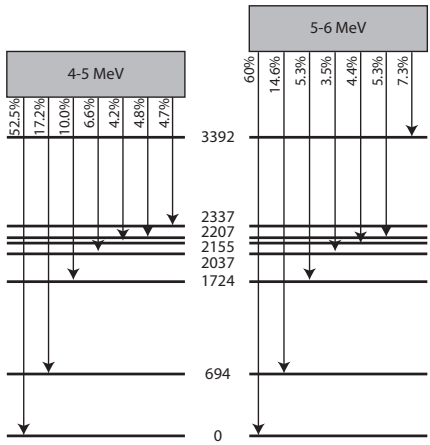

Figure 6.10: Top-feeding correction factors used to correct for the missed intensity from the 4-6 MeV energy region. The percentage quoted for the ground state transition equals the intensity observed in the high-energy γ transitions. For the other states the percentages indicate the fraction of unobserved top feeding for that level. See text for additional information.

low excitation energy (up to 2 MeV), with the intensity of the highly-energetic γ rays. After efficiency correction the deduced effect of the missed top feeding is shown in Figure 6.10. This indicates that for the 4-5 MeV energy region 52.5% of the total γ-decay is contained in the observed ground state transitions. For the 5-6 MeV excitation energy region this number is 60%. Hence, the feeding probabilities from the level scheme and γ-ray intensities are corrected by adding missed top-feeding based on the numbers presented in Figure 6.10. In this analysis the γ-decay branching ratios of the excited states below 3 MeV were also used to correct for possible γ cascades between these excited states.

By including these corrections some of the reconstructed feeding below 4 MeV excitation energy is shifted towards this energy region. This corrected curve is shown in Figure 6.8, using the same normalization procedure as before. The overall agreement between the experimental excitation spectrum in singles and the reconstructed curve is good. This supports the proposed level scheme and underlines the reliability of using proton-γ-coincidences in this analysis. This procedure of using γ-ray intensities and their position in the level scheme can be applied to all observed levels except the ground state. The following procedure allows the direct ground-state feeding to be included and determined from the comparison between the reconstructed curve and experimental feeding probability:

1. The experimental feeding probability is normalized to the reconstructed curve.

2. A gaussian at 0 MeV (the ground state, with fixed width) is added to the reconstructed curve and its contribution is fitted to the experimental

المنارة للاستشارات

data.

3. Again the experimental curve is normalized to the reconstructed curve, now including the ground-state contribution.

4. The ground-state contribution is again fitted for a second time to the experimental feeding probability.

5. This iterative process converges and a 4% feeding probability to the ground state is found.

6.4 Angular distributions

6.4.1 Extraction from experimental data

It is evident from Figure 6.8 that a single gate on the proton kinematics is insufficient to isolate one excited state and extract an angular distribution of the detected protons. With the knowledge of the improved level scheme, double gates can be imposed on proton-γ-events in order to obtain the angular distributions. The procedure followed is:

1. **Create a set of double gates**: all possible combinations of excitation energy and corresponding γ-gates are listed. For excitation energy gating this is the centroid and width, while for the γ gate six parameters define the borders of the peak window; and left and right background windows. Special flags are set for DCT gating and each set is assigned to a level.

2. **Event loop**: a loop is performed over all events checking first whether a proton was present within the event. Secondly, the agreement with all excitation energy gates is verified and if a match is found, then the γ gate is checked by looping over all coincident γ rays. For each set of gates six histograms are stored and depending on the type of γ coincidence (peak, left or right background; and prompt or random coincidence) the corresponding histogram is filled. These histograms count the number of protons observed within each θ_{LAB}-bin.
   For DCT-gating the procedure is similar and separate histograms are kept for DCT with 313 and 694 keV.

3. **Combine histograms** by rescaling the random windows to match the width of the prompt windows and subtract left and right background from the peak. A separate histogram is saved to calculate the uncertainties.

المنارة للاستشارات

4. **Conversion to differential cross section** by dividing by the $\Delta\Omega$ ($\propto \sin\theta_{\mathrm{LAB}}$) factor.

5. **Normalization** by dividing in each angular bin the value with the factor $ItN_t\epsilon_P(\theta)\epsilon_\gamma(E_{\gamma_{\mathrm{gate}}})P_{\mathrm{target}}I_\gamma$, with It the total amount of incident ^{66}Ni particles, N_t the number of target nuclei, $\epsilon_P(\theta)$ the proton detection efficiency for the state of interest obtained from GEANT4 simulations, $\epsilon_\gamma(E_{\gamma_{\mathrm{gate}}})$ the γ photo-peak detection efficiency, P_{target} the target purity and I_γ the branching ratio of the γ_{gate}. In order to exclude the edges of the detection range, only angular bins with a detection efficiency larger than 60% are handled.

6. **Rebinning of angular distribution**: by combining 5 bins statistical fluctuations are averaged out.

7. **Conversion to CM angles**: using a kinematics code the differential cross section corresponding to a given θ_{LAB} angle is converted to the CM frame of reference. This calculation includes the effects of ^{67}Ni excitation energy on the kinematics of the detected proton.

8. **Weighted average of differential cross sections**. In case multiple gates are applied to obtain the differential cross section of a given state (i.e. multiple γ-gates), for each angular bin the weighted average (weight factor $\propto$ inverse error) of these distributions is taken for the final differential cross section.

The width of the excitation energy gates does not include the full width of the peak in order not to include contributions from higher lying states which result in top-feeding on the level of interest. This effect was also simulated and absorbed in the efficiency correction factor. In the case of the 1724 keV state, special care is given to the intense 483 keV γ transition top feeding from the 2207 keV state. These differential cross sections can now be compared with DWBA theory.

6.4.2 Normalization

The normalization factor It used above, the product of measuring time and average beam intensity, is determined from the rate of elastically scattered deuterons detected in T-REX. As the measuring time t can be recovered from the data files themselves, only the average beam intensity has to be obtained. The differential cross section of the elastically scattered deuterons is best described by fitting a DWBA calculation (by varying the optical model potential parameters) to the experimental data. In the present case, the detectable range of the

المنارة للاستشارات

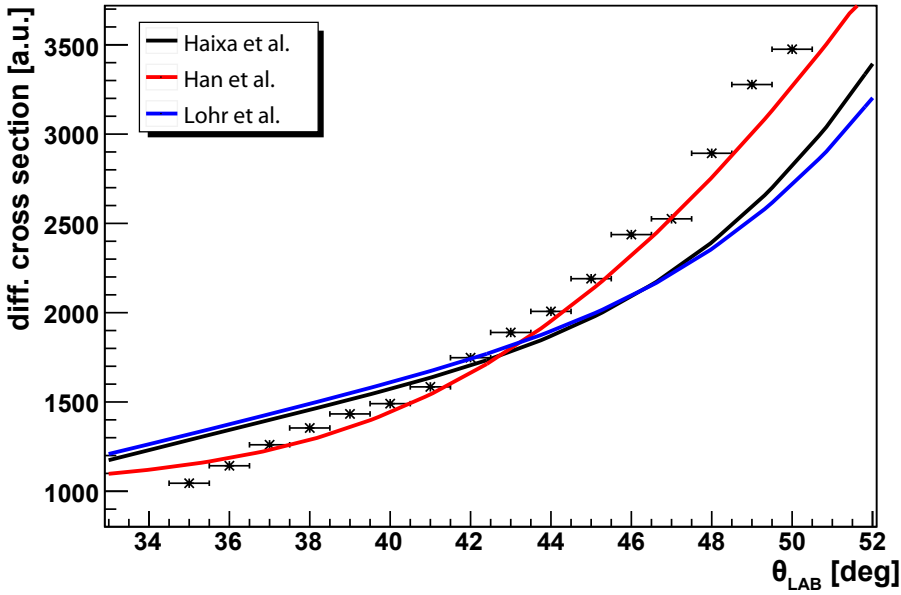

Figure 6.11: Differential cross section of elastically scattered deuterons. DWBA calculations using GOMP's from Refs. [Loh74, An06, Han06] are included and fitted to the experimental data.

deuterons was limited to θ_{LAB} between 36° and 50°, because the kinetic energy of the deuterons at angles greater than 50° becomes too low to ensure a proper particle identification. This limited range, in combination with the lack of data closer to $\theta_{\mathrm{LAB}} = 90°$, where the differential cross section is purely Rutherford and not depending on the optical model potentials, does not allow the optical potential parameters to be fitted to the data.

In literature three sets of GOMPs suitable for this mass and energy region can be found [Loh74, An06, Han06]. Of these, the GOMPs by Yinlu Han (Ref. [Han06]) gave the best fit with the experimental data. The best fits (by varying the scaling factor of the calculated differential cross sections) for all available GOMPs are shown in Figure 6.11. The fit of this DWBA calculation to the experimental data provides a factor that is linked to the product It and hence this fit factor can be used to extract the *average beam intensity* I. Using the fit value an average beam intensity of $I = 4.1(3)\ \mathrm{E}+6$ particles per second at the detection setup is found. This value is in agreement with less precise on-line estimations using a Faraday cup.

As a final note: the influence of the ^{66}Ni-^{2}H optical potential on the calculated

المنارة للاستشارات

	^{2}H	^{1}H
Counts	6.5 E + 5	9 E + 5
$\sigma_{\text{int},30^\circ\rightarrow40^\circ}$ [mb]	49	507

Table 6.3: Information used to obtain target purity.

differential cross sections for protons has been discussed in Section 2.5.4 and found to be limited. Furthermore, since only relative spectroscopic factors are quoted in this work, uncertainties in the factor It cancel out eventually.

For the ^{67}Ni-^{1}H optical model potentials, the detectable range of elastically scattered protons is even more confined, prohibiting any fitting of the parameters. The choice of GOMP's for this channel has been discussed in Section 2.5.4. In the DWBA analysis GOMPs from Ref. [Kon03] are used.

6.4.3 Target purity

In a limited range both elastically scattered deuterons and protons were observed. The elastically scattered protons, also evident in Figs. 6.7 and 6.8, are due to impurities in the target. If P_{target} labels the target purity (i.e. the ratio deuterons to deuterons and protons), then the number of observed elastically scattered deuterons and protons equals

$$\frac{N_{^2\text{H}}}{N_{^1\text{H}}} = \frac{\sigma_{^2\text{H}} P_{\text{target}}}{\sigma_{^1\text{H}}(1 - P_{\text{target}})} \tag{6.1}$$

after canceling out all the identical parameters. $\sigma_{^2\text{H}}$ and $\sigma_{^1\text{H}}$ denote the integrated elastic cross sections, obtained from DWBA calculations using GOMPs from Refs. [Han06, Kon03]. From the observed number of counts in the elastic channels the target purity could be calculated and the necessary information is tabulated in Table 6.3. The enhanced elastic scattering cross section for protons was due to the smaller CM energy of the ^{66}Ni-^{1}H system and hence smaller CM energy, leading to an enhanced Sommerfeld parameter. From the values in Table 6.3 a target purity of 88% was found.

The precise determination of the target purity was only relevant for absolute normalizations, just like the average beam intensity. When doing relative measurements, the target purity is canceled out.

المنارة للاستشارات

6.4.4 DWBA calculations

DWBA calculations were performed with the FRESCO code [Tho88] using GOMPs from Refs. [Han06, Kon03]. Here an example of the fresco input file for one excited state (1007 keV) is shown.

```
ni66(h2,h1)ni67 @ 2.95 MeV/u 1g92;
NAMELIST
 &FRESCO  hcm=0.1 rmatch=25. rintp=0.10 hnl=0.05 rnl=4.50
          centre=-0.25 jtmin=0.0 jtmax=80. absend=0.0001
          kqmax=10 thmin=0.00 thmax=180.00 thinc=1.00
          ips=0.00 it0=1 iter=1 nnu=30
          chans=1 xstabl=1
          elab=5.67  /

 &PARTITION namep='h2' massp=2. zp=1 namet='ni66' masst=66.
            zt=28 nex=1  /
 &STATES jp=1.0 bandp=1 ep=0.0 cpot=1 jt=0.0 bandt=1
         et=0.0000  /

 &PARTITION namep='h1' massp=1. zp=1 namet='ni67' masst=67.
            zt=28 qval=3.583 nex=1  /
 &STATES jp=0.5 bandp=1 ep=0.0 cpot=2 jt=4.5 bandt=+1
         et=1.006 /
 &partition  /

 &POT kp=1 ap=66.000 at=00.000 rc=1.35  /
 &POT kp=1 type=1 p1=83.4 p2=1.17 p3=0.809
                  p4=0.7 p5=1.328 p6=0.465  /
 &POT kp=1 type=2 p4=13.9 p5=1.563 p6=0.7 /
 &POT kp=1 type=3 p1=3.7 p2=1.234 p3=0.813 /
 &POT kp=2 ap=67.000 at=00.000 rc=1.25  /
 &POT kp=2 type=1 p1=56.71 p2=1.204 p3=0.668
                  p4=0.693 p5=1.204 p6=0.668  /
 &POT kp=2 type=2 p4=8.328 p5=1.278 p6=0.484 /
 &POT kp=2 type=3 p1=5.72 p2=1.025 p3=0.59
                  p4=-0.035 p5=1.025 p6=0.59 /
 &POT kp=3 at=1.000 rc=1.25  /
 &POT kp=3 type=1 p1=50.00 p2=1.25 p3=0.65   /
 &POT kp=4 at=66.0 rc=1.25  /
 &POT kp=4 type=1 p1=71.00 p2=1.25 p3=0.65   /
 &pot /
```

المنارة للاستشارات

```
&Overlap kn1=1 ic1=1 ic2=2 in=1 kind=0 nn=1 l=0 sn=0.5 ia=1
         j=0.5 ib=1 kbpot=3 krpot=0 be=2.2246 isc=1 ipc=0 /
&Overlap kn1=2 ic1=1 ic2=2 in=2 kind=0 nn=1 l=4 sn=0.5 ia=1
         j=4.5 ib=1 kbpot=4 krpot=0 be=4.8017 isc=1 ipc=0 /
&overlap /

&Coupling icto=2 icfrom=1 kind=7 ip1=0 ip2=0 ip3=0 /
&CFP in=1 ib=1 ia=1 kn=1 a=1.00  /
&CFP in=-2 ib=1 ia=1 kn=2 a=1.00  /
&CFP /
&coupling /
```

Important parameters that have to be modified for different states and configuration are:

- Partition and states: in the outgoing channel the spin and parity of the state should match the final spin coupling defined later (second point). Excitation energy should be set to the correct value.
- Overlap section: in the second line the parameters of the wave function binding the transferred neutron to the core should be set. nn (number of nodes), l (angular momentum) and j (total angular momentum after spin-orbit coupling) should match the values from point 1. Also the binding energy (be) should match the neutron separation energy minus the excitation energy of the state the calculation is performed for.

Finally it should be noted that the SO-coupling potential was not included in the calculations presented here. The correct inclusion of this potential can lead to small adjustments of the relative spectroscopic factors presented in this work.

المنارة للاستشارات

7

Results

In this chapter, all excited states for which a proton angular distribution has been extracted and fitted with DWBA calculations are discussed and arguments are presented leading to the final spin assignments. These arguments do not only include DWBA fits, but also information from other experiments, γ-branching ratios and systematics in the lighter nickel isotopes. All differential cross sections with a limited number of fits are shown (ascending excitation energy) in Figs. 7.1, 7.2 and 7.3.

Ground state

Spectroscopic studies of the ground state of ^{67}Ni have been performed by means of β decay [Run83] and multi-nucleon transfer reactions like ^{70}Zn(^{4}He,^{7}Be), ^{70}Zn(^{14}C,^{17}O) and ^{208}Pb(^{64}Ni,X) [Kou78, Gir88, Paw94, Mac03, Ish97, For95, Geo02, Run83]. The allowed β decay to the $3/2^-$ ground state of ^{67}Cu (log ft $\sim$ 4.7) [Run83] suggested a tentative spin assignment of $(1/2^-)$. This was also compatible with the non-observation of direct ground-state feeding in the β decay of ^{67}Co ($J^\pi = 7/2^-$) [Wei99].

In the ^{70}Zn(^{14}C,^{17}O) work of Ref. [Gir88], the observed angular distribution of the ejectiles for this state was also consistent with a $(1/2^-)$ assignment. From simple independent particle model predictions, a $1/2^-$ spin and parity was expected for the ground state since all other pf-orbitals are expected to be nearly filled.

المنارة للاستشارات

In the proton angular distribution of the current (d,p) experiment, a peak can be observed near 20° in the CM frame of reference. This is in good agreement with a $\ell = 1$ transfer (calculated for a $\nu p_{1/2}$ configuration), supporting the $1/2^-$ assignment. The spin and parity of the ground state can not be unambiguously fixed using the transfer data alone because the angular distributions make no distinction between parallel or anti-parallel spin-orbit couplings. But by taking into account the arguments mentioned in the first paragraph, a spin and parity assignment of $1/2^-$ is strongly favored.

The relative SF of the ground state (with respect to the $\nu g_{9/2}$ state (see below) and assuming a $\nu p_{1/2}$ configuration) is compatible with 1, indicating that the $\nu p_{1/2}$ orbital is as empty as the $\nu g_{9/2}$ orbital, assuming a pure configuration for this 1007 keV state. The emptiness of the $\nu p_{1/2}$ orbital is also expected as this low-j orbital does not contribute as significantly to the pairing energy as high-j orbitals like the $\nu f_{5/2}$ orbital.

This finding of a ground state containing a strong contribution from the $\nu p_{1/2}$ single-particle configuration is supported by on-line β-NMR measurements which found a magnetic moment $\mu(p_{1/2})$ for the ^{67}Ni ground state of $+0.601(5)\mu_N$. The small deviation from the Schmidt value of $\delta\mu = -0.037(5)\mu_N$, which is 4 times smaller than the correction to the Schimdt value based on an effective one-body magnetic moment operator, is seen as an indication for a rather pure $\nu p_{1/2}$ configuration[1] [Rik00].

694 keV

The spin and parity of the first excited state at 694 keV was previously tentatively fixed to $(5/2^-)$ based on the allowed β decay (log ft = 4.7) from the $7/2^-$ ground state of ^{67}Co [Wei99]. From an independent-particle model view, a $\nu f_{5/2}$ character can be assigned to this state. In the ^{70}Zn(^{14}C,^{17}O) reaction, a state at 770 keV was observed[2] but the measured angular distribution is not reproduced by calculations assuming a spin of $5/2^-$ (see Figure 1.12 on p. 25). In that analysis, a spin and parity of $(9/2^+)$ was proposed.

[1] In the same work also the measurement of the magnetic moment of the ground state of ^{69}Cu is reported. Here, the experimental value of $2.84(1)\mu_N$ deviates substantially from the Schimdt value and the difference of $\delta\mu = 0.95(1)\mu_N$ can, in this case, be explained by corrections incorporated in the effective one-body magnetic moment operator. The corrections encompass core polarization, meson exchange and relativistic corrections.

[2] It is not entirely clear if the reported state at 770 keV is the same state as the one at 694 keV discussed here. However, in general an offset between level energies reported here and those reported in Ref. [Gir88] can be noted.

المنارة للاستشارات

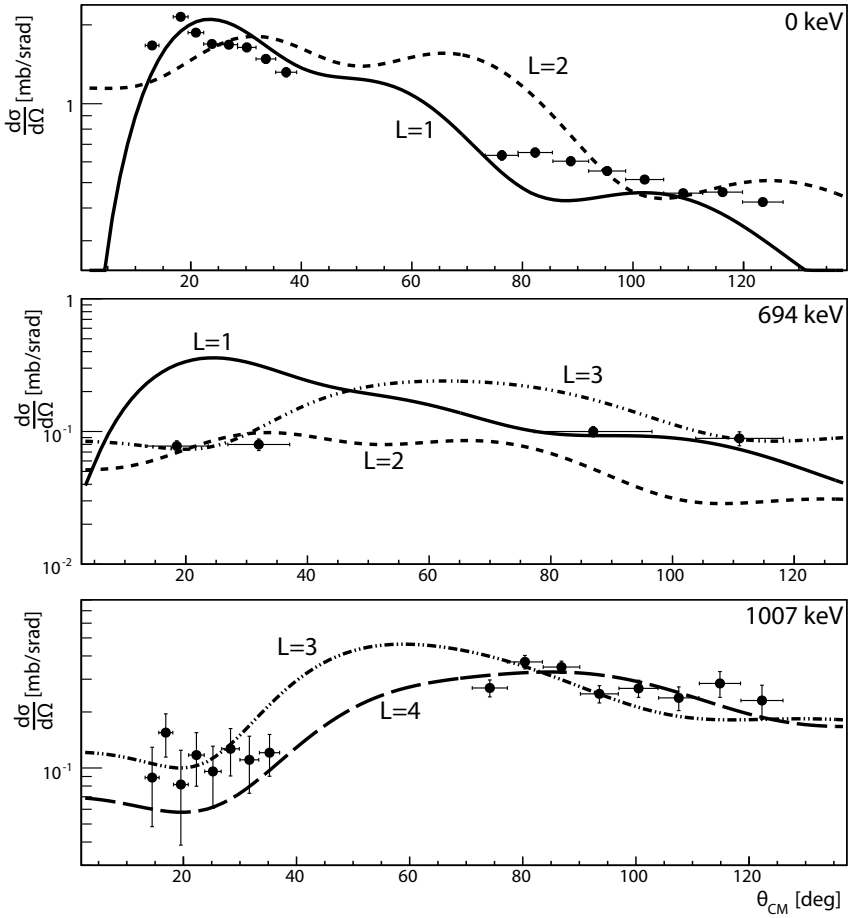

Figure 7.1: Absolute differential cross sections measured for states at 0, 694 and 1007 keV. Best ℓ fits are shown. In the case of 694 keV, a number of data points were summed due to the small magnitude of the measured cross section. See text for discussion.

المنارة للاستشارات

In the ^{66}Ni(d,p) reaction, the state at 694 keV is weakly populated, with a rather flat proton angular distribution, fitting with $\ell = 1$, 2 and 3. A direct identification of the spin and parity of this state is hence not possible but several arguments support a spin and parity assignment of $5/2^-$ for this state at 694 keV. The main argument is based on the delayed character of the 313-694 keV cascade, depopulating the 1007 keV state, with the first step (313 keV) as a delayed transition ($T_{1/2} = 13.3$ μs). Furthermore, it has been found that this sequence has a stretched quadrupole character [Zhu12]. The half-life of the prompt 694 keV transition to the $1/2^-$ ground state has been measured to be 150(4) ps [Mac03], compatible with a $B(E2,\downarrow)$ value of 1.46(4) W.u. This limits the spin and parity of the 694 keV state to $3/2^-$ or $5/2^-$. Combined with the log ft value from β decay, the spin and parity can be fixed to $5/2^-$.

The present data are not conclusive to confirm this spin assignment, but based on the measured differential cross section a relative spectroscopic factor could be deduced. The small value of this relative spectroscopic factor of 0.30 (9), assuming a $\nu f_{5/2}$ configuration, is also supporting the $5/2^-$ assignment since this orbital is expected to be rather full in ^{66}Ni due to the position of the Fermi surface. The fact that the relative spectroscopic factor is not zero indicates however that this orbital is not completely filled.

1007 keV

The 1007 keV state was previously observed in β-decay studies (log ft = 6.3) [Wei99] and multi-nucleon transfer reactions [Gir88, Kou78]. The $9/2^+$ spin and parity was proposed based on its isomeric features [Grz98] and similarities with ^{65}Fe where a similar transition was discovered [Blo08]. This interpretation is supported by the work of Pawłat *et al.* and the *l*-forbidden β decay also supports this assignment [Paw94, Wei99].

The purity of this proposed $\nu g_{9/2}$ configuration was questioned by g factor measurements which found a value only 50% of the expected value for a pure configuration [Geo02]. As mentioned in the introduction, this reduction was attributed to a 2% contribution of $M1$ proton excitations across the $Z = 28$ gap which strongly influences the g-factor [Geo02]. The data presented in Ref. [Gir88] show an excited state at 1.14 MeV identified as a $(5/2^-)$ state. However, if we assume that the angular distribution does not change too strongly with excitation energy, then the $9/2^+$ fit for the state at 0.77 MeV does reproduce the angular distribution of the 1.14 MeV state very well. This fit is shown in Figure 1.12.A on p. 25.

المنارة للاستشارات

In the present data, the proton angular distribution for the state at 1007 keV agrees with a $\ell = 3$ ($\chi^2_{\rm red} = 2.4$) and 4 ($\chi^2_{\rm red} = 1.8$) angular momentum transfer. Based on the discussion above, using the arguments of the isomeric features, the lack of ground-state transition and the stretched quadrupole character of the 313-694 keV γ-decay sequence, a $\ell = 4$ (and hence $\nu g_{9/2}$) interpretation is favored. This leads to a $M2$-delayed 313 keV transition ($9/2^+ \rightarrow 5/2^-$) with a $B(M2)$ value of 0.05 W.u. [Grz98], compatible with known transition strengths in this mass area [End79]. As this isomeric state decays by a cascade of two delayed gammas, the only way to obtain a proton angular distribution was to use the delayed coincidence technique. Based on systematics, the $\nu g_{9/2}$ orbital is expected to be nearly empty in ^{66}Ni and therefore the spectroscopic factor of this state was used to quote relative spectroscopic factors in this work.

1724 keV

The only evidence for an excited state around this energy was found in the work of Kouzes *et al.*, where neither spin nor parity assignment was reported [Kou78]. The energy of this excited state was found to be 1710 ± 22 keV, in agreement with the energy of 1724.0 (2) keV determined from the γ-ray energy.

The obtained differential cross section corresponding to the 1724 keV state is in good agreement with a $\ell = 1$ transfer. A spin and parity assignment of $3/2^-$ is proposed for two reasons based on the γ branching. First, substantial top feeding from the $5/2^+$ level at 2207 keV (see next section, $E_\gamma = 483$ keV) is observed. To account for this strong branching, the inclusion of an $E1$ component in the γ decay is necessary because a pure $M2$ transition would be too slow to explain the observed branching ratios. Also, a small γ branch to the $5/2^-$ state at 694 keV with a relative branching ratio of $I(1030)/I(1724) = 5\%$ is seen. When making use of the Weisskopf estimates for the γ transition probabilities, the theoretical branching ratio for this 1030 keV transition would be $8\ 10^{-5}$ in case of $1/2^-$ and 0.2 for a $3/2^-$ spin and parity of the 1724 keV state. It should be noted that an $\ell = 2$ interpretation can not be entirely discarded. However a $5/2^+$ spin and parity is not compatible with the observed γ-branching ratios. Indeed the hypothesis of a $5/2^+$ spin and parity assignment, a strong γ link with the $9/2^+$ state at 1007 keV is expected while no connection with the $1/2^-$ ground state should be observed. This will be illustrated for the excited states at 2207 and 3277 keV.

This leads to a $\nu p_{3/2}$ interpretation for this 1724 keV state, with a relative spectroscopic factor of 0.18(5). This small relative spectroscopic factor is in line with the interpretation because the $\nu p_{3/2}$ orbital is expected to be rather

المنارة للاستشارات

$5/2_1^+$ (2207 keV)			$B(\lambda L)$ [W.u.]	
E_γ [keV]	$J_i^\pi \rightarrow J_f^\pi$	$I_{\rm rel}$	Exp.	Nominal [End79]
1201	$5/2^+ \rightarrow 9/2^+$	100	10	10 (E2)
483	$5/2^+ \rightarrow 3/2^-$	45	1.2 E − 3	1 E − 4 (E1)
1513	$5/2^+ \rightarrow 5/2^-$	13	1.1 E − 5	1 E − 4 (E1)
$5/2_2^+$ (3277 keV)				
2270	$5/2^+ \rightarrow 9/2^+$	100	10	10 (E2)
1070	$5/2^+ \rightarrow 5/2^+$	21*	3.6 E − 2	1 E − 1 (M1)
			90	10 (E2)
1553	$5/2^+ \rightarrow 3/2^-$	7	1.4 E − 4	1 E − 4 (E1)
2583	$5/2^+ \rightarrow 5/2^-$	17	7.6 E − 5	1 E − 4 (E1)

Table 7.1: Overview of the main γ transitions from the identified $5/2^+$ states in ^{67}Ni to negative parity states and $5/2^+$, $9/2^+$ states. The two last columns show the theoretical $B(\lambda L)$-values for these transitions (assuming a 10 W.u. $E2$ $5/2^+ \rightarrow 9/2^+$), compared with the average values observed in this mass region (values from [End79]). * the $5/2_2^+ \rightarrow 5/2_1^+$ transition will have a mixed $M1/E2$ nature. The values quoted here are assuming either a pure $M1$ or $E2$ transition.

full in ^{66}Ni since it lies below the Fermi level. The low spin of this state also explains the non-observation of this state in the β decay of ^{67}Co [Wei99] due to the double forbidden character of the decay. In the neighboring nickel isotopes, the low-lying $3/2^-$ states are also only very weakly directly fed in the β decay of the corresponding cobalt isotopes. E.g. ^{65}Co decay: $I_\beta < 0.7\%$ [Pau09], ^{63}Co decay: $I_\beta = 0.11\%$ and 0.15% [Run85, Jon72, Roo75] and not observed in the ^{61}Co β decay [Kis69]. Recent analysis of the ^{67}Fe$\rightarrow^{67}$Co$\rightarrow^{67}$Ni β decay has shown traces of a γ transition at 1724 keV, compatible with a small feeding probability [Rad13].

2207 keV

The proton angular distribution of the excited state at 2207 keV fits well with both $\ell = 1$ and 2, with the latter giving in the best χ^2 fit.This state had not been observed before in other experiments.

A spin of $5/2^+$ is preferred for several arguments coming from the γ-branching ratios observed. The strongest link observed is the 1201 keV transition to the $9/2^+$ isomer, with other branches to the $3/2^-$ state at 1724 keV and $5/2^-$ state at 694 keV. In terms of the proposed spin of $5/2^+$, the 1201 keV $E2$ transition will compete with $E1$ transitions to the $3/2^-$ and $5/2^-$ states. Based on the

المنارة للاستشارات

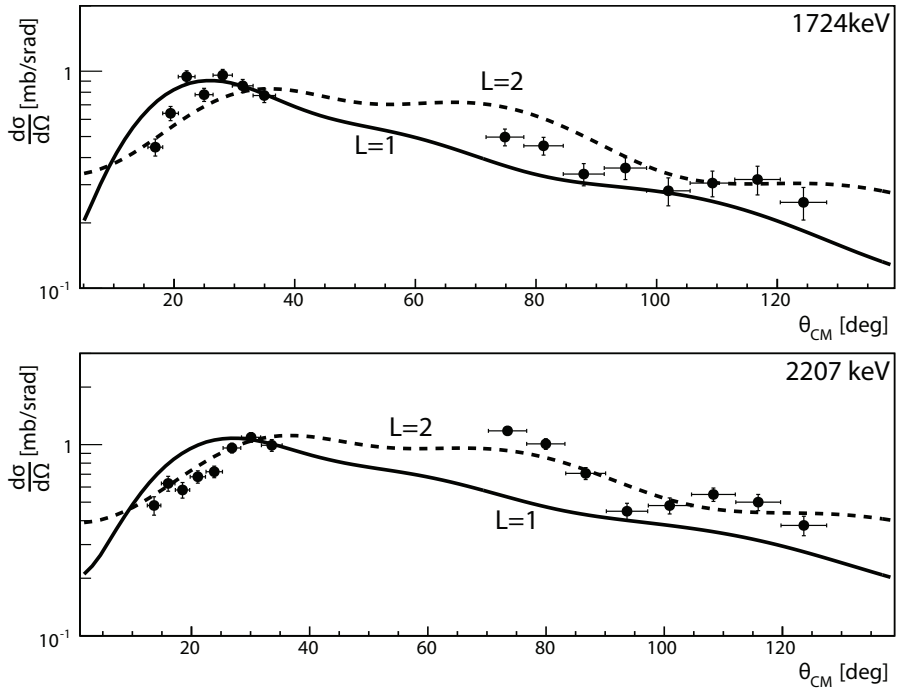

Figure 7.2: Absolute differential cross sections measured for 1724 and 2207 keV. Best ℓ fits are shown. See text for discussion.

measured branching ratios: $I(483)/I(1201) = 45\%$ and $I(1513)/I(1201) = 13\%$ and assuming a 10 W.u. transition strength[3] for the 1201 keV $E2$ transition, $B(E1)$ values for the 483 and 1513 keV transitions could be estimated. The retardation values for these transition are then found to be 1.2 E − 3 (483 keV) and 1.1 E − 5, which are typical values in this mass range (average for $E1$ transition is ≈ 1 E − 4 W.u.) [End79]. This information is summarized in Table 7.1. In case of a $3/2^{\pm}$ spin, the decay pattern would be different, favoring γ decay towards $1/2^{\pm}$, $1/2^{\pm}$ and $5/2^{\pm}$ states, in combination with a strong ground state transition. Decay to the $9/2^{+}$ isomer would be strongly hindered due to the $M3/E3$ character of the transition.

A relative spectroscopic factor of 0.25(7) is found for this state, assuming a $\nu d_{5/2}$ configuration.

[3]This value is based on the *average* E2 transition strength observed in the $A = 45 - 90$ mass region [End79].

المنارة للاستشارات

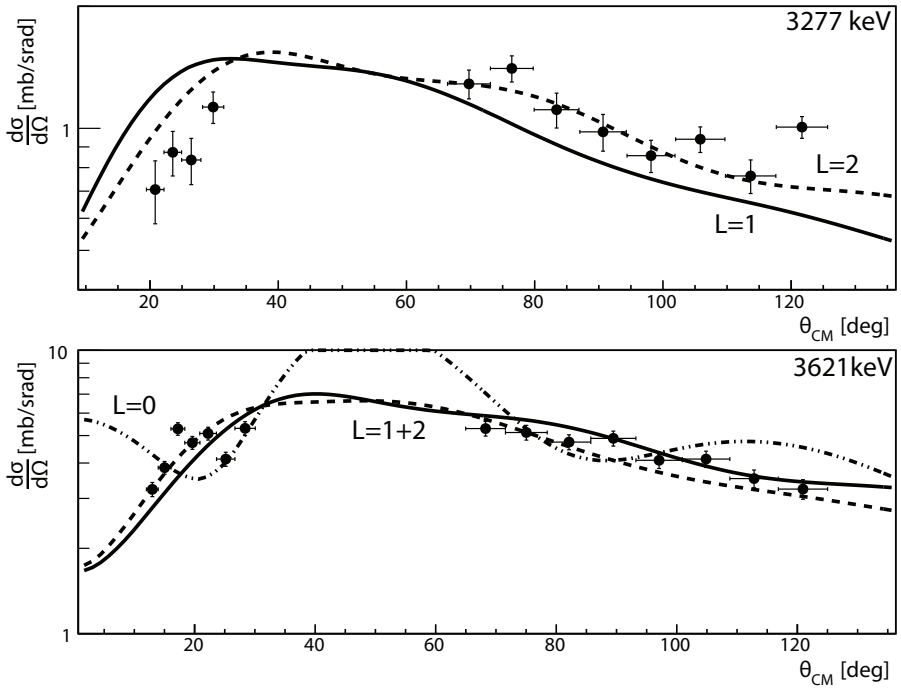

Figure 7.3: Obtained absolute differential cross sections for 3277 and 3621 keV. Best ℓ fits are shown. See text for discussion.

3277 keV

For the state at 3277 keV, the same line of thought than that for the 2207 keV state can be followed. The measured proton angular distribution fits again with both $\ell = 1$ and 2, with $\ell = 2$ giving the best agreement.

Regarding the information from γ-branching ratios, the same arguments as for the 2207 keV state apply. The observed relative intensities for γ transitions to $3/2^-$, $5/2^-$ and $9/2^+$ states are tabulated in Table 7.1. Here also the transition to the $5/2^+_1$ state which has a mixed $M1/E2$ multipole character is included. The values quoted in Table 7.1 are based on pure transitions and can thus be seen as upper limits, leading to reasonable agreement. This table also includes the calculated $B(E1)$ transition strength to $3/2^-$ and $5/2^-$ negative parity states. Again the absence of a direct transition to the $1/2^-$ ground state and strong $E2$ transition towards the 1007 keV isomer are essential in the assignment of the spin and parity of this state.

المنارة للاستشارات

Based on the interpretation of $\nu d_{5/2}$ configuration a relative spectroscopic factor of 0.28 (9) was found.

3392 keV

Despite a substantial amount of direct feeding, the measured proton angular distribution for the 3392 keV state is uncharacteristic and no reasonable fits with DWBA calculations could be made (see Figure 7.4).

Some indications on the spin of this state can be inferred from the γ-branching ratios. The lack of a ground state transitions disfavors low spins, while the absence of a transition towards the $9/2^+$ isomer is not compatible with high spins. This combination gives a slight preference for a $(5/2^{-/+})$ assignment as all observed transitions connect this state with $3/2^-$, $5/2^-$ and $5/2^+$ states. Of these combinations, a spin of $5/2^+$ is however unlikely as the branching ratio pattern differs significantly from the identified $5/2^+$ states at 2207 and 3277 keV. On the other hand, the relative spectroscopic factor for a $\nu f_{5/2}$ interpretation would be bigger than 1, which is not compatible with systematics and not expected.

Combining all these arguments, the nature and spin of this state remain unclear.

3621 keV

The excited state at 3621 keV, with prominent decay directly to the ground state, suggesting a low spin, has an associated proton angular distribution that fits with $\ell = 1$ and 2, and to a lesser extent $\ell = 0$. It should be noted that, since this state is only bound by 2 MeV, the differential cross section is becoming less sensitive to the amount of transferred angular momentum (see also Section 2.5.2).

The main source of information on the spin and parity of this state comes from the γ-branching ratios. The branch towards the 694 keV $5/2^-$ state is within error bars equal to zero, while the 1896 keV transition to the $3/2^-_1$ state has a relative branching ratio of 7% (with respect to the ground state branch). From this observation, a spin and parity of $(1/2^{-/+})$ is preferred and would result in a calculated branching ratio of 14% towards the 1724 keV state, based on Weisskopf estimates either via $M1$ or $E1$. Higher spins would lead to more intense branchings towards $5/2^{-/+}$ states, which are not experimentally observed.

المنارة للاستشارات

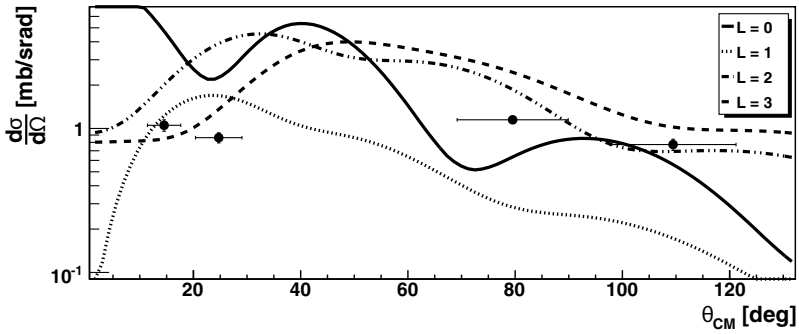

Figure 7.4: Proton angular distribution for 3392 keV state with different angular momentum transfer fits.

Assuming a $(1/2^{-/+})$ spin for this state, the obtained relative spectroscopic factors are 1.3(4) ($\nu s_{1/2}$) and 1.9(5) ($\nu p_{1/2}$) respectively. This observation supports a spin assignment of $1/2^+$ because in the case of a $1/2^-$ spin and parity, the global $\nu p_{1/2}$ single particle strength would be nearly 3 times the observed $\nu g_{9/2}$ strength and which would indicate a substantially filled $\nu g_{9/2}$ orbital in ^{66}Ni, with a large number of vacancies in the pf shell. This is not compatible with the low relative spectroscopic factors for the $5/2^-$ and $3/2^-$ observed in this study and also not consistent with transfer reaction data on lighter nickel isotopes, where no concentrated pf-single particle-strength is found above ≈ 2 MeV excitation energy (see e.g. Figure 1.10 on p. 22) [Cho73, Ful64, Wes91, Cos67, Ful63, Anf70, Hut74, Tur70]. The single-particle strength found at these excitation energies in the lighter nickel isotopes is limited to $\ell = 0$, 2 and in a limited amount of 4. This point will be discussed in more detail in the next chapter.

Finally, in the ^{70}Zn(^{4}He,^{7}Be)^{67}Ni work of by Kouzes *et al.* [Kou78], the strong population of an excited state at 3.680 MeV is seen. Based on the measured angular distribution, a spin and parity of $(3/2^-)$ was proposed. A remark is made that "*the three other states might be (3/2$^-$) but the shape of the angular distributions are not characteristic*". It is unclear whether the state observed by Kouzes *et al.* is the same as the 3621 keV state discussed here. If so, the ^{70}Zn ground state should have a sizable occupation of the $\nu s_{1/2}$ orbital (assuming this state is a $1/2^+$ state and the reaction is a direct reaction) which is very unlikely. A difference in excitation energy between the values quoted in this work and in Ref. [Gir88] can be noted. Since the excitation energies reported here rely on the measured γ-ray energies, a better energy resolution and precision is expected.

المنارة للاستشارات

Other states

Several other states not discussed above have been observed in the present experiment. The total direct feeding probability of these states is however too small to extract proton angular distributions. For excited states at low excitation energy (i.e. below 2.3 MeV) the main contribution to the wave functions of these states are most probably core-coupled structures, with small single-particle admixtures. For excited states above 4 MeV excitation energy the angular range for which a differential cross section could be extracted is limited to high θ_{CM} values and no ℓ-assignment can be made. The origin of these states will be discussed in the next chapter.

المنارة للاستشارات

المنارة للاستشارات

8

Discussion

In this chapter, the obtained results are compared with the systematics from reaction work on lighter nickel isotopes. A second comparison is made with the odd-Z nuclei in the $N = 50$ isotones near ^{90}Zr, which serves as a mirror-region of the area around ^{68}Ni. Based on the observed distribution of single-particle strength, the size and evolution of the $N = 50$ shell gap near ^{68}Ni is estimated.

8.1 Systematics in odd-A nickel isotopes

Figure 8.1 shows the distribution of the single-particle strength in the odd-A nickel isotopes by plotting the relative spectroscopic factors (with respect to the $9/2^+_1$ state for each isotope) measured in (d,p) reactions on ^{58,60,62,64}Ni at comparable CM energies [Cho73, Ful64, Wes91, Cos67, Ful63, Anf70, Hut74, Tur70, Sch13, Sch12]. Most of the systematics in the lighter isotopes have already been discussed in Section 1.3.1 (p. 20) but the information in Figure 8.1 can be used to track some of these evolutions and give an interpretation to the obtained results in ^{67}Ni.

When focusing on negative-parity states ($\ell = 1$ and 3), it is clear that the total single-particle strength observed gradually decreases when neutrons are being added due to the filling of the available valence space in the pf-shell. In ^{59,61,63}Ni, few negative parity states above 2 MeV have been identified and they have very small single-particle contributions to their wave functions. In ^{65}Ni all the excited states above 2 MeV are populated either by $\ell = 0$, 2 or 4

المنارة للاستشارات

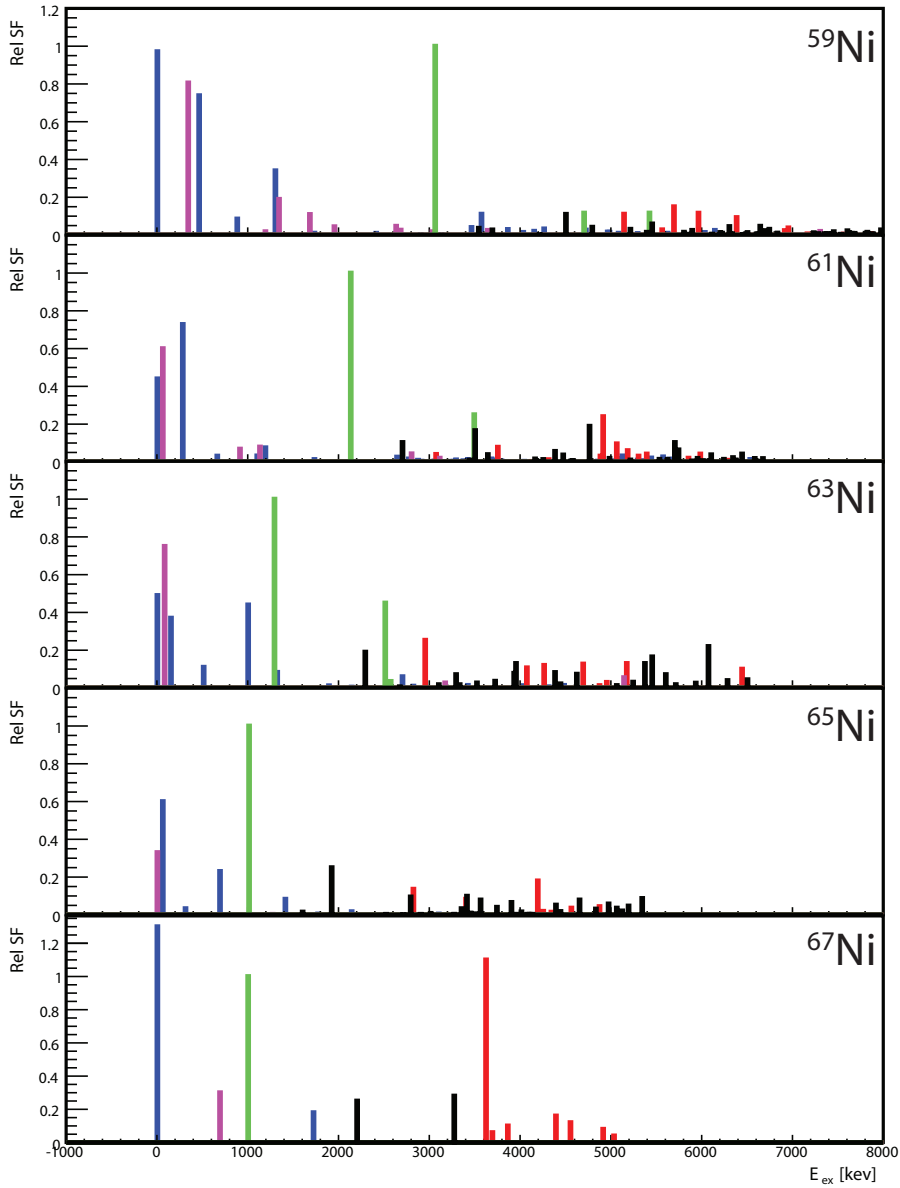

Figure 8.1: Evolution of the distribution of the single-particle strength (relative spectroscopic factors, $9/2^+_1$ as reference for each isotope) in the odd-A nickel isotopes. Color code: red: $\ell = 0$, blue: $\ell = 1$, black: $\ell = 2$, purple: $\ell = 3$ and green: $\ell = 4$. Data on lighter isotopes from Refs. [Cho73, Ful64, Wes91, Cos67, Ful63, Anf70, Hut74, Tur70]. Excited states above 3621 keV in ^{67}Ni have been labeled as $\ell = 0$, but no conclusion could be drawn on their single-particle character.

المنارة للاستشارات

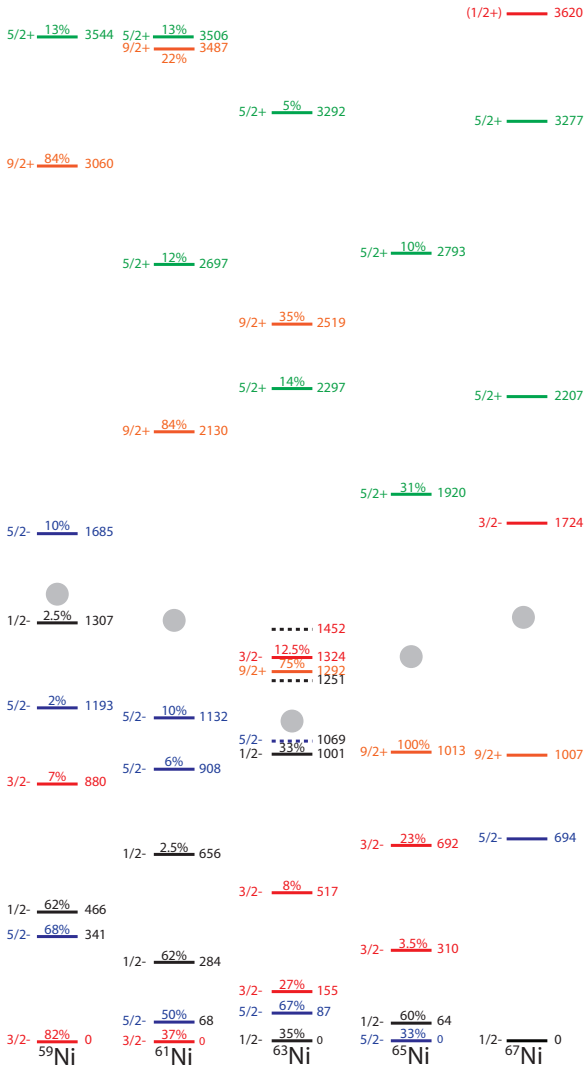

Figure 8.2: Level systematics in the odd-A nickel chain. Percentages above states indicate fraction of the total $2J + 1$ single-particle strength based on absolute spectroscopic factors. Data taken from Refs. [Cho73, Ful64, Wes91, Cos67, Ful63, Anf70, Hut74, Tur70]. The gray circles depicts the 2^+_{core} energy of the underlying core.

المنارة للاستشارات

transfer reactions, indicating that exclusively sdg single-particle strength resides at these excitation energies. As mentioned in the previous chapter, the state at 3621 keV in ^{67}Ni interpreted as $(1/2^{-/+})$ is thus expected to be of positive parity. Its spectroscopic factor in case of spin and parity $1/2^-$ would be 1.9, not consistent with these previously observed systematics. Also the combined relative single-particle strength of the $\nu p_{1/2}$-orbital would be ≈ 3. Such a high value would indicate a high occupancy of the $\nu g_{9/2}$-orbital in the ground state of ^{66}Ni, which is not expected. For this reason, the state at 3621 keV is labeled as $(1/2^+)$.

Concerning the negative parity states at low excitation energy, a higher amount of fragmentation of the pf-single-particle strength can be seen in ^{61,63,65}Ni. This can be understood because they are situated in between the "closed" neutron (sub)shells of ^{56}Ni and ^{68}Ni leading to an enhanced mixing between pure single-particle configurations and core-coupled structures in these isotopes. The total amount of pf-single-particle strength also gradually decreases when neutrons are filling up the pf-shell consistent with the increase of the Fermi surface. Figure 8.4 where the simulated excitation spectrum of (d,p)-studies on ^{58,60,62,64}Ni is shown as if the data were taken with the T-REX setup, displays this feature. From this figure the decrease in the cross section towards the pf-states can be traced.

The large relative spectroscopic factor for the $1/2^-$ state indicates that the $\nu p_{1/2}$ orbital in the ground state of ^{66}Ni should be equally empty as the $\nu g_{9/2}$ orbital. Furthermore, it suggests a sizable contribution of the $\nu p_{1/2}$ single-particle component to the wave function of the ^{67}Ni ground state. The high purity of the ^{67}Ni ground state configuration was also already noted as its magnetic moment only deviates slightly from the Schmidt-value for a pure configuration [Rik00].

Spectroscopic factors of the remaining negative-parity $3/2^-$ and $5/2^-$ states are small but not negligible: 0.18(5) $(3/2^-)$ and 0.30(9) $(5/2^-)$. The global trend in the summed relative single-particle strength is shown in Figure 8.7 and the values for $\nu p_{3/2}$ and $\nu f_{5/2}$ measured in ^{67}Ni follow these systematics.

Direct neutron occupation numbers of the available neutron orbitals in the even nickel isotopes can be inferred from applying the *sum-rule method* [Mac60] on both (d,p) and (p,d) reaction data. Such an evaluation has been performed in the stable nickel region by Schiffer *et al.* [Sch12]. This analysis has shown that all pf-orbitals are filled in parallel rather than sequential. This leads to neutron occupation numbers of 3.17 $(\nu p_{3/2})$, 3.41 $(\nu f_{5/2})$, 1.07 $(\nu p_{1/2})$ and 0.66 $(\nu g_{9/2})$ in ^{64}Ni, the heaviest nickel isotope for which these numbers could be determined [Sch12]. The distribution of the additional two neutrons in ^{66}Ni over these available orbitals is unclear. Assuming the filling of these

المنارة للاستشارات

	Expected		Rel SF	
Orbital	Occupancy	Vacancies	Expected	Experimental
$p_{1/2}$	1.335	0.665	0.37	1.3 (4)
$p_{3/2}$	3.875	0.125	0.035	0.18 (5)
$f_{5/2}$	4.23	1.77	0.33	0.30 (9)
$g_{9/2}$	0.98	9.02	1	1 (3)

Table 8.1: Expected occupancies, vacancies and relative spectroscopic factors in the ^{66}Ni(d,p) reaction.

neutron orbitals is linear, the expected occupancies in ^{66}Ni are 3.88 ($\nu p_{3/2}$), 4.23 ($\nu f_{5/2}$), 1.34 ($\nu p_{1/2}$) and 0.98 ($\nu g_{9/2}$). From these numbers, the expected relative spectroscopic factors (assuming pure configurations, exhausting the full available single-particle strength) can be calculated. These values are presented in Table 8.1.

The agreement between the expected relative spectroscopic factors and experimental values is reasonably good for the $\nu f_{5/2}$-orbital, but differs for the νp-orbitals. As the proton angular distribution corresponding to ground state transfer can only be obtained from protons in singles, the extracted relative spectroscopic factor can be influenced as the background in the singles proton spectrum can not be accurately corrected for. This might lead to an overestimation of the reaction cross section (resulting in an overestimated relative spectroscopic factor). However it is clear that the high relative spectroscopic factor is not compatible with the occupation numbers presented by Schiffer et al.

In the paper by Schiffer *et al.*, the spectroscopic weighted excitation energies for the negative-parity pf-orbitals are also presented. They are related to effective single-particle energies presented in Figure 8.6 later in this chapter [Sch13]. Some differences between the data presented in Figure 8.6 and Ref. [Sch13] can be noted due to the following reasons:

- In the compilations found in Ref. [NND13] on which Figure 8.6 is based, excited states up to 6 MeV are included. In case of the ^{58,60}Ni(d,p) reaction, also highly excited states with ℓ=1 character were identified. In the work of Schiffer *et al.* no ℓ=1 states above 3 MeV has been observed in these reactions. Despite their small relative spectroscopic factors, their contributions to the effective single-particle energies (or spectroscopic factor weighted excitation energies) are not negligible. If the data from Ref. [NND13] are limited to the range of excitation energies observed by Schiffer *et al.*, a good agreement is achieved.

المنارة للاستشارات

- No distinction can be made between the $\nu p_{1/2}$ and $\nu p_{3/2}$ orbitals, which leads to additional uncertainties and ambiguities. This is also noted in the paper by Schiffer *et al.*

Since the spectroscopic factor for the $9/2^+_1$ state is used a reference value, no conclusions can be drawn on its purity in ^{67}Ni. The fact that measured *absolute* spectroscopic factors in ^{59,61,63,65}Ni are consistent with a pure configuration, support the use of the $9/2^+_1$ as reference state [Cho73, Ful64, Wes91, Cos67, Ful63, Anf70, Hut74, Tur70, Sch13, Sch12]. It should be noted that absolute $(2J+1)S$ factors reported by Schiffer et al. are smaller by a factor of two compared to these previous studies. The analysis by Schiffer *et al.* has indicated that limited occupancy of the $\nu g_{9/2}$ orbital already starts in ^{64}Ni (0.34 neutrons). Due to the size of this orbital (10 neutrons at maximal occupation), a small occupation will not lead to distortions of the experimental relative spectroscopic factors presented here. The fact that only one $\ell = 4$ state is observed in the data support the validity of this approach in the presented ^{66}Ni(d,p) analysis.

Evolution of $5/2^+$ states

The identification of $5/2^+$ states and their evolution throughout the nickel chain is closely linked with the size and evolution of the $N = 50$ gap spanned between the $\nu g_{9/2}$ and $\nu d_{5/2}$ orbitals. It was noted in the introduction (and visible in Figure 8.1) that in the lighter nickel isotopes, the $\nu d_{5/2}$-single-particle strength is mostly fragmented over a large number of states. From ^{61}Ni onwards the $\nu d_{5/2}$-single-particle strength becomes gradually more concentrated in two states carrying respectively in total 31% (^{59}Ni), 27% (^{61}Ni), 23% (^{63}Ni) and 34% (^{65}Ni) of the available $\nu d_{5/2}$ single-particle strength relative to the single-particle strength of the $9/2^+_1$ state. In ^{67}Ni, the combined $\nu d_{5/2}$-single-particle strength in the $5/2^+_{1,2}$ states at 2207 and 3277 keV accounts for $\approx 50\%$ of the observed single-particle strength contained in the $9/2^+_1$ state. The other excited states in the 3 to 5 MeV excitation energy region are labeled as $\ell = 2$ in Figure 8.1 but no conclusion can be drawn on their spin and parity. However, it is expected that these states are either of $\ell = 0$ or 2 character based on a direct comparison with (d,p)-experiments on lighter nickel isotopes (see Figure 8.1). Since the integrated cross sections over the detectable range for $\nu s_{1/2}$ and $\nu d_{5/2}$ configurations are nearly identical, the relative spectroscopic factors in Figure 8.1 for these states are not depending on the spins of these states.

Concerning the nature of $5/2^+$ states in ^{67}Ni, various configurations can give rise to a $5/2^+$ spin and parity, and do not necessarily involve the $\nu d_{5/2}$ orbital. A schematical depiction can be found in Figure 8.3:

المنارة للاستشارات

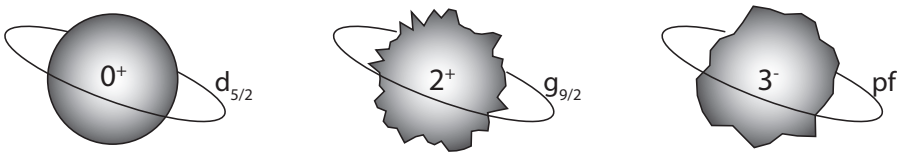

Figure 8.3: Schematic representation of different configuration leading to $5/2^+$ states. The distorted circles represent collective core excitations, while the ellipse depicts orbital single-particle motion. From left to right: single-particle excitation, core-coupled quadrupole excitation and core-coupled octupole excitation.

- **Single-particle excitation**: the most simple picture for creating a $5/2^+$ state is by placing the unpaired neutron into the $\nu d_{5/2}$ orbital above the $N = 50$ gap.
- **$\nu g_{9/2}$-core coupling**: this mode is best described by promoting the unpaired neutron to the $\nu g_{9/2}$ orbital which subsequently couples to a ^{66}Ni core excited 2^+ or 4^+ state found at low energy. The coupling of a $\nu g_{9/2}$ neutron to a 2^+ states provides a multiplet of positive-parity states between $5/2^+$ and $13/2^+$ (in case of coupling to a 4^+ state, the available couplings range between $1/2^+$ and $17/2^+$). There are various ways of depicting this kind of configuration but it always involves an odd number of neutrons in the $\nu g_{9/2}$ or higher lying orbitals. This issue will also be reviewed in the next section.
- **Octupole coupling** is another way to create positive parity states. In this case the unpaired neutron remains in the pf-shell and couples to a core-octupole excitation (3^- state). Depending on the spin of the unpaired neutron, different multiplets will arise[1], but in all cases a $5/2^+$ state will be part of the multiplet.

Hence, it is possible for shell model calculations to produce low lying $5/2^+$ states which do not encompass the $\nu d_{5/2}$ orbital in their valence space [Now13]. The contribution of these various types of configuration to the final wave functions will depend on the initial energy of these unperturbed states. The results presented here however show that the $\nu d_{5/2}$ orbital plays a significant role on the structure of the observed low-lying $5/2^+$ states for the following reasons:

- The observed proton angular distribution corresponding to these states fits with a $\ell = 2$ transfer.

[1] E.g. the $\nu p_{1/2} \otimes 3^-$ coupling will result in the $5/2^+$, $7/2^+$ doublet, while the $\nu f_{5/2} \otimes 3^-$ coupling produces spin between $1/2^+$ and $11/2^+$.

المنارة للاستشارات

- $\nu g_{9/2}$-core-coupled configurations require a higher order process and involve a $\ell = 4$ transfer in combination with multi-particle rearrangements (see Section 2.4.9). The measured cross section is not compatible with expected one for such a configuration. For these cross sections a comparison can be made with non-stripping reactions observed in ^{62,64}Ni(d,p) reactions, where the peak cross sections are orders of magnitude smaller than those of direct reactions [Anf70, Ful64].

- Due to the $\nu g_{9/2} \otimes 2^+_{\text{core}}$ coupling, other positive parity states in the vicinity of the observed $5/2^+$ states are expected (with spins ranging between $5/2^+$ and $13/2^+$). If the influence of the $\nu d_{5/2}$ orbital were absent and these states were purely due to core-coupled configurations then all these different states should be observed with comparable strength as the $5/2^+$ states observed here. This point will be highlighted in more detail in Section 8.2.

The combination of the arguments above leads to the conclusion that the $\nu d_{5/2}$ has an outspoken influence (25-30% of the wave function) on the structure of these low-lying $5/2^+$ states.

In conclusion, it is observed that the $\nu d_{5/2}$ strength evolves from a highly fragmented landscape in ^{59}Ni to a more concentrated picture in ^{67}Ni since nearly 50% of the $\nu d_{5/2}$-single-particle strength (relative to the observed $\nu g_{9/2}$-single-particle strength is divided over two $5/2^+$ states.

Structure of $1/2^+$ states

The excited state in ^{67}Ni at 3621 keV can most likely be interpreted as a $(1/2^+)$ spin state due to arguments given in the previous chapter. In (d,p) reactions on ^{58,60,62,64}Ni, the $\nu s_{1/2}$ strength is largely fragmented over a large number of states (Figure 8.1). The relative spectroscopic factor of 1 in ^{67}Ni shows that the $\nu s_{1/2}$ single-particle strength is highly concentrated in ^{67}Ni. No clear reasons can be given for this evolution and concentration of strength in ^{67}Ni.

Consequences of single-particle strength fragmentation

In Section 6.3, a short discussion on the missed top-feeding from highly excited states was presented. One of the possible origins for this missed intensity lies in the high level density at these excitation energies. This hypothesis is supported by the data presented in Figure 8.1 for ^{59,61,63,65}Ni. Besides the fact that the level density is high, the relative spectroscopic factors of these states are small

المنارة للاستشارات

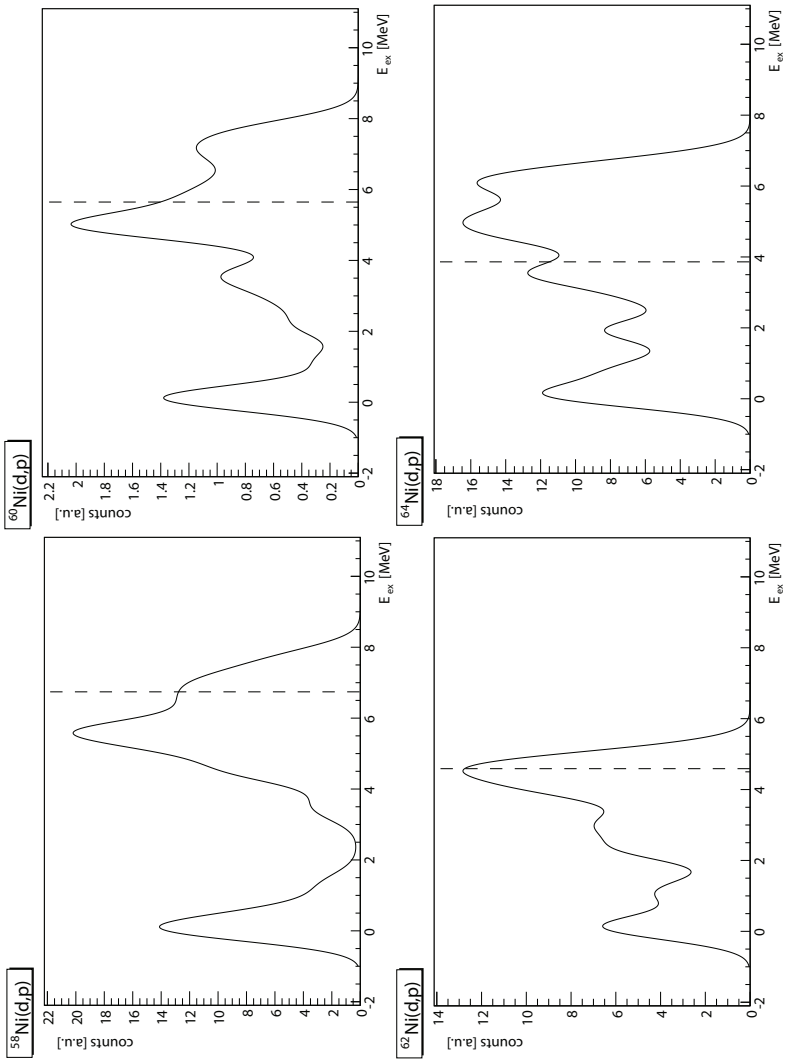

Figure 8.4: Simulation of the excitation spectrum of the ^{58,60,62,64}Ni(d,p)-reaction if they had been performed with the T-REX setup. The dashed line indicates the reaction Q-value. Data from [Cho73, Ful64, Wes91, Cos67, Ful63, Anf70, Hut74, Tur70].

المنارة للاستشارات

and as a consequence the reaction cross sections for populating these individual states will be small. This supports the assumptions made in Section 6.3.

This effect can be quantified by depicting the available data on the lighter nickel isotopes in a different way shown in Figure 8.4. Here the cross sections measured in the reaction work from Refs. [Cho73, Ful64, Wes91, Cos67, Ful63, Anf70, Hut74, Tur70] are translated into an excitation spectrum as if they were measured with the T-REX setup used in this work. Except for ^{62}Ni(d,p), broader and undefined structures can be seen in all simulations and the global picture is comparable to the measured spectrum in the ^{66}Ni(d,p) experiment (see Figure 6.8). These simulated curves, containing all states shown in Figure 8.1, show that the combination of high level density and small relative spectroscopic factors can indeed lead to a sizable global cross section for populating states in this high excitation energy region. It should be noted that the Q value is an additional and important parameter in the exact cross section balance.

8.2 Positive parity states in ^{67}Ni

The work of Zhu *et al.* identified numerous medium to high spin (positive parity) states on top of the 1007 keV isomer [Zhu12]. The central part of Figure 8.5 is based on the information from the work in Ref. [Zhu12] and includes positive parity states identified in that study. By offsetting the level structures of ^{66,68}Ni to the energy of the $9/2^+$ isomer in ^{67}Ni at 1007 keV, corresponding core-coupled structures can be identified. The highlighted box shows the correspondence in energy between the 2^+_1 energy in ^{66}Ni and the energies of the $5/2^+_1$, $11/2^+_1$ and $13/2^+_1$ states in ^{67}Ni. From this perspective, it is reasonable to assume that these states originate from the $\nu g_{9/2} \otimes {}^{66}\mathrm{Ni}(2^+_1)$ coupling scheme. Since the deep inelastic study in Ref. [Zhu12] is only sensitive to yrast states, the other members of this coupling multiplet: $7/2^+$ and $9/2^+$ are not identified. The observation of these $\nu g_{9/2} \otimes 2^+_1$ structures in the (d,p) data requires a two-step process. No traces of these states are found in the data, except for the $5/2^+_1$ state, indicating that the $5/2^+_1$ state partially has a different structure than the $11/2^+$ and $13/2^+$ states.

The same arguments are valid for the $5/2^+_2$ state at 3277 keV, which lies close the energy of $\nu g_{9/2} \otimes {}^{68}\mathrm{Ni}(2^+_1)$ and $\nu g_{9/2} \otimes {}^{66}\mathrm{Ni}(3^+_1, 2^+_2, 4^+_1)$ couplings. Here, also the proposed core-coupled structures seen in Ref. [Zhu12] are also not populated in the (d,p) experiment and the observation of the $5/2^+_2$ state with an $\ell = 2$ character again hint to the influence of the $\nu d_{5/2}$-orbital on the structure of this $5/2^+$ state.

المنارة للاستشارات

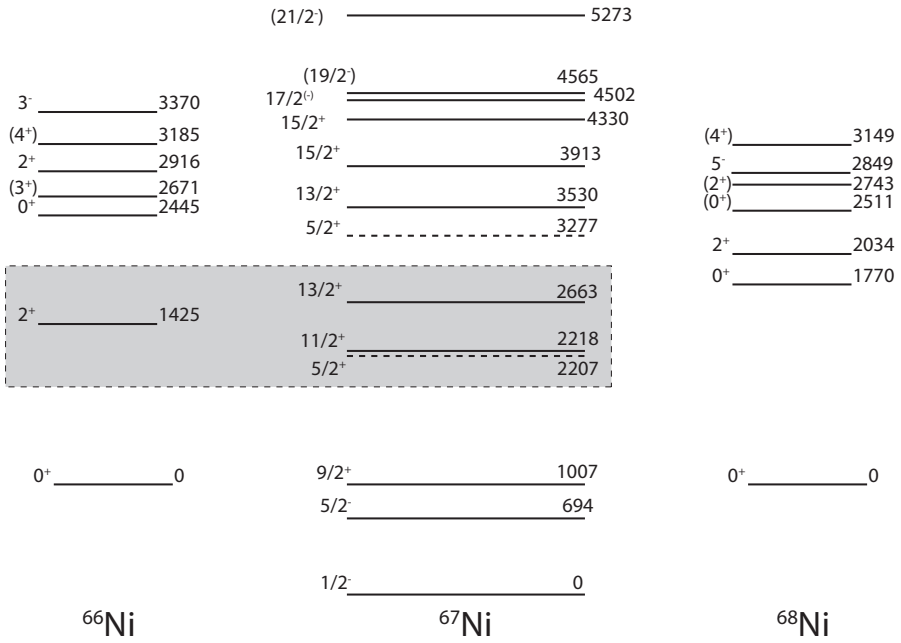

Figure 8.5: States identified by Zhu *et al.* and $5/2^+$ states found in this work. Even-A ^{66,68}Ni level schemes are shown (1007 keV is used as reference) for comparison [NND13].

Shell-model calculations using jj44b [Lis04] and JUN45 [Hon09] effective interactions are compared with the experimental data in Ref. [Zhu12]. The main conclusion is that "*[..] the levels above the 9/2$^+$ isomeric state can be understood as neutron excitations, with contributions of protons across the $Z = 28$ gap playing a minor role at best. Calculations with both interactions are in fair agreement with the data. They attribute a significant role to the $g_{9/2}$ neutron orbital for every state observed in this measurement. In fact, in most cases, significant $\nu g^2_{9/2}$ and $\nu g^3_{9/2}$ configurations are part of the wave functions. [..] Even though the level structure of ^{67}Ni appears to exhibit a single-particle character based on comparisons [..] with the results of shell-model calculations, it is suggested that the yrast and near-yrast states are associated with rather complex configurations. In fact, calculations indicate that the wave functions of the yrast states involve a large number of configurations without a dominant ($\approx 50\%$) specific one, the latter being more prevalent in the near-yrast levels*". Since the $\nu d_{5/2}$ orbital is not included in the valence space ($f_{5/2}p_{3/2}p_{1/2}g_{9/2}$ outside a ^{56}Ni core) and no discussion on $5/2^+$ state is made, no theoretical

المنارة للاستشارات

interpretation can be given to these $5/2^+$ states observed in the presented (d,p) data based on the shell-model calculations of Ref. [Zhu12].

8.3 Estimated size of the $N = 50$ shell gap

The size of the $N = 50$ gap between the $\nu g_{9/2}$ and $\nu d_{5/2}$ orbitals can be inferred from the distribution of the single-particle strength of these orbitals over the excited states of a nucleus (see Eq. 2.22). Two problems must be considered here when estimating the gap size for the lighter nickel isotopes and in ^{67}Ni:

- In the ^{58,60,62,64}Ni(d,p) data at high excitation energy, multiple $\ell = 2$ states are identified. Because no distinction can be made between parallel and anti-parallel spin-orbit couplings, it is not clear whether these contributions originate from $\nu d_{3/2}$ or $\nu d_{5/2}$ neutron orbitals. In the case of the strongly fed states at lower excitation energies, it is reasonable to assume contributions from the $\nu d_{5/2}$ orbital due to the order of the neutron orbitals.
- In ^{67}Ni, it is highly unlikely that the full $\nu d_{5/2}$ single-particle strength is observed in the present data. In total, the two $5/2^+$ states account for nearly 50% of the total $\nu d_{5/2}$ single-particle strength relative to the $\nu g_{9/2}$-single-particle strength.

Combining these two arguments leads to the fact that the $N = 50$ shell gap size cannot be precisely determined. However, based on the observed distribution a rough estimate of the gap size can be made relying on two assumptions.

- For ^{59,61,63,65}Ni, all observed $\ell = 2$ states are assumed to be contributions from the $\nu d_{5/2}$ orbital. The motivation for this point stems from the fact that both orbitals are spin-orbit partners and are expected to be separated by several MeV in energy, limiting the influence of the $\nu d_{3/2}$ orbital.
- In ^{67}Ni, a number of states assumed to be either $\ell = 0$ or 2 have been observed with small relative spectroscopic factors. In order to estimate the $N = 50$ shell gap size in ^{67}Ni, all these states are assumed to be of $\ell = 2$ character. Likewise, when calculating the center of gravity of the $\nu s_{1/2}$, all these highly excited states are assumed to be of $\ell = 0$ character.

The results of this analysis are shown in Figure 8.6 showing the spectroscopic factor weighted energy of all pfgds orbitals observed. Based on the data from Refs. [Cho73, Ful64, Wes91, Cos67, Ful63, Anf70, Hut74, Tur70, NND13], the

المنارة للاستشارات

$N = 50$ gap remains constant between ^{59}Ni and ^{65}Ni with an average gap size of 2.5-2.7 MeV. The position of the $\nu s_{1/2}$ orbital also lies in the vicinity of the $\nu d_{5/2}$ orbital. The evolution of the summed relative spectroscopic factors for a given orbital relative to the summed $\nu g_{9/2}$ single-particle strength in a given isotope is shown in Figure 8.7. Here the summed strengths of the $\nu d_{5/2}$ and $\nu s_{1/2}$ orbitals both exceed unity. It should be noted that the unidentified $\ell = 0$ and 2 states are counted twice in this evaluation. The results of this analysis are shown in Figure 8.6 showing the spectroscopic factor weighted energy of all pfgds orbitals observed. Based on the data from Refs. [Cho73, Ful64, Wes91, Cos67, Ful63, Anf70, Hut74, Tur70, NND13], the $N = 50$ gap remains constant between ^{59}Ni and ^{65}Ni with an average gap size of 2.5-2.7 MeV. Also the position of the $\nu s_{1/2}$ orbital lies in the vicinity of the $\nu d_{5/2}$ orbital. The evolution of the summed relative spectroscopic factors for a given orbital relative to the summed $\nu g_{9/2}$ single-particle strength in a given isotope is shown in Figure 8.7. Here, the summed strengths of the $\nu d_{5/2}$ and $\nu s_{1/2}$ orbitals both exceed unity. It should be noted that the unidentified $\ell = 0$ and 2 states are counted twice in this evaluation.

Within the limitations of the data available for ^{67}Ni, the size of the $N = 50$ shell gap remains constant with an estimated gap size of 2.6 MeV. This observation hints towards limited occupation of the $\nu g_{9/2}$ orbital in this ^{66}Ni ground state configuration since the $N = 50$ gap is expected to open up while adding neutrons to this orbital (see Section 1.2.4). Despite the fact that this value for the $N = 50$ gap size is 1.2 MeV larger than the $E(2_1^+)$ in ^{66}Ni (1.425 MeV) the influence of the $\nu d_{5/2}$ orbital on the structure of the $5/2_{1,2}^+$ states is substantial as inferred from their relative spectroscopic factors.

The summed relative spectroscopic factor of the uncharacterized states above 3 MeV equals 0.55. This means that the total summed $\ell = 0$ and 2 relative spectroscopic factor is compatible with 2 and suggests that the full $\nu d_{5/2}$ and $\nu s_{1/2}$ single-particle strength is exhausted. It should be noted that this discussion relies on the purity of the $9/2_1^+$ state which is here assumed to include the full $\nu g_{9/2}$ single-particle strength. In that sense, the data points in Figure 8.7 for ^{67}Ni can be regarded as upper limits.

Because the determination of the center of gravity is done for each orbital individually, systematic errors in the determination of the (relative) spectroscopic factors do not influence the determined energy position of the orbital under investigation. Sources of systematic errors might be the geometry of the nucleon binding potentials and strength of the spin-orbit interaction.

As a final note, this estimated gap size can be compared to the calculations performed in [Sie12] (see Figure 1.6 on p. 14). These calculations estimate the $N = 50$ shell gap size to be around 1.5-2 MeV near ^{68}Ni. The observed and

المنارة للاستشارات

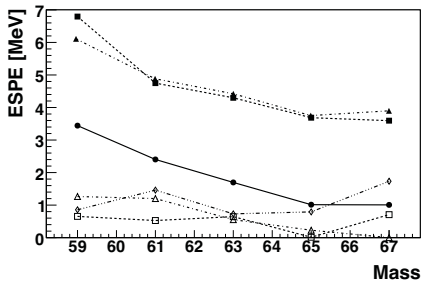

Figure 8.6: Evolution of effective single-particle energies in the odd-A nickel chain. Evaluation of orbital centroids in $^{59-65}$Ni based on [NND13].

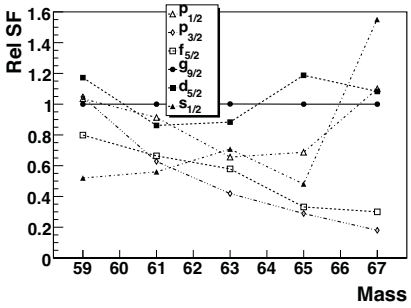

Figure 8.7: Evolution of relative spectroscopic factors in the odd-A nickel chain. Data for $^{59-65}$Ni taken from [NND13].

constant $N = 50$ shell gap of ≈ 2.6 MeV along the $^{59-67}$Ni chain is slightly bigger and tracking the evolution of this gap with increasing $\nu g_{9/2}$-occupation would provide valuable information to verify the proposed evolution of the effective single-particle energy due to three-body monopole interactions present in atomic nuclei [Ots10a].

8.4 Comparison with ^{90}Zr region ($Z = 40, N = 50$)

Additional information can be obtained by studying systematics in the ^{90}Zr-region ($Z = 40, N = 50$). Here the Fermi level for the protons is located near the $Z = 40$ HO shell closure, while the neutrons form a solid closed $N = 50$ shell (see Figure 8.8). Hence, this region serves, by looking at proton single-particle structure in the $N = 50$ odd-Z isotones, as a mirror for the neutron structures in ^{68}Ni.

In Figure 8.9, the limited systematics obtained from single-proton transfer reactions for the odd-A $N = 50$ isotones are shown. $5/2^+$ and $9/2^+$ positive-parity states and negative-parity states with a dominant single-particle contribution to the wave function have been included [NND13, Pic69, Knö70, Med75]. As the $Z = 40$ HO shell closure is approached, the observed strength in the negative parity orbitals (below $Z = 40$) gradually vanishes as expected. When focusing on the positive-parity states a swift change in structure can be observed between ^{87}Rb and ^{91}Nb. The single-particle $d_{5/2}$ strength at low energy gradually increases and one dominant single-particle state is found in

المنارة للاستشارات

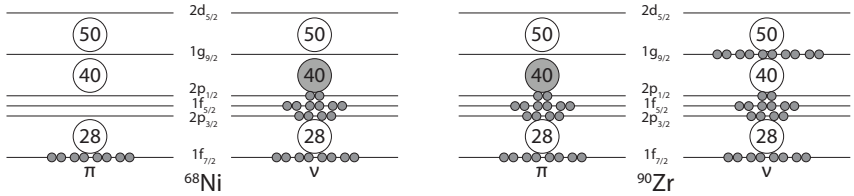

Figure 8.8: Comparison between orbitals occupied in ^{68}Ni and ^{90}Zr, having a closed N and $Z = 40$ HO shell respectively.

^{91}Nb (across the $Z = 40$ gap). In ^{87}Rb, a collection of positive-parity $(5/2^+)$ states is observed in the 3 to 4 MeV region. This energy corresponds to the sum of the energy of $9/2^+_1$ and the energy of the 2^+_1 or 4^+_1 in the underlying ^{86}Kr core. These excitation energies have been indicated by the circles and squares in Figure 8.9. The fact that these states have only marginal single-particle strength contained in them and that $1/2^+$ to $13/2^+$ (4152 keV) states are observed [Zha04] confirm this picture. In ^{89}Y, the situation is slightly different because the $5/2^+_1$ state at 2222 keV is very weakly observed in the (^{3}He,d) reaction, indicating its nearly purely core-coupled. The $5/2^+$ at 3715 keV carries a more pronounced amount of single-particle strength, but still the strength is mainly fragmented over a large number of excited states [Vou71]. Once past $Z = 40$ one dominant single-particle $5/2^+$ state emerges, carrying 43% of the available strength.

A direct comparison between ^{67}Ni and its ^{89}Y counterpart near ^{90}Zr is shown in Figure 8.10. Both the energy and relative spectroscopic factors of the negative parity pf-states are in good agreement. Only the $5/2^-$ state shows a deviation. The energy difference can be attributed to the attractive $\pi f_{5/2}\nu g_{9/2}$ tensor interaction, which binds the $\pi f_{5/2}$ orbital more strongly as the $\nu g_{9/2}$ is filled in ^{89}Y. This is not the case in ^{67}Ni and explains the energy difference. The $1/2^-$ ground state in ^{89}Y also has a strong relative spectroscopic factor, similar to the one measured in ^{67}Ni. Data from the ^{88}Y(d,^{3}He)^{87}Rb reaction can be used to estimate the ground state neutron orbital occupancies in ^{88}Y [Li87]. From this, $(2J + 1)S$ factors of 3.8 ($\pi p_{3/2}$), 6.0 ($\pi f_{5/2}$), >0.4 ($\pi p_{1/2}$) and 1.0 ($\pi g_{9/2}$) are found. Despite the high occupation of the $\pi p_{3/2}$ and $\pi f_{5/2}$ orbitals, some single-particle strength can be found in the proton adding reaction. The occupation of the $\pi p_{1/2}$ in ^{89}Y is lower than the one of the $\nu p_{1/2}$ in ^{67}Ni, but despite this, at least 25% occupancy a high relative spectroscopic factor is measured in the proton-adding reaction.

The main difference between ^{67}Ni and ^{89}Y can be seen in the distribution of positive-parity single-particle strength. In ^{67}Ni, two $5/2^+$ states carry in total

المنارة للاستشارات

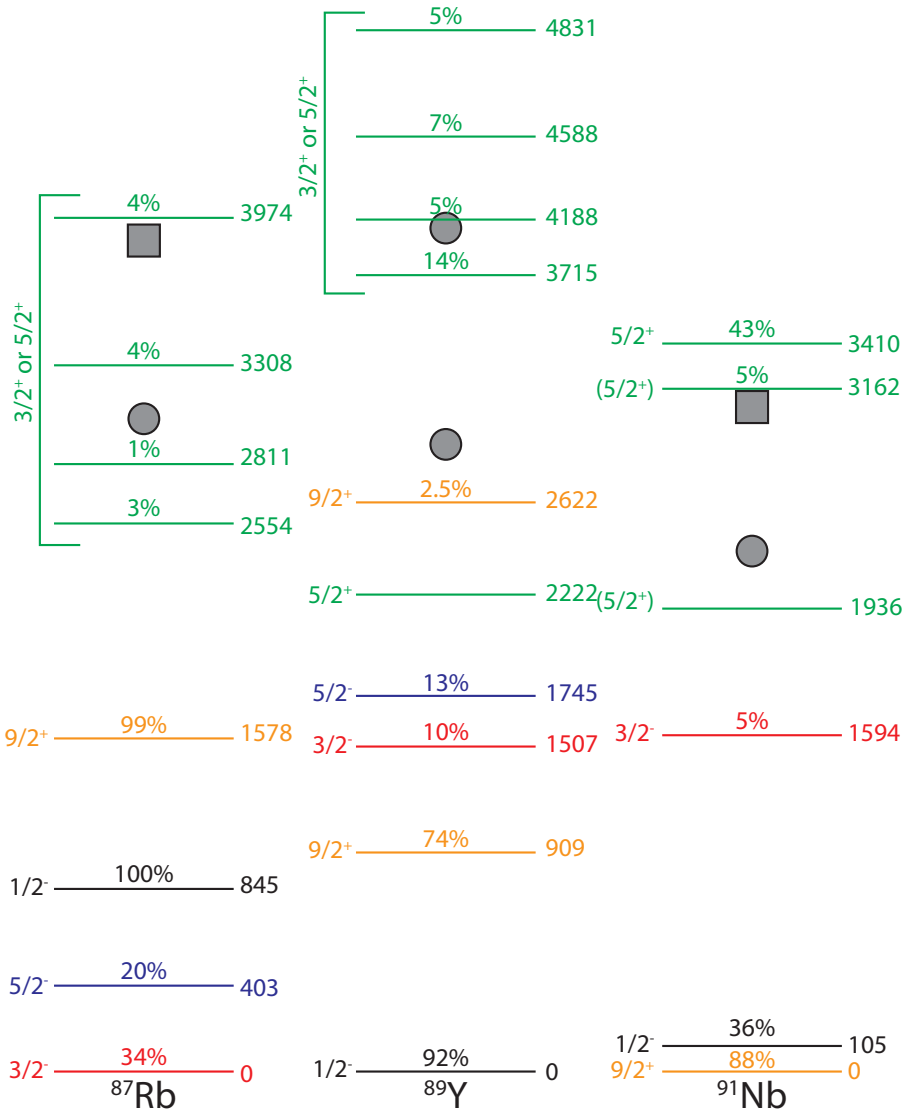

Figure 8.9: Systematics of low-lying states in the $N = 50$ odd-A isotones. Low-lying and positive parity $5/2^+$ and $9/2^+$ states have been included. The percentages indicate the fraction of the $(2J + 1)$ single-particle strength in the level. The circles and squares denote the energy of 2^+ and 4^+ states in the underlying core increased with the energy of the $9/2^+_1$ state. Data taken from [NND13, Pic69, Knö70, Med75, Vou71]

المنارة للاستشارات

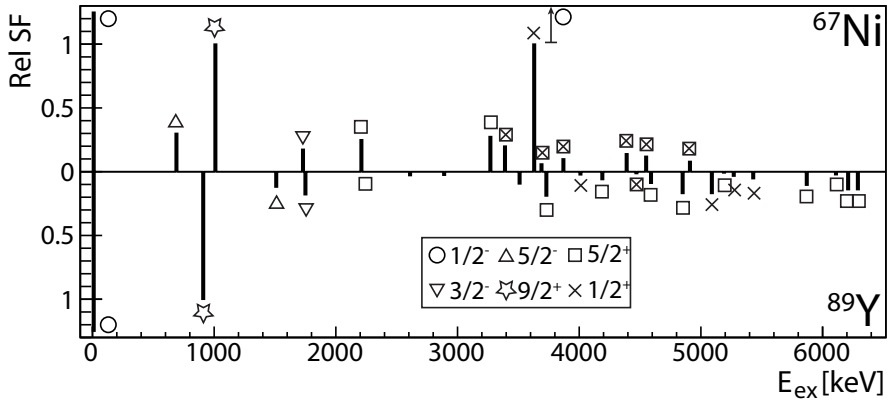

Figure 8.10: Direct comparison of relative spectroscopic factors ($9/2^+_1$ is reference state) in ^{67}Ni and ^{89}Y. Data of ^{89}Y taken from [Vou71].

$\approx 50\%$ of the $\nu d_{5/2}$ single-particle strength (relative to the $9/2^+_1$) at excitation energies of 2207 and 3277 keV. At comparable excitation energies (2222 and 3720 keV) in ^{89}Y $5/2^+$ states are found. However, the former is very weakly populated in proton-adding reactions, indicating no contributions from $\pi d_{5/2}$ single-particle configurations, while the later has a 0.11 relative spectroscopic factor. This comparison indicates a more outspoken influence of the $\nu d_{5/2}$ orbital on the structure near ^{68}Ni than the $\pi d_{5/2}$ orbital has near ^{90}Zr. This hints to the conclusion that the $Z = 50$ shell gap is more pronounced and stronger in the ^{90}Zr mass region, leading to less influence at lower excitation energy. From the distribution of $\ell = 2$ single-particle strength, the $Z = 50$ shell gap in ^{89}Y and ^{91}Nb is estimated to be ≈ 3.9 MeV [Vou71, Knö70], which is 1.3 MeV wider than the estimated $N = 50$ gap size in ^{67}Ni.

In Ref. [Ji 89], a systematic comparison is made between the $N = 50$ isotones (both odd and even masses) and shell-model calculations using an inert ^{78}Ni core and active $0f_{5/2}, 1p_{3/2}, 1p_{1/2}$ and $0g_{9/2}$ proton valence space, with a vertical truncation limiting only four protons at most to be excited to the $0g_{9/2}$ orbital. Note that the $1d_{5/2}$ orbital is not included in the model space. In the case of ^{87}Rb two $5/2^+$ states are predicted by the calculations at 2792 keV and 3239 keV. The corresponding levels in the experimental level scheme of ^{87}Rb are reported to be 2811 keV and 3308 keV. The information from (^{3}He,d) proton transfer data [Med75] and shell model calculations [Ji 89] are shown in Table 8.2. The $5/2^+$ states reported in the SM calculations are due to seniority > 1 couplings in the $g_{9/2}$ orbital since they appear without including the $d_{5/2}$ orbital in the calculation. This picture is in agreement with the discussion

المنارة للاستشارات

$5/2^+$

SM [Ji 89]			Experiment [Med75]	
E_{calc}	$E_{\text{corresponding}}$	J^π [Med75]	E_{exp}	$(2J+1)S$
		$3/2^+$,$5/2^+$	2555	0.11
2792	2811	$3/2^+$,$5/2^+$	2811	0.024
3239	3308	$3/2^+$,$5/2^+$	3308	0.25
		$3/2^+$,$5/2^+$	3974	0.24
		$3/2^+$,$5/2^+$	4146	0.021
		$3/2^+$,$5/2^+$	4379	0.35
		$3/2^+$,$5/2^+$	4492	0.19

Table 8.2: Comparison of energies of $5/2^+$ states in ^{87}Rb. Data taken from Refs. [Ji 89, Med75]

above, showing that no substantial $\nu d_{5/2}$ single-particle strength is present up to 4 MeV. However, the first $\ell = 2$ state at 2554 keV is identified as a $7/2^+$ state in the SM calculation, in contradiction with the available data. From Figure 8.9 it is clear that clusters of positive parity states are found in the vicinity of the energy of $E(9/2^+) + E(2^+, 4^+{}_{\text{core},^{86}\text{Kr}})$ (indicated as a circle (2^+) and square (4^+)). As $S(2J+1)$-values for these states are small (see Table 8.2 and Ref. [Med75]), a core-coupled or high seniority interpretation is supported for the majority of these states, with only small contributions from νgds single-particle strength.

Other SM studies like e.g. Ref [Her97], using only the $1p_{1/2}, 0g_{9/2}$ valence space ($A = 86-100$, $N, Z < 50$) manage to reproduce most spectroscopic information in this neighborhood, supporting the limited influence of the $1\pi d_{5/2}$-orbital in the ^{90}Zr-region. A more recent SM study found in Ref. [Hon09] using the $p_{3/2}, f_{5/2}, p_{1/2}$ and $g_{9/2}$ model space also reproduces the the low-lying structure in the odd-Z $N = 50$ isotones, but no mention is made of $5/2^+$ states. However it is noted that "*for nuclei in the middle of the present $f_{5/2}g_{9/2}$ shell, very large B(E2) values are observed [..] suggesting significant deformation. [..] The present model space is insufficient to describe such a large quadrupole collectivity because of the lack of the $f_{7/2}$ and $d_{5/2}$ orbitals [..]*".

The evolution of the $\ell = 2$ single-particle strength distribution (relative to the $9/2^+_1$ state) both in the nickel and zirconium region is shown in Figure 8.11. This includes both the distribution of $\nu d_{5/2}$ and $\nu d_{3/2}$ single-particle strength because no distinction can be made between these two in transfer reactions. However, since the $\nu d_{3/2}$-orbital is expected to be found at high energy, contributions to $3/2^+$ states at low energy are expected to be small. From this picture, the evolution of the split of the $\nu d_{5/2}$ single-particle strength can be seen. The evolution in the nickel chain has been discussed before and the increasing

المنارة للاستشارات

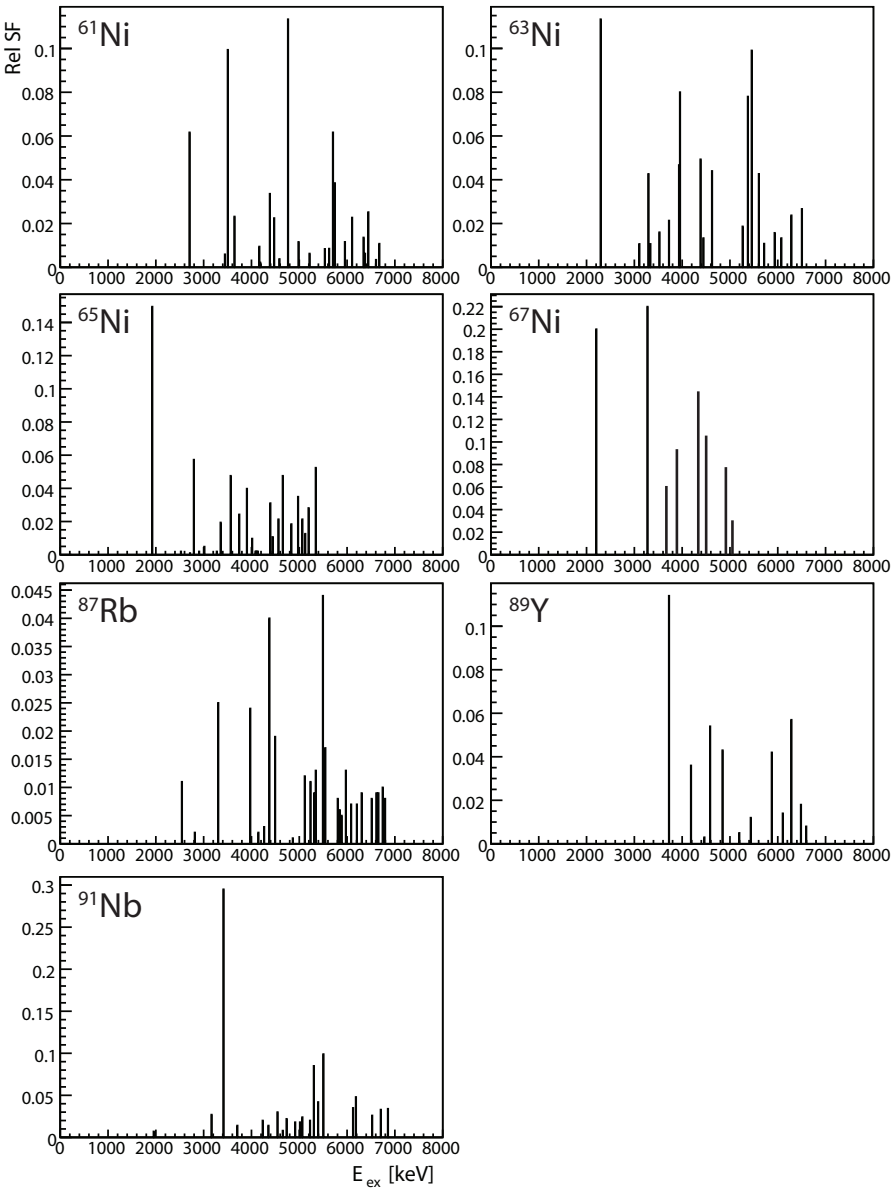

Figure 8.11: Distribution of the $\ell = 2$ strength (relative to $9/2^+_1$) in the nickel region (top) and zirconium region (bottom). See text for discussion. Data taken from Refs [NND13, Cho73, Ful64, Wes91, Cos67, Ful63, Anf70, Hut74, Tur70, Pic69, Knö70, Med75].

المنارة للاستشارات

importance of the $\nu d_{5/2}$ orbital can be tracked in this picture. If compared to the Zr-region, the picture looks different since the $\nu d_{5/2}$ single-particle strength gets concentrated at $Z = 39$ in a single level around 3.720 MeV. $5/2^+$ states below this state carry little or no single-particle strength, indicating limited mixing with $\pi g_{9/2}$ core coupled states.

المنارة للاستشارات

9

Conclusion

In this work, the experimental conditions, analysis and results of the ^{66}Ni(d,p)^{67}Ni one-neutron transfer reaction study in inverse kinematics have been compiled. This research aims at the characterization of the neutron single-particle structures and $N = 50$ shell gap in ^{67}Ni. Since the sequence of the $\nu g_{9/2} d_{5/2} s_{1/2}$ neutron orbitals is believed to generate the quick onset of deformation in the Fe and Cr isotopes below the nickel chain, probing these neutron orbitals could provide insight in this phenomenon.

The combination of the T-REX particle detection array and Miniball γ detectors were used for the first time to study successfully direct reactions in this mass region. The combination of these two detection arrays was crucial to isolate the different excited states populated in the reaction. The radioactive beam was produced at the ISOLDE facility and post-accelerated by REX to an energy of 2.95 MeV/A with an average intensity of 4 10^6 pps and purity of at least 99%.

A dedicated delayed coincidence technique was developed for this experiment, aiming specifically at studying μs-isomers and was successfully used to characterize the 1007 keV isomer in ^{67}Ni.

Based on information from γ-γ coincidences, γ-DCT coincidences and ^{67}Ni excitation energy deduced from proton kinematics the level and γ-decay scheme of ^{67}Ni has been significantly improved. Excited states up to an excitation energy of 5.8 MeV were observed. Due to limitations of the particle detection setup only proton angular distributions up to the 3621 keV state have been extracted reliably.

المنارة للاستشارات

The extracted angular distributions have been compared with DWBA calculations performed using FRESCO. Negative-parity pf states have been identified as well as positive-parity sdg states. Besides the characteristic shapes of the proton angular distribution, information from γ-branching ratios was used to fix spin and parities of the excited states. In this discussion, the firm spin assignment of the ground state ($1/2^-$) and 1007 keV isomer ($9/2^+$) were a key factor. For the identified states, relative spectroscopic factors were extracted with respect to the 1007-keV isomer.

At excitation energies of 2207- and 3277-keV $5/2^+$ states were discovered with a total summed relative spectroscopic factor of nearly 0.5, assuming $\ell = 2$ transfer. This observation of a significant contribution and concentration of $\nu d_{5/2}$ single-particle strength at low excitation energy hints towards the impact of the $\nu d_{5/2}$ orbital on the structure in this region.

The obtained results have been compared with systematics in the lighter $^{59-65}$Ni isotopes. The evolution of the distribution of $\nu d_{5/2}$ single-particle strength indicates an increased concentration of the single-particle strength with increasing neutron number. A comparison has been made with single-proton strength in ^{89}Y. An excellent agreement, both in excitation energy and single-particle strength, can be observed for the pfg-states. The $\ell = 2$ single-particle strength in ^{89}Y is however more fragmented and resides at higher excitation energy as opposed to ^{67}Ni. From the distribution of single-particle strength the size of the $N = 50$ (in the nickel isotopes) and $Z = 50$ shell gap (^{90}Zr region) could be estimated. In the case of the nickel isotopes, the shell gap remains constant at ≈ 2.6 MeV, while the $Z = 50$ shell gap is more pronounced around ^{90}Zr: 3.9 MeV. The more shallow $N = 50$ shell gap near ^{68}Ni can be seen as a reason for the influence and concentration of the $\nu d_{5/2}$ orbital at low excitation energy.

In ^{67}Ni an excited state at 3621 keV was found and is believed to be of $\ell = 0$ character fixing the spin and parity to $1/2^+$. The associated relative spectroscopic factor is consistent with 1. This would mean a high concentration of the $s_{1/2}$ single-particle strength in ^{67}Ni in contrast with large fragmentation in the lighter nickel isotopes. The reason for this remains unclear.

Outlook

In order to make a better estimation of the $N = 50$ shell gap size near ^{68}Ni, the ℓ character of all excited states should be pinned down. With the limitations of the present data and detection setup, it has been shown that excited states up to the neutron binding energy of 5.8 MeV are indeed populated in the one-neutron

المنارة للاستشارات

transfer reaction. In order to extract ℓ-transfer values some improvements are necessary:

- **Better energy resolution in the detection of reaction ejectiles**. In this way the individual excited states can be disentangled, which is not possible with the current setup.
- **Increased angular coverage for the detection of the ejectiles** is essential to correctly characterize excited states.
- **Higher beam energies** will lead to more pronounced angular distributions of the reaction ejectiles, facilitating ℓ-transfer assignments. See e.g. Figure 2.9.
- **Recoil identification** either by a ΔE-E_{rest} detector or mass spectrometer.

These four improvements can be achieved by the proposed project of coupling a Helical Orbit Spectrometer (HELIOS) [Lig10, Fre10] to the HIE-ISOLDE post-accelerated beams of 10 MeV/A [Lin08]. The principle of the HELIOS spectrometer [Wuo07] is to place the reaction target on the magnetic axis of a large superconducting solenoid. The ejectiles emitted in the reaction with the target are guided back to the magnetic axis in a helical motion and detected by position-sensitive detectors. The time-of-flight is related to the mass-to-charge ratio and is used for particle identification. The distance over which an ejectile is transported back is linearly related together with its energy to the energy in the center of mass. Hence, the measured energy spectrum under a fixed distance along the position sensitive detector will reflect the energy spacings in the CM frame of reference thus eliminating kinematical compression [Lig10]. Here, also the use of a single position sensitive detector rather than a ΔE-E_{rest} detector improves the energy resolution of the detected ejectiles. Coupling this system to a mass spectrometer or recoil identification system is not essential but is useful as an additional filter to select transfer reaction events. The downside of this measuring system is its size which prevents the use of a highly efficient γ-detection array such as Miniball.

The HELIOS system has been built and tested at Argonne National Laboratory using ^{28}Si beams at 6 MeV/A [Lig10], showing encouraging results.

A side product of the ^{66}Ni(t,p) two-neutron transfer experiment [Els13] performed in 2011 using the same experimental setup aiming at the characterization of excited states in ^{68}Ni is the (t,d) channel. The Q-value for this reaction is slightly negative (-449.5 keV) and will thus preferentially populated low-lying excited states. The analysis of this data can hence verify the results presented in this work [Cal13].

المنارة للاستشارات

Extending the odd-A systematics towards ^{78}Ni would ultimately allow the evolution of the $N = 50$ shell gap to be tracked and the doubly-magic character of ^{78}Ni to be probed. Furthermore, this allows the properties of the three-body monopole interaction responsible for the creation of the $N = 50$ shell gap to be verified and derived [Ots10b, Sie12]. However, producing these neutron-rich species in ISOL facilities is severely hampered by the slow diffusion of nickel out of the primary production targets. In-flight separators are able to produce these neutron-rich beams, but generally at higher energies with inferior ion-optical quality. At GANIL, the ^{68}Ni(d,p) reaction has been studied at 25 MeV/A. In this data, the splitting of $\nu d_{5/2}$ single-particle strength is also suggested [Mou11, Mou12]. Performing a study of the ^{68}Ni(d,p) experiment at ISOLDE would provide complementary data to those measured at GANIL and allow the combined method of extracting spectroscopic factors described in Ref. [Muk05] to be performed. During the ^{66}Ni(d,p) experiment, a fraction of the available beam time was dedicated to perform test with a post-accelerated ^{68}Ni beam. The beam intensity was estimated to be on the order of $\sim$ 1 E+5 pps with a ^{68}Ni purity of $\approx$ 15%.

It was mentioned on p. 160 that the SO potential was not taken into account when calculating the neutron bound states involved in the transfer reaction and possible consequences were discussed. Incorporating this SO-coupling term in the DWBA analysis will lead to small changes in the relative spectroscopic factors quoted in this work. It was also noted that for SO radii which are 10% smaller than those of the overall binding potential the effect of the non-inclusion of the SO term was small and does not alter the quoted spectroscopic factors within the present error bars. However it might be instructive to analyze the data presented here with different (more modern) reaction models (including e.g. deuteron break up, non locality and SO potentials) to assess the effect of these phenomena on the (relative) spectroscopic factors.

From the perspective of nuclear theory and shell-model calculation, the inclusion of the $\nu d_{5/2}$ orbital in the neutron valence space seems necessary. The detailed comparison between such calculation with the findings reported here would provide valuable input, both in the interpretation of the experimental data and understanding the structural driving mechanisms present in these nuclei.

المنارة للاستشارات

A

Various spectra

In the following pages, a collection of spectra is printed which was used during the analysis of the ^{66}Ni(d,p)-data, without further discussion as to improve the readability of the main text. Each page contains, for a given γ-ray energy used as primary gate, the proton-γ-γ-coincident spectrum, coincident ^{67}Ni excitation spectrum (deduced from proton kinematics) and p-γ-Delayed Coincidence spectrum. The gray part of the spectra are the sum of the background left and right of the primary γ gate.

المنارة للاستشارات

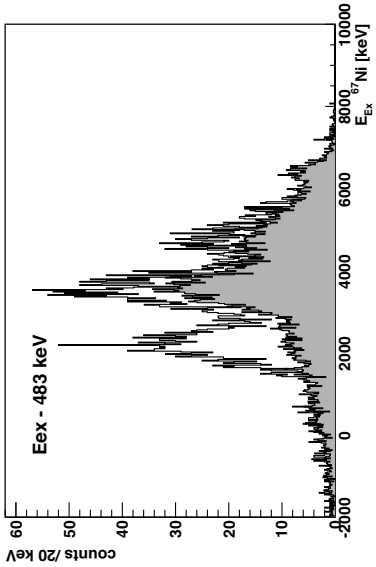

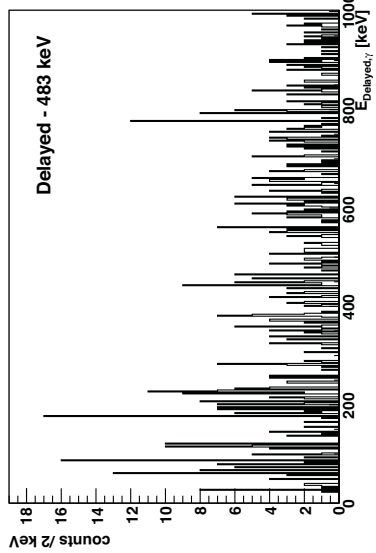

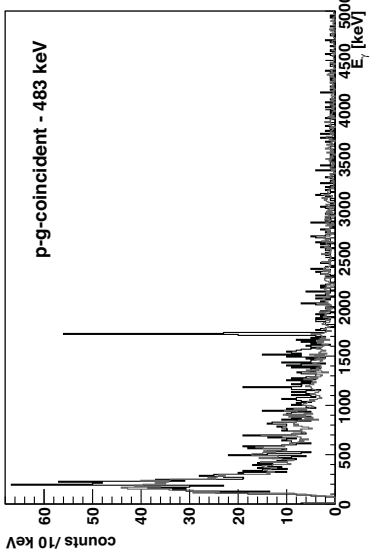

المنارة للاستشارات

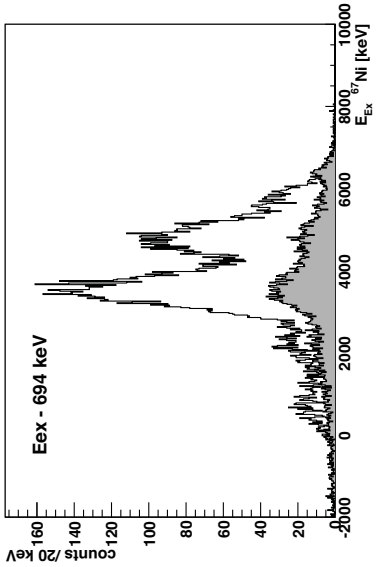

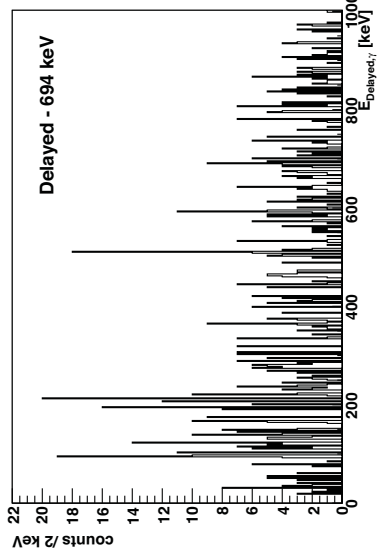

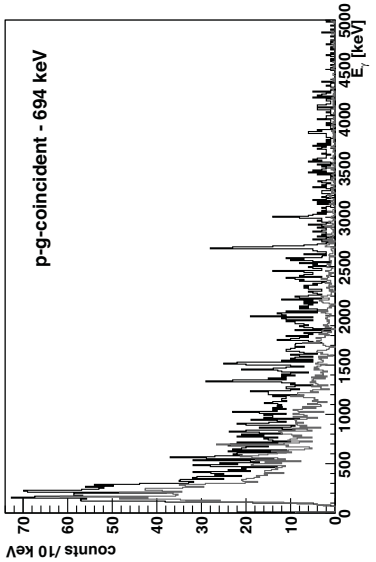

المنارة للاستشارات

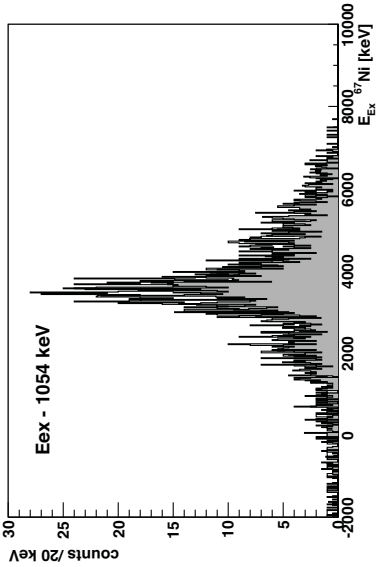

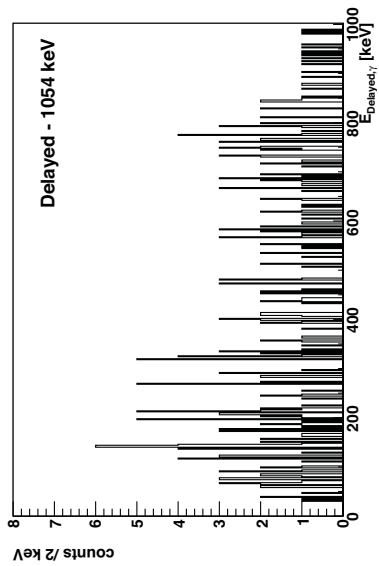

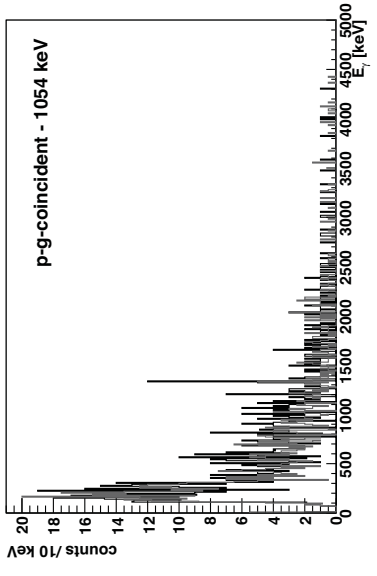

المنارة للاستشارات

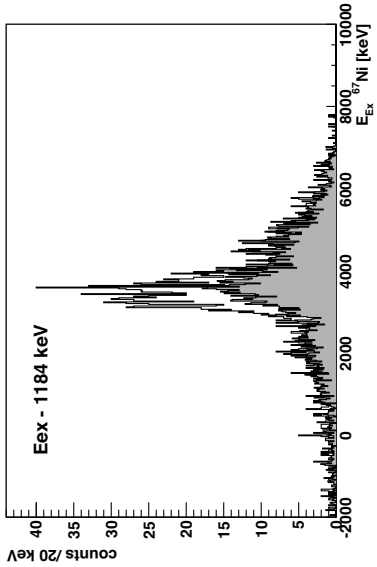

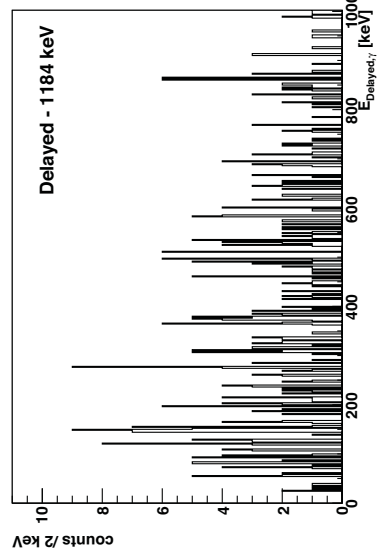

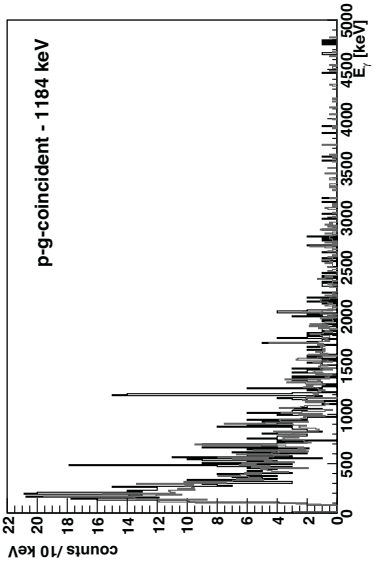

المنارة للاستشارات

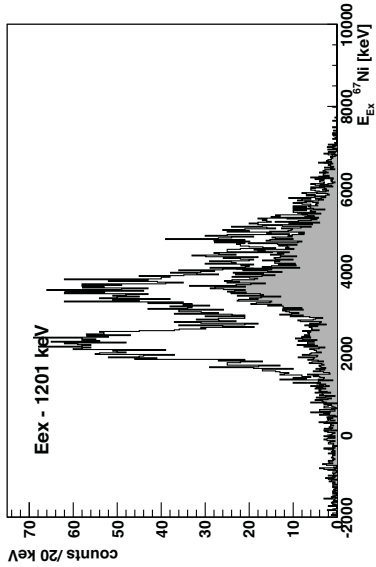

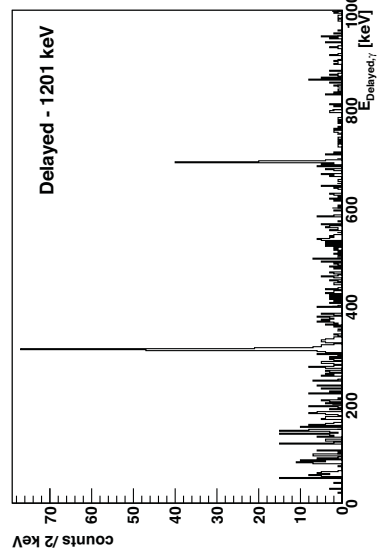

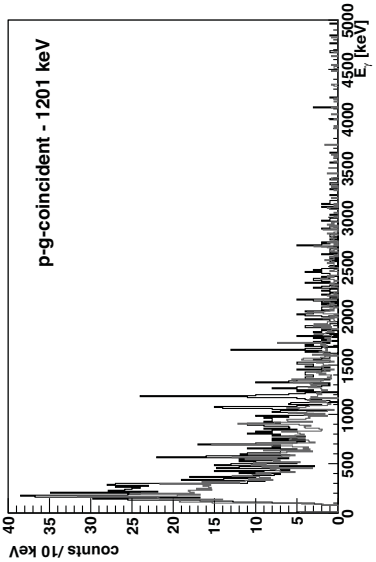

المنارة للاستشارات

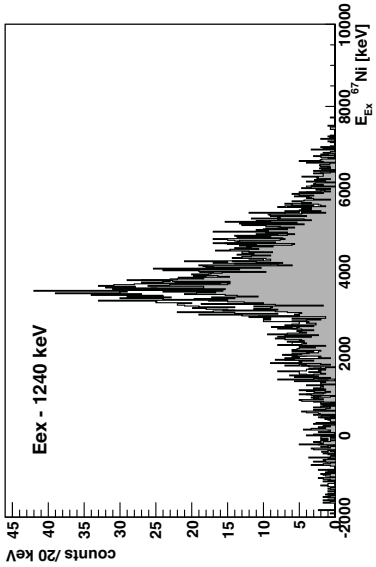

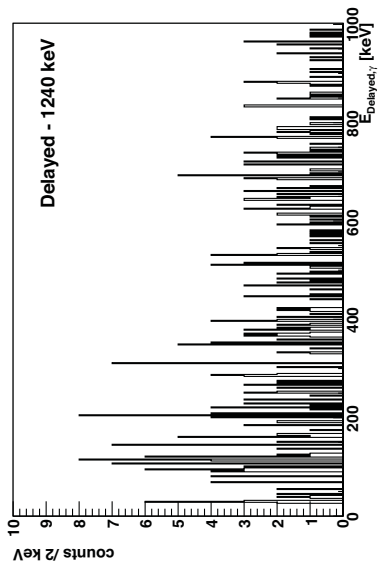

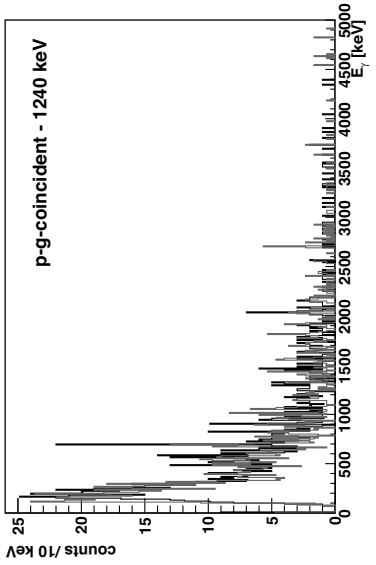

المنارة للاستشارات

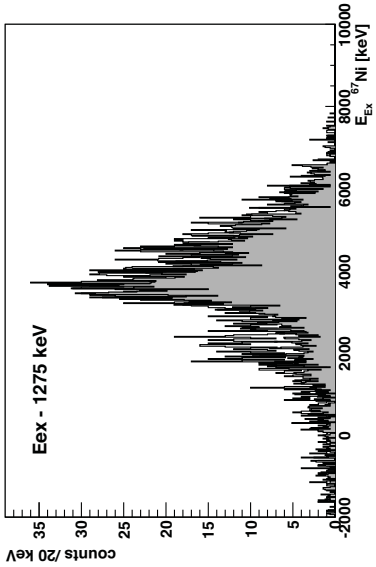

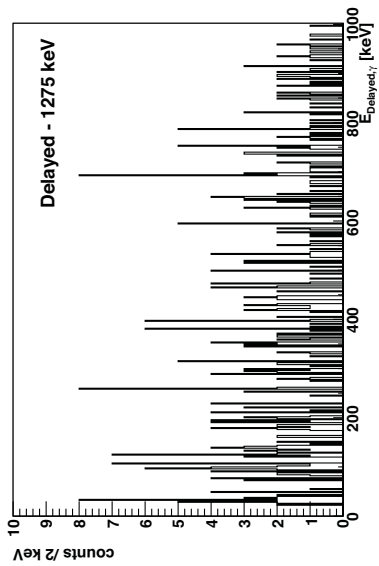

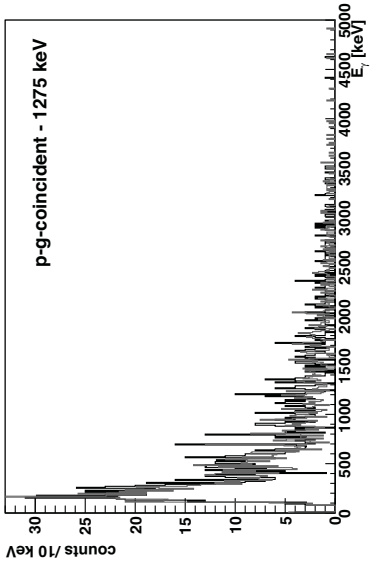

المنارة للاستشارات

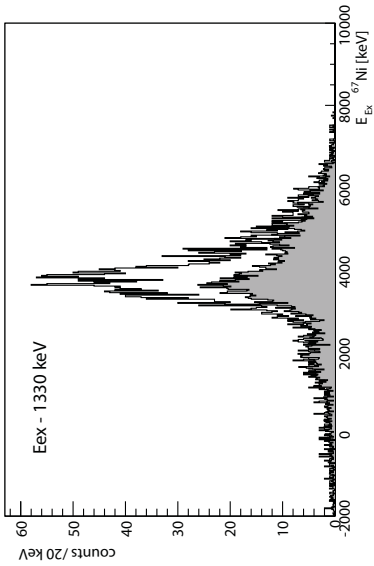

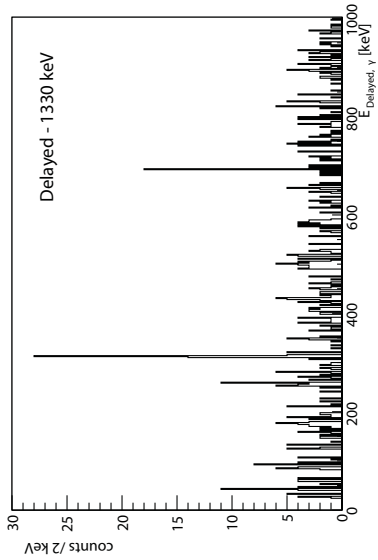

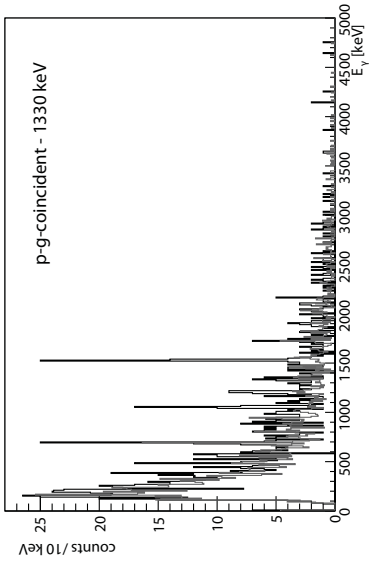

المنارة للاستشارات

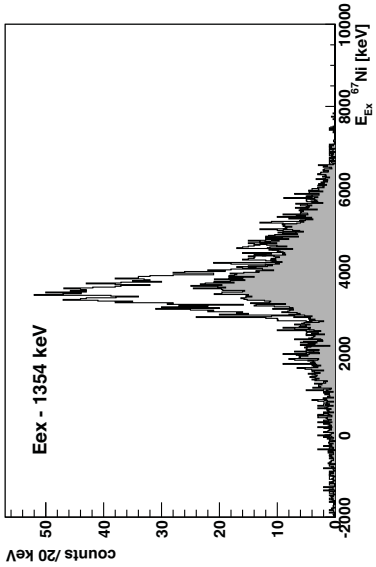

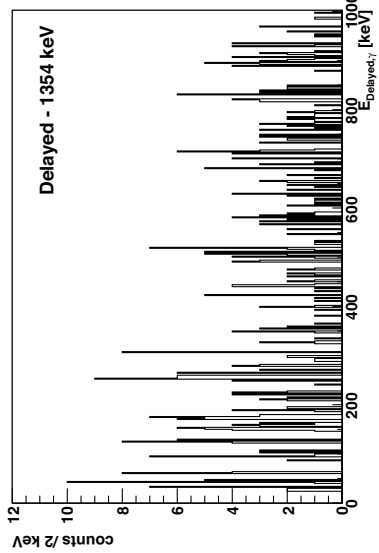

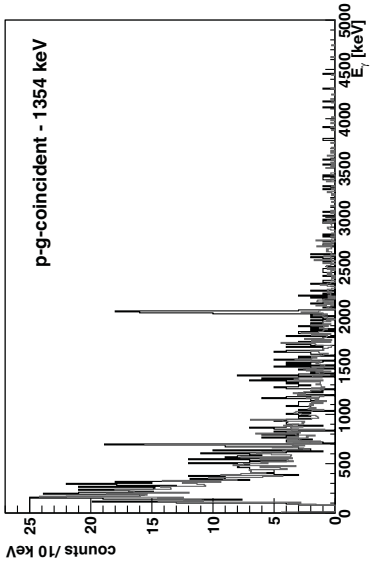

المنارة للاستشارات

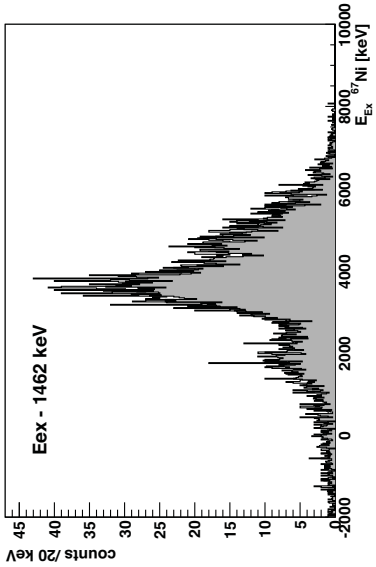

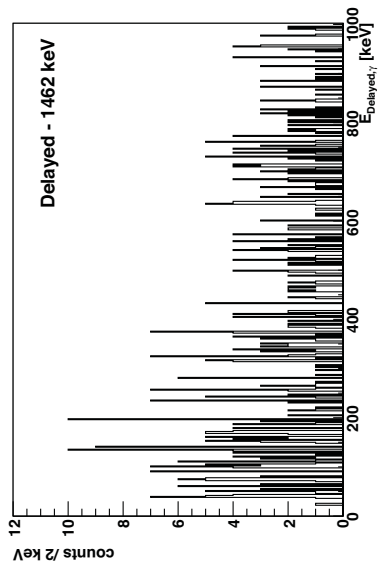

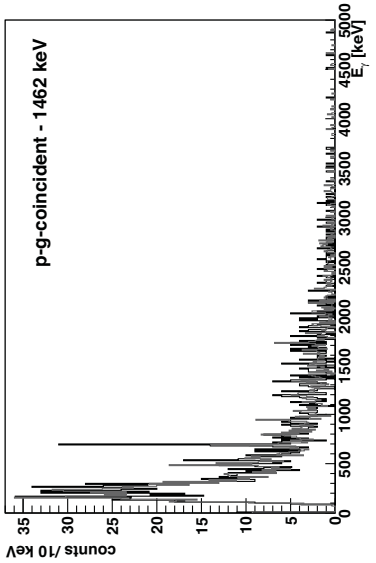

المنارة للاستشارات

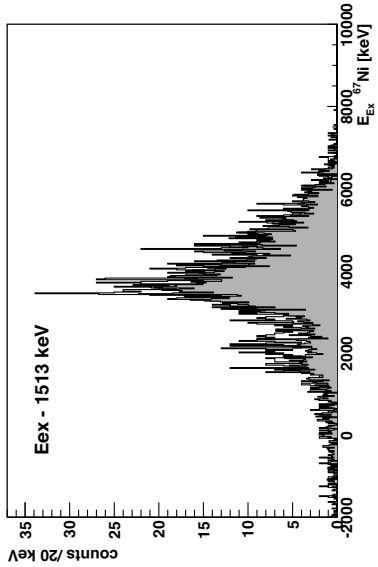

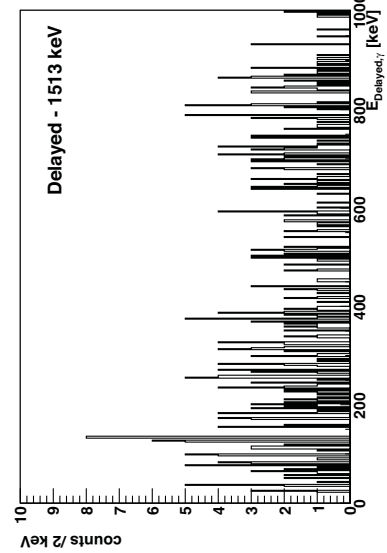

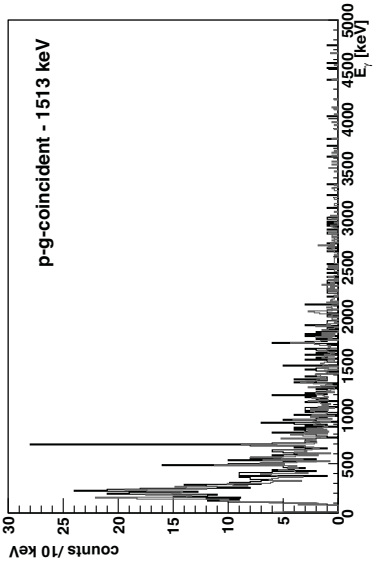

المنارة للاستشارات

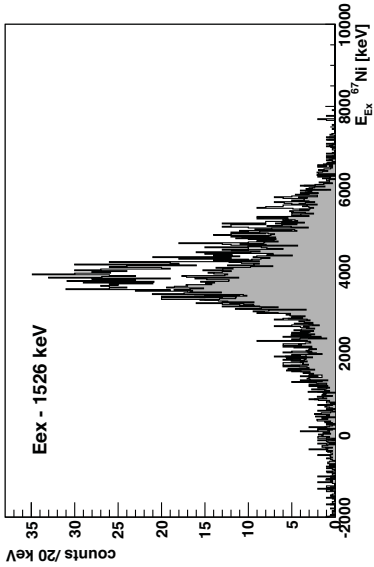

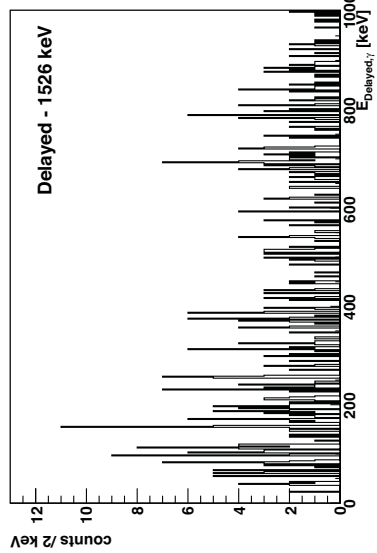

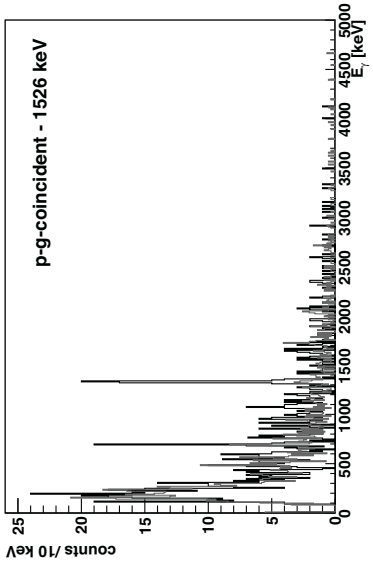

المنارة للاستشارات

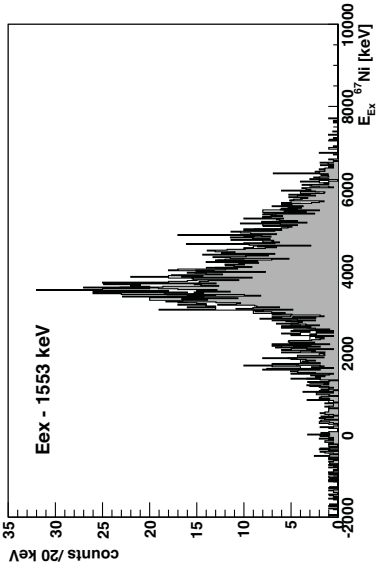

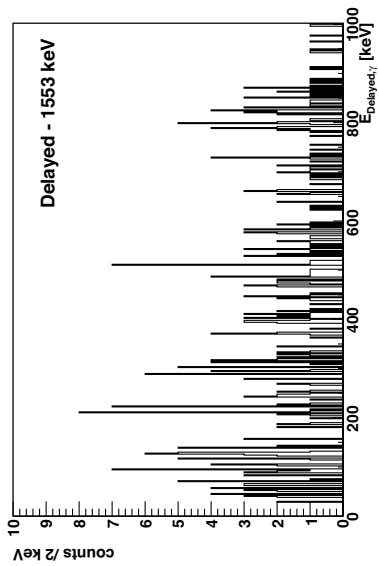

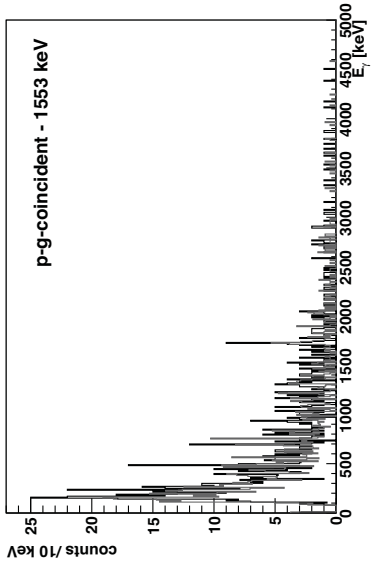

المنارة للاستشارات

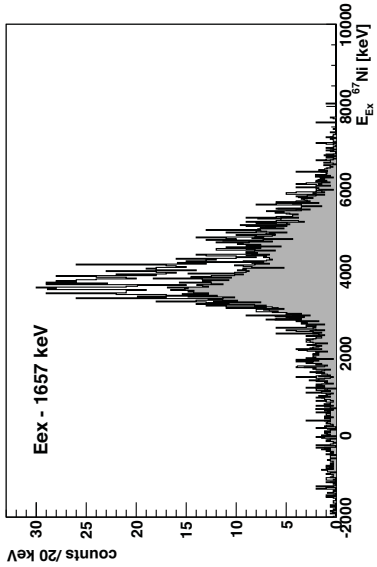

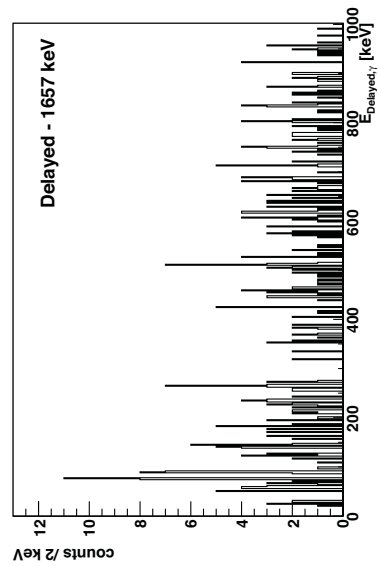

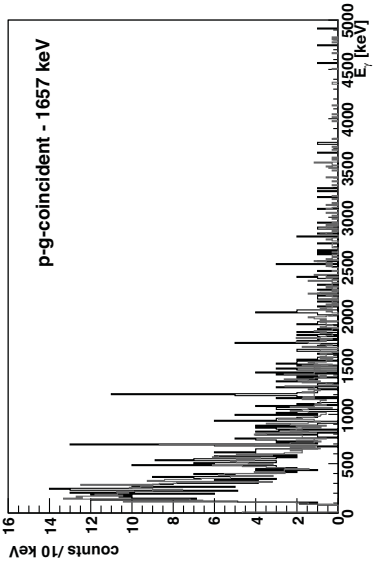

المنارة للاستشارات

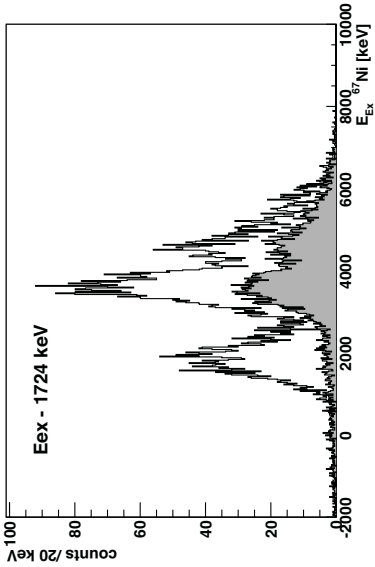

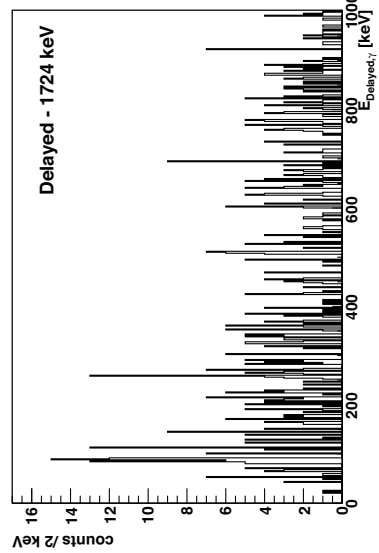

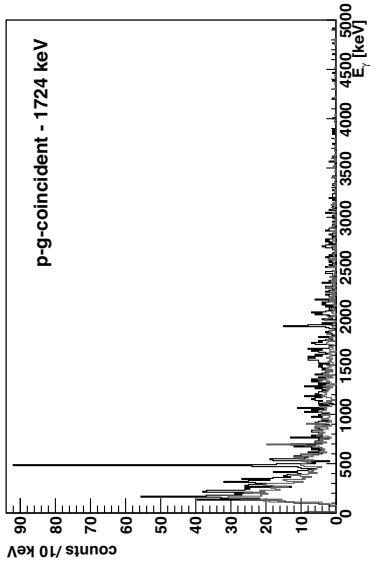

المنارة للاستشارات

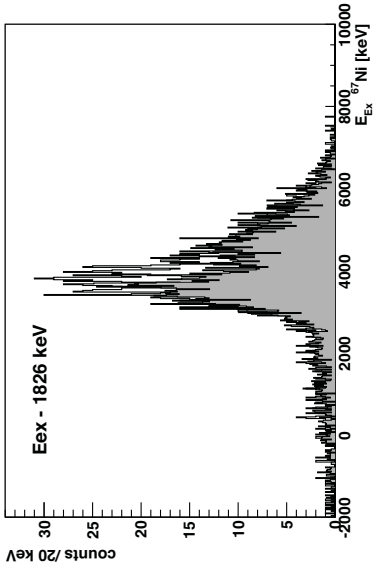

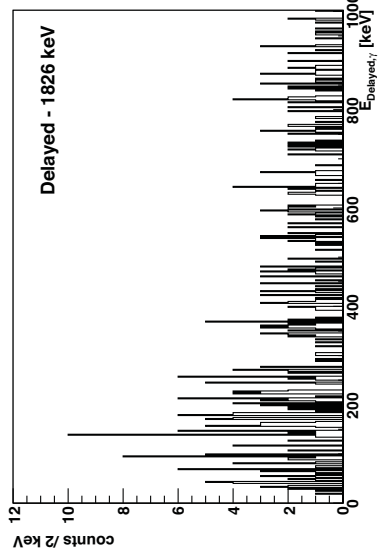

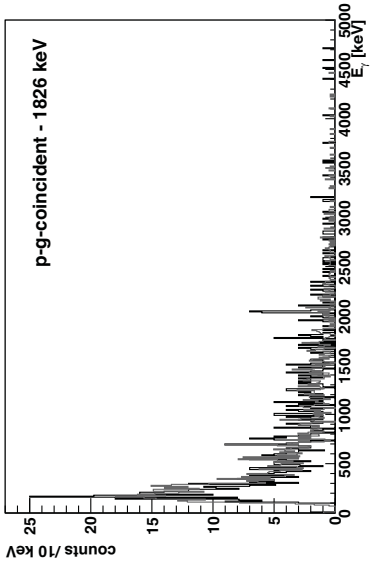

المنارة للاستشارات

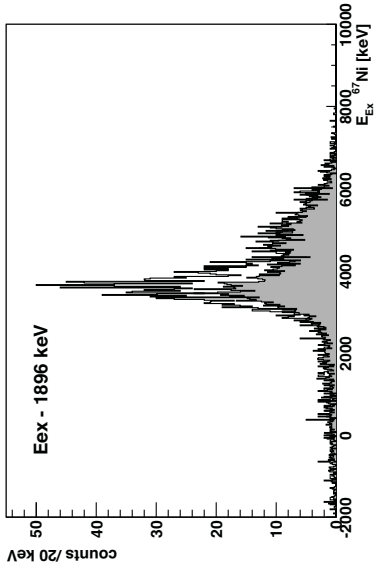

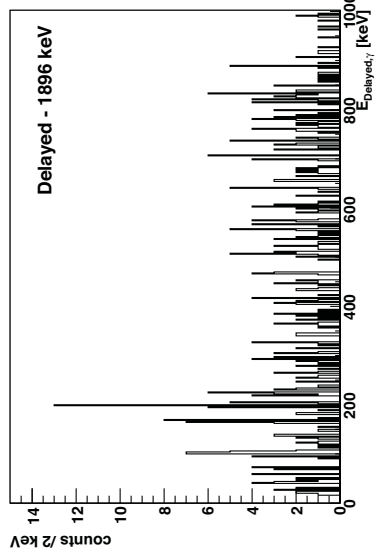

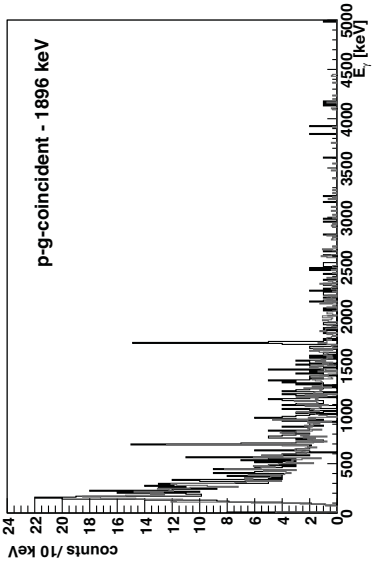

المنارة للاستشارات

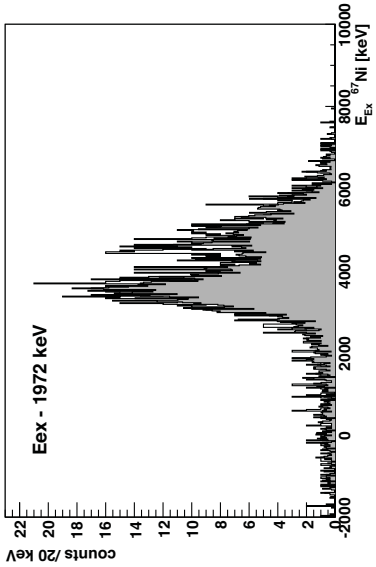

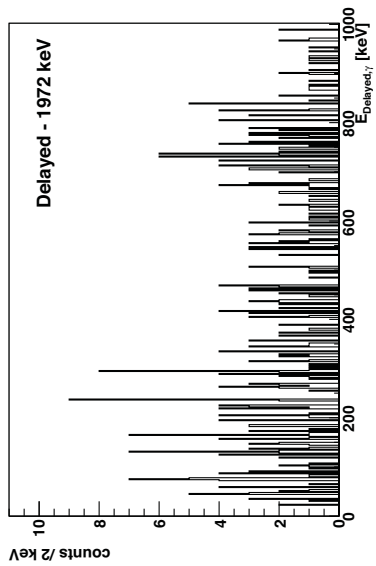

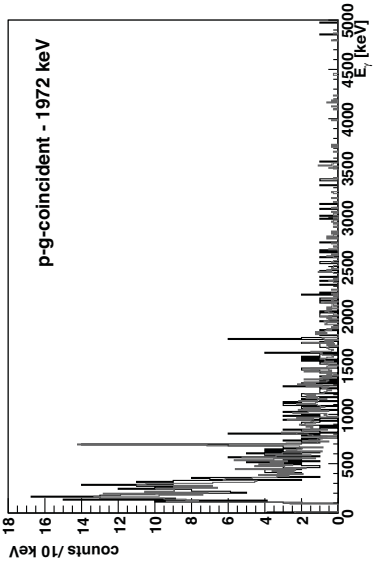

المنارة للاستشارات

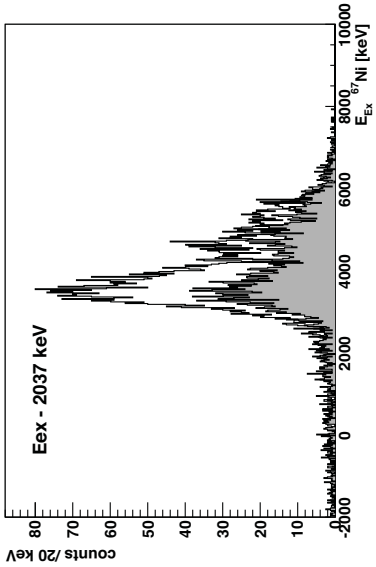

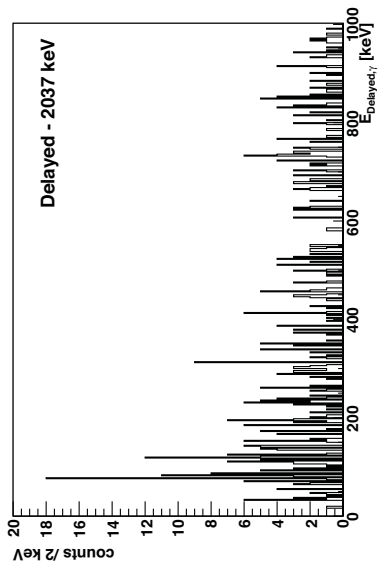

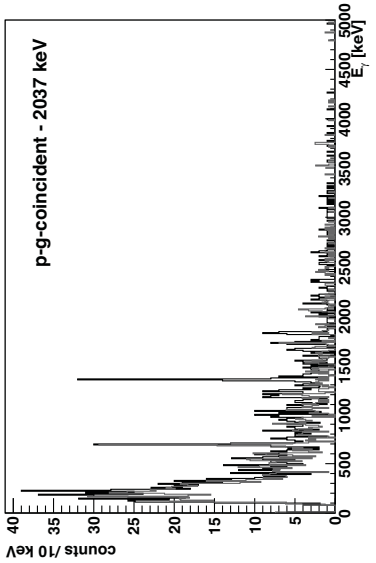

المنارة للاستشارات

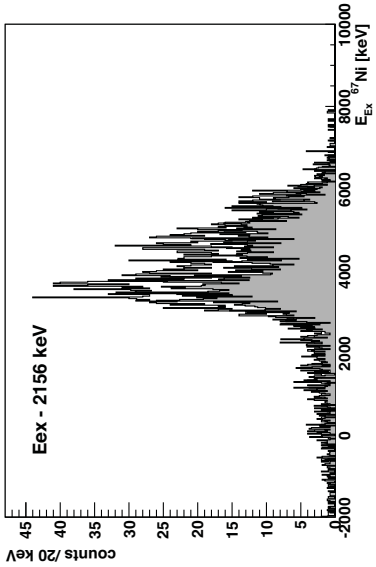

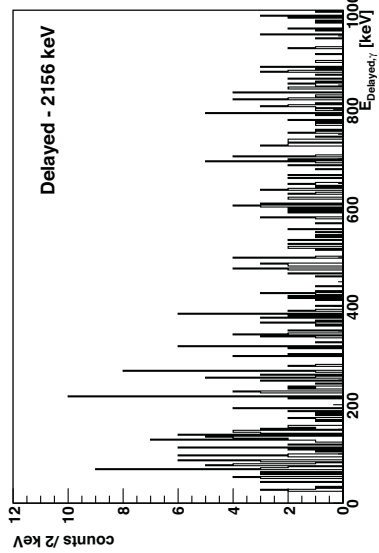

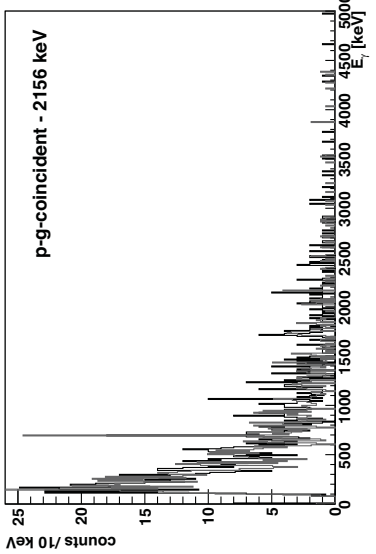

المنارة للاستشارات

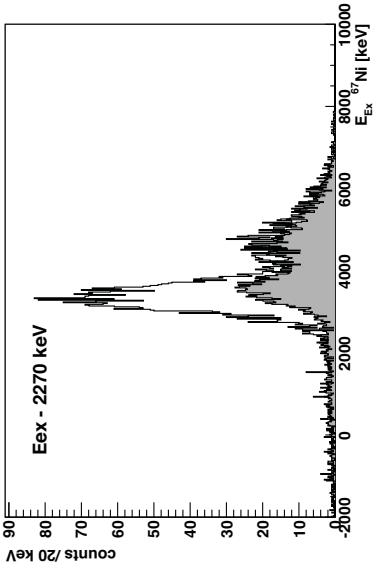

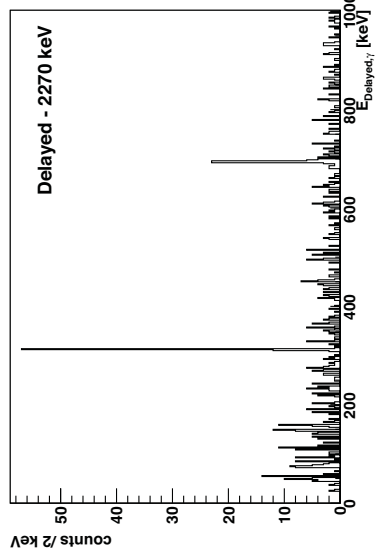

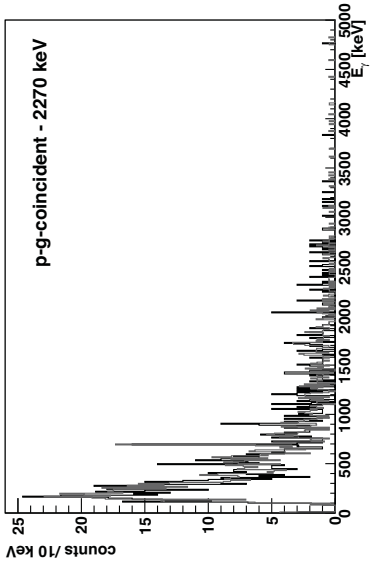

المنارة للاستشارات

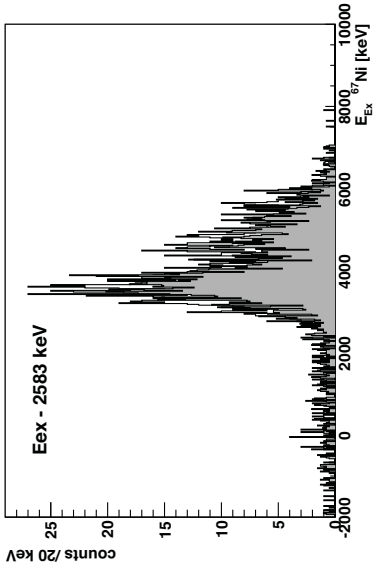

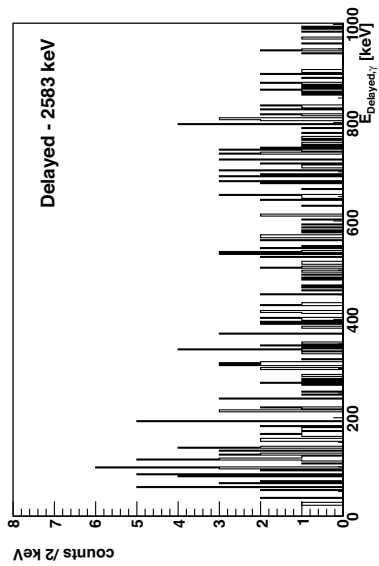

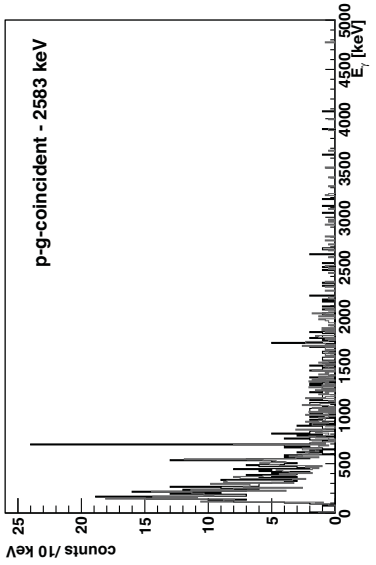

المنارة للاستشارات

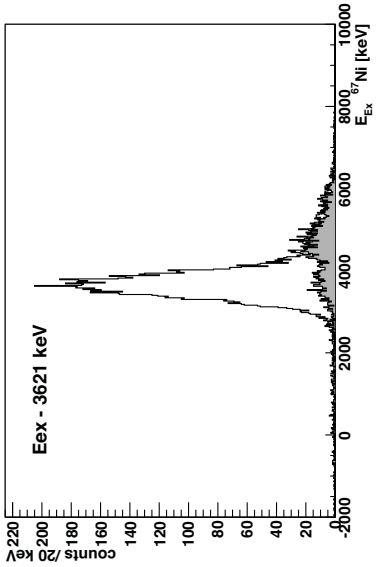

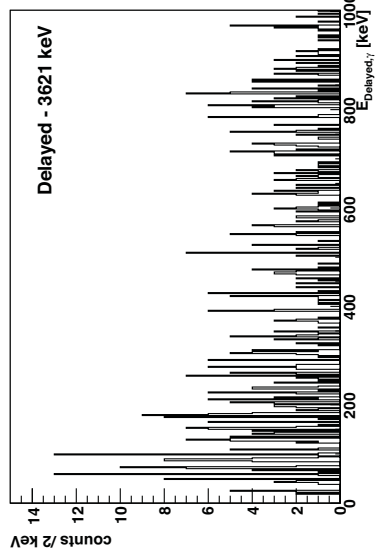

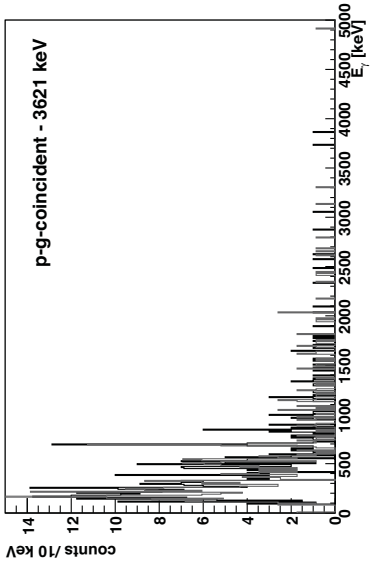

المنارة للاستشارات

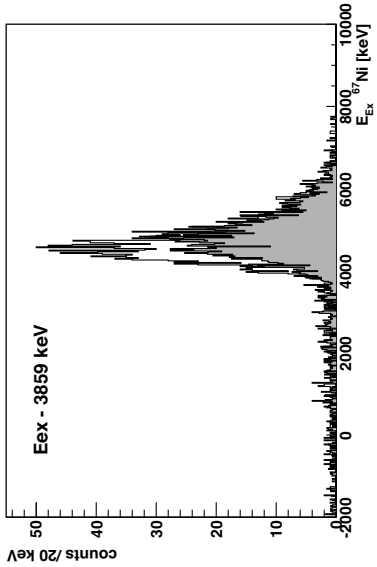

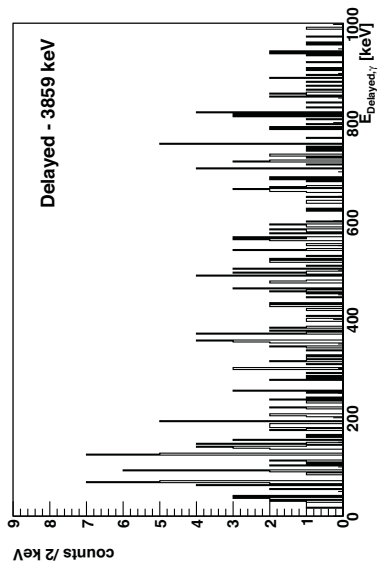

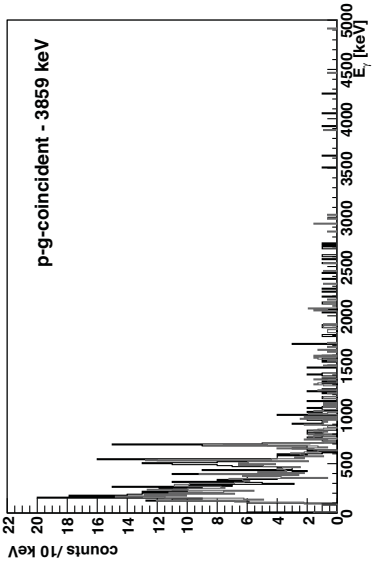

المنارة للاستشارات

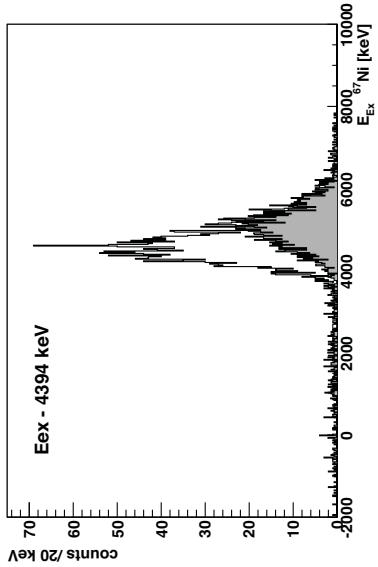

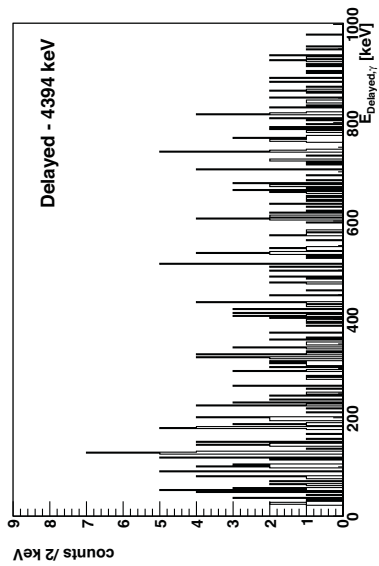

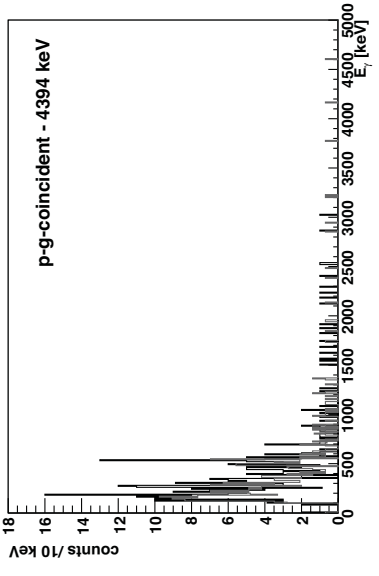

المنارة للاستشارات

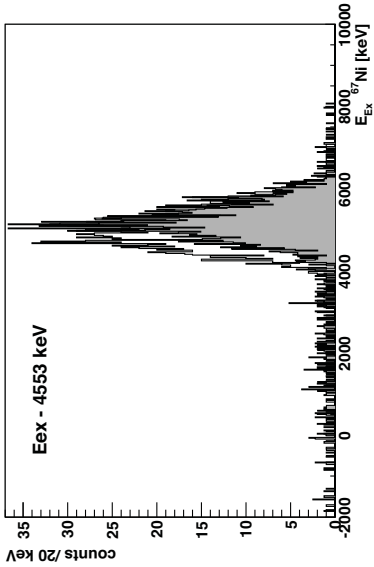

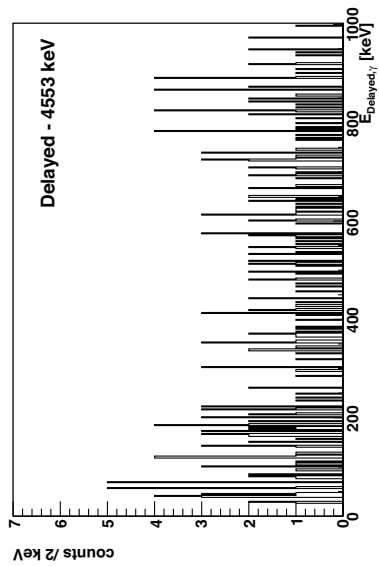

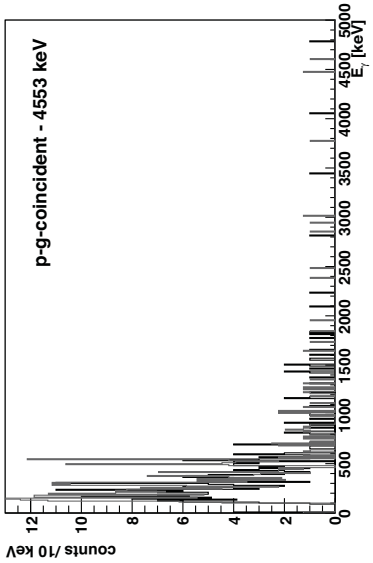

المنارة للاستشارات

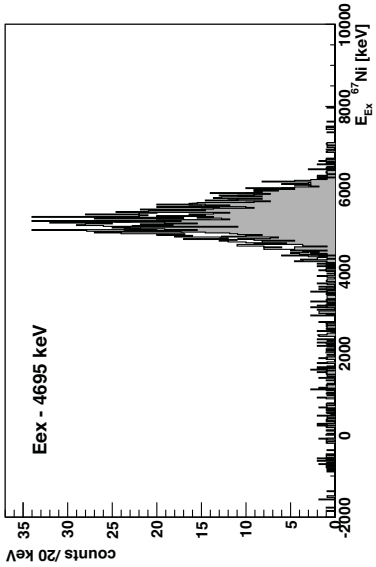

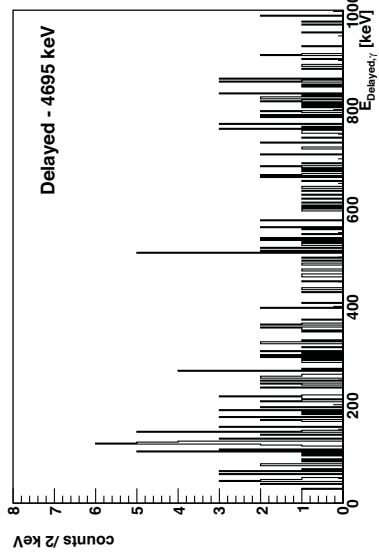

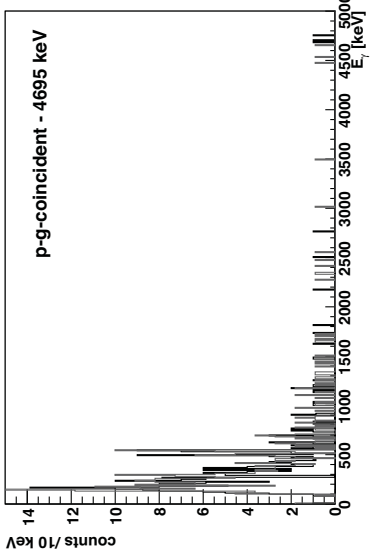

المنارة للاستشارات

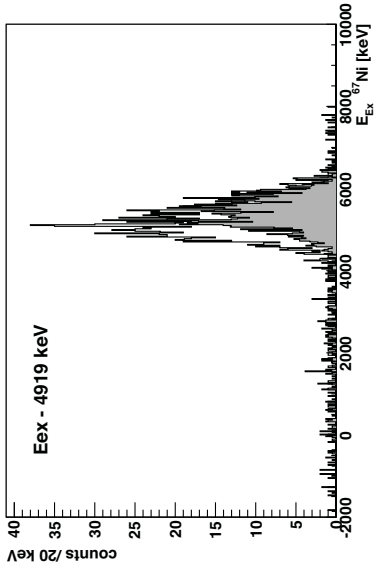

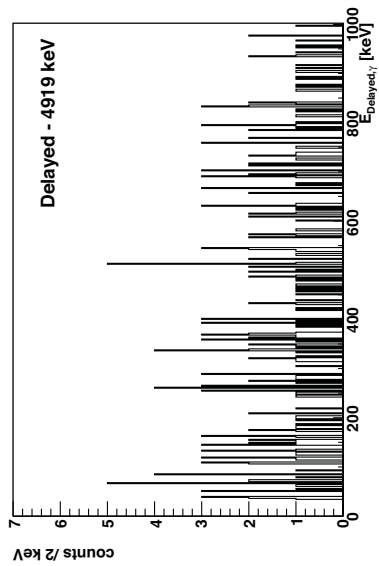

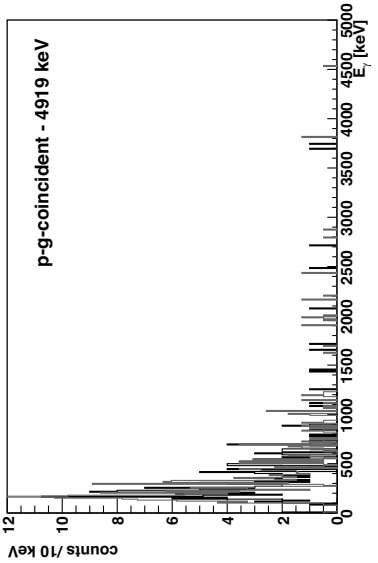

المنارة للاستشارات

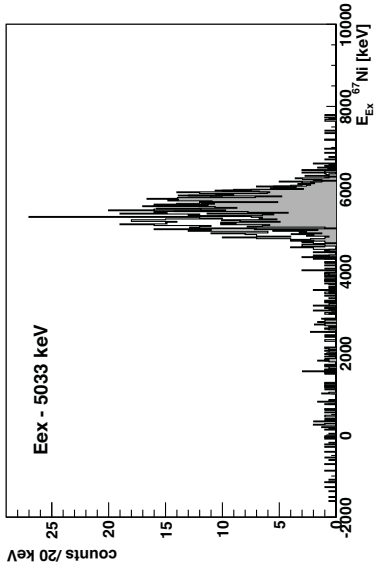

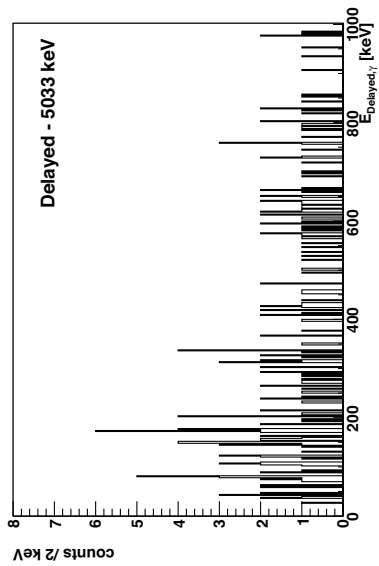

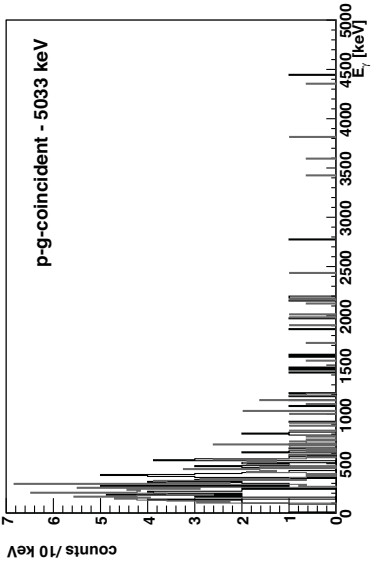

المنارة للاستشارات

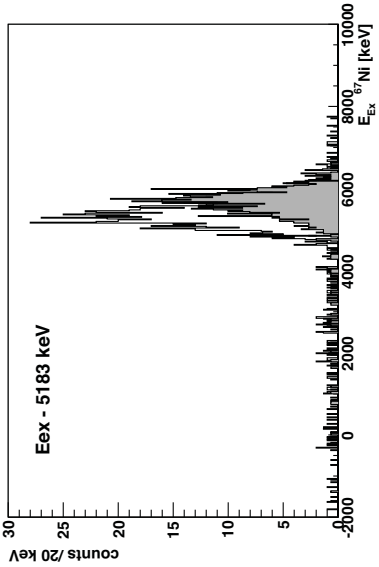

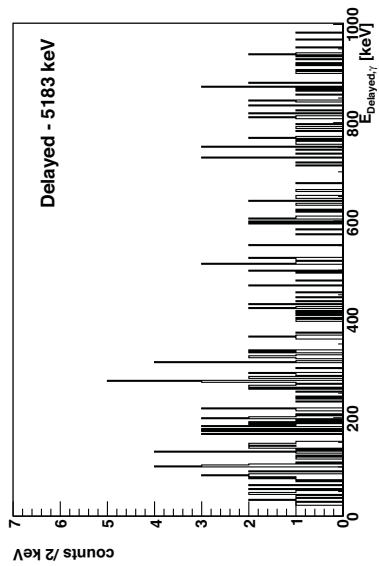

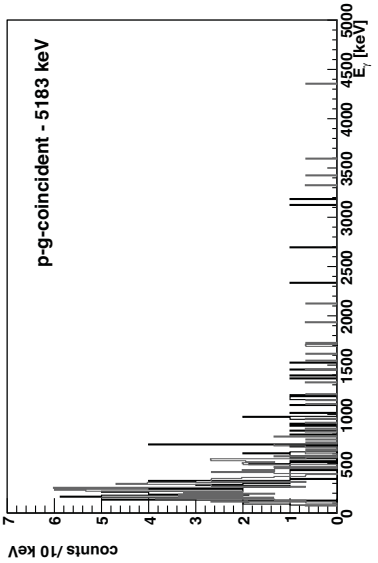

المنارة للاستشارات

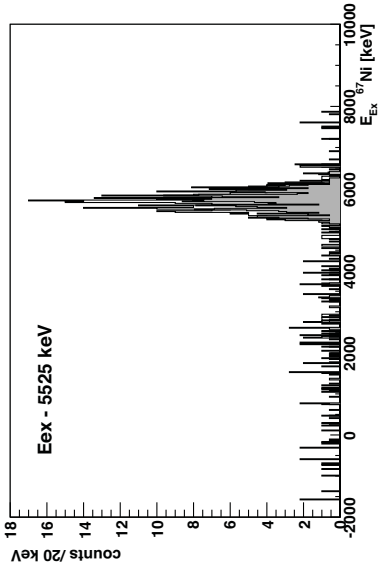

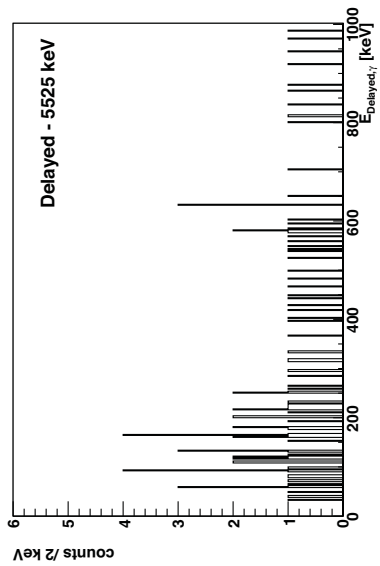

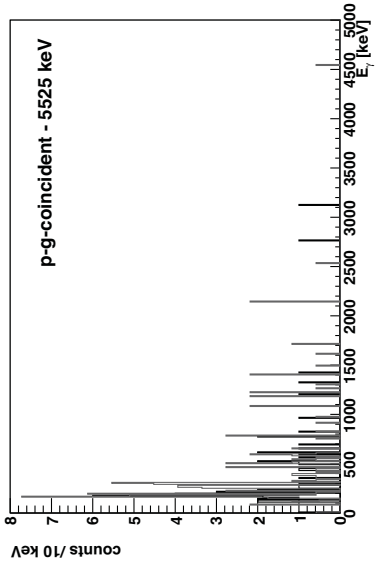

المنارة للاستشارات

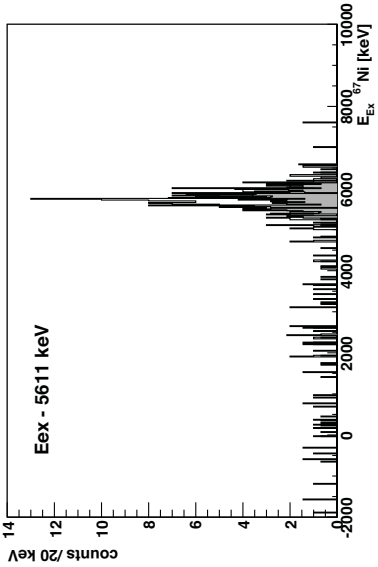
Eex - 5611 keV
counts /20 keV
E_{Ex} ^{67}Ni [keV]

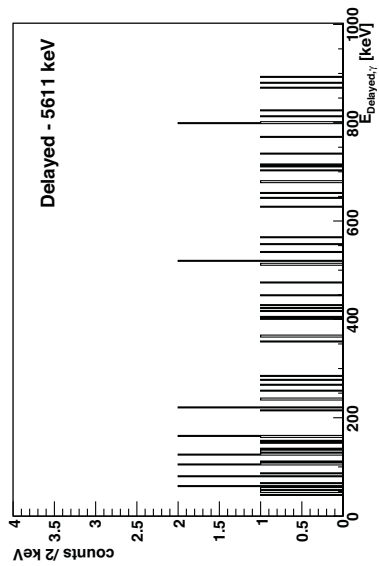
Delayed - 5611 keV
counts /2 keV
$E_{Delayed\gamma_i}$ [keV]

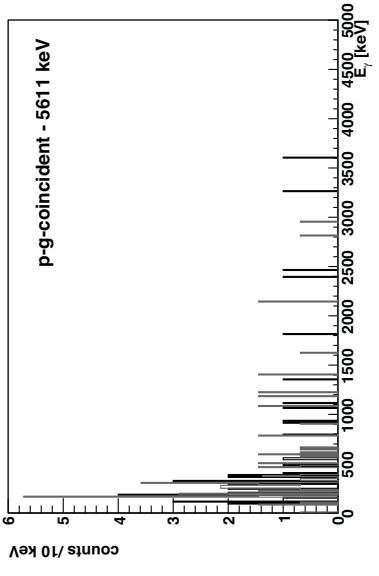
p-g-coincident - 5611 keV
counts /10 keV
E_γ [keV]

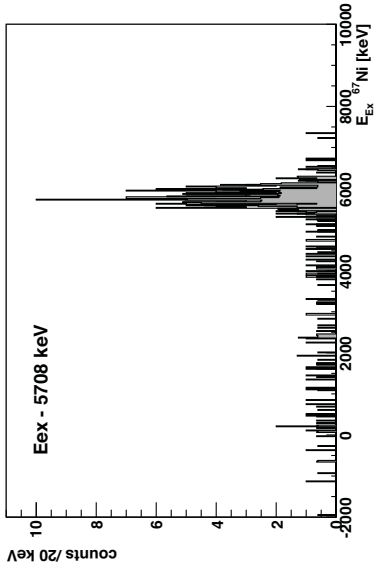

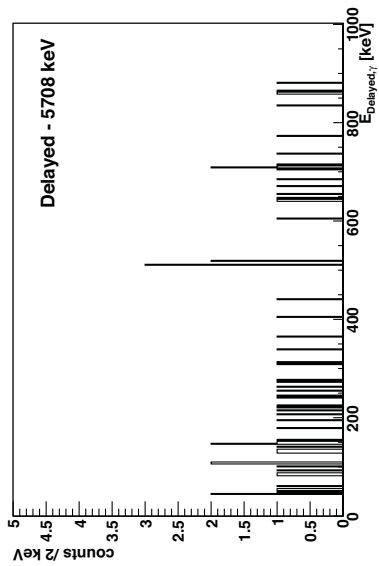

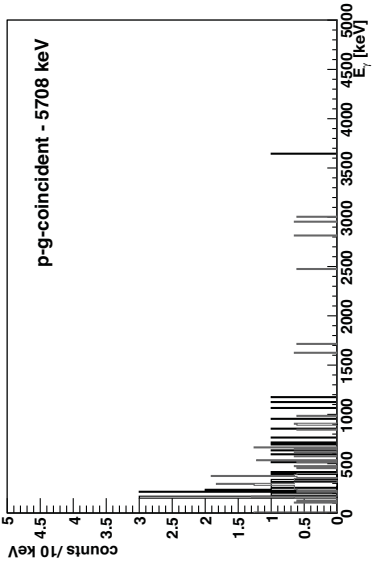

المنارة للاستشارات

B

Cross section tables

In this appendix tables containing the numerical values of the differential cross section for the population of the excited states in ^{67}Ni are given. These values can be used to compare future reaction model calculations to the measured data.

θ_{CM}	$\frac{d\sigma}{d\Omega}$ [mb/srad]	$\delta\frac{d\sigma}{d\Omega}$ [mb/srad]
13.0	1.67	0.03
18.2	2.18	0.06
20.9	1.87	0.05
23.8	1.69	0.05
26.9	1.68	0.06
30.1	1.64	0.06
33.6	1.48	0.06
37.3	1.32	0.05
76.3	0.64	0.03
82.4	0.65	0.03
88.7	0.60	0.02
95.3	0.55	0.02
102.1	0.51	0.018
109.1	0.46	0.015
116.2	0.46	0.013
123.5	0.42	0.011

Table B.1: Differential cross section for ^{67}Ni ground state

المنارة للاستشارات

θ_{CM}	$\frac{d\sigma}{d\Omega}$ [mb/srad]	$\delta\frac{d\sigma}{d\Omega}$ [mb/srad]
18.5	0.078	0.007
32.1	0.080	0.008
87.0	0.100	0.009
111.0	0.089	0.011

Table B.2: Differential cross section for ^{67}Ni 694 keV state

θ_{CM}	$\frac{d\sigma}{d\Omega}$ [mb/srad]	$\delta\frac{d\sigma}{d\Omega}$ [mb/srad]
14.5	0.09	0.04
16.9	0.15	0.04
19.6	0.08	0.04
22.3	0.12	0.04
25.2	0.10	0.04
28.3	0.13	0.04
31.7	0.11	0.04
35.2	0.12	0.03
74.2	0.27	0.03
80.4	0.37	0.03
86.8	0.35	0.03
93.5	0.25	0.03
100.5	0.27	0.03
107.6	0.24	0.03
114.9	0.28	0.05
122.3	0.23	0.05

Table B.3: Differential cross section for ^{67}Ni 1007 keV state

المنارة للاستشارات

θ_{CM}	$\frac{d\sigma}{d\Omega}$ [mb/srad]	$\delta\frac{d\sigma}{d\Omega}$ [mb/srad]
16.9	0.45	0.04
19.4	0.64	0.05
22.1	0.93	0.06
25.0	0.78	0.05
28.1	0.96	0.06
31.4	0.86	0.06
35.0	0.77	0.06
74.8	0.50	0.04
81.3	0.45	0.04
87.9	0.34	0.04
94.8	0.36	0.04
101.9	0.28	0.04
109.3	0.31	0.04
116.7	0.32	0.05
124.3	0.25	0.04

Table B.4: Differential cross section for ^{67}Ni 1724 keV state

θ_{CM}	$\frac{d\sigma}{d\Omega}$ [mb/srad]	$\delta\frac{d\sigma}{d\Omega}$ [mb/srad]
13.8	0.48	0.05
16.1	0.63	0.06
18.5	0.58	0.05
21.1	0.68	0.05
23.9	0.72	0.05
26.8	0.96	0.06
30.1	1.09	0.06
33.6	0.99	0.07
73.5	1.18	0.06
80.0	1.01	0.06
86.7	0.71	0.05
93.7	0.45	0.05
100.9	0.48	0.05
108.3	0.55	0.04
115.9	0.50	0.05
123.6	0.38	0.04

Table B.5: Differential cross section for ^{67}Ni 2207 keV state

المنارة للاستشارات

θ_{CM}	$\frac{d\sigma}{d\Omega}$ [mb/srad]	$\delta\frac{d\sigma}{d\Omega}$ [mb/srad]
20.8	0.71	0.12
23.6	0.87	0.11
26.6	0.83	0.11
29.9	1.13	0.10
69.7	1.29	0.10
76.4	1.41	0.10
83.4	1.11	0.11
90.7	0.98	0.10
98.1	0.86	0.08
105.8	0.94	0.07
113.7	0.76	0.07
121.7	1.01	0.06

Table B.6: Differential cross section for ^{67}Ni 3277 keV state

θ_{CM}	$\frac{d\sigma}{d\Omega}$ [mb/srad]	$\delta\frac{d\sigma}{d\Omega}$ [mb/srad]
11.6	0.50	0.19
13.6	0.89	0.17
15.7	1.29	0.32
18.0	1.49	0.17
20.4	0.57	0.14
23.1	1.29	0.14
26.1	0.87	0.14
29.4	0.66	0.14
69.3	1.22	0.09
76.0	1.59	0.09
83.0	0.87	0.10
90.3	0.78	0.10
97.8	0.81	0.10
105.5	0.85	0.14
113.4	0.64	0.12
121.4	0.7	0.6

Table B.7: Differential cross section for ^{67}Ni 3392 keV state

المنارة للاستشارات

θ_{CM}	$\frac{\mathrm{d}\sigma}{\mathrm{d}\Omega}$ [mb/srad]	$\delta\frac{\mathrm{d}\sigma}{\mathrm{d}\Omega}$ [mb/srad]
13.0	3.2	0.2
15.0	3.9	0.2
17.2	5.3	0.3
19.6	4.7	0.2
22.3	5.1	0.3
25.2	4.1	0.2
28.4	5.3	0.3
68.3	5.3	0.3
75.0	5.1	0.3
82.1	4.7	0.3
89.5	4.9	0.3
97.1	4.1	0.3
104.9	4.1	0.3
112.8	3.5	0.3
120.9	3.2	0.3

Table B.8: Differential cross section for ^{67}Ni 3621 keV state

المنارة للاستشارات

المنارة للاستشارات

Bibliography

[Ago03] S. Agostinelli *et al. Nucl. Instr. Meth. A*, 506 (2003) 250.

[Ajz85] F. Ajzenberg-Solve. *Nucl. Phys. A*, 433 (1985) 1.

[Ajz90] F. Ajzenberg-Solve. *Nucl.Phys. A*, 506 (1990) 1.

[Ald56] K. Alder *et al. Rev. Mod. Phys.*, 28 (1956) 432.

[Ald75] K. Alder and A. Winther. *Electromagnetic excitation: theory of Coulomb excitation.* Elsevier Science & Technology, 1975.

[An06] Haixia An and Chonghai Cai. *Phys. Rev. C*, 73 (2006) 054605.

[Anf70] T.R. Anfinsen *et al. Nucl. Phys. A*, 157 (1970) 561.

[Aoi09] N. Aoi *et al. Phys. Rev. Lett.*, 102 (2009) 012502.

[Asc72] R. J. Ascuitto *et al. Phys. Rev. Lett.*, 29 (1972) 1106–1108.

[Asc74] R.J. Ascuitto *et al. Nucl. Phys. A*, 226 (1974) 454 – 492.

[Aud97] G. Audi *et al. Nucl. Phys. A*, 624 (1997) 1.

[Aud03] G. Audi *et al. Nucl. Phys. A*, 729 (2003) 337.

[Aul97] T. Auler *et al. Phys. Rev. B*, 56 (1997) 11294.

[Bas07] B. Bastin *et al. Phys. Rev. Lett.*, 99 (2007) 022503.

[Bau12] T. Baugher *et al. Phys. Rev. C*, 86 (2012) 011305.

[Ben08] M. Bender. *Eur. Phys. J. Special Topics*, 156 (2008) 217–228.

[Ber82] M. Bernas *et al. Phys. Lett. B*, 113 (1982) 279.

[Ber03] M. Bernas *et al. Nucl. Phys. A*, 725 (2003) 213.

المنارة للاستشارات

[Ber04] C.A. Bertulani and P. Danielewicz. *Introduction to Nuclear Reactions*. Taylor & Francis, 2004.

[Bil12] V. Bildstein *et al. Eur. Phys. J. A*, 48 (2012) 1–10.

[Bla00] B. Blank *et al. Phys. Rev. Lett.*, 84 (2000) 1116–1119.

[Blo08] M. Block *et al. Phys. Rev. Lett.*, 100 (2008) 132501.

[Boh21] N. Bohr. *Nature*, 106 (1921) 104.

[Bol87] G. Bollen *et al. Hyperfine Interactions*, 38 (1987) 793–802.

[Bra97] M. Bradley *et al. Hyperfine Interact.*, 108 (1997) 227–238.

[Bre08] N. Bree *et al. Phys. Rev. C*, 78 (2008) 047301.

[Bre13] N. Bree. *Coulomb excitation of neutron deficient Hg isotopes*. PhD thesis, University of Leuven, 2013.

[Bro95] R. Broda *et al. Phys. Rev. Lett.*, 74 (1995) 868.

[Bru77] P.J. Brussaard and P.W.M. Glaudemans. *Shell Model Applications in Nuclear Spectroscopy*. North Holland Publishing, 1977.

[Cal13] M. Callens. private communication, 2013.

[Cas01] R.F. Casten. *Nuclear Structure from a Simple Perspective*. Oxford University Press, second edition, 2001.

[Cat04] R. Catherall *et al. Rev. Sci. Instrum.*, 75 (2004) 1614.

[Cau99] E. Caurier *et al. Phys. Rev. C*, 59 (1999) 2033–2039.

[Cau02] E. Caurier *et al. Euro. Phys. J. A*, 15 (2002) 145.

[CER12] CERN. Cern website, dec 2012.

[Cho73] M.S. Chowdhury *et al. Nucl. Phys. A*, 205 (1973) 454.

[Com12] XIA Company. Digital gamma finder documentation, dec 2012.

[Coo82] S. Cooper *et al. J. Phys. G: Nucl. Phys.*, 8 (1982) 559.

[Cos67] E. R. Cosman *et al. Phys. Rev.*, 163 (1967) 1134.

[Dar09] I.G. Darby. private communication, 2009.

[Dea04] D.J. Dean *et al. Prog. Part. Nucl. Phys.*, 53 (2004) 419.

[Dob94] J. Dobaczewski *et al. Phys. Rev. Lett.*, 72 (1994) 981–984.

المنارة للاستشارات

[Dup07] P. Van Duppen. *Lect. Notes Phys.*, 700 (2007) 37.

[Ebe01] J. Eberth *et al.* volume 46 of *Prog. Part. Nucl. Phys.*, pages 389–398, 2001.

[Els13] J. Elseviers. private communication, 2013.

[End79] P.M. Endt. *Atom. Data. Nucl. Data.*, 23 (1979) 3.

[Eng96] J. Engel *et al. Phys. Lett. B*, 389 (1996) 211.

[Fes74] H. Feshbach, A. De Shalit. *Theoretical Nuclear Physics.* John Wiley & Sons Inc, 1st edition, 1974.

[Fla09] K.T. Flanagan *et al. Phys. Rev. Lett.*, 103 (2009) 142501.

[For95] B. Fornal *et al. Acta Phys.Pol.*, B26 (1995) 357.

[Fra98] S. Franchoo *et al. Phys. Rev. Lett.*, 81 (1998) 3100.

[Fre10] S. J. Freeman *et al.* Technical Report CERN-INTC-2010-031. INTC-I-099, CERN, Geneva, May 2010.

[Ful63] R. H. Fulmer *et al. Phys. Rev.*, 131 (1963) 2133.

[Ful64] R. H. Fulmer *et al. Phys. Rev.*, 133 (1964) B955.

[Ful75] R. C. Fuller. *Phys. Rev. C*, 12 (1975) 1561–1574.

[Gad10] A. Gade *et al. Phys. Rev. C*, 81 (2010) 051304.

[Gau06] L. Gaudefroy *et al. Phys. Rev. Lett.*, 97 (2006) 092501.

[Geo02] G. Georgiev *et al. J. Phys. G: Nucl. Part. Phys.*, 28 (2002) 2993.

[Gir88] M. Girod *et al. Phys. Rev. C*, 37 (1988) 2600.

[Gle04] N.K. Glendenning. *Direct Nuclear Reactions.* World Scientific Pub Co Inc, 2004.

[Gol66] L. J. B. Goldfarb, G. W. Greenlees, and M. B. Hooper. *Phys. Rev.*, 144 (1966) 829–833.

[Gra04] H. Grawe. Shell modelfrom a practitioner's point of view. Jim Al-Khalili and Ernst Roeckl, editors, *The Euroschool Lectures on Physics with Exotic Beams, Vol. I*, volume 651 of *Lecture Notes in Physics*, pages 33–75. Springer Berlin Heidelberg, 2004.

[Gre66a] G. W. Greenlees and G. J. Pyle. *Phys. Rev.*, 149 (1966) 836–843.

المنارة للاستشارات

[Gre66b] G. W. Greenless, G. J. Pyle, and Y. C. Tang. *Phys. Rev. Lett.*, 17 (1966) 33–36.

[Grz98] R. Grzywacz *et al. Phys. Rev. Lett.*, 81 (1998) 766.

[Han99] M. Hannawald *et al. Phys. Rev. Lett.*, 82 (1999) 1391.

[Han06] Yinlu Han, Yuyang Shi, and Qingbiao Shen. *Phys. Rev. C*, 74 (2006) 044615.

[Her97] H. Herndl *et al. Nucl. Phys. A*, 627 (1997) 35.

[Hey90] K. Heyde. *The Nuclear Shell Model.* Springer-Verlag, 1990.

[Hey11] K. Heyde and J. L. Wood. *Rev. Mod. Phys.*, 83 (2011) 1467–1521.

[Hjo95] M. Hjorth-Jensen *et al. Phys. Rep.*, 261 (1995) 125.

[Hon02] M. Honma, T. Otsuka, B. A. Brown, and T. Mizusaki. *Phys. Rev. C*, 65 (2002) 061301.

[Hon04] M. Honma *et al. Phys. Rev. C*, 69 (2004) 034335.

[Hon09] M. Honma *et al. Phys. Rev. C*, 80 (2009) 064323.

[Hos05] P. T. Hosmer *et al. Phys. Rev. Lett.*, 94 (2005) 112501.

[Hot10] N. Hoteling *et al. Phys. Rev. C*, 82 (2010) 044305.

[Hut74] G.A. Huttlin *et al. Nucl. Phys. A*, 227 (1974) 389.

[Huy04] M. Huyse. *Lect. Notes Phys.*, 651 (2004) 1.

[Ish97] T. Ishii *et al. Nucl. Instr. Meth. A*, 395 (1997) 210.

[Ji 89] X. Ji *et al. Phys. Rev. C*, 40 (1989) 389.

[Joh56] Noah R. Johnson, Raymond K. Sheline, and Richard Wolfgang. *Phys. Rev.*, 102 (1956) 831–833.

[Joh70] R. C. Johnson and P. J. R. Soper. *Phys. Rev. C*, 1 (1970) 976–990.

[Joh74] R.C. Johnson and P.C. Tandy. *Nuclear Physics A*, 235 (1974) 56 – 74.

[Joh09] J. Johansen. private communication, 2009.

[Jon72] H. W. Jongsma *et al. Z.Phys.*, 251 (1972) 425.

[Jon93] B. Jonsen *et al. Nucl. Phys. News*, 3 (1993) 5.

[Kan08] K. Kaneko *et al. Phys. Rev. C*, 78 (2008) 064312.

المنارة للاستشارات

[Kim03] I.J. Kim, C.S. Park, and H.D. Choi. *Applied Radiation and Isotopes*, 58 (2003) 227 – 233.

[Kis69] B. G. Kiselev *et al. Yad.Fiz.*, 9 (1969) 1113.

[Knö70] K.T. Knöpfle. *Nucl. Phys. A*, 159 (1970) 642.

[Kon03] A.J. Koning *et al. Nucl. Phys. A*, 713 (2003) 231.

[Kou78] R. T. Kouzes *et al. Phys. Rev. C*, 18 (1978) 1587.

[Kra87] K.S. Krane. *Introductory Nuclear Physics*. John Wiley & Sons, 1987.

[Lac80] M. Lacombe *et al. Phys. Rev. C*, 21 (1980) 861–873.

[Lan03] K. Langanke *et al. Nucl. Phys. A*, 728 (2003) 109.

[Len10] S. M. Lenzi *et al. Phys. Rev. C*, 82 (2010) 054301.

[Li87] P.C. Li, W.W. Daehnick, Swapan K. Saha, J.D. Brown, and R.T. Kouzes. *Nucl. Phys. A*, 469 (1987) 393 – 406.

[Li08] Xiaohua Li and Chonghai Cai. *Nucl. Phys. A*, 801 (2008) 43.

[Lig10] J.C. Lighthall *et al. Nucl. Instr. Meth. A*, 622 (2010) 97.

[Lin08] M. Lindroos, P. A. Butler, M. Huyse, and K. Riisager. *Nucl. Instr. Meth. B*, 266 (2008) 4687–4691.

[Lis04] A. F. Lisetskiy *et al. Phys. Rev. C*, 70 (2004) 044314.

[Lju10] J. Ljungvall *et al. Phys. Rev. C*, 81 (2010) 061301.

[Loh74] J.M. Lohr *et al. Nucl. Phys. A*, 232 (1974) 381.

[Lut00] R. Lutter *et al. Nucl. Sci.*, 47 (2000) 280.

[Mac60] M. H. Macfarlane and J. B. French. *Rev. Mod. Phys.*, 32 (1960) 567–691.

[Mac87] R. Machleidt, K. Holinde, and Ch. Elster. *Phys. Rep.*, 149 (1987) 1 – 89.

[Mac03] H. Mach *et al. Nucl. Phys. A*, 719 (2003) C213.

[Med75] L. R. Medsker *et al. Phys. Rev. C*, 12 (1975) 1516.

[Mer70] E. Merzbacher. *Quantum mechanics [by] Eugen Merzbacher*. J. Wiley New York„ 2d ed. edition, 1970.

المنارة للاستشارات

[Mes12a] Mesytec. Madc-32 documentation, dec 2012.

[Mes12b] Mesytec. Msi-8 documentation, dec 2012.

[Mes12c] Mesytec. Mux-32 documentation, dec 2012.

[Mey90] R. A. Meyer. *Fiz.*, 22 (1990) 153.

[Mil82] D. J. Millener *et al. Phys. Rev. C*, 26 (1982) 1167.

[Moi69] M. Moinester *et al. Phys. Rev.*, 179 (1969) 984–995.

[Mor04] D.J. Morrissey *et al. Lect. Notes Phys.*, 651 (2004) 113.

[Mor07] B. Morillon *et al. Phys. Rev. C*, 76 (2007) 044601.

[Mou11] M. Moukaddam *et al. Acta. Phys. Pol. B*, 42 (2011) 541–544.

[Mou12] M. Moukaddam. *Evolution of the shell structure in medium-mass nuclei: Search for the $2d_{5/2}$ neutron orbital in ^{69}Ni.* PhD thesis, IPHC Strasbourg, March 2012.

[Müc11] D. Mücher. private communication, 2011.

[Muk05] A. M. Mukhamedzhanov *et al. Phys. Rev. C*, 72 (2005) 017602.

[Nav07] P. Navrátil *et al. Phys. Rev. Lett.*, 99 (2007) 042501.

[NND13] NNDC. Evaluated nuclear structure data file (ensdf), jan 2013.

[Now13] F. Nowacki. private communication, 2013.

[Nun11] F. M. Nunes and A. Deltuva. *Phys. Rev. C*, 84 (2011) 034607.

[Oro00] A.M Oros-Peusquens *et al. Nucl. Phys. A*, 669 (2000) 81.

[Ost02] A.N Ostrowski *et al.* 480 (2002) 448.

[Ots98] T. Otsuka *et al. Phys. Rev. Lett.*, 81 (1998) 1588.

[Ots05] T. Otsuka *et al. Phys. Rev. Lett.*, 95 (2005) 232502.

[Ots10a] T. Otsuka *et al. Phys. Rev. Lett.*, 104 (2010) 012501.

[Ots10b] T. Otsuka *et al. Phys. Rev. Lett.*, 105 (2010) 032501.

[Ots12] T. Otsuka *et al. Nucl. Phys. News*, 22 (2012) 12.

[Pau09] D. Pauwels *et al. Phys. Rev. C*, 79 (2009) 044309.

[Paw94] T. Pawłat *et al. Nucl. Phys. A*, 574 (1994) 623 – 641.

المنارة للاستشارات

[Per63] F. G. Perey. *Phys. Rev.*, 131 (1963) 745.

[Per74] C.M. Perey *et al. Atom. Data Nucl. Data*, 13 (1974) 293.

[Per06] O. Perru *et al. Phys. Rev. Lett.*, 96 (2006) 232501.

[Pic69] J. Picard *et al. Nucl. Phys. A*, 131 (1969) 636.

[Pom11] M. Pomorski *et al. Phys. Rev. C*, 83 (2011) 061303.

[Pré04] A. Prévost. *European Physical Journal A*, 22 (2004) 391.

[Rad13] D. Radulov. private communication, 2013.

[Rah07] S. Rahaman *et al. Eur. Phys. J. A*, 34 (2007) 5.

[Rik00] J. Rikovska *et al. Phys. Rev. Lett.*, 85 (2000) 1392.

[Roo75] S. Roodbergen *et al. Z.Phys.*, A275 (1975) 45.

[Ros71] E. Rost *et al. Nucl. Phys. A*, 162 (1971) 376.

[Ros75] E. Rost *et al. Phys. Lett. B*, 59 (1975) 413.

[Rot98] H. Rothard. *Nuc. Instr. Meth. B*, 146 (1998) 1.

[Rot11] W. Rother *et al. Phys. Rev. Lett.*, 106 (2011) .

[Run83] E. Runte *et al. Nucl. Phys. A*, 399 (1983) 163.

[Run85] E. Runte *et al. Nucl. Phys. A*, 441 (1985) 237.

[Sat90] G.R. Satchler. *Introduction to Nuclear Reactions.* Oxford University Press, USA, 2nd edition, 1990.

[Sch72] H. Schulz *et al. Nucl. Phys. A*, 180 (1972) 625.

[Sch12] J. P. Schiffer *et al. Phys. Rev. Lett.*, 108 (2012) 022501.

[Sch13] J. P. Schiffer *et al. Phys. Rev. C*, 87 (2013) 034306.

[See91] M. Seeger, Th. Kihm, and K.T. Kn˙ *Nucl. Phys. A*, 533 (1991) 1.

[See92] M. Seeger, Th. Kihm, and K.T. Kn˙ *Nucl. Phys. A*, 539 (1992) 223.

[Sei11] M. Seidlitz *et al. Phys. Rev. C*, 84 (2011) 034318.

[Sem12] Micron Semiconductors. Micron semiconductors position sensitive detector x1, dec 2012.

المنارة للاستشارات

[Sha04] A. de Shalit and I. Talmi. *Nuclear Shell Theory.* Dover Publication, Inc., 2004.

[Sic70] I. Sick *et al. Nucl. Phys. A*, 150 (1970) 631.

[Sie12] K. Sieja *et al. Phys. Rev. C*, 85 (2012) 051301.

[Sin92] J. Sinatkas *et al. J. Phys. G: Nucl. Part. Phys.*, 18 (1992) 1377.

[Sor02] O. Sorlin *et al. Phys. Rev. Lett.*, 88 (2002) 092501.

[Sor03] O. Sorlin *et al. Euro. Phys. J. A*, 16 (2003) 55.

[Sor08] O. Sorlin *et al. Prog. Part. Nucl. Phys.*, 61 (2008) 602.

[Spr67] Donald W. L. Sprung and P. C. Bhargava. *Phys. Rev.*, 156 (1967) 1185–1187.

[Sta12] National Institute of Standards and Technology. Pstar and astar database for protons and helium ions, dec 2012.

[Ste57] E. J. Sternglass. *Phys. Rev.*, 108 (1957) 1.

[Ste08] I. Stefanescu *et al. Phys. Rev. Lett.*, 100 (2008) 112502.

[Str06] Oscar Straniero, Roberto Gallino, and Sergio Cristallo. *Nucl. Phys. A*, 777 (2006) 311 – 339. <ce:title>Special Isseu on Nuclear Astrophysics</ce:title>.

[Tho26] L.H. Thomas. *Nature*, 117 (1926) 514.

[Tho88] I.J. Thompson. *Comput. Phys. Rep.*, 7 (1988) 167.

[Tho09] I.J. Thompson, F.M. Nunes. *Nuclear Reactions for Astrophysics.* Cambridge University Press, 2009.

[Tim13] N. K. Timofeyuk and R. C. Johnson. *Phys. Rev. Lett.*, 110 (2013) 112501.

[Tur70] I.M. Turkiewicz *et al. Nucl. Phys. A*, 143 (1970) 641.

[Van06] J. Van de Walle. *Coulomb excitation of neutron rich Zn isotopes.* PhD thesis, University of Leuven, September 2006.

[Van07] J. Van de Walle *et al. Phys. Rev. Lett.*, 99 (2007) 142501.

[Van09] J. Van de Walle *et al. Euro. Phys. J. A*, 42 (2009) 401.

[Var11] J.P. Vary *et al. Acta Physica Polonica A*, 42 (2011) 397.

المنارة للاستشارات

[Vas05] S. I. Vasiliev *et al.* Technical Report JINR-P13-2005-84, 2005.

[Vin70] C. M. Vincent *et al. Phys. Rev. C*, 2 (1970) 782.

[Vou71] G. Vourvopoulos *et al. Nucl. Phys. A*, 174 (1971) 581.

[War13] N. Warr *et al.* to be published, 2013.

[Wei99] L. Weissman *et al. Phys. Rev. C*, 59 (1999) 2004.

[Wes91] E. Wesolowski *et al. J. Phys. G Nucl. Partic.*, 17 (1991) 955.

[Wim09] K. Wimmer. private communication, 2009.

[Wir95] R. B. Wiringa, V. G. J. Stoks, and R. Schiavilla. *Phys. Rev. C*, 51 (1995) 38–51.

[Wuo07] A.H. Wuosmaa, J.P. Schiffer, B.B. Back, C.J. Lister, and K.E. Rehm. *Nucl. Instr. Meth. A*, 580 (2007) 1290 – 1300.

[Zha04] Y. H. Zhang *et al. Phys. Rev. C*, 70 (2004) 024301.

[Zhu12] S. Zhu *et al. Phys. Rev. C*, 85 (2012) 034336.

[Zie10] J.F. Ziegler *et al. Nuc. Instr. Meth. B*, 268 (2010) 1818.

[Zuk95] A. P. Zuker *et al. Phys. Rev. C*, 52 (1995) R1471.

[Zuk03] A. P. Zuker. *Phys. Rev. Lett.*, 90 (2003) 042502.

المنارة للاستشارات

المنارة للاستشارات

Curriculum Vitae

Jan Diriken was born on August 2nd 1985, in Leuven, Belgium. After finishing high school at the Virga Jesse College in Hasselt, he started studying physics at the Katholieke Universiteit Leuven in 2003. In July 2007, he received the degree of Master in Physics (Magna cum laude; master thesis titled: *Coulomb excitation of* ^{67}Cu). In October 2007, he joined the Nuclear Spectroscopy group (Nuclear and Radiation Physics section) of the Department of Physics and Astronomy of the KU Leuven to pursue a Ph.D. on nuclear structure infered from nuclear reactions under the supervision of Prof.dr. Piet Van Duppen and Prof.dr. Mark Huyse. Since October 2008, his research was funded by a personal joint grant of the Fund for Scientific Research Flanders (FWO Vlaanderen) and Study Center for Nuclear Energy (SCK-CEN, Mol).

المنارة للاستشارات

المنارة للاستشارات

List of Publications

Journal Articles

- I. Stefanescu, G. Georgiev, D.L. Balabanski, N. Blasi, A. Blazhev, N. Bree, J. Cederkall, T.E. Cocolios, T Davinson, J. Diriken, J. Eberth, A. Ekstrom, D. Fedorov, V.N. Fedosseev, L.M. Fraile, S. Franchoo, K. Gladnishki, M. Huyse, O. Ivanov, V. Ivanov, J. Iwanicki, J. Jolie, T. Konstantinopoulos, T. Kroll, R. Krucken, U. Koster, A. Lagoyannis, G. Lo Bianco, P. Maierbeck, B.A. Marsh, P. Napiorkowski, N. Patronis, D. Pauwels, G. Rainovski, P. Reiter, K. Riisager, M. Seliverstov, G. Sletten, J. Van de Walle, P. Van Duppen, D. Voulot, N. Warr, F. Wenander, K. Wrzosek (2008).
  "Interplay between single-particle and collective effects in the odd-A Cu isotopes beyond $N = 40$"
  In *Physical Review Letters* 100(11), page 112502.

- I. Stefanescu, D. Pauwels, N. Bree, T.E. Cocolios, J. Diriken, S. Franchoo, M. Huyse, O. Ivanov, Y. Kudryavtsev, N. Patronis, J. Van De Walle, P. Van Duppen, W.B Walters (2009).
  "Evidence for a β-decaying $1/2^-$ isomer in ^{71}Ni"
  In *Physical Review C* 79(4), page 044325.

- J. Van de Walle, V. Bildstein, N. Bree, J. Cederkall, P. Delahaye, J. Diriken, A. Ekstrom, V.N. Fedosseev, R. Gernhauser, A. Gustafsson, A. Herlert, M. Huyse, O. Ivanov, T. Kroll, R. Krucken, B.A. Marsh, N. Partronis, P. Van Duppen, D. Voulot, N. Warr, F. Wenander, K. Wimmer, S.M. Lenzi (2009).
  "In-trap decay of ^{61}Mn and Coulomb excitation of ^{61}Mn/^{61}Fe"
  In *European Physical Journal A* 42(3), pages 401-406.

- K. Wimmer, T. Kroll, R. Krucken, V. Bildstein, R. Gernhauser, B. Bastin, N. Bree, J. Diriken, P. Van Duppen, M. Huyse, N. Patronis,

المنارة للاستشارات

P. Vermaelen, D Voulot, J. Van de Walle, F. Wenander, L.M. Fraile, R. Chapman, B. Hadinia, R. Orlandi, J.F. Smith, R. Lutter, P.G. Thirolf, M. Labiche, A. Blazhev, M. Kalkuhler, P. Reiter, M. Seidlitz, N. Warr, A.O. Macchiavelli, H.B. Jeppesen, E. Fiori, G. Georgiev, G. Schrieder, S. Das Gupta, G. Lo Bianco, S. Nardelli, J. Butterworth, J. Johansen, K. Riisager (2010).
"Discovery of the Shape Coexisting 0^+ State in ^{32}Mg by a Two Neutron Transfer Reaction"
In *Physical Review Letters* 105(25), page 252501.

- J. Diriken, I. Stefanescu, D. Balabanski, N. Blasi, A. Blazhev, N. Bree, J. Cederkall, T.E. Cocolios, T. Davinson, J. Eberth, A. Ekstrom, D.V. Fedorov, V.N. Fedosseev, L.M. Fraile, S. Franchoo, G. Georgiev, K. Gladnishki, M. Huyse, O.V. Ivanov, V.S. Ivanov, J. Iwanicki, J. Jolie, T. Konstantinopoulos, T. Kroll, R. Krucken, U. Koster, A. Lagoyannis, G. Lo Bianco, P. Maierbeck, B.A. Marsh, P. Napiorkowski, N. Patronis, D. Pauwels, P. Reiter, M. Seliverstov, G. Sletten, J. Van de Walle, P. Van Duppen, D. Voulot, W.B. Walters, N. Warr, F. Wenander, K. Wrzosek (2010).
"Coulomb excitation of ^{73}Ga"
In *Physical Review C* 82(6), page 064309.

- A.N. Andreyev, J. Elseviers, M. Huyse, P. Van Duppen, S. Antalic, A. Barzakh, N. Bree, T.E. Cocolios, V.F. Comas, J. Diriken, D. Fedorov, V. Fedosseev, S. Franchoo, J.A. Heredia, O. Ivanov, U. Koster, B.A. Marsh, K. Nishio, R.D. Page, N. Patronis, M. Seliverstov, I. Tsekhanovich, P. Van den Bergh, J. Van De Walle, M. Venhart, S. Vermote, M. Veselsky, C. Wagemans, T. Ichikawa, A Iwamoto, P. Moller, A.J. Sierk (2010).
"New Type of Asymmetric Fission in Proton-Rich Nuclei"
In *Physical Review Letters* 105(25), page 252502.

- J. Elseviers, A.N. Andreyev, S. Antalic, A. Barzakh, N. Bree, T.E. Cocolios, V.F. Comas, J. Diriken, D. Fedorov, V.N. Fedosseyev, S. Franchoo, J.A. Heredia, M. Huyse, O. Ivanov, U. Koster, B.A. Marsh, R.D. Page, N. Patronis, M. Seliverstov, I. Tsekhanovich, P. Van den Bergh, J. Van De Walle, P. Van Duppen, M. Venhart, S. Vermote, M. Veselsky, C. Wagemans (2011).
"Shape coexistence in ^{180}Hg studied through the β decay of ^{180}Tl"
In *Physical Review C* 84(3), page 034307.

- E. Rapisarda,I. Stefanescu, D.L. Balabanski, B. Bastin, A. Blazhev, N. Bree, M. Danchev, B. Bruyneel, T. Davinson, P. Delahaye,J. Diriken, J. Eberth, G. Georgiev, D. Fedorov, V. N. Fedosseev, E. Fiori, S.

المنارة للاستشارات

Franchoo, Ch. Fransen, K. Geibel, K. Gladnishki, K. Hadynska, H. Hess, K. Heyde, M. Huyse, O. Ivanov, J. Iwanicki, J. Jolie, M. Kalkuehler, Th. Kröll, R. Krücken, U. Köster, G. Lo Bianco3, R. Lozeva, B. A. Marsh, S. Nardelli, F. Nowacki, N. Patronis, P. Reiter, M. Seidlitz, K. Sieja, N. Smirnova, J. Srebrny, J. Van de Walle, P. Van Duppen, N. Warr, F. Wenander, K. Wimmer, K. Wrzosek, S. Zemlyanoi, M. Zielinska (2011).
"Coulomb excitation of the 3^- isomer in ^{70}Cu"
In *Physical Review C* 84(6), page 064323.

- M. Albers, N. Warr, K. Nomura, A. Blazhev, J. Jolie, D. Mücher, B. Bastin, C. Bauer, C. Bernards, L. Bettermann, V. Bildstein, J. Butterworth, M. Cappellazzo, J. Cederkäll, D. Cline, I.G. Darby, S. Das Gupta, J.M. Daugas, T. Davinson, H. De Witte, J. Diriken, D. Filipescu, E. Fiori, C. Fransen, L.P. Gaffney, G. Georgiev, R. Gernhäuser, M. Hackstein, S. Heinze, H. Hess, M. Huyse, D. Jenkins, J. Konki, M Kowalczyk, Th. Kröll, R. Krücken, J. Litzinger, R. Lutter, N. Marginean, C. Mihai, K. Moschner, P. Napiorkowski, B.S.N. Singh, K. Nowak, T. Otsuka, J. Pakarinen, M. Pfeiffer, D. Radeck, P. Reiter, S. Rigby, L.M. Robledo, R. Rodríguez-Guzmán, M. Rudigier, P. Sarriguren, M. Scheck, M. Seidlitz, B. Siebeck, G. Simpson, P. Thöle, T. Thomas, J. Van de Walle, P. Van Duppen, M. Vermeulen, D. Voulot, R. Wadsworth, F. Wenander, K. Wimmer, K.O. Zell, M. Zielinska (2012).
  "Evidence for a Smooth Onset of Deformation in the Neutron-Rich Kr Isotopes"
  In *Physics Review Letters* 108(6), page 062701.

- D.D. DiJulio, J. Cederkall, C. Fahlander, A. Ekstrom, M. Hjorth-Jensen, M. Albers, V. Bildstein, A. Blazhev, I. Darby, T. Davinson, H. De Witte, J. Diriken, C. Fransen, K. Geibel, R. Gernhauser, A. Gorgen, H. Hess, J. Iwanicki, R. Lutter, P. Reiter, M. Scheck, M. Seidlitz, S. Siem, J. Taprogge, G.M. Tveten, J. Van de Walle, D. Voulot, N. Warr, F. Wenander, K. Wimmer (2012).
  "Coulomb excitation of Sn-107"
  In *European Physics Journal A* 48(7), page 105.

- D.D. DiJulio, J. Cederkall, C. Fahlander, A. Ekstrom, M. Hjorth-Jensen, M. Albers, V. Bildstein, A. Blazhev, I. Darby, T. Davinson, H. De Witte, J. Diriken, C. Fransen, K. Geibel, R. Gernhauser, A. Gorgen, H. Hess, J. Iwanicki, R. Lutter, P. Reiter, M. Scheck, M. Seidlitz, S. Siem, J. Taprogge, G.M. Tveten, J. Van de Walle, D. Voulot, N. Warr, F. Wenander, K. Wimmer (2012).
  "Excitation strengths in Sn-109: Single-neutron and collective excitations near Sn-100"
  In *Physical Review C* 86(3), page 031302.

المنارة للاستشارات

- D. Pauwels, D. Radulov, W. B. Walters, I. G. Darby, H. De Witte, J. Diriken, D. V. Fedorov, V. N. Fedosseev, L. M. Fraile, M. Huyse, U. Köster, B. A. Marsh, L. Popescu, M. D. Seliverstov, A. M. Sjödin, P. Van den Bergh, J. Van de Walle, P. Van Duppen, M. Venhart, K. Wimmer (2012)
  "Gamow-Teller decay population of ^{64}Ni levels in the decay of 1^+ ^{64}Co"
  In *Physical Review C* 86(6), page 064318.

- M. Albers, K. Nomura, N. Warr, A. Blazhev, J. Jolie, D. Mücher, B. Bastin, C. Bauer, C. Bernards, L. Bettermann, V. Bildstein, J. Butterworth, M. Cappellazzo, J. Cederkäll, D. Cline, I.G. Darby, S. Das Gupta, J.M. Daugas, T. Davinson, H. De Witte, J. Diriken, D. Filipescu, E. Fiori, C. Fransen, L.P. Gaffney, G. Georgiev, R. Gernhäuser, M. Hackstein, S. Heinze, H. Hess, M. Huyse, D. Jenkins, J. Konki, M Kowalczyk, Th. Kröll, R. Krücken, J. Litzinger, R. Lutter, N. Marginean, C. Mihai, K. Moschner, P. Napiorkowski, B.S.N. Singh, K. Nowak, T. Otsuka, J. Pakarinen, M. Pfeiffer, D. Radeck, P. Reiter, S. Rigby, L.M. Robledo, R. Rodríguez-Guzmán, M. Rudigier, P. Sarriguren, M. Scheck, M. Seidlitz, B. Siebeck, G. Simpson, P. Thöle, T. Thomas, J. Van de Walle, P. Van Duppen, M. Vermeulen, D. Voulot, R. Wadsworth, F. Wenander, K. Wimmer, K.O. Zell, M. Zielinska (2013).
  "Shape dynamics in neutron-rich Kr isotopes: Coulomb excitation of ^{92}Kr, ^{94}Kr and ^{96}Kr"
  In *Nuclear Physics A* 899, page 1.

- D.D. DiJulio, J. Cederkall, C. Fahlander, A. Ekstrom, M. Hjorth-Jensen, M. Albers, V. Bildstein, A. Blazhev, I. Darby, T. Davinson, H. De Witte, J. Diriken, C. Fransen, K. Geibel, R. Gernhauser, A. Gorgen, H. Hess, J. Iwanicki, R. Lutter, P. Reiter, M. Scheck, M. Seidlitz, S. Siem, J. Taprogge, G.M. Tveten, J. Van de Walle, D. Voulot, N. Warr, F. Wenander, K. Wimmer (2013).
  "Coulomb excitation of ^{107}In"
  In *Physics Review C* 87(1), page 017301.

- N. Warr, J. Van de Walle, M. Albers, F. Ames, B. Bastin, C. Bauer, V. Bildsteina, A. Blazhev, S. Bönig, N. Bree, B. Bruyneel, P.A. Butler, J. Cederkäll, E. Clément, T.E. Cocolios, T. Davinson, H. De Witte, P. Delahaye, D.D. Di Julio, J. Diriken, J. Eberth, A. Ekström, J. Elseviers, S. Emhofer, D.V. Fedorov, V.N. Fedosseev, S. Franchoo, C. Fransen, L.P. Gaffney, J. Gerl, G. Georgiev, R. Gernhäuser, T. Grahn, D. Habs, H. Hess, A.M. Hurst, M. Huyse, S. Ilieva, O. Ivanov, J. Iwanicki, D.G. Jenkins, J. Jolie, N. Kesteloot, O. Kester, U. Köster, T. Kröll, R. Krücken, M. Lauer, J. Leske, K.P. Lieb, R. Lutter, L. Maier, B.A. Marsh,

المنارة للاستشارات

D. Mücher, M. Münch, O. Niedermaier, J. Pakarinen, M. Pantea, G. Pascovici, N. Patronis, D. Pauwels, A. Petts, N. Pietralla, R. Raabe, E. Rapisarda, P. Reiter, A. Richter, O. Schaile, M. Scheck, H. Scheit, G. Schrieder, D. Schwalm, M. Seidlitz, M. Seliverstov, T. Sieber, H. Simon, K.-H. Speidel, C. Stahl, I. Stefanescu, P.G. Thirolf, H.-G. Thomas, M. Thürauf, P. Van Duppen, D. Voulot, R. Wadsworth, G. Walter, D. Weißhaar, F. Wenander, A. Wiens, K. Wimmer, B.H. Wolf, P.J. Woods, K. Wrosek-Lipska, K.O. Zell (2013).
"The Miniball Spectrometer"
In *European Physics Journal A* 49(3), page 1.

- L.P. Gaffney, P.A. Butler, M. Scheck, A.B. Hayes, F. Wenander, M. Albers, B. Bastin, C. Bauer, A. Blazhev, S. Bönig, N. Bree, J. Cederkäll, T. Chupp, D. Cline, T.E. Cocolios, T. Davinson, H. De Witte, J. Diriken, T. Grahn, A. Herzan, M. Huyse, D.G. Jenkins, D.T. Joss, N. Kesteloot, J. Konki, M. Kowalczyk, Th. Kröll, E. Kwan, R. Lutter, K. Moschner, P. Napiorkowski, J. Pakarinen, M. Pfeiffer, D. Radec, P. Reiter, K. Reynders, S.V. Rigby, L.M. Robledo, M. Rudigier, S. Sambi, M. Seidlitz, B. Siebeck, T. Stora, P. Thoele, P. Van Duppen, M. Vermeulen, M. von Schmid, D. Voulot, N. Warr, K. Wimmer, K. Wrzosek-Lipska, C.Y. Wu, and M. Zielinska (2013).
"Studies of nuclear pear-shapes using accelerated radioactive beams"
In *Nature* 497(7448), page 199.

- A.N. Andreyev, V. Liberati, S. Antalic, D. Ackermann, A. Barzakh, N. Bree, T.E. Cocolios, J. Diriken, J. Elseviers, D. Fedorov, V.N. Fedosseev, D. Fink, S. Franchoo, S. Heinz, F.P. Heszligberger, S. Hofmann, M. Huyse, O. Ivanov, J. Khuyagbaatar, B. Kindler, U. Koumlster, J.F.W. Lane, B. Lommel, R. Mann, B.A. Marsh, P. Molkanov, K. Nishio, R.D. Page, N. Patronis, D. Pauwels, D. Radulov, S. Scaronaacutero, M. Seliverstov, M. Sjoumldin, I. Tsekhanovich, P. Van den Bergh, P. Van Duppen, M. Venhart and M Veselskyacute (2013).
"α-decay spectroscopy of the chain ^{179}Tl $\rightarrow$ ^{175}Au $\rightarrow$ ^{171}Ir $\rightarrow$ ^{167}Re^{m}"
In *Physical Review C* 87(5), page 054311.

- D. Radulov, I.G. Darby, H. De Witte, J. Diriken, D.V. Fedorov, V.N. Fedosseev, L.M. Fraile, M. Huyse, U. Köster, B.A. Marsh, D. Pauwels, L. Popescu, M.D. Seliverstov, A.M. Sjödin, P. Van den Bergh, P. Van Duppen, M. Venhart, W.B. Walters, K. Wimmer (2013).
"Beta-Decay of ^{61}Mn"
Submitted for publication in *Physical Review C*

المنارة للاستشارات

- J. Diriken, N. Patronis, A. Andreyev, A. Antalic, V. Bildstein, A. Blazhev, I.G. Darby, H. De Witte, J. Eberth, J. Elseviers, V.N. Fedosseev, F. Flavigny, G. Georgiev, R. Gernhauser, M. Huyse, J. Jolie, Th. Kröll, R. Krücken, S. Lenzi, R. Lutter, T. Mertzimekis, B.A. March, D. Muecher, F. Nowacki, R. Orlandi, A. Pakou, R. Raabe, G. Randisi, P. Reiter, T. Roger, M. Seidlitz, M. Seliverstov, K. Sieja, C. Sotty, H. Tornqvist, J. Van De Walle, P. Van Duppen, D. Voulot, N. Warr, F. Wenander, and K. Wimmer (2013).
  "Study of the deformation-driving $\nu d5/2$ orbital in $^{67}_{28}Ni_{39}$ using one-neutron transfer reactions"
  Submitted for publication in *Physical Review Letters*

- J. Diriken, N. Patronis, A. Andreyev, A. Antalic, V. Bildstein, A. Blazhev, I.G. Darby, H. De Witte, J. Eberth, J. Elseviers, V.N. Fedosseev, F. Flavigny, G. Georgiev, R. Gernhauser, M. Huyse, J. Jolie, Th. Kröll, R. Krücken, S. Lenzi, R. Lutter, T. Mertzimekis, B.A. March, D. Muecher, F. Nowacki, R. Orlandi, A. Pakou, R. Raabe, G. Randisi, P. Reiter, T. Roger, M. Seidlitz, M. Seliverstov, K. Sieja, C. Sotty, H. Tornqvist, J. Van De Walle, P. Van Duppen, D. Voulot, N. Warr, F. Wenander, and K. Wimmer (2013).
  "Study of the ^{66}Ni(d,p)^{67}Ni one-neutron transfer reaction"
  Submitted for publication in *Physical Review C*

Presentations and Posters at Conferences and Workshops[1]

- BRIX-IAP Workshop, Mol, Belgium, *"Coulomb Excitation of odd-A Cu Isotopes"*, April 2008
- Scientific Seminar, IKS-KU Leuven, *"Coulomb Excitation of odd-A Ga Isotopes"*, May 2008
- MINIBALL Workshop, Munich, Germany, *"Coulomb Excitation of odd-A Ga Isotopes"*, December 2008
- WOG Workshop '09 "Nuclear Structure of the Neutron-Rich Region around Z=28 towards and beyond N=50", IKS-KU Leuven, Leuven, Belgium, March 2009: *"Coulomb excitation of the neutron rich odd-A Cu isotopes and ^{71,73}Ga"*

[1] All oral contributions unless specified otherwise

المنارة للاستشارات

- Scientific Seminar, IKS-KU Leuven, *"One-nucleon transfer reactions in the neutron-rich Ni region"*, April 2009
- BRIX-IAP workshop, Leuven, Belgium, *"One-nucleon transfer reactions in the neutron-rich Ni region using REX-ISOLDE"*, June 2009
- EURISOL User's group Topical Meeting, Catania, Italy, *"Coulomb excitation in the neighbourhood of ^{68}Ni using MINIBALL at REX-ISOLDE"*, December 2009
- Scientific Seminar, IKS-KU Leuven, *"The ^{66}Ni(d,p)^{67}Ni transfer reaction using MINIBALL - First results from IS469"*, February 2010
- MINIBALL Workshop, Leuven, Belgium, *"The ^{66}Ni(d,p)^{67}Ni transfer reaction using MINIBALL - First results from IS469"*, April 2010
- EURORIB'10 Conference, Lamoura, France, *"Single particle states in ^{67}Ni"*, June 2010
- BRIX-IAP workshop, Leuven, Belgium, *"Single particle states in ^{67}Ni"*, December 2010
- Scientific Seminar, IKS-KU Leuven, *"Single particle states in ^{67}Ni: ^{66}Ni(d,p)^{67}Ni transfer reaction using MINIBALL - First results from IS469"*, March 2011
- ECT Workshop "Recent Developments in Transfer and Knockout Reactions", Trento, Italy, *"Single particle states in ^{67}Ni"*, May 2011
- ARIS 2011, Leuven, Belgium, *"Single particle states in ^{67}Ni"*, Poster, May 2011
- EGAN Workshop 2011, Padua, Italy, *"Single particle states in ^{67}Ni"*, June 2011
- Rutherford Centennial Conference on Nuclear Physics, Manchester, United Kingdom, *"Single particle states in ^{67}Ni"*, August 2011
- MINIBALL Workshop, Cologne, Germany *"Single particle states in ^{67}Ni. Status of ^{66}Ni(d,p)^{67}Ni analysis"*, March 2012

المنارة للاستشارات

المنارة للاستشارات

المنارة للاستشارات

FACULTY OF SCIENCE
DEPARTMENT OF PHYSICS AND ASTRONOMY
NUCLEAR AND RADIATION PHYSICS SECTION
Celestijnenlaan 200D box 2718
B-3001 Heverlee
first.name@dept.kuleuven.be
www.website.kuleuven.be